Doctoral Thesis

Development of hyperspectral and RGB imaging systems for under-ice mapping of fine scale sea-ice biophysical properties

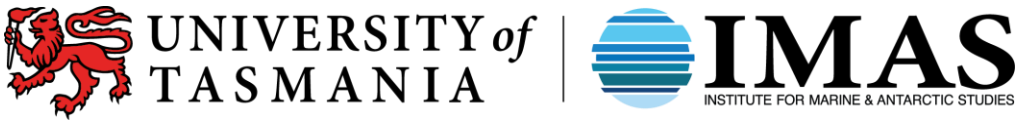

Author:

Emiliano Cimoli (BSc, MSc)

Supervisors:

Dr. Vanessa Lucieer, Dr. Klaus Meiners, Prof. Arko Lucieer, Prof. Andrew McMinn

A thesis submitted in fulfilment of the requirements for the degree of Doctor of Philosophy

In

Physical and Natural Sciences

Institute of Marine and Antarctic Studies, University of Tasmania

"Nobody ever figures out what life is all about, and it doesn't matter. Explore the world [and beyond]. Nearly everything is really interesting if you go into it deeply enough"

Richard P. Feynman

Acknowledgments

Nothing along these pages would have been achieved without the support of the marvelous people I have worked with and met during this epic journey and of course the ones supporting me from back "home" (whatever that is). Most importantly, these people made this journey an exciting and fun adventure, which at the end, is what stays with us the most.

My greatest gratitude goes first to my entire supervisory team for their stellar support through all stages of this project; teachers from whom I still have so much to learn. To my primary supervisor and colleague **Vanessa** for making all this possible in the first place. During the entire course of this venture, her teachings were more than purely academic, and without her support, this dream project would not have even started. I could not have had a better teacher to transmit me the love for the underwater world, its unexplored corners and the fascinating technology that drives its exploration and understanding. There was no obstacle she did not help me move forward and no opportunity that was left uncharted thanks to her. Thank you for your great guidance, the countless field adventures, the underwater tech adrenalin, the laughs, the patience, the core slicing, cable wrangling and *those* GPS coordinates.

To **Klaus** who will always remain to me as the ultimate sea-ice legend (either as *sub-zero* or *snappy* alike). Thanks for accepting me countless of times into your office to cover all my sea-ice and biology gaps and fueling my sea-ice algae hype no matter which idea I would come in with. Thanks also for caring for me beyond my pure academic performance. It's been an honour to share cigarettes with you in the field and to core as there was no tomorrow on the harshest of the continents.

To **Arko** for making all this technical feat feasible and manageable for me. Your aerial HI work and expertise was constant inspiration and encouragement for me to push HI to the under-ice world. Thanks for the many HI technical development and data processing discussions and for all the daydreaming together about all sort of new cool sensors and tech gear we could implement (we love that). Now we call it the TIE-FIGHTER, but perhaps, one day, it will be a Millennium Falcon.

To **McMinn** for giving me a sense me that there are deeper scientific purposes beyond spectral image analysis, thus, enticing my curiosity beyond my study field, and of course, for the engaging twitching conversations.

Thanks to **Antarctic Gateway Partnership (AGP)** and all the **AGP** and **IMAS staff, IT and media colleagues** for being so nice, helpful and effective under every occasion. In particular thanks to **Jenna P.** and **David L.** that made for me Gateway something of a beautiful family.

My greatest thanks to the **K043 2018-19 team FTW** and **ANTNZ staff.** In particular to **Andrew M.** and **Fraser K.** for their huge support, teachings and for making me appreciate that there is a marvelous world to study within a single diatom. Thanks for all the uncountable laughs and creativity for cooking. Thanks to **Kat**, best lab manager ever, and sample processing machine. Your

joyful presence in the field made me feel back into my beloved Mediterranean even over the frozen seas of Antarctica. To **Ken** and **Uncle Nev**, for their excellent field support and amazing company. Thanks to our official sponsor brands such as "**Café du sol**" (aka *shitty coffee*), "**Continental CNS**" (aka *shitty soup*), that kept the engine of these dirty drillers running under the harshest conditions. *Lililiu* to all **K043 family** and all the winching patience, it's been a privilege to be on the ice with you all. You have all gained a lifetime free pass to my Auntie's 5-layers parmigiana… *No Hurries Nooo Rushhh*!

To **R. Ballard**, whose technical support and constant advice was fundamental for the development of the TIE-FIGHTER. Thank you for being a friend and the best SOS mechatronic phone line on the planet, and thanks for humiliating my handicap (portable!) hammer.

I am grateful to **Lars C.** for his great support and feedback on various stages of this project and all the wise advices. May future *Julefrokosts* and *Flæskesteg* be with us!

A lot of thanks also to **Zbynek! Zbynek!** For his assistance on the final battlegrounds of this project, for the spectral camaraderie and for teaching me the importance of spectral rigor. It all began in *Antarctica-ca-ca-ca*, but who knows what will be next!

Special thanks as well to **Arjun** for his hyperspectral brotherhood and data processing support and sharing of ideas. Hoping for more Indian foodies in the future!

To **Juliane B.** and **Terra Luma group** for being so kind, helpful and patient with my several SOS calls and supporting every radiometric paradox.

To **Botty**, **IcyBot** and the **TIE-FIGHTER** itself that considering their nature, they battled gloriously in the difficulties of the Antarctic and made for some of the of the most adrenaline pumping moments of my life (and for the realization that all those years of Play Station had not been in vain).

Infinite thanks to my real family (**Pope, Mom & Bro**) that was as usual of crucial moral and spiritual support. Thanks for having imbued in me the capability to become passionate and curious about the weirdest things, one of the greatest gifts ever given to me in life.

Thanks to **Veronique**, for joining this adventure with me and giving me the courage to start with. Thank you for your kind support, company and affection. Nothing is forever and it was a joyful adventure until it lasted. Except for MF piggybank and company.

Finally, the most special thanks to my friends and PhD colleagues during these crazy years. They made this odyssey full of beautiful distractions and their company was a blessing until the very end. **Ole, Cristina, PB, Vecio, Flo, Sahan, Volpin, Campus, Gustavo, Pauline, Sandrita, JC, Giulia, Leo** and the many others that know who they are! A very peculiar thanks to the special persons I have met near the finish line of this journey. In particular to the ones who transformed the finish line existential void into a locomotive of dreams & lavender.

Thank you, **O-rings**.

Declaration

This thesis contains no material which has been accepted for a degree or diploma by the University or any other institution, except by way of background information and duly acknowledged in the thesis, and to the best of my knowledge and belief no material previously published or written by another person except where due acknowledgement is made in the text of the thesis, nor does the thesis contain any material that infringes copyright.

Emiliano Cimoli

January 2020

Authority of Access

Emiliano Cimoli

January 2020

Statement of Co-Authorship

This thesis has been written as a series of manuscripts, as a result there is some repetition of general methods and background information. The following people contributed to the publication of the following manuscripts:

Chapter 2 - has been published as:

Cimoli, E., Meiners, K.M., Lund-Hansen, L.C., Lucieer, V., 2017c. Spatial variability in sea-ice algal biomass: an under-ice remote sensing perspective. *Adv. Polar Sci.* 268–296. https://doi.org/10.13679/j.advps.2017.4.00268

- **Emiliano Cimoli** - University of Tasmania (94%)
- Klaus Meiners – Australian Antarctic Division (2%)
- Lars Chresten Lund-Hansen – Aarhus University (2%)
- Vanessa Lucieer - University of Tasmania (2%)

Chapter 3 - has been published as:

Cimoli, E., Lucieer, A., Meiners, K.M., Lund-Hansen, L.C., Kennedy, F., Martin, A., McMinn, A., Lucieer, V., 2017a. Towards improved estimates of sea-ice algal biomass: experimental assessment of hyperspectral imaging cameras for under-ice studies. *Ann. Glaciol.* 1–10. https://doi.org/10.1017/aog.2017.6

- **Emiliano Cimoli** - University of Tasmania (89%)
- Arko Lucieer - University of Tasmania (2%)
- Klaus Meiners – Australian Antarctic Division (2%)
- Lars Chresten Lund-Hansen - Aarhus University (1%)
- Fraser Kennedy - University of Tasmania (2%)
- Andrew Martin - University of Tasmania (1%)
- Andrew McMinn - University of Tasmania (1%)

– Vanessa Lucieer - University of Tasmania (2%)

Chapter 4 – has been published as:

Cimoli, E., Meiners, K.M., Lucieer, A., Lucieer, V. An Under-Ice Hyperspectral and RGB Imaging System to Capture Fine-Scale Biophysical Properties of Sea Ice. Remote Sens. 2019, 11, 2860. https://doi.org/10.3390/rs11232860

– Emiliano Cimoli - University of Tasmania (94%)

– Klaus Meiners – Australian Antarctic Division (2%)

– Arko Lucieer - University of Tasmania (2%)

– Vanessa Lucieer - University of Tasmania (2%)

Chapter 5 - is currently in preparation for publication as:

Cimoli, E., Lucieer, V., Meiners, K.M., Chennu, A., Castrisios. K., Ryan, K., Lund-Hansen, F., Martin, A., Lucieer, A., in prep. Hyperspectral imaging of sea ice cores to map microspatial variability of ice algal biomass. *Scientific Reports (Nature)*

– **Emiliano Cimoli** (89%)

– Klaus Meiners – Australian Antarctic Division (2%)

– Arjun Chennu – University of Bremen (2%)

– Arko Lucieer - University of Tasmania (1%)

– Andrew Martin - University of Tasmania (1%)

– Ken Ryan – Victoria University of Wellington(2%)

– Lars Chresten Lund-Hansen – Aarhus University (1%)

– Vanessa Lucieer - University of Tasmania (2%)

Details of authors roles:

Vanessa Lucieer, Klaus Meiners and Arko Lucieer contributed to project development and supervision. Andrew Martin and Fraser Kennedy provided field, logistics and laboratory support.

Arjun Chennu provided technical advice on specific section of Chapter 5. Ken Ryan contributed to the filed campaign and provided advice on sampling strategies. Katerina Castrisios and Neville Higginson contributed to field assistance and sample processing. Lars-Chresten Lund-Hansen provided feedback to manuscript revisions and general advice.

I the undersigned agree with the above stated proportion of work undertaken for each of the above published (or submitted) peer-reviewed manuscripts contributing to this thesis:

Emiliano Cimoli	Dr. Vanessa Lucieer	Assoc. Prof. Catriona MacLeod
Candidate	Primary Supervisor	Head of School
University of Tasmania	University of Tasmania	University of Tasmania
January 2020	January 2020	January 2020

Abstract

Polar sea ice is one of the largest biomes on Earth covering up to 6.1% of the area of the global ocean. Within this biome, sea-ice algae constitute a large, yet poorly quantified fraction of biomass contributing to polar marine productivity and large-scale biogeochemical cycles. Ice algae support the foundation of polar marine food webs by sustaining pelagic fauna, seeding planktonic blooms, and exporting organic material to the benthos. Advancing the capability to capture spatio-temporal dynamics of ice algae and its drivers is highly desirable.

Modern understanding of ecology advocates that the analyses of large-scale ecological patterns require the acknowledgment and integration of small-scale processes and that complex interactions occur at multiple scales. In sea ice, traditional sampling methods have struggled to capture and quantify patterns in algal community distributions due to a lack of methods that do not destroy the community and address microscale patterns (<0.1 m). Compounded with the challenges of surveying in polar regions, datasets remain fragmentary and coarse, hampering a mechanistic understanding and an ability to extrapolate and predict responses to environmental change. This doctoral research thesis aims to fill this methodological gap**.** It deals with the development, application, and assessment of passive hyperspectral imaging (HI) and photogrammetric approaches for quantitative microscale mapping of key sea-ice biophysical properties. The research developed a novel *in situ* under-ice platform and a field-deployable ice-core scanner. Their integration allowed for the retrieval of bio-optical regression algorithms to map chlorophyll-*a* both on ice cores and in linear transects beneath Antarctic sea ice

The thesis provides an under-ice close-range remote sensing perspective to the multidisciplinary problem of mapping biophysical properties in sea ice (Chapter 2). It starts by reviewing the current understanding of ice algal biomass variability, its environmental drivers, and highlights the missing links, thereby establishing the need for research development in this field. Radiative transfer in sea ice and the possibility to establish bio-optical relationships are the theoretical foundation of the proposed approaches and are therefore elucidated. A compilation of studies employing bio-optical models to retrieve biomass in sea ice is presented while discussing caveats and potentials for improvement. Technical and logistical trade-offs to be considered in under-ice radiation transfer mapping are discussed and illustrated, together with advances in emerging marine technologies that are changing the spatial scales of the surveys.

Chapter 3 presents an initial assessment of pushbroom HI technology to capture the variability of ice algae at the microscale using an innovative inverted sea-ice simulation tank. Through artificial illumination and controlled concentrations of algal consortia, HI was tested for a range of key HI parameters (e.g., different spectral resolutions). Exploratory image analysis revealed proxies of biomass matching inoculated abundances at unprecedented scales (a 0.8 x 0.8 m area at sub-mm

resolution). Considerations for sensor selection relevant to ice algal mapping were narrowed down through this assessment (e.g., ≤ 3.4 nm spectral resolution). The study laid out the fundamental steps for the deployment of *in situ* HI, whilst highlighting the suitability of artificial sea-ice tanks to mimic the under-ice light environment and for testing of key parameters to improve the methodology.

Chapter 4 details the development of a novel underwater sled system for capturing referenced and overlapping HI and RGB imagery of the under-ice habitat. The chapter focuses on the technical, logistical, and theoretical considerations that are behind the system development and design. Tested under fast ice off Cape Evans, Antarctica, the system proved to be capable of capturing proxies of ice algal biomass and under-ice topography for the first time *in situ* at sub-mm spatial resolution. A transect 20.1 m long with a 0.61 m swath was presented, and data quality over a 0.7 by 0.61 m subsample was assessed. Image acquisition parameters for meaningful data acquisition in a cold (-1.8 °C) and low-light ($E_{d,\ 400-700\,nm}$ = 0.35 ± 0.20 λ, W m^{-2}) environment were assessed. Overall this study established the foundation of an adaptable solution that unlocks many research opportunities for marine under-ice mapping. Potential scientific applications for the system, its limitations and future developments are discussed.

Chapter 5 describes a complementary, field-deployable, hyperspectral scanning set-up that enables spatially-explicit quantification of both the vertical and horizontal microspatial variability of chlorophyll-*a* proxies in sea-ice cores. It further enables the retrieval of bio-optical regression algorithms relating sampled chlorophyll-*a* to spectra. New spectral indices tailored to our test area were developed with this scanning system explaining up to 85% of variation in chlorophyll-*a*. The performance of novel indices is statistically validated and compared to traditional ones (e.g., NDIs). Chapter 5 presents a first attempt to apply the retrieved regression models applied to both the *in situ* and horizontal ice-core sections of hyperspectral images, yielding per-pixel chl-*a* in mg m^2. The unique under-ice habitat patterns captured are discussed in a biophysical context.

Underwater HI is a very novel technology and can be expected to revolutionise close-range underwater remote sensing of marine biogeochemical systems. This thesis pioneered HI coupled with photogrammetric approaches for the first time in extremely challenging polar marine waters beneath the ice. The trials of this technology and associated methodology have shed new light onto undocumented features of the under-ice habitat, which may permit the development of new research questions to understand this important biome.

Table of contents

List of figures

positive relationship. Blue connectors refer to a variable relationship. The black line connectors indicate that the factors are highly correlated. More information can be found in the text. Overall, sensor specifications need to be set according to deployment mode and to the environmental constraints (symbolized by the black dotted line). The optical system efficiency includes optical throughput of the lenses, the dispersive element efficiency, and the detector quantum efficiency. The scheme is valid for both non-imaging radiometers and HI. Spatial resolution refers to the ground sample distance of an imaging spectrometer. The spatial footprint refers to the circular footprint of normal spectrally resolved radiometer. SNR refers to Signal to Noise Ratio.

Figure 3.1 Illustration of the inverted sea-ice simulation tank and spectral signature of the LED artificial light source. The hyperspectral pushbroom scanner was mounted onto a motorized sliding rail at 1.2 m distance above the ice/water interface. The layered surfaces (glass, ice, water) cover an area of 0.85 m× 0.85 m. The distance from the camera fore-optics to the ice layer is 1 m. The illustration is not to scale.

Figure 3.2 a) Image of the inverted sea-ice simulation tank in the dark room setting with all external light sources off. b) Image of the inverted ice tank together with the motorized slider and the cylinder's set-up. c) The SPECIM AISA Kestrel 10 hyperspectral imager. d) High (H) algae abundance cylinder after two days of algae inoculation.

Figure 3.3 Results of PCA applied to the 1.7 nm spectral resolution frame of the ice surface. a) RGB composite of the hyperspectral image after algae inoculation displaying the performed biomass redistribution among cylinders. The RGB composite image is similar to what is observable by the human eye or normal imagery. b) First principal component (PC1) representing light intensity variability within the image. c) PCA loadings for each of the principal components. Algae absorption bands are clearly visible in PC2 at ~450 and 680 nm. d) Second principal component (PC2) representing algae biomass abundance variability. The colour bar is unit-less as representing PC intensities.

Figure 3.4 Principal component 2 (PC2) representing algae biomass variability for different spectral resolutions 1.7 nm a), 3.4 nm b), 6.8 nm c), respectively. The difference in biomass PC2 loadings between 1.7 and 3.4 nm is minimal. The figure outlines the working spectral resolution range for hyperspectral imaging aimed to capture algae biomass abundance. The test suggests that sensors with spectral resolution above 6.8 nm cannot be used for the purpose and for example discards the use of snapshot hyperspectral sensors compared to pushbroom scanners. The colour bar is omitted.

Figure 3.5 Comparison of radiance levels measured in the inverted ice tank with a series of Arctic under-ice radiance transects measured *in situ* with a Remotely Operated Vehicle (ROV) for different sea-ice conditions. The ice tank radiance is obtained from the hyperspectral frames. Mean ICE TANK is the mean between all pixels in the frame whereas Min ICE TANK is the pixel with minimum intensity (taken in a non-shadowed area). ROV transects data are publicly available from the study performed by Nicolaus and Katlein (2013) in Arctic sea ice. Sea-ice conditions varied from snow to no snow cover (from 2 to 10 cm

thickness), from First Year Ice (FYI) to Multi Year Ice (MYI) (from 0.3 to 3.8 m thickness) and ROV water depth varied from 1 to 8 m.

Figure 4.1 Concept design of the under-ice hyperspectral and RGB imaging system to capture fine-scale biophysical properties of sea ice. The system is designed to retrieve bio-optical relationship from downwelling sea-ice transmitted radiance. The sliding system aims to smoothly scan transects tenths of meters. It has a variable ski span of 0.82 to 1.2 m, a ski length of 1.48 m and a height of approximately 2 m. Its modular buoyancy system allows adjustment of the upward push against the ice and stabilizes the structure under different payload set-ups. The figure also shows the payload attitude reference system relative to the sensors orientation (heading, roll, and pitch). HI refers to Hyperspectral Imaging and FOV to Field of View.

Figure 4.2 Field deployment and operation concept for the under-ice hyperspectral imaging and RGB scanning system. Two worm gear winches provide highly controllable slow movement back and forth along predefined transect. Movement commands are provided via radio communication and manual winching. The support remotely operated vehicle (ROV) is used to establish a tow-line between the deployment hole and the opposite transect endpoint. The deployment and operation require at least three people. Figure is not to scale.

Figure 4.3 An overview of the payload main internal components, their allocation within the enclosure and volume required to host the payload. AK10 stands for AISA Kestrel 10. The figure also includes the payload attitude reference system relative to the sensors orientation (heading, roll and pitch).

Figure 4.4 Schematics of the electronic power and communication streams for the internal and the additional external under-ice payloads.

Figure 4.5 Field pictures of the first deployment at Cape Evans, Antarctica. a) The system control station together with the removable payload tray. **b**) The system deployed in the water prior to under-ice immersion. Visible is the external payload composed of the TriOS Ramses ACC and a set of four Lumen Subsea LEDs, and the prop maneuvering cradles. c) The system scanning over the selected transect underneath the highly productive fast-ice of Cape Evans. d) One of the worm gear winches at the opposite side of the transect in speed-up mode using a drill adapter.

Figure 4.6 Overview of the surveyed western transect produced with structure from motion (SfM) digital photogrammetry using the RGB imagery. Camera positions and Ramses ACC irradiance samples were synchronized to the same sampling frequency, so they match in space. Blocks A and B within the transect were selected for further image analysis. On top is a photograph of the transect direction viewed from above the surface. Displaying the typical survey conditions (little to zero snow) of the study area.

Figure 4.7 Display of the main data products of the developed under-ice payload. Block A and block B refer to two different subsections within the western transect that were selected for further analyses. **a**) Under-ice orthomosaic produced from the RGB imagery. b) Hillshade of the SfM derived digital elevation model (DEM) illustrating relief structure produced by the large cavities. **c**) Visual representation of the hyperspectral data cube for block A including block B as an RGB composite. Panel d) and e) display the high variability of radiance spectra for a selected variety of spots within block B (both unprocessed and smoothed with a Savitzky-Golay filter respectively). Panel f) display four of the darkest pixels within the image associated to extremely dense algal clumps. For all plots, spectrum shows a × 4 pixels spectral average which corresponds to approx. 1.2 mm pixel size. Native pixel size is 0.624 mm. A 0.14 m Kovacs ice core areal coverage is provided for scale reference only.

Figure 4.8 Two upward looking RGB image samples taken from the Sony a6300 camera dataset shown at full resolution. Both images display some examples of spotted under-ice feeders (circled). Left image shows a ctenophore (comb jelly) and right image shows a couple of circled amphipods. **a**) Image taken nearby the visible deployment ice hole. The image zooms into a large brine channel and further on the highly detailed under-ice skeletal layer. b) Image taken midway on the transect displaying the high concentration of oxygen bubbles produced by the photosynthesizing ice algae.

Figure 4.9 a) Mean ± one standard deviation of downwelling under-ice irradiance (E_d) spectra from the TriOS RAMESES ACC-VIS located near the ice water interface for the full 20.1 m transect. b) Mean ± one standard deviation of under-ice downwelling radiance spectra (L_d) from all the pixels of block B hyperspectral image subsample from the AK10. c) Mean ± one standard deviation of under-ice irradiance and radiance spectra normalized by area under curve for the Ramses ACC-VIS over all the transect and for all pixels of block B AK10 hyperspectral image. d) Mean ± one standard deviation of under-ice downwelling radiance (L_d) normalized by the maximum radiance pixel of all block B and corresponding to one of the cavities or secondary brine channels seen in the image ($L_{d\text{-}cavity}$) .

Figure 4.10 Results of principal component analysis (PCA, also known as EOF), applied to the spectral dimension of block B (hyperspectral image subsample of the western transect). Top images display the first three PC scores applied to every pixel of the image using corresponding loadings for each component. Bottom plots display the loadings for each wavelength for each principal component. Plot display as well the proportion of variance explained by each corresponding component. Light grey areas highlight the maximum chl-a absorption regions at 440 and 670 nm. Spatial resolution for PCA was maintained to a native 0.625 mm.

Figure 4.11 Application of spectral indexes as proxies of chl-a distribution over block b HI subsample. a) Results from the application of a commonly used index in sea-ice bio-optical literature, the normalized difference index (NDI), applied for wavelengths 648:567 nm on block B hyperspectral image subsample. b) Application of a novel index to sea-ice bio-optical literature, the area under curve normalized to maximal band depth (ANMB) between wavelengths 650 to 700, applied to the same block B. c) Plot of

continuum removed spectrum of three random pixels within block B to help visualizing the $ANMB_{650–700}$ concept and its association with chl-a absorption. For the color bars, higher values (towards red) correspond to higher expected biomass. Spatial resolution for the indices was binned to 1.2 mm.

Figure 5.1 An overview of the data acquisition workflow and hyperspectral imaging optical set-up. a) The ice core scanning set-up based on transmitted artificial illumination. b) and c) illustrate the mean ± standard deviation of radiance (*L*) emitted by the white and solar LED lamps entering the acrylic glass tray surface, respectively. d) 3D model reconstruction using Structure from Motion (SfM) digital photogrammetry on horizontal bottom-core sections. **e)** Ice core sample preparation for hyperspectral image acquisition along vertical and horizontal ice-core surfaces. A total of 6 vertical scans and 54 horizontal scans were acquired in this study.

Figure 5.2 A flowchart of the data-processing procedure to yield per-pixel biomass (as chl-a) estimates from hyperspectral imagery of core sections and *in situ.* a) and b) display the mean ± standard deviation of directional transmittance at 668 nm through an example ice core (ice core 37) and the under-ice imagery, respectively. The under-ice HI procedure is detailed in Cimoli et al. (2019) or Chapter 4. $L(\lambda)$ stands for spectral radiance and $T(\lambda)$ and $T_d(\lambda)$ for spectral transmittance and downwelling spectral transmittance, respectively. DN stands for Digital Number of raw imagery data.

Figure 5.3 a) The distinct under-ice habitat encountered at Cape Evans, Antarctica during Spring 2018, characterized by scattered large cavity features varying widely in diameter and depth. b) Block B under-ice image location and acquisition using the under-ice HI sliding system described in Cimoli et al. (2019) or Chapter 4. c), d) and e) display an oblique view of the bottom-core surface 3D models (top) and the complex micro-spatial variability of the under-ice structural features (below). Skeletal layer characteristics of land-fast sea are visible along with scale of observable brine channels and cavities.

Figure 5.4 Results of Principal Component Analysis (PCA) applied to three selected vertical ice-core scans (cores 22, 42 and 30). a) PCs loadings, PC1 accounts for >99.8 % of variation and loadings embody the spectral signature of the light source. PC1 scores map a proxy of light intensity. PC2 accounts for <0.05 % of variation and loadings are strongly associated with the chl-*a* absorption spectrum. PC2 scores map a proxy of biomass within the ice core vertical and horizontal dimensions. b) Horizontal scans and analysis of core 30 characterized by a large cavity feature (see Figure 3e). Panels c)-f) illustrate zoomed views of selected features of interest such as brine pockets and channels inhabited by ice algae. PCA was performed separately on vertical and horizontal section data.

Figure 5.5 Linear regressions between log-transformed fluorometrically-derived chl-*a* values and derived spectral indices using index computation method (1). Panel a) shows the Pearson correlation surface between all NDI waveband combinations and chl-a values displaying the selected optimal wavelengths. a) and b) illustrate NDI(587:621) and NDI(517:449) tested against sampled chl-*a.* d), e) and f) display regression performance of newly developed integrative spectral indices when tested against sampled chl-*a.* All regression plots differentiate samples coming from different light sources (e.g., white versus solar

LEDs) and vertical positioning (e.g., bottom, middle, or top). Regressions lines include 95% confidence interval of the coefficients (shadowed grey areas).

Figure 5.6 Panels a-d) display the RGB composite of selected bottom-core sections (top) and the application of the best performing regression model to the respective preprocessed hyperspectral images (below). The best performing linear model was derived using the log($AUC_{650-700}$) index (see Table 1). Sampled fluorometrically-derived chl-a values of each core section are provided to indicate scale of magnitude of biomass to be compared with the mapped ln(chl-a[mg m^{-2}]). High variability in biomass abundance can be observed within the 0.015 m^2 core surfaces as well as across cores.

Figure 5.7 Application of best performing regression model to the under-ice imagery. a) Framing of block B hyperspectral image subsample within the entire transect provides an idea of scale. b) Displays a GoPro HERO5 image taken post under-ice hyperspectral image acquisition and ice coring over block B. Panel c) shows the first attempt for quantitative mapping of chl-a by applying the log(AUC) index regression model on a per pixel basis to the preprocessed block B imagery. d) A high-resolution image of one of the large cavity features from block B and comprising an overlapping algal-web like structure. These algal-webs were common features on top of the cavities.

List of tables

Chapter 1

Introduction and thesis objectives

The sea-ice biome is extensively vast, covering up to 4-5 % of the global ocean surface during its maximum extent (for both the Arctic and the Antarctic) (Meier, 2016; Stammerjohn and Maksym, 2016). Sea ice algae, together with under-ice phytoplankton, constitute a large, yet poorly quantified fraction of polar primary production. Ice algal communities are typically dominated by diatoms, and estimates suggests that they are potentially highly productive amounting to 2-24 % of total primary production in -ice-covered marine areas (Arrigo, 2017; van Leeuwe et al., 2018). Beyond their role as primary producers, ice algae lay the foundation of key ecological interactions in polar marine environments. As ice algal growth occurs early in the season, ice algae provide a crucial food source for pelagic herbivores (Kohlbach et al., 2017, 2016; Meiners et al., 2018). As the season progresses, sea-ice declines, and the release of organic material from the ice can seed phytoplankton blooms or sink to the sea floor in support of benthic systems that have adapted to such seasonal cycles (Boetius et al., 2013; Gradinger, 2009; Leu et al., 2015; Wing et al., 2018).

The description of ecological patterns includes the description of variation in abundance of populations and communities over space and time (Levin, 1992). To develop a predictive theory, and enhance predictive capabilities, we are required to examine the ecological patterns in nature and develop theories that help assimilate observations across different scales (Chave, 2013; Levin, 1992). In particular, in order to understand large-scale patterns, we must integrate the effect of small-scale processes that operate within specific areas.

As polar sea-ice environments face imminent perturbation due to environmental change (Massom and Stammerjohn, 2010; Parkinson, 2019; Tedesco et al., 2019), it is of paramount importance to be able to map and understand the processes that control the patterns of ice algal biomass distribution over the sea-ice biome.

A characteristic feature of the ice algal habitat is that it features sharp physical and biological gradients that generate remarkably dynamic and variable spatio-temporal organizations at different spatial scales; from the micro- to the mesoscale. In this thesis, the tightly interlinked sea-ice biological (e.g., algal biomass, community composition and physiology) and physical (e.g., sea-ice and snow thickness and ice structure) properties are referred to sea-ice biophysical properties.

Understanding biophysical patterns in sea ice and their underlying drivers must begin by capturing their spatial variability quantitively through time. Nonetheless, as will be detailed further on in this

thesis, current methodologies to sample biomass in sea ice have struggled to accomplish integration across scales, and often lack the spatial and temporal resolutions required to properly quantify scales of variability – particularly at the microscale. Lack of information is accentuated if we consider the remote and inaccessible nature of polar under-ice environments that has rendered our datasets fragmentary and coarse.

At the macro- and geographical scales, we assume that the interplay of sea-ice biophysical properties is continuously varying as atmospheric and oceanographic conditions fluctuate and dictate ice formation and decline processes according to the region and time of the year (seasonality). Both ice formation and decline processes play important roles in the incorporation and release of organic content into the sea-ice matrix yet mechanistically little is known (Leu et al., 2015; Olsen et al., 2017; Ryan et al., 2006).

Concentrations of certain algal pigments in sea ice can be used as a proxy for the amount of biomass present or of other biological properties (e.g., photoacclimation) (Galindo et al., 2017; Meiners et al., 2018). This thesis focuses in particular on the variability and spectral retrieval of chlorophyll-a (chl-a) as the main pigment encompassing algal abundance and distribution (Cimoli et al., 2017c or Chapter 2). Estimates of chl-a in sea ice can be derived from fluorometric measurements of melted ice-core samples or from emerging under-ice radiation mapping using upward looking spectral radiance or irradiance sensors (e.g., Lange et al., 2016; Mundy et al., 2007). Spectral data retrieved from these sensors can be correlated to concentrations of chl-a through targeted spectral indices and linear regression (also referred in this thesis as bio-optical regression models) (e.g., Melbourne-Thomas et al., 2015). Under-ice optical radiation methods have allowed to greatly extend the spatial extent of the surveys through sensor integration onto Remotely Operated Vehicles (ROVs) (e.g., Meiners et al., 2017). Their non-invasive nature further permits to track the temporal evolution of biomass, for example, over a single spatial point using radiometers equipped onto L-arms (further described in Chapter 2) (e.g., Campbell et al., 2015).

At the mesoscale, both ice coring and under-ice radiation transfer mapping have been utilized to explore horizontal patterns of variability and its determinants for large >10s kms transects or for floe sized areas (e.g., Gosselin et al., 1986; Lange et al., 2016; Meiners et al., 2017; Swadling et al., 1997). Patterns were governed mostly by variability in light transmission, which depends on the sea ice and the overlying snow properties (e.g., thickness and depth), but also on the algal photoadaptation conditions and history (Campbell et al., 2015; Lund-Hansen et al., 2014). More complex interactions have also been observed at this scale including the interplay between currents, tides, bathymetry, under-ice topography and nutrient exchange processes (e.g., Dalman et al., 2019; Katlein et al., 2015; Monti et al., 1996).

The issue with pigment extraction approaches derived from melted ice core samples is that it entails destructive sampling of a single point in space and is also a highly laborious process. Under-ice spectral estimates remain rather coarse as the point samples integrate over relatively wide under-ice footprints (Forrest et al., 2019; Lange et al., 2016a; Wongpan et al., 2018). This can greatly

impact ecological interpretations both spatially and temporally. It results in under-sampling and underestimation of biomass variability and distribution in sea ice at most scales observed, and particularly at the microscale.

In fact, at the microscale, various physical, chemical and biological drivers interplay to shape the ice algal communities' variability across the interstitial pore spaces and along brine channels of the sea-ice matrix (Arrigo, 2017, 2014; Lund-Hansen et al., 2016). In addition, vertical dynamics of algal biomass are largely understudied, partially because it's very challenging to capture the fine scale dynamics at which these processes evolve. The available methods consist of cutting discrete sections (1-3 cm) along the core length, followed by filtration and laboratory processing (e.g., Aumack et al., 2014; Fritsen et al., 2011).

In response to these limitations, the essence of this research project is to assess the feasibility and potentials of close-range Hyperspectral Imaging (HI) to be adapted to map the microspatial variability of sea-ice algal biomass *in situ* and on sea-ice cores and develop the means to achieve this. A side-goal is to explore the potential of using underwater digital photogrammetry in-tandem with HI to retrieve fine-scale under-ice topography (a poorly understood biomass driver). The methodology is also termed Structure from Motion (SfM) and further supports in providing highly detailed visual information of the under-ice habitat from the RGB imagery.

HI is more correctly referred to as imaging spectroscopy. HI as a term has gained increasing popularity in the remote sensing community and is thus here preferred (Bioucas-Dias et al., 2013). HI combines optical imaging and radiative spectroscopy at high spectral resolutions (hence the term "hyper"). The first deals with the visual representation of a target by capturing electromagnetic radiation on a sensor following transmission through its fore-optics, the latter deals with the acquisition and analysis of spectral signatures following light-matter interactions.

Processing of hyperspectral images deals with the detection, classification or quantification of features of interest for each of the finely resolved spatial pixels (Aasen and Bolten, 2018; Amigo et al., 2015; Bioucas-Dias et al., 2013). Quantification is of particular interest in this thesis, and deals with the development of finely tuned relationships between the spectra and an ever-growing array of retrievable biochemical properties of a target (e.g., chl-a) that can then be applied on a per-pixel basis (Aasen and Bolten, 2018; Adão et al., 2017; Amigo et al., 2015).

Terrestrial remote sensing of ecological systems is undergoing a real renaissance through the application of close-range HI and photogrammetric approaches (e.g., Aasen and Bolten, 2018; Näsi et al., 2015). A great example is mapping of fine scale biochemical properties *in situ* from payloads being equipped onto Unmanned Aerial Systems (UASs) (e.g., Adão et al., 2017; Arroyo-Mora et al., 2019; Fraser et al., 2016). Ex situ, under controlled illumination conditions, HI has been further employed to: a) better understand light interactions of the surveyed targets and their spectral imprints explicitly, b) to create baselines and calibrate spectral indices with benchmark laboratory measurements or c) to look at perspectives of the target that are non-retrievable or hidden from the

in situ perspective (e.g., vertical variability from cores) (e.g., Garzonio et al., 2018; Hobley et al., 2018).

Analogously to terrestrial HI applications, close-range and *in situ* underwater HI holds tremendous potential to create biogeochemical maps of seafloor properties (Johnsen et al., 2013). Proximity sensing using HI in marine science is an emerging methodology with only three other systems being documented in the literature that can be deployed underwater. These include a diver-operated system for coral mapping in shallow tropical waters (Chennu et al., 2017), a stationary rail system for repeat imaging microphytobenthic habitats (Chennu et al., 2013) and a commercial solution that can be mounted onto ROVs or Unmanned Surface Vehicles (USVs) (Dumke et al., 2018a; Foglini et al., 2019). Other advantageous applications of HI in a marine science context involve the analysis of organism samples ex situ (e.g., Barillé et al., 2017; Chennu et al., 2015; Letnes et al., 2019) or stationary set-ups located above the water surface for repeat monitoring of quadrats in shallow water (e.g., Caras and Karnieli, 2015).

There have not been any studies that have explored the application of HI and digital photogrammetry to map biophysical properties of the productive under-ice environment before, nor has HI been tested in polar marine waters prior to the inception of this project. The sea ice acts as a shield to any aerial based optical remote sensing application that aims to monitor biophysical properties beneath the sea ice. We are therefore required to deploy underwater payloads that can navigate underneath it with upward looking sensors that measure light transmitted through the sea ice. Passive HI (in the absence of artificial illumination) of light transmitted through the sea ice is substantially different than applications dealing with light being reflected from the imaged target. Primarily, we need to deal with the technical and logistical complexities associated with HI technology being deployed under-ice. Light transmitted through the ice pack can be reduced from 0.1 to 10% of the incoming solar radiation. Sensors measuring under such conditions are expected to be pushed to their sensitivity limits, with cascading implications for hyperspectral image acquisition parameters and system development.

Secondarily, we need to understand the complex interactions of light being transmitted through a highly scattering and variable medium and how this influences the retrieved spectral imprints. In addition to system development and meaningful HI data acquisition, chl-a needs to be detectable in quantitative units (e.g., concentration per m^2) through the development of bio-optical relationships linking retrieved spectra with chl-a.

A variety of spectral indices and regression approaches have been applied to map chl-concentrations *in situ* through under ice radiation mapping with radiance or irradiance (cosine corrected) sensors mounted on L-arms, with varying degrees of success (Forrest et al., 2019; Melbourne-Thomas et al., 2015; Wongpan et al., 2018). Research from different biomes shows that developed bio-optical regression models still reserve considerable potential for improvement (e.g., Feng et al., 2017; Malenovský et al., 2013; Verrelst et al., 2019) and the large promise of hyperspectral data for habitat mapping is then to enhance the development of such relationships.

This doctoral thesis comprises a combination of technical and scientific objectives which are summarized in Figure 1.1. As with the development of any new methodology, it required to undergo gradual testing and exploratory phases. Indeed, the thesis starts with a thorough appraisal of the scientific research needs to develop such methodology, together with its theoretical and technical foundations (aims of Chapter 2). The research project then proceeds with the first laboratory trials during which HI was assessed for sea ice algal biomass mapping in an inverted sea-ice simulation tank with inoculated algal consortia (Chapter 3). Chapter 3 further aims to inquire about the capabilities of the ice tank to physically resemble the under-ice environment and wants to advertise its capabilities to further investigate key aspects of under-ice HI research.

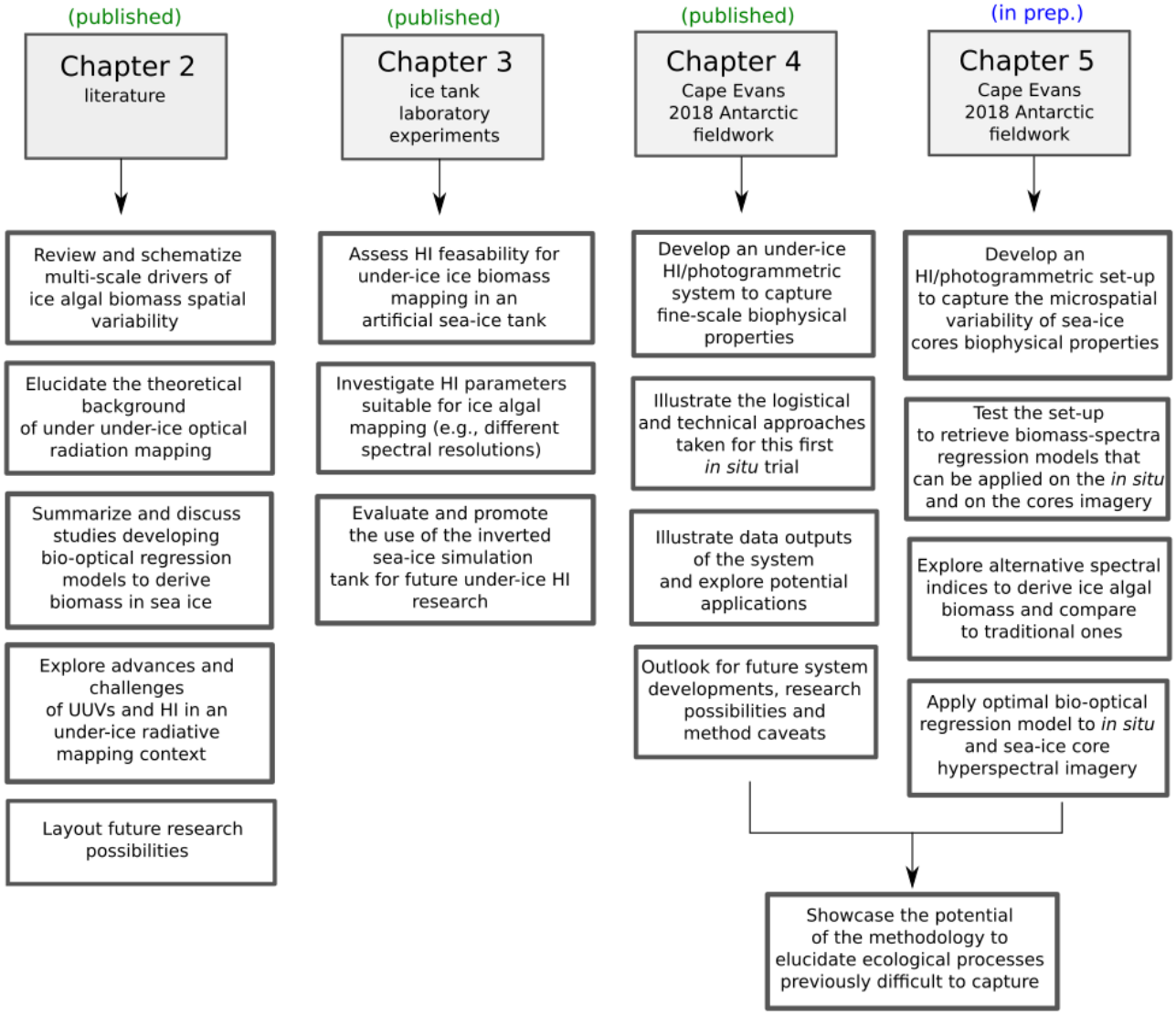

Figure 1.2 Summary of objectives and data sources for each of the thesis chapters. UUVs stands for Unmanned Underwater Vehicles (UUVs). HI stands for Hyperspectral Imaging.

The proof-of-concept work conducted in the laboratory led to critical insights for the development of payloads that are able to be deployed *in situ*. Chapters 4 and 5 provide a description of hyperspectral and RGB imaging systems and associated data processing workflows to retrieve quantitative chl-a in the field and 3D models of the under-ice surface using photogrammetry. Data for these two chapters were collected under the highly productive Antarctic fast ice of Cape Evans (McMurdo Sound), in the Ross Sea during the field season November-December 2018.

Chapter 4 first describes the actual field-instrument for *in situ* HI of algal biomass mapping beneath the ice and focuses on the technical and logistical means undertaken for coherent hyperspectral and RGB image acquisition. In order to develop a methodology that exploits this technology to derive bio-optical regression models, Chapter 5 presents an ice-core imaging set-up that not only permits to baseline spectral data from HI with fluorometric chl-a estimates, but also allows to capture the microspatial variability of chl-a of sectioned ice-core surfaces and along the vertical dimension. For this purpose, traditional and novel indices were tested and compared with the aim to identify the optimal regression algorithm for the surveyed study site suitable for validation of HI data.

While Chapters 4 and 5 are of methodological in nature, further objectives were to showcase the potential of the unprecedented empirical data gathered to understand the microscale variability of ice algal biomass and elucidate some of the underlying ecological processes that regulate its abundance and distribution.

Chapter 6 concludes with a summary of the technical achievements of the thesis and provides an overview of the ecological insights gained during testing; insights that entail the significance of the proposed methodology in an under-ice context. Encountered difficulties, together with the way forward towards the standardization of HI and RGB photogrammetry for under-ice studies are also provided.

Chapter 2

Spatial variability in sea-ice algal biomass: an under-ice remote sensing perspective

2.1 Introduction

Sea ice is a complex and dynamic three-phase medium consisting of an ice matrix permeated by brine pockets and channels, and containing air bubbles (Arrigo, 2014; Petrich and Eicken, 2009). It serves as a habitat for a variety of organisms such as viruses, bacteria, ice algae, heterotrophic protists as well as small metazoans (Arrigo, 2014; Thomas and Dieckmann, 2002). Sea ice algae assimilate carbon through photosynthesis and contribute to primary production of the polar oceans (Kohlbach et al., 2016; Lizotte, 2001; McMinn et al., 2007), influence large-scale biogeochemical cycles (Vancoppenolle et al., 2013), and determine rates of carbon export (Boetius et al., 2013). Ice algal communities form the base of the polar marine food web by providing a crucial food source for herbivore grazers during winter and spring, when pelagic food is very scarce (Flores et al., 2012; Kohlbach et al., 2017; Leu et al., 2015). Ice algae released into open waters during spring melt of the ice, can seed phytoplankton blooms (Mundy et al., 2014; Smith and Nelson, 1985; Søreide et al., 2010), with flow-on ecological effects in the underlying water column, coastal benthic zones and the deep sea (Boetius et al., 2013; McMinn et al., 2012; Post et al., 2013). In addition, ice algae can affect sea-ice physical properties due to absorption and conversion of solar energy into heat, thereby enhancing the localized melting of the ice (Castellani et al., 2017; Zeebe et al., 1996).

Sea-ice algae biomass is characterized by high spatio-temporal variability (Arrigo, 2017; Leu et al., 2015) (Figure 2.1). Reported depth-integrated biomass values per unit area can range from 1 to 340 mg chlorophyll-a (chl-a) m^{-2} in the Arctic and from <1 to 1090 mg chl-a m^{-2} in the Antarctic (Arrigo, 2017), however, they are typically <100 mg chl-a m^{-2} and often <10 mg chl-a m^{-2} in Antarctic pack ice (Meiners et al., 2012).

High ice algal horizontal patchiness has been observed across multiple spatial scales by different means (Figure 2.1). These include ice-coring studies using chl-a as a biomass proxy (Gradinger, 2009; Meiners et al., 2012) as well as fluorometric measurements of the ice-water interface *in situ* (Rysgaard et al., 2001).

At the millimeter-scale, ice algae display poorly understood distribution patterns across the skeletal ice layer (Hawes et al., 2012; Lund-Hansen et al., 2016). At the decimeter scale, chl-a concentrations can vary by one order of magnitude within less than one meter (Spindler and Dieckmann, 1986; Steffens et al., 2006). At the meter to kilometer scale (mesoscale), considerable variations in chl-a concentrations between sampling stations have been observed and linked to different sea-ice types and environmental properties such as snow cover (Gradinger, 2009; Lange et al., 2016a; Meiners et al., 2017; Ryan et al., 2006) (Figure 2.1).

Greater complexity of ice algal biomass variability is added if the vertical distribution (Arrigo et al., 2014; Meiners et al., 2012) and the temporal evolution are considered (Leu et al., 2015). Ice algal biomass is typically concentrated in the bottom-ice layers (< 0.1 m) and at the ice-water interfaces with access to nutrient-rich under-ice water (Arrigo et al., 2014). However, high biomass can occur in surface and internal sea-ice layers directly depending on variations in the sea-ice physical properties influenced by snow-loading, melt and flushing, infiltration from seawater, as well as ice growth processes (Arrigo et al., 2014; Fritsen et al., 2011; Meiners et al., 2012).

High ice algal biomass temporal variability has been observed on seasonal, monthly and weekly scales (Campbell et al., 2015; Leu et al., 2015; Sibert et al., 2010). Following a typically dormant winter season, biomass growth can encompass 3−4 orders of magnitude over the course of the spring bloom. Consequently, the differentiation between temporal and spatial variability blurs for measurements taken during the spring season with inevitable consequences for the comparison of observational studies from different areas (Leu et al., 2015).

Furthermore, distinct regions and sea-ice types demonstrate different ice algal community structures and biomass ranges (Arrigo et al., 2014; Meiners et al., 2012). Algal species composition and biomass concentrations differ significantly between Arctic, Antarctic and non-polar ice-covered marine ecosystems (Arrigo, 2017; Horner et al., 1992; Kaartokallio et al., 2017). Differences in ice type (e.g., land-fast or pack ice) or ice age (e.g., multi-year or first-year ice) play key roles in the observed chl-a distributions (Kattner et al., 2004; Lange et al., 2017).

Abiotic drivers of algal spatial variability are multiple and interrelated in various ways. Large-scale horizontal patchiness can be mostly attributed to the continually changing physical properties of the snow cover and of the sea ice (e.g., temperature, brine salinity and thickness), as well as nutrients and the overall light availability. These drivers are governed by latitude, season, ice dynamic and thermodynamic growth processes, seawater salinity and meteorological conditions that change on synoptic time scales (Arrigo, 2017; Arrigo et al., 2014; Mundy et al., 2005). Also, ice-bottom roughness and sub-ice hydrography, both driving ocean-ice exchange processes, have been shown to control ice algal distribution on various scales ranging from millimeters to kilometers (Lund-Hansen et al., 2016; Sibert et al., 2010). Determining how sea ice algal biomass varies and fluctuates together with different physical and biogeochemical parameters is critical to enhancing knowledge of polar marine ecosystem function and its response to environmental changes (Leu et al., 2015; Massom and Stammerjohn, 2010).

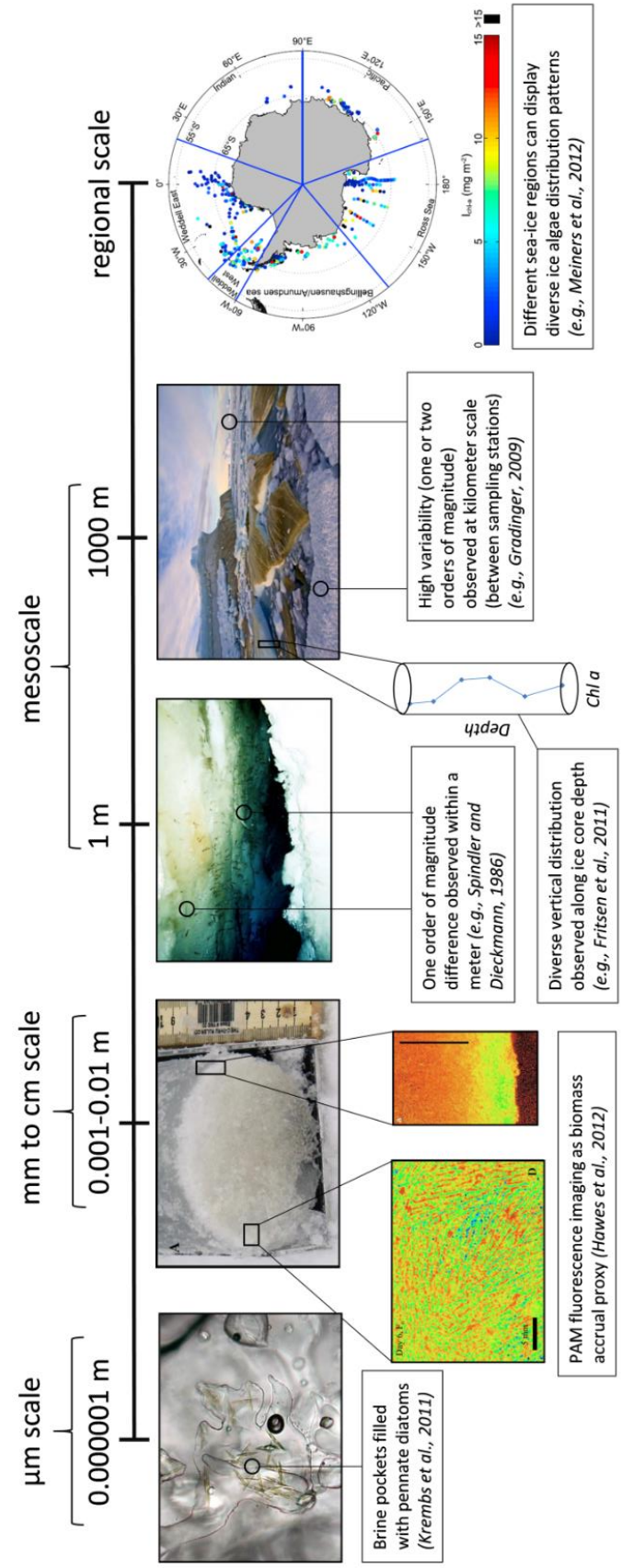

Figure 2.1 Overview of scales in sea-ice algae biomass spatial variability. At millimeter scale, fluorescence yield provides a good proxy of their distribution horizontally and vertically. Over the centimeter to meter scale, ice coring is the main method to estimate ice algal biomass (using chl-*a* as proxy). Vertical variability is measured by dissection of the ice cores in multiple sections providing discrete samples of the vertical distribution. Sea ice algae display diverse distribution patterns and concentration ranges across different regional sea-ice zones as well as in different ecosystems (e.g. Arctic, Antarctic and sub-Arctic areas).

Contrary to phytoplankton biomass and primary production which can be derived from satellite-based ocean color data, sea-ice algae cannot be monitored with above surface sensors, and conventional sea-ice biomass sampling is conducted via ice-coring (Miller et al., 2015). This results in deficits in spatial and temporal observations which are primarily attributed to the coarse nature of ice-coring surveys. Other methods used to determine ice algal biomass include diver-operated fluorometers (Rysgaard et al., 2001) or simple imagery data (such as video or still photographs)(Ambrose et al., 2005; Gutt, 1995; Katlein et al., 2015b), but are also rather limited as they are either highly demanding, logistically expensive or don't provide quantitative information.

This becomes particularly critical when considering the vast areal coverage of sea ice which affects 7 % of the surface of the Earth and about 12 % of the oceans. Any attempts to extrapolate point data to these vast areas are inaccurate if the investigated parameters exhibit the aforementioned variability and if the magnitude of such spatial variations is unknown. Assessing spatial variability is also critical to guide sampling efforts towards suitable scales (Swadling et al., 1997). The current lack of knowledge also impedes the formulation of quantitative relationships between ice algal patchiness and other sea ice physical parameters such as snow depth and ice thickness (Meiners et al., 2017).

Together this prevents accurate estimation of ice algal biomass and ice-associated production through up-scaling and hampers improvements in parametrization and evaluation of biogeochemical sea ice models (Leu et al., 2015; Steiner et al., 2016; Vancoppenolle et al., 2013).

In response to these sampling limitations, close-range under-ice optical remote sensing techniques are emerging as a non-invasive alternative method to quantify ice algal biomass from underneath the ice (Campbell et al., 2014; Meiners et al., 2017; Melbourne-Thomas et al., 2015; Mundy et al., 2007). Based on measured light spectra transmitted through the sea ice, empirical biomass-spectra relationships can be retrieved and used to estimate chl-a biomass in sea ice. An example is the identification of optimal Normalized Difference Indexes (NDIs), technique that has gained popularity due to its relative simplicity and accuracy (Lange et al., 2016a; Melbourne-Thomas et al., 2015). Once a relationship for a specific area is established, sensors can be mounted onto Unmanned Underwater Vehicles (UUVs) or ship-based under-ice trawl nets (Lange et al., 2016a; McDonald et al., 2015; Meiners et al., 2017), thereby significantly improving the spatial coverage of surveys. Further advances in the methodology are in the field of Hyperspectral Imaging (HI), which has strongly improved close-range surveying approaches in other disciplines (Amigo et al., 2015; Huang et al., 2014; Lu and Fei, 2014). Unlike normal radiometers, HI sensors can collect spatially continuous information from across the electromagnetic spectrum of the feature of interest, in this case, the ice-water interface. The first assessment of its application under controlled laboratory conditions has highlighted the potential of HI to provide an unprecedented view of ice algae spatial distribution through millimeter-scale resolution imagery of a square meter surface area (Cimoli et al., 2017a or Chapter 3).

While the application of under-ice optical hyperspectral technologies *in situ* is a desirable step-forward, considerable research effort is required before its implementation as a standard field-sampling technique. Aside from understanding the complex optical properties of the target, we also need to understand the complexity associated with both dynamic under-ice sensor deployments and associated data processing techniques.

In this context, under-ice optical remote sensing methods display a highly multidisciplinary nature involving fields of marine optics, radiative transfer, photobiology and cold region engineering. Contrary to above-surface remote sensing which collects spectral data from downward looking sensors in reflection mode, upward-looking sensors under ice gather light in transmission mode. Along with optically active components within the sea-ice cover (e.g., algae, detritus, brine and air pockets, Chromophoric Dissolved Organic Matter (CDOM), and inorganic materials such as mineral particles), the light traverses an optical complex multi-phase scattering medium (the sea-ice layered matrix) and the water-column before reaching the sensor (Perovich, 1996). Therefore, a series of geometric and transmissive properties of the light field need to be considered when measuring and interpreting hyperspectral data from underneath the ice (Katlein et al., 2016). Also, the layered and vertically variable sea-ice structure provides diverse microhabitats for algae with concomitant implications for their photophysiological adaptations and bio-optical properties and thus influencing spectra-biomass relationships and their inter-regional validity (Lange et al., 2016a; Melbourne-Thomas et al., 2015; Wongpan et al., 2018).

Considering the growing need of observational studies capturing the highly variable sea-ice environment (Miller et al., 2015; Steiner et al., 2016; Vancoppenolle et al., 2013), the aims of this review are to provide a comprehensive overview of under-ice optical remote sensing techniques to measure algal biomass, their limitations and research prospects. This includes a discussion of the potential opportunities to improve our understanding of variability in sea-ice algal biomass, as well as the complex interactions between the associated environmental drivers.

The aims of this review can be summarized as follows:

• Review observational studies treating sea-ice algae biomass spatial variability at multiple spatial scales, and briefly schematize its environmental drivers and outline some key relationships.

• Provide a brief overview of sea-ice radiative transfer and bio-optical research relevant to sea-ice algae under-ice remote sensing methods.

• Summarize current studies employing sea-ice biomass-spectra regression algorithms derived from under-ice optical remote sensing, chart identified relationships and outline the caveats and future research fronts of the methodology.

• Explore the advances and future challenges associated with underwater camera mounting platforms such as UUVs and the implications for HI.

• Layout the research possibilities of the methodologies to improve our understanding of sea-ice algal spatial variability and identify the environmental drivers.

It should be noted that this review provides a summary of the environmental parameters that drive ice algal variability, this is not an ecological review of the sea-ice environment. The focus here is given to observational studies involving measured spatial variation of biomass at multiple spatial scales, and the efforts towards its quantification using emerging techniques. We refer to other recent comprehensive studies treating sea-ice algal phenology (Castellani et al., 2017; Leu et al., 2015) and ice-associated ecosystem function (Arrigo, 2017, 2014).

2.2 The drivers of sea-ice algal spatial variability

Table 2.1 lists relevant studies coupling biomass proxies (such as chl-a) with other sea-ice environmental parameters in a spatial analysis context. We refer to spatial variability as to any variation of the biomass proxy's magnitude over space associated with changes in the sea-ice environment. It's important to notice that the magnitude of variation is typically relative to the studied site. For instance, in Kangerlussuaq (Greenland), measured biomass varies around 0.5-1 mg chl-a m^{-2} (Lund-Hansen et al., 2016) and an increase by 0.5 mg chl-a m^{-2} is considered very high. In contrast, at Cape Evans (Antarctica), biomass abundance has been observed to vary spatially between 4.4 and 143 mg chl-a m^{-2} (Ryan et al., 2006).

For each study, Table 2.1 includes location, ice type, date of the survey, sampling method employed, spatial scale examined, main environmental parameters measured or discussed, and the spatial analysis method applied (if any). Rows of Table 2.1 follow an increase of spatial sampling scale. The table emphasizes the high spatial variability observed at all the scales ranging from the millimeter to the mesoscale for both polar regions as well as temperate ice-covered areas.

The most employed proxy for mapping ice-algae biomass distribution in sea ice is chl-a (Miller et al., 2015). Estimates of chl-a concentration are mainly derived from fluorometric analyses on melted sea-ice core samples (Miller et al., 2015). However, other techniques have been used to measure algal biological properties *in situ* such as the fluorescence-based Diving-PAM (Pulse Amplitude Modulated fluorometry) (McMinn and Hegseth, 2007) and on ice cores with the Imaging-PAM (Hawes et al., 2012). While these are mostly used to detect chl-a fluorescence kinetics, in these examples they have been used as proxies of biomass distribution. Other methods for qualitative mapping of algal distribution rely on standard RGB imagery (Gutt, 1995; Katlein et al., 2015b). At this stage, only a few studies employ under-ice light spectra to biomass conversion algorithms to monitor spatial variability. A limited number of emerging numerical models feature tests on drivers of biomass variability on large-scales (Castellani et al., 2017; Sibert et al., 2010; Tedesco and Vichi, 2014), though numerical models are out of the scope of the review and will not be considered further.

Table 2. 1 Compilation of observational studies on sea-ice algal biomass spatial variability (as chl-*a* or other proxy) and associated environmental drivers. The table follows an increasing order of spatial sampling scale and resolution. FYI refers to First Year Ice, MYI to Multi-Year Ice. PAM refers to Pulse Amplitude Modulated (fluorometry). Statistical method used refers to the method employed (if any) to assess spatial variability or to estimate the correlations between biomass proxies and any of the analysed co-variates. ANOVA stands for analysis of variance.

Study	Region/Ice type/Date	Methods	Biomass variability scale observed	Main biomass variability drivers assessed, and statistical method employed (if any)
Hawes et al., 2012	• Kangerlussuaq, West Greenland • FYI in a frozen fjord • March-April 2011	Ice coring and PAM fluorescence imaging	Daily time series of sub-millimeter resolution PAM imagery (30 × 23 mm).	Brine channel evolution, ice crystal development, and salinity.
Lund-Hansen et al., 2014			Visualization of brine channels, ice crystals and	Snow-cover (through artificial removal) and photophysiology.
Lund-Hansen et al., 2016			mm-scale distribution and accrual.	Ice growth, surface roughness, water flow and nutrient availability. Inquires role of ice-water boundary layer and ice roughness.
Krembs et al., 2002	• Experimental ice tanks with water flows and observable structure relief	Ice tank samples and visual inspection	cm scale variability observed along specific sections of experimental ice tank.	Under-ice relief structure. Water flow altering pore water flux regimes and influencing nutrients exchange.
Rysgaard et al., 2001	• Young Sound, Northeast Greenland • FYI and MYI. • June-July 1999	Ice coring and diving PAM	Incremental cm scale samples over L-shape 10 m transects. Process repeated for multiple sampling stations (100 $s \cdot m^{-1}$). High variability on 50—100 m patches. Low variability on 0.025—5 m patches.	Light availability, algae photosynthetic activity, influence of grazing and physical removal/inhibition of algae by salinity fluctuations. Differences in pack ice and fast ice. Employs spatial autocorrelation to analyse the 2-dimensional distribution.
Eicken et al., 1991	• North-western Weddell Sea • MYI (2 years) ice floes • October-November 1988 and September-October 1989	Ice coring	Grids of gradual spacing (0.25 m, 2 m, and 20-m). Process repeated at mesoscale (km) distance on different floes. Variations up to one order of magnitude on < 2 m. Variability found almost independent of scale.	Ice texture, salinity, pore structure, and nutrient concentrations. Differences in second-year ice and first-year ice.

Continued

Study	Region/Ice type/Date	Methods	Biomass variability scale observed	Main biomass variability drivers assessed, and statistical method employed (if any)
Swadling et al., 1997	• Davis Station, East Antarctica • Fast Ice • April 1994	Ice coring	Hierarchical sampling at the mesoscale (m to km). High variability between locations at the km scale and high patchiness at 0.5—1 m apart.	Salinity, chl-*b*, and metazoan abundance. Employs 3-factor nested analysis of variance (ANOVA) to assess variation.
Ambrose et al., 2005	• Chukchi Sea • FYI • June 1998	ROV algal cover imagery and ice coring	Mesoscale transects of 20—85 m for different stations which are tenths of km apart. 1 m deployment depth. 1 cm resolution of the images.	Snow depth, ice thickness, ice structure, ice salinity, water pigments. Algae cover correlation with floe edge distance. Discuss transport over benthic systems. Employs Pearson correlation coefficients to examine relationships.
Welch and Bergmann, 1989	• Resolute, N.W-T, Canada • FYI (congelation ice) • 1984-86	Ice coring	Long-term study of variability controls over different sampling stations at tenths of km distance.	Grazer's abundance, light availability, nutrients and habitable pore space. Differences in old and new ice.
Arrigo et al., 2014	• Amundsen Sea. • Diverse ice types. • December 2010-January 2011	Ice coring	Zonal transect surveys at multiple sampling stations distanced hundreds of km.	Nutrients, salinity, temperature, ice thickness, snow depth, optical properties (including pigment composition) and surface flooding.
Gutt, 1995	• Northeast Greenland • FYI • June 1993	ROV imagery descriptive analysis	One 150 m transect.	Under-ice topography linked with different types of under-ice algal aggregations.
Fritsen et al., 2011	• Bellingshausen Sea • FYI • September 2007	Ice coring	Different vertical distributions of chl-a within three sites 50—75 m distant.	Snow cover, ice thickness and optical properties on vertical variability.
Lange et al., 2015	• Lincoln Sea • FYI and MYI. • Three consecutive spring seasons from 2010 and 2012	Ice coring	m distance samples for various stations at km scale distance.	Snow depth, ice thickness, ice texture, salinity and presence of hummock features. ANOVA for effect of ice age classes and texture. Logistic regression for influence of snow depth and derived optical properties.
Li et al., 2016	• Weddell Sea • Different types of sea ice • August-October 2006	Ice coring	Samples at several stations separated by km distance and mainly looks at vertical distribution.	Ice core texture, porosity, ice thickness, temperature, salinity and pigment content.
Spindler and Dieckmann, 1986	• Weddell Sea • January-February 1985 • One fast ice station and one Ice floe	Ice coring	Parallel sampling at 30 cm apart and transects of 3 km separated. Observed high variability at 30 cm apart meanwhile at 3 km distances did not observe high variability.	Foramiferal abundances and salinity.
Steffens et al., 2006	• Gulf of Bothnia, Baltic Sea • Different types of ice • March 2004	Ice coring	Hierarchical sampling with spacings of 10 cm, 2.5 m, 25 m, 250 m and 2.5 km. Observed high variability for all the spatial scales.	Ice salinity, pheophytin content, dissolved nitrate plus nitrite, dissolved organic carbon and nitrogen, snow depth, ice thickness and ice structure. Parameters analysed

				with nested ANOVA. Pairwise relationships using Spearman correlation. Multivariate relationships using principal component analysis.

Continued

Study	Region/Ice type/Date	Methods	Biomass variability scale observed	Main biomass variability drivers assessed, and statistical method employed (if any)
Meiners et al., 2017	• Weddell Sea • Pack ice floe • September 2017	ROV based under-ice optical remote sensing	100 m by 100 m area. Effective grid resolution of 1 m. Observed within floe scale patchiness of sea ice algae.	Snow depth, ice thickness and sea ice freeboard. Empirical variograms to explore scales of spatial variability. Relationships analysed with Generalized Additive Model approach.
Granskog et al., 2005	• Gulf of Finland, Baltic Sea • FYI, Landfast ice • February, March and April 2003	Ice coring	Mesoscale transects from 40 km to small <20 m scales. At small scales samples in arrays with core spacing of 0.2 m, 2 m, and 20 m. No evidence patchiness at scales <20 m. Sampled over ice season for small-scale patchiness.	Salinity (ice porosity), stable oxygen isotopes, nutrients and dissolved organic carbon. Relationships between parameters studied using non-parametric Spearman rank-order correlation.
Robineau et al., 1997	• Saroma-ko Lagoon, Sea of Okhotsk • March 1992	Ice coring	Three scales of variation were considered. From the mesoscale (0.02－4 km) to small horizontal variability (0.2－10 m).	Snow depth, ice thickness and ice-bottom salinity. Assessment using linear correlations complemented by path analysis.
Lange et al., 2016	• Central Arctic Ocean • Different ice types from ponded ice, snow and ponds frozen, no snow and ponds, frozen surface (FYI, MYI) • August-October 2011	ROV and SUIT based under-ice optical remote sensing	Various transects from 30 to 210 m for the ROV. Two transects of 800 and 1500 m respectively with under-ice trawl system. Finds high variability at the mesoscale.	Focus on regression model performance.
Garrison and Kurt, 1991	• Weddell Sea /Scotia Sea • Pack ice both FYI and MYI floes • Austral Spring 1983	Ice coring	Multiple sampling stations at km distance. Investigates vertical variability, mainly surface layer assemblages. Higher biomass at the edge of the floes.	Snow depth, floe thickness, floe size, salinity and other chemical measurements/nutrients. Infers on grazing influence. Correlation analysis among parameters.
Fiala et al., 2006	• Pointe Géologie Archipelago, Terre Adelie • Land-fast FYI • April to December 1998	Ice coring	Multiple seasonal and spatial samples at different stations at km scale distance. Investigates vertical variability and surface assemblages.	Nutrients and ice formation and inclusion of available phytoplankton in underlying water column.
Lange et al., 2017a	• Lincoln Sea • MYI and FYI sites including land-fast and pack ice • May 2010, 2011 and 2012	Ice coring	A set of three ice cores for a total of 18 different sites at km distance.	Ice types, differences in MYI-Hummock ice and FYI. ANOVA was performed to investigate correlations.
Meiners et al., 2012	• Antarctic circum-polar study • 25 years of data.	Ice coring	Data compilation analysing vertical variability over several regions in Antarctica.	Ice thickness, vertical distribution and regional characteristics.

Table 2.1 gives qualitative insights into the main drivers of ice-algal variability, the survey locations and ice types and highlights the diversity among studies ranging from FYI and MYI to pack and fast ice. The observed spatial scales and seasons vary significantly across the tabulated investigations which are scattered from years 1982 to 2018. Consequently, a clear differentiation between inter-annual, seasonal and the multiple scales of spatial variability remains problematic. Also, some studies only sample the bottom of the ice core, while others have integrated chl-a over the entire ice thickness, raising questions on the studies comparability and potential biases in the auxiliary parameters (Meiners et al., 2012).

Here we differentiate drivers of ice-algal biomass spatial variability between sea-ice physical properties and the properties of the ice algae biological medium. While the first refers to sea-ice physical properties that can be measured in units of distance and space, the latter refers to properties of the medium (e.g., sea brine) which immediately surrounds the organisms.

Sea-ice physical properties and properties of the ice algae medium are highly inter-correlated and are driven by continually varying temperature gradients at the ice-atmosphere interface (e.g., influenced by wind and precipitation) and at the ice-water interface (e.g., influenced by the properties of the underlying water column and overall hydrographic regime) (Meiners and Michel, 2017). Figure 2.2 provides a schematic of this complex and closely coupled system. The physical properties of sea-ice include snow depth, ice thickness, under-ice topography, surface conditions and ice structure (including porosity, brine/gas volumes, and ice crystal type). The properties of the ice algae medium include nutrient concentrations, salinity and temperature among others. While the sea ice physical properties govern the light distribution and habitat conditions for ice algae, the medium properties, together with light, govern growth and physiological activity of the organisms.

Overall, sea-ice physical properties and ice algae medium properties are strongly dependent on the particular geographic region as well as the time of the year (Fritsen et al., 2011; Gosselin et al., 1986; Rysgaard et al., 2001; Steffens et al., 2006). From Table 2.1, depending on the spatial scale and the time of the year considered, the primary drivers promoting ice algal spatial variability can differ and are briefly presented in the next section.

2.2.1 Sea ice formation, decay and age

Sea-ice physical processes play a significant role in the vertical and horizontal distribution of sea-ice algal biomass (Arrigo et al., 2014; Meiners et al., 2012). They shape available space for the sea ice algae to inhabit and determine whether algal communities thrive at the bottom of the sea-ice cover, within the internal brine channel system or in surface layers (Arrigo, 2014). The initial inputs of algae to the sea-ice system occurs during the inclusion of biological material during ice formation and thereafter through accrual at the deformed ice sub-surface (Figure 2.2) (Arrigo, 2014; Janssens et al., 2016; Lange et al., 2015; Lund-Hansen et al., 2016). Algal growth rates and accumulation from the underlying water column are controlled by the interplay of sea-ice physical properties and

medium conditions. Biomass loss can be attributed to brine loss (flushing) from increased permeability, ablation at the ice underside (Li et al., 2016), and release into open waters during ice melt (Arrigo et al., 2014; Leu et al., 2015). Grazing losses may also occur but grazing on ice algae by heterotrophs remains poorly (Bluhm et al., 2017; Meiners and Michel, 2017).

Depending on the surface ocean conditions, which can be either being calm or turbulent, sea ice can form as congelation or frazil ice, respectively (Arrigo, 2014; Petrich and Eicken, 2009). In calm conditions, and once an initial ice cover has been established, congelation ice formation takes place as vertically parallel ice crystals forming a continuous sheet that propagates downward. The propagation margin is referred as the skeletal layer and gives origin to the sea ice columnar/lamellar structure (Petrich and Eicken, 2009). This type of ice is a common feature for coastal fast ice. Frazil ice is instead associated with turbulent conditions (more typical of open ocean conditions) and induces ice crystals to consolidate first into grease ice and later into pancake ice. Pancake ice is then merged to form a consolidated sheet which can then initiate vertical ice growth (e.g., with a skeletal layer margin at the bottom) (Arrigo, 2014; Petrich and Eicken, 2009). Frazil ice formation is more typical for open ocean conditions, and when sea ice is free-drifting, it is referred to as pack ice.

High spatial variability of biomass has been observed for both land-fast and pack ice (Table 2.1), with similar factors influencing settlement and accumulation of algae in both ice types. However, there are fundamental differences between pack ice and land-fast ice formation (Gradinger and Ikävalko, 1998; Spindler, 1994). In the early stages of ice formation, the open ocean setting of pack ice is associated with the scavenging of suspended biological material by raising frazil crystals and higher initial seawater and salt content in the pre-dominant frazil ice type compared to newly formed congelation ice (Arrigo et al., 2014; Spindler, 1994). This facilitates the consequent development of so-called internal communities which are a common feature in Antarctic pack ice (Meiners et al., 2017; Arrigo, 2014). Internal communities are also associated with ridging and rafting of ice floes, as well as with melting and refreezing processes of multi-year sea ice (Welch and Bergmann, 1989). Pressure ridges, for example, can incorporate water pockets during formation, which are suspected to represent a nutrient reservoir for algae (Spindler, 1994).

An additional type of ice originates from flooding and refreezing of seawater that has infiltrated into the overlying snow layer. Flooding can happen either via snow loading of sea ice or through deformation of ice floes. Seawater at the ice surface forms slush ice and snow ice if it refreezes (Arrigo, 2014; Petrich and Eicken, 2009). Surface flooding and the snow-ice formation are characteristic of Antarctic pack ice but have also been reported for other ice types (Petrich and Eicken, 2016). In the Antarctic pack-ice zone, mesoscale differences in these physical processes are often the main factors that drive the high biomass variability (both on horizontal and vertical dimensions) as a result from flooding and increased supply of nutrients and biological material (Fritsen et al., 2011; Garrison and Kurt, 1991; Meiners et al., 2012).

The influence of ice age on biomass still requires further research efforts. Some Arctic studies report no significant differences between FYI and MYI (Lange et al., 2015), while others suggest that repeated melting and re-freezing cycles favor ice algal accumulation, build up and inclusion in MYI (Eicken et al., 1991; Granskog et al., 2005; Welch and Bergmann, 1989). For Antarctica, Fiala et al., (2006) reported high biomass in FYI fast ice when compared to pack ice. Meiners et al., (2011) hypothesized that persistence of sea-ice into the late spring/early summer might increase biomass build-up in East Antarctic first-year pack ice. The role of ice age is also suspected to play a role in the seeding and distribution of algal populations in a phenomenon referred as the "multiyear ice seed repository hypothesis" (Olsen et al., 2017). The hypothesis suggests that cells trapped in surface layers of ice that survives a summer season function as a seed repository. They are released as temperatures increase in the spring season and seed the ice algal spring bloom in sea-ice bottom layers and adjacent ice floes.

2.2.2 Sea-ice structure, temperature, nutrients and salinity

Sea-ice is characterized by strong time-varying vertical gradients in temperature, brine salinity, pore space, and permeability that continuously shape the habitability of the sea-ice environment (Arrigo, 2014; Vancoppenolle et al., 2013; Petrich and Eicken, 2009). These gradients, together with other sea ice physical processes mentioned above, control nutrient availability and brine salinity in the interstitial channel system in which the ice algae thrive and play an important role in the small-scale vertical distribution of algae communities within the ice (e.g., bottom, internal or surface) (Arrigo, 2014; Legendre and Gosselin, 1991).

Sea-ice porosity is considered as a particular index in evaluating the relationship between sea-ice physical parameters and chl-a because porosity comprises the ice temperature, salinity, and density (Li et al., 2016). Ice algae prefer conditions that provide ready access to nutrients in the seawater, salinity levels that do not limit growth rates, and sufficient light for photosynthetic activity (Arrigo, 2014). During spring, as a result of increasing ice temperatures, habitable pore space (porosity) at the bottom is higher than in other sea-ice layers (Tedesco and Vichi, 2014) and most of the biomass is usually found in the lowermost 0.05 – 0.1 m of the ice, due to the direct contact with sea water allowing the infiltration of nutrients and resulting in favourable brine salinities (Arrigo, 2017; F. Cota and Ralph E. H., 1991). Looking at these bottom communities, microscale studies using novel PAM fluorescence imaging approaches have provided different proxies (such as minimal fluorescence yield, F_o) for evaluating changes in algal biomass over time (Hawes et al., 2012; Lund-Hansen et al., 2016). Hawes et al., (2012) highlighted how brine channel evolution and skeletal layer development triggered algae population growth. In fact, while sea ice algal cells can grow despite exposure to extremes in temperature and salinity, the high salinities found within the brine channels, reaching up to 100 or higher, can reduce growth rates of internal communities (Arrigo et al., 2014; Krembs et al., 2000).

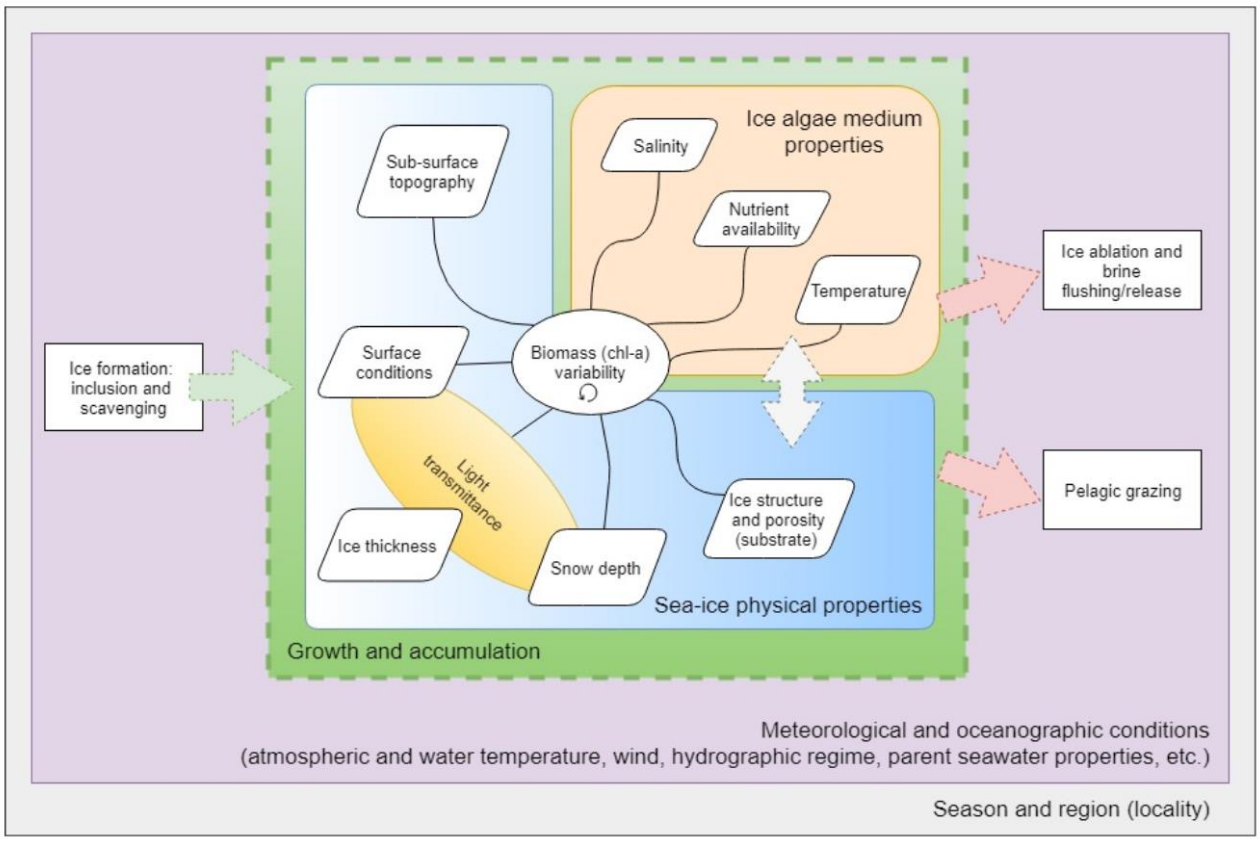

Figure 2.2 Simplified schematic of drivers influencing the spatial distribution of biomass in sea ice. Green arrows imply the initial biomass input to the system and red arrows the system output. The grey arrow symbolizes the close correlation between sea-ice physical properties and the properties of the ice algae medium. Some sea-ice physical properties are also closely correlated with each other. Overall, all parameters are heavily influenced by temperature and by the meteorological and oceanographic conditions which in turn are dependent on the location and season of the year.

The influence of sea-ice physical properties such as the ice texture, crystal type and brine volume, on sea ice biological properties, has been highlighted by Li et al., (2016) and Spindler, (1994) to mention a few. The more recent study by Li et al., (2016) showed a strong statistical relationship between chl-a and brine volume (porosity). Quantitative relationships such as this are rare due to the great effort involved in acquiring extensive ice coring datasets. They are, however, extremely useful for augmenting our understanding ice algae variability drivers towards improved modeling results (Steiner et al., 2016). More studies are required coupling proxies of porosity, such as temperature and bulk salinity, with chl-a for diverse types of ice covers and over time for a better parametrization of these drivers.

Ice salinity and temperature can also vary horizontally from the sub-meter to regional scales (Eicken et al., 1991; Tucker et al., 1984). As habitable pore space co-varies with the salinity and temperature of the ice (Cox and Weeks, 1983), they also consequently influence the horizontal distribution of ice algae. It's important to consider that ice-bottom salinity (and nutrients) are not

only correlated to the sea-ice structure but are also directly influenced by properties of the underlying waters. Observational studies at the mesoscale have consequentially observed biomass variability along with variations in seawater salinity (Gosselin et al., 1986), nutrients (F. Cota and Ralph E. H., 1991; Maestrini et al., 1986) and under-ice currents (Monti et al., 1996)

2.2.3 Under-ice topography

There are very few qualitative studies and no quantitative studies treating under-ice roughness and topography as a parameter influencing ice algal biomass distribution. However, it is suspected that under-ice topography plays an influential role in shaping hydrographic regimes at the ice-water boundary layer, partially explaining the high natural variability of the sea-ice organisms. A pioneering study investigated this aspect in experimental set-ups and monitored brine channel evolution, drainage and surface roughness (topography) together with biomass (Krembs et al., 2001, 2000). The study suggested that water flow under varying under-ice topographies alters pore water flux regimes and nutrient exchange promoting differential algal biomass accumulation.

At the millimeter scale, in a PAM imaging study, biomass distribution was compared to ice growth, surface roughness, water flow, and nutrient availability among other factors in the Arctic (Lund-Hansen et al., 2016). The study identified ice roughness as the most relevant factor in the accrual of diatoms at the water-ice interface. The relative importance of advection and accrual of biomass from the underlying ocean was emphasized rather than *in situ* growth from biomass initially incorporated into the sea ice. Physical accumulation of biomass through advection remains a poorly understood aspect of ice algae bloom dynamics.

In the Arctic, at the sea-ice floe scale, the topography and hydrographic regime under the ice have been found to influence algae distribution through trapping of ice algal aggregates (e.g., Katlein et al., 2015). During late summer ice algal aggregates accumulate in dome-shaped structures and at the edges of pressure ridges. Overall, more investigations are required to better understand processes at the water ice boundary layer regarding nutrient exchange and algal aggregation at both small and large spatial scales, and at different times of the year.

2.2.4 Snow, light and surface properties

Together with nutrient availability, light is the most critical factor influencing ice algal photosynthesis and growth (F. Cota and Ralph E. H., 1991) and several studies have recognized light as the main limiting factor controlling bloom initiation during the winter-spring season (Gosselin et al., 1986; Leu et al., 2015; Rysgaard et al., 2001). While at small scales the ice microstructure influences algae distribution patterns (Lund-Hansen et al., 2016), boosts growth by allowing nutrients to permeate (Li et al., 2016) and fosters accrual of biologic material (Krembs et al., 2002), at the mesoscale level, ice algae patchiness is mostly associated with the spatial variability in

physical sea-ice properties governing light transmittance (Gosselin et al., 1986; Palmisano, 1987) (Figure 2.2). Indeed, light availability in a given under-ice environment is not only a function of the location (latitude) and incoming Photosynthetic Active Radiation (PAR) (Ehn and Mundy, 2013) but also of the meteorological conditions (e.g. cloud cover) (Raymond et al., 2009), sea ice surface conditions and ice thickness (Perovich, 1996). Light available for photosynthesis of sea-ice algae is mostly influenced by the snow cover (depth and age) due to its high attenuation coefficients and the high albedo rather than the ice itself (Palmisano, 1987; Perovich, 2017).

Ice thickness and related variations in ice morphology, being compounded by deformational processes, also contribute to variability in light intensities. As an example, a recent Arctic study highlighted that chl-a concentrations in thick MYI are unusually high due to the presence of surface hummocks which have a relatively thin overlying snowpack, thereby fostering algal accumulation due to increased light levels (Lange et al., 2017, 2015). Surface properties such as melt-pond coverage or surface flooding due to snow loading also play a role in the amount of light available for ice algae beneath the snow and ice pack (e.g., Arndt et al., 2017; Katlein et al., 2015a). Increasingly frequent leads in Arctic sea ice are also capable of re-defining the ice structure and optical properties and have a significant impact on light transmittance and availability for under-ice communities (Kauko et al., 2017).

Although increased light intensities are typically associated with favorable growth conditions, the relationship is not straightforward in sea ice and varies depending on the season, and ice algae light exposure history. For example, while Arctic land-fast sea-ice algae biomass is inversely correlated with snow depth early in the season due to less light availability (Mundy et al., 2005), multiple studies have observed that higher snow depth is linked to higher biomass later in the season (Campbell et al., 2015; Fritsen et al., 2011; Melbourne-Thomas et al., 2015).

Late-season positive snow depth-biomass relationship in the Arctic have been attributed to photoacclimation and photo-inhibition due to excess of light following dark adaptation by the ice algae. Ice algae experience a significant increase in irradiance between late winter and spring. They are initially light limited by the snow cover (characterised by a negative relationship), but as snow cover is removed, biomass for shade adapted communities have been observed to decline due to increases in light transmission (inducing strong photoinhibition) (Galindo et al., 2017; Lund-Hansen et al., 2014), and due to heat fluxes triggering under-ice ablation loss (Campbell et al., 2015; Juhl and Krembs, 2010). Ablation loss can also happen as a result of lowered thermal insulation under a thin snow cover. This results in stronger desalination and increased warming of the ice and eventually flushing and ice melt at the bottom. Algal stocks then get sloughed off, a process that has been proposed in various studies (Campbell et al., 2014; Mundy et al., 2005; Welch and Bergmann, 1989).

Using fluorescence imaging, the effect of snow cover removal on algae was also assessed at the millimeter scale (Lund-Hansen et al., 2014). This study further confirmed a decrease in biomass in areas with no snow due to possible increased UV light exposure and discussed the possible role of

algae behavioral changes such as emigration under potentially photo-damaging conditions rather than ablation loss.

In the Antarctic, wind-driven snow re-distribution has been suggested as an important factor masking snow depth-biomass relationships (Melbourne-Thomas et al., 2015). In fact, the snow cover present on the ice at the time of sampling does not necessarily reflect the conditions during the earlier stages of ice development. This is particularly true for Antarctic sea ice where snow is a prominent feature, and continuous drift provides a rapidly changing snow cover and under-ice light conditions (Massom et al., 2001). Compared to the Arctic, studies emphasizing snow-biomass relationship in the Antarctic are less frequent, and the complex response of ice algal growth, photo-physiology, and distribution under changing snow and light fields requires further research efforts through higher spatial and temporal resolution monitoring and on both land-fast and pack ice.

Finally, is worth noting that since ice algae are commonly distributed in distinct layers that can reach several centimeters in thickness, and can exhibit diverse vertical distributions over the ice thickness, they can further influence light availability to the nearby and underlying communities in the ice column through a phenomenon known as self-shading (F. Cota and Ralph E. H., 1991; Johnsen and Hegseth, 1991; Kirk, 2011). Self-shading can limit algal growth, influencing patchiness, induce packaging effects (SooHoo et al., 1987; Wongpan et al., 2018) and is represented in Figure 2.2 as an internal loop within biomass variability.

2.2.5 Grazing

A challenging loss-term to account for in biomass variability is grazing by under-ice fauna and zooplankton (Werner, 1997; Welch and Bergmann, 1989, Figure 2.2). It is speculated that feeding dynamics of the under-ice realm might, however, contribute to the mesoscale variability of measured ice algal abundance (Gradinger and Bluhm, 2004; Michel et al., 2002; Werner, 1997). More investigation over different seasons and on different types of ice covers are required to enhance our understanding of grazing impacts on ice algal biomass distribution. Furthermore, physical properties of different ice types such as ice texture and porosity are also suspected to impact on predator-prey interactions in the sea-ice brine channel system (Krembs et al., 2000). For example, larger predators can be excluded from brine channels depending on the architecture of the channel network. Smaller channels may provide refuge space but may be unfavorable for algal growth due to limitations in diffusive transport of nutrients (Krembs et al., 2000).

2.2.6 Regional characteristics

As schematized in Figure 2.2, all the parameters described above are highly dependent on the season, meteorological conditions and in particular on the geographic region that shapes the sea-ice physical environment (Eicken et al., 1991; Petrich and Eicken, 2009). Indeed, not only is the

horizontal distribution of sea-ice algae naturally related to latitudinal gradients in solar irradiance (F. Cota and Ralph E. H., 1991; Raymond et al., 2009), but other unique regional features will also affect the distribution of ice algae. For example, freshwater drainage from melt ponds and nearby river discharges can both remove or inhibit the algae growth at the sea-ice-water interface through physical disturbance and exposure to freshwater (Rysgaard et al., 2001). In areas affected by warm Atlantic water inflow, bottom ice ablation, which deteriorates the ice algal habitat, is suggested to be a limiting factor for Arctic ice algal biomass build-up (Leu et al., 2015). In the Antarctic, loss of algae from underneath the ice has been linked to the effect of underwater currents at specific locations (Ryan et al., 2006). Another example are the hemispheric differences between Arctic and Antarctic sea ice, as these display very different vertical distribution patterns and total biomass values (Arrigo, 2017; Arrigo et al., 2014; Spindler, 1994). For instance, surface flooding and snow-ice formation is a characteristic feature of Antarctic pack ice (Kattner et al., 2004), whereas melt ponds are a predominant feature of Arctic sea ice.

The two polar regions can exhibit very different types of ice algae communities (Leeuwe et al., 2018). A feature of the Antarctic is the occurrence of platelet ice which hosts very high ice algal biomass (Arrigo, 2017). Platelet ice consists of thin ice plates in the water column below the sea ice which largely increases the surface area for the ice algae to colonize, and with direct access to nutrients in the water (Arrigo, 2014). Ice platelets accumulate loosely under, or occur frozen into, the bottom of sea ice resulting in a highly porous and productive ice algae (Arrigo et al., 1995). Platelet ice is associated with supercooled Ice Shelf Water, and its occurrence is generally limited to specific areas across the Antarctic continent (Langhorne et al., 2015). Nonetheless, platelet ice communities are considered of high importance, as any change in the highly productive platelet ice habitat in a warming ocean can have consequential effects across the rest of the Southern Ocean ecosystem (Langhorne et al., 2015). A feature more common to the Arctic, is the colonial diatom, *Melsosira arctica* which can form strands attached to the ice and suspended into the water column. By living suspended into the upper ocean, they can consume nutrients directly from the water column (Arrigo, 2014).

Non-polar sea ice such as found in the Baltic Sea or Saroma-ko lagoon (Northern Japan) also presents particular characteristics in algal biomass spatial variability with reported observations of variability to be negligible at scales < 20 m despite evident variations in snow depth (Granskog et al., 2005; Robineau et al., 1997). For more detailed information on differences in ice algal communities from Arctic, Antarctic and sub-Arctic areas we refer to recent reviews by Arrigo, (2017) and Kaartokallio et al., (2017).

2.3 Concepts of bio-optics and radiative transfer in sea ice

The layered sea-ice matrix, here comprising snow and ice (and the water below) is characterized by the inclusion of brine and air pockets, precipitated salts, dust and sediments, algae, heterotrophic

organisms, dead organic particulate material (detritus) and CDOM (Figure 2.3). As in any remote sensing application, the medium between the sensor and the light-interacting object will have an impact on the measured signal. A brief overview of the path that light traverses before reaching hypothetical sensors placed underneath the ice is essential for adequately applying and developing close-range under-ice optical remote sensing methods. A comprehensive introduction to radiometry and hydrologic optics can be found in (Kirk, 2011) and to the optical properties of sea ice and snow in Perovich, (2017, 1996) and Warren, (1982).

2.3.1 Basic elements of close-range under-ice optical remote sensing of algal biomass

Recent studies have reported empirical correlations between traditional ice-core chl-a measurements and under-ice spectral signatures for both the Arctic (Campbell et al., 2015, 2014; Mundy et al., 2007) and Antarctic (Wongpan et al., 2018; Meiners et al., 2017; Melbourne-Thomas et al., 2015). The most basic application of the technique involves the deployment of upward-looking hyperspectral radiometers under the ice at close distances (0.15-0.6 m) using L-shaped deployment arms (Lange et al., 2016; Melbourne-Thomas et al., 2015) (Figure 2.4a). To correlate the transmitted spectra with chl-a, traditional ice cores are then collected just above the radiometer measurements, and fluorometric estimates of chl-a are performed in the laboratory from the melted cores using standard methods (Holm-Hansen and Riemann, 1978) (Figure 2.4a). The technique takes advantage of the wavelength specific absorption of chl-a, with peaks at around 480 and 665 nm, and being the dominant absorbing pigment in ice algae. Measured transmitted spectra at multiple points are then calibrated against the sampled chl-a values through the use of derived spectral indexes or other regression models. Additional measurements of under-ice spectra can then be used to estimate chl-a concentrations using the radiometer data alone (Lange et al., 2016; Melbourne-Thomas et al., 2015). The spatial coverage of the survey can then be considerably increased by using Remotely Operate Vehicles (ROVs) or ship-based under-ice trawls equipped with the radiometric sensors (Meiners et al., 2017; Lange et al., 2016). Hyperspectral radiometers employed under sea-ice typically collect light in either irradiance or radiance mode (Figure 2.3). Irradiance sensors have a cosine-corrected receptor which gathers light with a 180° field of view (FOV). Radiance sensors have a narrow (finite) FOV (usually around 9° to 25°). While irradiance sensors provide a coarser footprint and are more frequently used for energy budget purposes, radiance sensors are used to infer optical properties at finer scales due to their narrow FOV (Lange et al., 2016). Figure 2.3 displays the hypothetical FOV coverage of both types of sensors. The transmitted under-ice light can be normalized with data from upward-looking irradiance sensors placed at the ice surface (Figure 2.3) (Nicolaus et al., 2010). Under-ice irradiance relative to incoming solar irradiance at the surface is termed transmittance whereas under-ice radiance normalized to incoming solar irradiance is termed transflectance (Nicolaus et al., 2013).

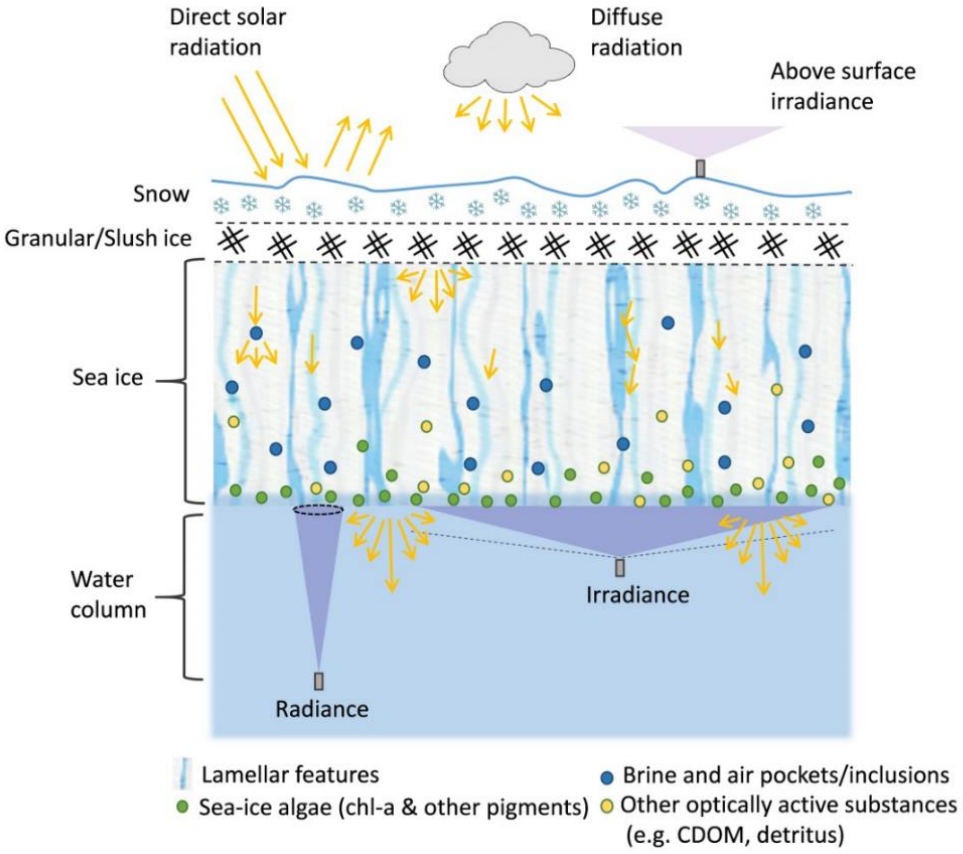

Figure 2.3 Conceptual illustration of radiative transfer in sea ice (for shortwave radiation between 350 and 700 nm) as described in text. The complex system features both absorbing and scattering (elements that shape the geometric and spectral properties of the under-ice light field. The illustration provides a concept idea of typical under-ice light sensor settings employed for close-range remote sensing applications. Radiance sensors have a finite angle of view and are intended for finer mapping resolutions and deeper deployment modes (2-5 m). Irradiance sensors have to be deployed nearby the ice sub-surface due to their cosine field of view. Figure was partially adapted from Katlein et al., 2014.

2.3.2 Scattering and absorption in sea ice

The attenuation through the ice, comprising both absorption and scattering, is typically expressed by the diffuse attenuation coefficient K_d (PAR) or spectrally resolved K_d (λ) (Lund-Hansen et al., 2015; Perovich, 1989). Both scattering and absorption govern the magnitude of the attenuation, but only the latter is considered wavelength dependent (Arrigo et al., 1991; Perovich, 1996). Scattering in sea ice depends on the scattering volume function, which is dominant compared to absorption, and is mostly attributed to the refraction of photons traveling between the different media such as ice, gas or brine inclusions and precipitated salts (Light et al., 2004; Perovich, 1996). Through continuously varying temperature gradients, the volume fractions of these optical media are far from being constant. Indeed, as a consequence of a dynamic physical environment, light attenuation

and optical properties in sea-ice are continuously varying over space and time (Light et al., 2004; Perovich, 1996).

If we describe the light path starting from the surface, snow has a high albedo in the PAR range and the amount of light reflected is dependent on the conditions of the overlying snow cover (type, age, and temperature) (Perovich, 2007; Warren, 1982). Snow cover conditions are critically important as the overall amount of light transmitted/attenuated through the sea-ice matrix is mostly dependent on the thickness of the snowpack, rather than the ice, as snow attenuates light approximately 10-fold higher (Perovich, 2007).

If no snow is present, light transmission is mostly influenced by the surface properties of the sea-ice environment such as on the presence of melt-ponds or bare ice (Katlein et al., 2015a; Mundy et al., 2005). In Antarctica, thicker snow packs can induce surface flooding (Wadhams et al., 1987) which has been shown to slightly increase attenuation compared to non-flooded sea ice (Arndt et al., 2017). The authors hypothesized that although the different geometry of the slush layer allows more light to be transmitted, the higher snow loads and the promotion of infiltration waters (fostering algal communities living at the surface) resulted in the increased attenuation (Arndt et al., 2017).

Continuing downwards through the ice cover, absorption in sea-ice is often dominated by ice algae (Fritsen et al., 2011, 1992) and is enhanced by the highly scattering sea-ice environment they are embedded in (Ehn and Mundy, 2013). Here we focus on the 400 – 700 nm wavelength band termed the Photosynthetically Active Radiation (PAR), which is the spectral range relevant for under-ice optical remote sensing of biomass. Below 570 nm, absorption of snow and ice is low, and therefore ice algae dominate the spectral signature of transmitted light which is shaped by algae absorption features (Fritsen et al., 2011). This is what makes under-ice optical remote sensing methods possible. The spectral signature measured underneath the ice is dominated by effects associated with variability in algae absorption over certain bands of the PAR spectrum, rather than variability in snow and ice properties.

The irradiance that reaches the ice-water interface can be reduced to 0.1%-1% of the surface irradiance (Perovich, 2017), and thus the under-ice realm can be thought of as a low light environment. Nevertheless, ice algae can shade-adapt efficiently to these circumstances, and a recent Arctic study showed that active photosynthesis can occur at extremely low irradiances (0.17 $\mu mol\ m^{-2}\ s^{-1}$) equal to 0.02% of surface irradiance (Hancke et al., 2018).

Overall, the quantification of the effects of algal biomass on the optical properties of sea-ice is non-trivial. The quality of the light is influenced by the amount of chl-a, but it also varies as a function of algal photosynthetic and accessory pigment composition within the algal cells, as well as with the effect of photosynthetic discreteness which combines the influence of size and of pigment concentration in the cells (e.g., packaging effect) (Kirk, 2011; Morel and Bricaud, 1981; SooHoo et al., 1987). For example, the specific absorption of the ice algal community varies as a function of the

diverse photoacclimation strategies of ice algae adapted to different light levels. These can induce the production of diverse cellular pigment compositions (Galindo et al., 2017), which can lead to distinct spectral absorption profiles (Johnsen and Sakshaug, 2007).

Although spectrally resolved visible light signals measured below the ice are mostly shaped by absorption of organic matter (algae and detritus) within the ice, the signal also comprises the absorption effect of other optically active components, and thus the discrimination of chl-a is not always straightforward. Chl-a has absorption peaks at around 480 and 665 nm, whereas CDOM absorption is strongest in the blue part of the spectrum (400-450 nm), but low in the red. In the red part snow absorption starts to increase (over 550 nm). The concentration and distribution of other optically active components are dependent on the study region. Analyses of CDOM and its optical properties remain sparse but are available for both Arctic (Lund-Hansen et al., 2015; Xie et al., 2014) Antarctic (Norman et al., 2011) sea ice.

2.3.3 Geometrical considerations of the under-ice light field

Considering the high scattering coefficients of snow, with only a few centimeters of snow cover, light that reaches the surface-ice layer is mostly present in a diffuse (highly scattered) form rendering the sun-angle induced directional component of light negligible (Petrich et al., 2012). A similar effect is achieved by the granular ice surface layers characteristics of melt (or flooding) and refreezing processes at the snow-ice interface (Arndt et al., 2017; Petrich et al., 2012) or by overcast conditions.

Therefore, for most of the cases, light that reaches the ice sub-surface can be considered diffuse, and it follows an exponential decrease through the ice and thereafter through the water column (Lund-Hansen et al., 2015). Exceptions are made for non-homogenous ice in pond covered areas typical of the Arctic (Frey et al., 2011) or near ice floes with cracks and ridges which can include an azimuthal directional component in the under-ice light field measured nearby, and different depth profiles (Katlein et al., 2016, 2015a).

While light that has traversed the initial sea-ice surface layers results considerably scattered and diffuse, radiative transfer within sea ice is subject to a degree of substantial anisotropy and multiple scattering (Katlein et al., 2015a; Petrich et al., 2012). This means that the scattering coefficient is dependent on the direction in which light is traveling, which in turn is dependent on a volume scattering function (Hamre et al., 2004). The lamellar crystal structure of sea ice is responsible for such particular geometric and radiometric light field properties (Katlein et al., 2016; Perovich, 1989). More specifically, the sea ice vertical lamellar crystal structure, and brine and gas inclusions funnel the light downwards changing the shape of the radiance distribution under-ice to a downward-peaked shape along the zenith angular component (Figure 2.3) (Katlein et al., 2014; Light et al., 2004). This reduced lateral deflection within sea ice is further enhanced by absorbing particulates such as algae, detritus, dust and sediment (Petrich et al., 2012). The overall

consequence of this phenomena is an anisotropic under-ice light field characterized by a narrowed spread of flux (Figure 2.3), which remains constant over time through various sea ice temperature regimes (Light et al., 2004).

In terrestrial remote sensing, an anisotropic light field is typically characterized by the bidirectional reflectance distribution function (BRDF) which defines the geometric radiance distribution (Palmer and Grant, 2010). The BRDF effect can hinder the retrieval of accurate information from remotely sensed data (Buchhorn et al., 2016). Measurements obtained by an under-ice sensor are inevitably subject to such considerations as well (e.g., Matthes et al., 2019). The impact of an anisotropic under-ice light field should be subject of further investigation towards the development of accurate under-ice light measurements that aim to be flexible regarding sensor characteristics and deployment mode (e.g., from underwater vehicles, using wide FOVs or HI comprising sensor inclination and multiple viewing angles). In addition, more studies analyzing the effect of different ice types and sea-ice surface properties on the under-ice lights field geometrical properties (e.g., surface flooding), are of interest for further extending under-ice chl-a remote sensing under a wide range of survey scenarios.

2.4 Advances in under-ice optical remote sensing of biomass

2.4.1 Regression algorithms

The first studies describing correlations between transmitted under-ice irradiance spectra and sea-ice chl-a were performed by Legendre and Gosselin (1991) and Maykut and Grenfell (1975). The studies employed ratios between selected spectral bands (671 nm : 540 nm) and produced a relationship accounting for up to 55% of total variation in ice algal biomass. Subsequent studies have employed Normalized Difference Indexes (NDIs) as a method to correlate under-ice spectra with sea ice algal biomass estimates in Resolute Passage, Canada (e.g., Mundy et al., 2007). The study pointed out the negligible effect of snow on biomass estimations if NDIs were calculated with wavebands where snow had reduced influence (<570 nm). The authors provide a single-best NDI wavelength combination (485 nm : 472 nm) accounting for 89% in the total variation of ice algal biomass. This study was complemented by two more Arctic studies (Campbell et al., 2015, 2014) also conducted in Resolute Passage. Taking advantage of the non-invasive nature of the method, the studies were able to infer algae environmental drivers (such as snow depth) and found the best NDI wavelength combination (478 nm : 490 nm) to account for 81% of sea ice chl-a biomass variability.

The same method was also applied in Antarctic pack ice, explaining 81% of algae biomass variability using the ratio of wavelengths (555 nm : 472 nm) (Fritsen et al., 1992). This was followed by the first study comparing data from different locations on a regional scale (Melbourne- Thomas et al., 2015). The later tested different types of spectral feature models (NDIs, ratios of spectral irradiance,

scaled band area, and Empirical Orthogonal Functions, EOFs) and highlighted NDIs to be the most effective index accounting for biomass variation (Melbourne-Thomas et al., 2015). Different optimal NDI wavelengths were identified for East Antarctic sea ice (422 nm : 418 nm) and the Weddell sea ice (479 nm : 468 nm) (Melbourne-Thomas et al., 2015). Generally, best NDIs are selected by plotting Pearson correlation surfaces which display correlation strengths among all combinations of spectral wavebands (each combination produces an NDI) (e.g., Melbourne- Thomas et al., 2015). NDIs should, however, be composed of wavebands that are separated by at least 15 nm to avoid artificial correlations of neighboring wavebands and, for chl-a, preferably wavelengths between 405 and 550 nm to avoid both edge effects and the influence of snow on transmitted radiance spectra beyond 550 nm.

It is important to note that all these tests have only used irradiance sensors at a very close distance to the ice subsurface (0.15-0.6 m), providing scattered point samples over limited areal extents. The first comparison of algorithms to include long-range transects using radiance sensors was conducted by Lange et al. (2016) for Arctic sea ice.

Table 2.2 Compilation of studies using measured under-ice spectra for estimating chl-*a* (in mg·m^{-2}) in sea ice. All studies correlate optimal spectral bands with measured chl-a obtained through traditional ice coring techniques. Location, ice type and date of the survey are shown together with the method employed, produced relationships and the statistical strength of the correlations as R^2. Sba refers to the scaled band area found in the respective studies. S refers to the EOF scores found in the respective studies. E(chl-a_{adj}) indicates that a log-link function was applied for the formulation of the relationship. ln indicates that a natural logarithm was employed to formulate the relationship. Sensor mode refers to the FOV (radiance or irradiance) and if it was normalized to downwelling surface radiation (transflectance or transmittance).

Study	Region/Ice type/Date	Method used/Optimal bands (if any)/Sensor mode	Relationship	R^2
Legendre and Gosselin, 1991	• South-eastern Hudson Bay, Canadian Arctic • FYI • May 1986	*Ratios* 671:540 Irradiance	chl-*a* = 100 × ratio + 49	0.55
		NDIs 415:400 Transmittance	chl-*a* = 80.2 − 588 × *NDI*	0.81
Mundy et al., 2007	• Resolute Passage, Canada • Land-fast FYI • May 2003	*NDIs* 485:472 Transmittance	chl-*a* = −8.3 + 1000 × *NDI*	0.89
		NDIs 663:655 Transmittance	chl-*a* = −26.72 + 344 × *NDI*	0.85
		NDIs 685:675 Transmittance	chl-*a* = 43.87 + 204 × *NDI*	0.81

Continued

Study	Region/Ice type/Date	Method used/Optimal bands (if any)/Sensor mode	Relationship	R^2
Campbell et al., 2015, 2014	• Allen bay. Northwest of Resolute Bay, Nunavut, Canada • Land-fast FYI • May—June 2011	*NDIs* 478:490 Transmittance	chl-*a* = −497.2 × *NDI* + 15.2	0.81
Fritsen et al., 2011	• Bellingshausen Sea • FYI • September 2007	*NDIs* 555:442 Irradiance and transmittance	n/a	0.71(for irradiance) 0.81(for transmittance)
		NDIs 422:418 Irradiance	ln(chl-*a*) = −4.27 – 351 × *NDI* (for East Antarctica)	0.64
		NDIs 479:468 Irradiance	ln(chl-*a*) = 0.39 + 31.7 × *NDI* (for Weddell sea, updated with corrigendum)	0.79
		Ratios (555:443) Irradiance	ln(chl-*a*) = −1103 + 1948 × Ed(555)/Ed(443) − 859 × [Ed(555)/Ed(443)]^2 (for East Antarctica)	0.56
Melbourne-Thomas et al., 2015	• Antarctic sea ice. Weddell Sea and East Antarctica • Pack-ice (Ice floes) • September—October 2007—2012	*Ratios* (555:443) Irradiance	ln(chl-*a*) = − 33.9 + 31.0 × Ed(555)/Ed(443) (for Weddell sea)	0.67
		Scale band area Irradiance	ln(chl-*a*) = −16.36 + 9.52 × *sba* − 1.34 × *sba*^{2} (for East Antarctica)	0.64
		Scale band area Irradiance	ln(chl-*a*) = −2.40 + 1.64 × *sba* − 0.13 × *sba*^{2} (for Weddell sea)	0.60
		EOFs Irradiance	ln(chl-*a*) = 0.36 + 6.41 × S_1 − 143.5 × S_2 − 20970 × S^2_2 + 393.3 × S_3 − 512.6 × S_4 (for East Antarctica)	0.52
		EOFs Irradiance	ln(chl-*a*) = 1.55 + 43.0 × S_1 + 112.5 × S_2 − 243.7 × S_3 (for Weddell sea)	0.67
Nicolaus and Katlein, 2013	• Barrow, Alaska, Arctic sea ice • Land-fast sea ice, snow covered • March, May, and June 2010	No correlation could be applied.	n/a	n/a
		NDIs 669:683 Irradiance	ln[E(chl-a_{adj})] = 2.2 + 10.8 × *NDI*	0.73
Lange et al., 2016	• Central Arctic Ocean • Different ice types from ponded ice, snow, and ponds frozen, no snow and ponds, frozen surface (FYI, MYI) • August—October 2011	*NDIs* 678:684 Transmittance	ln[E(chl-a_{adj})] = 1.2 − 11.1 × *NDI*	0.70
		EOFs Transflectance	ln[E(chl-a_{adj})] = 0.3 + 1.5S_2 − 1.7S_4 − 2.0S_7 + 3.2S_9 + 8.6S^2_9	0.74
		EOFs Transmittance	ln[E(chl-a_{adj})] = 0.7 − 3.0S_2 + 1.1S_4 + 2.4S_6 − 6.5S^2_7 + 3.9S^2_9	0.90
		EOFs Radiance	ln[E(chl-a_{adj})] = 2.0 + 2.7S_4 – 1.7S_5 – 1.0S_6 − 2.3S^2_2 − 10.0S^2_8	0.95

Continued

Study	Region/Ice type/Date	Method used/Optimal bands (if any)/Sensor mode	Relationship	R^2
Meiners et al., 2017	• The Weddell Sea • Pack ice floe • September 2017	*NDIs* 479:468 Irradiance	ln(chl-*a*) = 0.39 + 31.7 × *NDI* (from Melbourne-Thomas et al., 2015)	0.79
Wongpan et al., 2018	• Antarctic sea-ice, McMurdo Sound and Davis Station. • Fast ice (First-year) • Austral spring 2015	*NDIs* 471: 416 Transmittance	$\log_{10}$(chl-*a*) = 1.27 + 3.763 × *NDI* (for McMurdo Sound)	0.70
		NDIs 439: 424 Transmittance	$\log_{10}$(chl-*a*) = 2.07 – 18.163 × *NDI* (for Davis Station)	0.79
		NDIs 441: 426 Transmittance	$\log_{10}$(chl-*a*) = 2.58 – 16.85 × *NDI* (for both sampling sites)	0.70

The study examined different regression models (EOFs, NDIs, and Multi-NDI) and observed a better performance for the EOFs-based approach to represent increased areal coverages (therefore representing a more extensive range of sea-ice conditions). Also, this study outlined that a better model performance can be achieved by using transmittance or transflectance data as spectral model inputs rather than only under-ice irradiance or radiance data. Studies testing and comparing different models under different conditions are useful for progressing more generalized relationships and robust regression models. The latest study investigating under-ice spectra-biomass relationships was done in Antarctic fast ice, and it showed that NDI wavelength pairs near the first chl-a absorption peak (440 nm) explain up to 70% of the total variability in high ice algal standing stocks (Wongpan et al., 2018). The authors also pointed out the importance and difficulty of sampling on one of their study areas, McMurdo Sound, characterized by the presence of platelet ice. The sub-ice platelet layer is characterized by one of the highest biomass concentrations. However, the produced relationships in the study were hampered by a low overall variability in the sampled algal biomass and the potential biases in sampling the fragile unconsolidated sub-ice platelet layer. The authors highlighted that further work is required to advance quantitatively robust sampling techniques for platelet ice and to develop optical methods to understand phenology and spatial variability of platelet ice algal communities.

Table 2.2 provides a summary of the studies producing spectra-biomass relationships retrieved from the close-range deployment of radiometers. The differences in optimal spectral indices and produced relationships suggest that it is challenging to develop cross-regional relationships between transmitted spectra and chl-a (Wongpan et al., 2018; Melbourne-Thomas et al., 2015). The differences in sea-ice physical properties, in algal community composition and photophysiological adaption strategies, together with the spatio-temporal variability impedes the formulation of a universal relationship. This is particularly true if relationships are derived from univariate statistical models. In fact, Lange et al. (2016) pointed out that the EOF approach provided better

correlations because it accounted for a broader range of spectral variability by including multiple regions of the spectra.

Different types of sea-ice cover at different locations over different seasons control algal community composition, biomass accumulation and ice algal bio-optical characteristics (Galindo et al., 2017; AlouFont et al., 2013). As an example, low light availability may trigger shade acclimation leading to an increase in the chl-a per cell ratio and increased production of accessory pigments, thereby boosting the ice algal package effect (decreased absorption efficiency per chl-a) (Wongpan et al., 2018; Melbourne- Thomas et al., 2015; Kirk, 2011). Theoretically, the effect induces a flattening of the absorption spectrum of the bulk algae composite (Morel and Bricaud, 1981) and could consequentially result in an underestimation of chl-a due to the presence of other ice algal pigments such as fucoxanthin and diadinoxanthin, affecting absorption but not chl-a concentration.

Also, it has been shown that the absorption spectra of algal communities change vertically over the sea-ice cover (Fritsen et al., 2011). Due to different light levels, ice physical properties, and nutrient availability along the vertical gradient in the sea ice, algae communities at different depth layers will adopt distinct acclimation strategies which have an impact on their pigment composition which can affect absorption spectra (AlouFont et al., 2013). Even though populations are generally found at the bottom of the ice, the effect of different vertical distributions and diverse species composition on the optical method has not been assessed and requires further investigation.

In this context, future studies should include pigment determination using High-Performance Liquid Chromatography (HPLC) to measure the entire suite of photosynthetic and photoprotective algal pigments (Miller et al., 2015), and measurements of particulate and algal absorption spectra using spectrophotometers equipped with integrating spheres (Wongpan et al., 2018; Lund-Hansen et al., 2014).

Another limitation of the described optical method is related to the minimum amount of chl-a in the ice that can be detected by under-ice remote sensing (Lange et al., 2016; Nicolaus et al., 2013). Studies have attempted to correlate fluorometric chl-a estimates with under-ice spectra without success. This has been attributed either to low algal biomass or the high concentrations of other substances in the few cores sampled for cross-calibration (Katlein et al., 2016; Nicolaus et al., 2013). With low chl-a concentrations in the ice, the correlations are dominated by effects of other optically active components and hinder the development and establishment of accurate models.

Nevertheless, whilst the strength of correlation within the models is noticeably variable (Table 2.2), opportunities for improvement for model robustness exists. From a remote sensing perspective, the goal is to provide more accurate correlations able to determine chl-a from spectral data and other remotely sensed physical parameters without the need to calibrate with local chl-a measurements for every single survey. So far, mostly univariate models have been tested, and further research could be conducted in this area with regression models attempting to take advantage of multiple spectral bands or additional parameters as shown in studies on other targets (Liu et al., 2011).

There is an extensive library of algorithms available that could be tested for developing improved relationships between measured spectra and sampled chl-a (e.g., in the field of machine learning). Adequate algorithms can be selected based on the amount of data available and characteristics of the algorithm with references from comparable studies applied in remote sensing of other environments. For example, studies have successfully estimated biomass in wheat employing multiple univariate indexes as input parameters for different machine learning models such as random forest or artificial neural networks (Wang et al., 2016). In the case of sea-ice algae, different statistical indexes such as NDI, ratios, scaled band area, and EOFs can be tested together as model parameters potentially providing more robust regression models. The reasoning behind this is that the different properties of some indexes are more capable of accounting for specific differences in the sea-ice environment, resulting in overall more robust models (Lange et al., 2016; Melbourne-Thomas et al., 2015).

To overcome regional dependence, predictive statistical models could be trained over the acquired high spectral and spatial resolution datasets for developing regressions models using diverse input parameters such as the hyperspectral data, ice thickness, snow depth, sub-surface roughness, geographical location and proxies of algal photoadaptation among others. The scheme of environmental drivers in Figure 2.2 suggests some possible parameters, representative of fine and large-scale processes, which could be used in the parametrization of new predictive models.

The problem for sea ice training datasets is that they are generally scarce due to the remoteness of the study areas and the difficulty of sampling sea ice. New, more robust algorithms will require considerable amounts of data and variables to develop accurate predictions. Producing datasets coupling physical and biological parameters would not only assist in a better understanding of the natural process governing algae distribution but could also provide indicators useful for modeling the relationships. In this context, future chl-a sampling campaigns should be, when possible, paired with under ice spectral measurements, proxies of algae photophysiological adaptations and other parameters to create an extensive cumulative dataset over time and for multiple ice types.

2.4.2 Possibilities beyond biomass regression models

Outside the range of statistical regression models, hyperspectral data may also improve our understanding of sea-ice algae beyond simple biomass distribution estimates. This might include the possibility of discretely distinguishing algae physiological conditions (e.g., Perkins et al., 2016) and detection of community compositions from the under-ice signals as analogously done in phytoplankton and vegetation studies (Moisan et al., 2011; Zhang et al., 2015). This could be achieved through hyperspectral signal decomposition and analyses aimed to resolve relative amounts of different types of algae pigments, CDOM or other detritus presence. Hyperspectral and multispectral airborne data have been used to estimate pigment composition of terrestrial plants for example (Blackburn, 2006). The differentiation between algae species in sea ice is important for

improving the understanding of ice algal primary productivity, phenology and in support of predictive modelling efforts (Leu et al., 2015; Lizotte, 2001). For this purpose, different spectral decomposition techniques could be tested a priori through laboratory approaches with known algae species and concentrations in controlled environments (e.g., Mehrubeoglu et al., 2013; Moberg et al., 2002).

2.4.3 Under-ice platforms for sea-ice radiation transfer mapping

Accurately mapping spectrally-resolved under-ice shortwave radiation with high-frequency point sampling is paramount for the development of under-ice optical remote sensing methods aimed to improve biomass spatial variability estimates in sea ice. In this context, UUVs and trawl based system are showing high capabilities to survey under-ice areas in a spatially and temporally efficient manner where usually difficult access is the norm (e.g., Lange et al., 2016). UUVs include both ROVs (Figure 2.4b) and AUVs (Figure 2.4c). A general overview on UUVs describing each platform type, potentials and limitations is given in Wynn et al., (2014), and a description of their differences and complimentary use for scientific operations by Ludvigsen et al., (2013).

Radiance and irradiance hyperspectral radiometers mounted on ROVs have recently been deployed for mapping under-ice radiation transfer under both Arctic land-fast and a pack ice (Lund-Hansen et al., 2018; Katlein et al., 2015a; Nicolaus et al., 2013; Nicolaus and Katlein, 2013), and under Antarctic pack ice (Arndt et al., 2017; Meiners et al., 2017). Table 2.3 provides a compilation of all studies employing UUVs for under-ice radiation transfer mapping. Surveying transects up to 150 m long and areal point sample grids up to 100×100 m have been measured. For sea ice, the use of remotely operated platforms also solves issues related to the bias of sampling towards stable ice floes due to the practical and safety requirements associated with deploying personnel for ice coring. Sampling with remotely operated platforms allows researchers to efficiently survey various types of sea ice, such as newly formed ice, ponded ice as well as snow-covered sea ice and pressure ridges within the same survey. For these first approaches, vehicle depths have ranged from 1 m to a maximum of 10 m from the ice sub-surface (Table 2.3). However, data are typically filtered so that only spectral measurements within 2 m from the ice bottom are accounted for. An exception is for Lund-Hansen et al. (2018) which successfully developed and deployed and ROV for measuring under-ice irradiance fields, sliding at a fixed distance of 0.25 m between the ice bottom and sensor head, using spacer poles.

Compared to under-ice L-arm measurements, UUVs introduce a higher degree of complexity in terms of sensor settings, specifications, and deployment. Particularly if these are to be operated at increasing water depths and in a dynamic setting. Figure 2.5 summarizes all components that require consideration when performing under-ice studies employing UUVs and spectral radiometers. There are trade-offs between the typical remote sensing ambitions and the technical and environmental constraints of the survey.

Figure 2.4 Traditional and emerging deployment modes for under-ice optical sensors. a, L-arms have been the starting point for acquiring under-ice spectral radiometric measurements due to their low-cost and relative ease of applicability; b, ROVs are emerging as a versatile tool to cover larger profiling transects compared to L-arms. The panel displays the Australian Antarctic Division's ROV under Antarctic sea ice (photo credit: Ulrich Freier); c, Autonomous Underwater Vehicles (AUVs) are still being assessed for the particular application of mapping under-ice associated biomass due to the challenges described in the text. However, they present the potential to become a powerful tool towards large-scale mapping of biomass and method automation. The panel displays the GAVIA AUV under algae-populated Antarctic fast ice (photo credit: Vanessa Lucieer).

For example, signal to noise ratio (SNR) is a primary parameter for evaluating hyperspectral data quality (Adão et al., 2017). As underwater platforms are constantly in motion, they require shorter integration times to avoid blurred/displaced sensor footprints (e.g., Lange et al., 2016), with concomitant implications for the SNR (less light gathered per sample) (Figure 2.5). Also, as vehicle distance from the ice increases, the sensor footprint widens, and the resolution of the survey data will decrease (e.g., will become coarser). Constantly moving vehicles deployed at specific depths will by necessity make a trade-off between spatial footprint resolutions, integration times and quality of the signal (Figure 2.5). While some of these underwater vehicles allow for longer integration times by moving at very slow speeds or hovering/parking in a relatively fixed position (e.g., ROVs), other approaches such as the ship trawls or modern AUVs are limited in this aspect. Furthermore, sensor integration times need be set according to the continuously varying environmental conditions such as daylight availability, the sea-ice physical properties (e.g., ice and snow thickness controlling total under-ice irradiance levels) and the water column properties (e.g., destabilizing currents or other optically active materials in the water) (Figure 2.5). While there would be no "best" setting for every surveying scenario, as this will depend on the sea-ice conditions, desired spatial-sampling resolutions and equipment availability, surveys benefit from stable ocean current conditions, clear waters and constant-upward looking sensor attitude.

Table 2.3 A compilation of published studies employing UUVs or any other kind of underwater platform (e.g., under-ice sleds or under-ice trawls) for radiation transfer mapping under sea-ice.

Study	Region/Ice type/Date	Platform and sensor	Survey information
Lange et al., 2016; Nicolaus and Katlein, 2013	• Central Arctic Ocean • Different ice types from ponded ice, snow and ponds frozen, no snow and ponds, frozen surface (FYI, MYI) • August—October 2011	ROV. Radiance and irradiance sensors (TriOS, RAMSES-ACC/ARC)	Various transects of 30 to 210 m. Depths from 1 to 10 m. Filtered to <1.5 m for biomass estimates.
		Under-ice trawls. Radiance and irradiance sensors (TriOS, RAMSES-ACC/ARC)	Two transects of 800 and 1500 m respectively. Depths from 0 to 200 m. Filtered to <1.5 m for biomass estimates.
Nicolaus et al., 2013	• Barrow, Alaska, Arctic Ocean • Land-fast sea ice, snow covered • March, May, and June 2010	Under ice sled. Irradiance (TriOS, RAMSES ACC)	Three transects of 20, 40 and 80 m. No depth. Spectroradiometer at 2±1 cm from the ice subsurface.
Katlein et al., 2015a	• Arctic Ocean • Ice floe with melt ponds • July 2014	Nereid Under Ice (NUI) (hybrid ROV). Radiance and Irradiance (TriOS, RAMSES-ACC/ARC)	100 m transects at approx. Depths of 5 m.
Arndt et al., 2017; Meiners et al., 2017	• Weddell Sea • Ice floe of flooded pack-ice • September 2013	ROV, Irradiance (TriOS, RAMSES-ACC)	100 m-by-100 m grid. Depths filtered to < 2 m.
Lund-Hansen et al., 2018	• Kangerlussuaq, West Greenland • Landfast first-year ice • March 2016	Low-cost portable ROV. Irradiance (TriOS RAMSES ACC-UV/VIS)	15 m transects. Sensor fixed depth of 0.25 m.
Matthes et al., 2019	• Qikiqtarjuaq, Southern Baffin Island • Landfast sea ice • May–June 2015 and June–July 2016.	ROV, Irradiance (TriOS, RAMSES-ACC)	Multiple transects of several tenths' meters in length. Sensor depth at around 2 m.

Compared to ROVs, AUVs are underwater drones that are capable of executing pre-programmed routes to cover significant distances (10's of kilometers). Although there are no published studies employing AUVs for biomass estimates in sea ice except for a study by Forrest et al. (2016), AUVs are increasingly being used for sea-ice research and are showing great potential (Lucieer et al., 2016; Norgren and Skjetne, 2014; Singh et al., 2017; Williams et al., 2014). However, all the aforementioned problems would be accentuated when mounting sensors on AUVs due to the mechanisms for AUV operation. These include deeper operating depths to avoid collision hazards, constant but relatively fast traveling speeds, and geo-referencing the motion of the vehicle to the finely tuned sensors. When using irradiance sensors, increased distance to the ice sub-surface will lead to a strong areal averaging of light levels and a loss of spatial resolution (Figure 2.3). Therefore, surveys would require radiance sensors to be deployed according to the desired mapping footprint by regulating vehicle depth based on the FOV of the sensor and vehicle capabilities. Radiance sensors with a narrow FOV are therefore fundamental if the sensor is to be deployed at increasing depths while still aiming to achieve specific mapping resolutions and to avoid the light influence of the surrounding water column (Nicolaus and Katlein, 2013). The trade-off with radiance sensors (and HI sensors) is that they can less sensitive compared to irradiance sensors since reduced collection angle inevitably results in a reduced amount of light collected per a defined integration time (Figure 2.5).

Furthermore, considering the anisotropic nature of the under-ice light field, sampling radiance distribution would not be accurate if the light field varies considerably across the field of view of the sensor as previously mentioned. This is because radiance sensors collect light from a finite solid angle (Figure 2.3), but radiance is mathematically defined for an infinitely small solid angle. Sensor settings and deployment mode would, therefore, need to be regulated for the desired outcome, considering the constraints outlined in Figure 2.5 as well as the under-ice geometric light field. Katlein et al. (2016) used a geometric light field model to investigate this aspect and suggested that radiance measurements (with a 10° FOV sensor) conducted more than 4 m away from the ice underside would need to be converted to under-ice irradiance using a conversion method based on the C value outlined in Katlein et al. (2014). The C value depends on the angular distribution of radiance underneath the ice and can be obtained from a direct measurement of the radiance distribution under the ice, or either from sea-ice physical properties. Considerable work is required to standardize the application of finite FOV sensors in under-ice remote sensing studies.

2.4.4 Hyperspectral imaging

Hyperspectral imaging (HI) aims to obtain the spectrum for each pixel in the image of a scene, with the purpose of finding objects, identifying materials, or detecting and quantifying processes (Bioucas-Dias et al., 2013). As the technology becomes more portable and accessible, it has found an immense range of applications ranging from environmental monitoring (Adão et al., 2017), chemometrics (Amigo et al., 2015), precision agriculture (Mäkynen et al., 2012) forensic analyses (Edelman et al., 2012) and medicine (Lu and Fei, 2014) to mention a few. Depending on the desired aims and settings, these sensors can capture features at different scales ranging from millimeter close-range imagery to continuous swaths of data at the mesoscale depending on the sensor distance from the target and the mounting platform.

The hyperspectral images consist of a three- dimensional (x, y, λ) data cube where x and y represent the spatial dimension (with pixel sizes that can vary depending on the survey type), and λ the spectral dimension. The modality in which the frame is acquired can be in either push-broom or snap-shot mode (e.g., Huang et al., 2014). Each type of sensor presents both advantages and disadvantages with the choice purely based on user preferences. HI data processing involves pre-processing of raw data cubes, compression, exploration, regression, and segmentation to finally providing abundance estimates or classification of the desired features (e.g., Amigo et al., 2015; Bioucas-Dias et al., 2013).

Application of HI in the underwater domain is relatively new and presents several optical and technical challenges that still require considerable research effort. However, pioneering studies are highlighting the potential for creating high resolution, georeferenced, optically corrected digital underwater maps of different habitats, minerals, substrates, and organisms (Dumke et al., 2018; Chennu et al., 2017, 2013; Johnsen et al., 2013).

A recent study assessed the use of HI for mapping sea-ice algae biomass variability at the ice-water interface in an experimental sea-ice simulation tank (Cimoli et al., 2017a or Chapter 3). Using a pushbroom hyperspectral camera at 1 m distance over a 0.72 m^2 ice surface, variability in ice algal biomass was captured in images at very high spatial resolutions (0.9 mm square pixels). The sensor acquired radiometric data over the PAR range (400-700 nm) and following repeated tests at multiple spectral resolutions the study concluded that spectral resolutions > 6 nm could not be suitable for ice algal habitat mapping. For an under-ice algal mapping context, the high spatial variability at the microscale, the varying photophysiological adaptations of ice algae (modifying absorption spectra), and the highly variable under-ice light environment need to be considered when selecting an HI sensor. Snapshot HI sensors are easier to use (more portable and not constantly requiring a set of six orientation parameters) than pushbroom sensors which require a relatively constant and accurate forward motion across the imaged target and are drift sensitive. Pushbroom sensors require the integration time (or frames per second) to be set according to the moving speed for reconstructing the images (Figure 2.5). The aim is to attain adequate SNR, and due to the finite number of pixels on a focal plane array, snapshot HI sensors make a trade-off in the resolution of the various dimensions of data of the data cube sacrificing either spatial or spectral resolution. This can be limiting depending on the surveyed target, the desired mapping resolution and in particular under low light conditions.

Analogously to standard point sampling radiometers, Figure 2.5 outlines for HI the relevant under-ice tradeoffs between the typical optical remote sensing ambitions that need to be balanced with both technical and environmental factors. For HI cameras, finer spectral resolution can be offset by a lower SNR when compared to multispectral sensors because of the fewer number of photons captured by each detector due to the narrower width of the spectral channels (Figure 2.5). Furthermore, SNR associated with this type of sensor are accentuated compared to standard radiometers due to the light redistribution across spatial pixels along the sensor. Such systems necessarily need to involve a more sensitive instrument set-up by considering deployment depth, integration times (or frames per second) and moving speeds (for pushbroom sensors) (Figure 2.5).

There is also a series of other technical considerations in HI sensor and settings selection. To mention a few, the fore-optics need to match the light collection capability of the diffracting element (Figure 2.5). If the lens' F-number is too low, the slit can overfill causing increased stray light (reduced SNR); if the F-number is too high, it will limit the throughput of the system (thus the SNR). On the other hand, the slit size of the instrument is inversely proportional to the spectral resolution of the system, but positively correlated with the amount of light reaching the sensor and thus also affect the SNR (Figure 2.5). Other technical sensor specific capabilities include pixel binning, which merges pixels to increase SNR at the expense of either spatial or spectral resolution, or the overall optical system efficiency and quality (Figure 2.5).

From a remote sensing perspective, the goal is to deploy sensors deeper (to increase the spatial footprint and areal coverage), to make them move faster (to reduce operational times and increase

efficiency) and to capture as much light as the conditions allow. Eventually, HI technology could be routinely mounted onto UUVs as proposed for underwater benthic mapping (Johnsen et al., 2013) or deep-sea classification of features of interest (Dumke et al., 2018). However, there is a complex trade-off between all the aforementioned parameters that will need to be assessed for each case (Figure 2.5). Deployment of wide FOV sensors might be constrained due to under-ice anisotropic and surface dependent light fields (Katlein et al., 2016, 2014; Petrich et al., 2012). SNR and dynamic range performance under dim and dynamic light conditions are also key considerations that could potentially be limiting the technology.

Application limits of the technology need therefore to be thoroughly investigated. These include delimiting light levels where the technology is not applicable and other environmental or logistical deployment constraints impeding target detection, underwater georeferencing and image composition (Dumke et al., 2018). For example, image composition and quality might be limited for a scanning pushbroom sensor under a turbulent underwater regime (Figure 2.5). In addition, as HI can be expensive and prohibitive, we need to work towards identifying the most cost-effective solutions for each specific situation and target (e.g., testing band specific imaging cameras). Simulation sea-ice tanks with controlled algae cultures and light levels will be useful platforms for further testing of key parameters for the development of this methodology (Cimoli et al., 2017a or Chapter 3).

From a data processing perspective, the amount of HI data can be overwhelming and is not straightforward to identify relevant information with such a vast array of data. Multivariate and other statistical approaches have led to several powerful tools in support of hyperspectral remote sensing data analysis (Amigo et al., 2015; Chang and Chang, 2013). However, there are fundamental differences between applications of the technology in typical, above surface, remote sensing applications. Hyperspectral frames from hypothetical upward looking under-ice sensors would acquire images in transmission mode rather than reflection mode, and there are challenges associated with transmission HI compared to reflected light HI which would need to be considered and further investigated for an *in situ* application (Cimoli et al., 2017a or Chapter 3).

2.4.5 Water column correction and immersion effect

In marine optical remote sensing, the water column can have a considerable impact in the traversing electromagnetic radiation depending on its composition and presence of optically active elements such as phytoplankton, suspended particles and CDOM (Morel and Maritorena, 2001). Except for some cases of very high and concentrated algal blooms below the ice (Arrigo et al., 2012), polar under-ice waters are generally characterised by low concentrations of biomass in the water column compared to those observed in the ice (albeit this is depending on the season and region) (Arrigo et al., 2014; Gradinger, 2009; Spindler, 1994). Assuming no phytoplankton blooms, for sensors deployed near the ice sub-surface, the effect of the water column can be considered negligible at

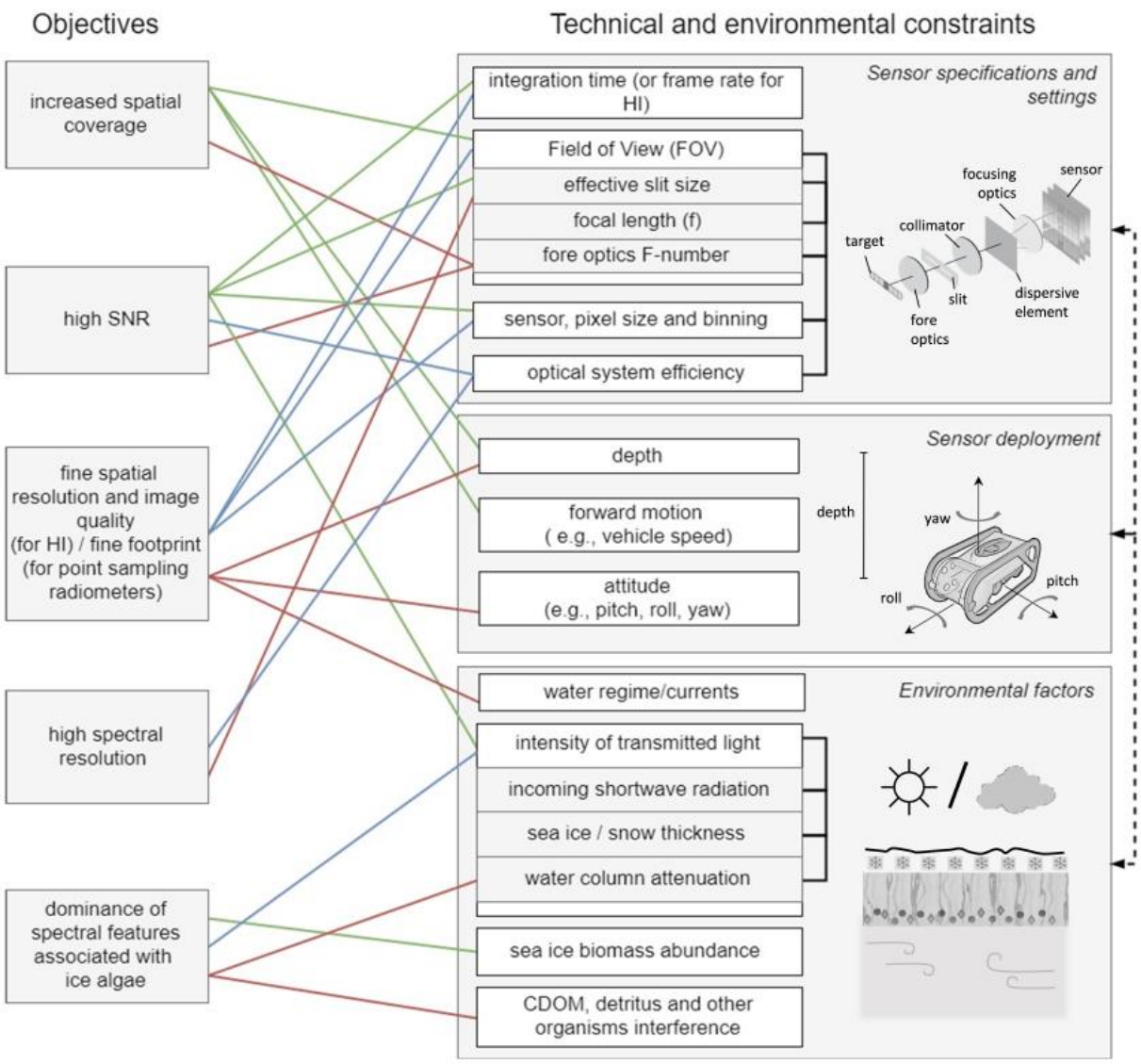

Figure 2.2 Schematic of the trade-offs between the typical remote sensing objectives (left), and the technical and environmental factors to consider in an under-ice surveying context. Red links indicate that there is an inverse relationship between the ideal objective and the factor whereas green links indicate a positive relationship. Blue connectors refer to a variable relationship. The black line connectors (inside contour boxes) indicate that the factors are highly correlated. More information can be found in the text. Overall, sensor specifications need to be set according to deployment mode and to the environmental constraints (symbolized by the black dotted line on the right side of figure). The optical system efficiency includes optical throughput of the lenses, the dispersive element efficiency, and the detector quantum efficiency. The scheme is valid for both non-imaging radiometers and HI. Spatial resolution refers to the ground sample distance of an imaging spectrometer. The spatial footprint refers to the circular footprint of normal spectrally resolved radiometer. SNR refers to Signal to Noise Ratio.

low distances < 0.5 m (Campbell et al., 2015; Melbourne-Thomas et al., 2015). However, increasing the distance between the ice subsurface and the sensor would increase the amount of matter in the optical path and thus disqualifying the previous assumption, e.g., in cases where UUVs are required to be deployed at increased water depth. Increased water depths would result not only in a reduction of light availability and changed spectral and geometrical properties of the measured light field but could result in the overestimation of biomass in the ice due to the interference of phytoplankton and thus chl-a in the overlying water column (Figure 2.5) (Matthes et al., 2019). Overall, it is not possible to define locations or periods of the year where the water column effect could be considered negligible, and this should be verified at every survey when possible.

To correct for water-column effects, the most straightforward method is to estimate the water column spectral attenuation coefficient K_d (λ) by means of irradiance profiles (Morel and Maritorena, 2001). This yields the extinction characteristics of the local seawater and can be applied to the optical data collected at depth by UUVs (Nicolaus and Katlein, 2013).

If larger distances are to be covered (e.g., through UUVs), it is important to account for any variability of the water column optical properties under-ice (Frey et al., 2011). Spatial variability in water column optical properties could be assessed by performing multiple vertical irradiance profiles to assess spatial variability of such properties.

For hypothetical long-range UUVs transects, water column correction methods would open a challenging research front involving the acquisition of optical properties of the water column simultaneously with the hyperspectral data collection. Measured absorption and scattering properties can then be input into radiative transfer equations to calculate the influence of the water column over the composed imagery (Johnsen et al., 2013). Nevertheless, methods usually applied in marine remote sensing such as modeling of the water column trough radiative transfer will remain challenging in under-ice waters due to the high horizontal variations in structure producing highly variable under-ice light fields (Katlein et al., 2015a).

In case of small-scale HI of the ice-water interface, water column effects can be corrected using standard techniques such as the empirical line method with known reflectance targets (Chennu et al., 2013; Smith and Milton, 1999) or through localized, depth-integrated, irradiance measurements and estimations of inherent and apparent optical properties (Johnsen et al., 2013).

Finally, for radiometers or hyperspectral imagers alike to be immersed in water, specifically designed enclosures are required to safeguard the instrument integrity and efficiency (Zibordi, 2006). Usually, calibration files are provided for off-the-shelf sensors that are designed for underwater deployment. However, HI cameras or other desirable radiometric instruments that have not been designed for in water use would require customized sealed enclosures. These enclosures can introduce spectral and geometrical aberrations whose description is out of the scope of this review. Due to the significant influence on any optical calibrations, and compounding uncertainties associated with different lens materials and geometries, it suffices to say that

calibration might be necessary for any additional medium between the sensor and the target under investigation. Particularly if high accuracy radiometric and geometric data are required (Zibordi and Voss, 2014).

Chapter 3

Towards improved estimates of sea-ice algal biomass: experimental assessment of hyperspectral imaging cameras for under-ice studies

3.1 Introduction

Sea-ice algae are important contributors to primary production in the polar oceans (Arrigo et al., 2014; Kohlbach et al., 2016; McMinn et al., 2012), and play an active role in large-scale biogeochemical cycles determining rates of carbon export (Boetius et al., 2013) and ocean-atmosphere exchange (Vancoppenolle et al., 2013). During winter and spring, sea-ice algae are vital for polar marine ecosystems as they provide an essential food source for pelagic herbivores (Arrigo et al., 2014; Flores et al., 2012). During the melt season, ice algae can seed the spring phytoplankton bloom following ice ablation (Brugel et al., 2009; Mundy et al., 2014; Søreide et al., 2010).

Chlorophyll *a* (chl-a) concentrations in sea ice are considered a useful proxy for algal biomass abundance (Gradinger, 2009; Meiners et al., 2012). The highest algal standing stocks are usually found at the bottom of the ice cover near the ice-water interface (Arrigo et al., 2010). Using chl-a as proxy, several studies have reported high spatial variability in ice algal biomass, e.g. changes across multiple orders of magnitude on spatial scales ranging from millimetre (Hawes et al., 2012) to the mesoscale (metres to kilometres) (Gradinger, 2009; Steffens et al., 2006).

Unlike phytoplankton and ocean colour, chl-a concentrations in sea ice cannot be monitored with aerial or satellite remote sensing techniques. Current sea-ice chl-a sampling methods include ice-core sampling (Miller et al., 2015), diver operated fluorometers (Rysgaard et al., 2001) or simple imagery data (such as video or still photographs) (Gutt, 1995; Katlein et al., 2015b). These established methodologies are labour intensive, invasive or have a coarse resolution and are not appropriate for capturing the high spatial and temporal variability of ice-algae biomass. This has consequences for our understanding of ice algal dynamics, with associated implications for estimating their overall contribution to marine production and how they respond to environmental changes (Meiners et al., 2012). Due to the high logistical costs involved in monitoring in the harsh polar environments, there is a need to develop new and efficient methodologies that can efficiently track ice-algal biomass across multiple spatial scales.

Recent studies have explored methods for quantifying chl-a (as proxy for biomass) within sea ice by measuring the spectral composition of downward transmitted visible light that is measured beneath the ice-water interface (Campbell et al., 2014; Melbourne-Thomas et al., 2015; Mundy et al., 2007). Transmitted light measurements at the ice bottom can provide information on algal biomass due to the light absorption by algal pigments such as chl-a (Maykut and Grenfell, 1975; Perovich, 1996). Quantitative methods are usually performed by deploying upward looking spectral irradiance sensors below the ice (at 15-50 cm distance) using an L-arm. The measured spectrum of transmitted irradiance can then be statistically correlated to the amount of measured chl-a (determined from ice core samples) using empirical correlations methods and univariate models such as Normalized Difference Indices (NDI) or Empirical Orthogonal Functions (EOFs) (Lange et al., 2016b; Melbourne-Thomas et al., 2015; Mundy et al., 2007). These novel methods are providing new opportunities for monitoring ice-algal biomass at an increased sampling rate in a non-invasive manner. For example, irradiance sensors can be mounted on Remotely Operated Vehicles (ROVs) for further enhancing the spatial extent of these surveys (Lange et al., 2016b). The use of transmitted irradiance spectra, however, only determines the integrated (over the entire ice thickness) ice-algal biomass.

We are taking advantage of such considerations and for the first time we experimentally assess the possibility of employing hyperspectral imaging (HI) cameras in transmission mode (measuring transmitted instead of reflected light) to map sea-ice algae biomass distribution at the ice-water interface. In contrast to the wide and disconnected footprint of radiance and irradiance sensors, HI cameras are able to map spectral signatures across a target area at high spatial resolutions (Amigo et al., 2015; Johnsen et al., 2013). HI is usually employed in reflectance mode and these systems are gaining considerable momentum in the natural sciences and close-range remote sensing domain as the technology becomes more accessible and portable (e.g. Holzinger et al., 2016; Lucieer et al., 2014; Malenovský et al., 2015). Recent applications in related disciplines include mapping of benthic algae distributions and biomass (Chennu et al., 2013), coral physiology (Perkins et al., 2016), and algae pigment composition (Nogami et al., 2014). Sea ice is an optically complex medium and there are many challenges in measuring transmitted radiance through the ice that need to be overcome through gradual testing and evaluation both in laboratory and *in situ* studies. Aside from understanding the target spectral signature, we also need to understand the complexity associated with both under-ice HI deployment and data processing.

In the present study, a HI camera was used to image an inverted sea-ice simulation tank specifically designed for growing and monitoring sea-ice microbial consortia at the ice-water interface. The tank is termed 'inverted' due to its "upside down" representation of the sea-ice environment, i.e. the light source is beneath the ice and a water layer is above it (Figure 3.1). This configuration provides an ideal environment for testing different hyperspectral imaging scenarios in a controlled environment.

This first test is a proof of concept, aimed to developing a near remote sensing method that can identify ice-algae patchiness at different spatial scales in a non-invasive manner. For this purpose, we inoculated the tank with ice-algal communities to establish six spatially variable algal patches at the tank's ice-water interface. This study starts by outlining our novel experimental set-up and the data acquisition methodologies. We then employ exploratory image analysis to assess the feasibility of HI to resolve ice-algal spatial variability. The study concludes by comparing our sea ice tank to an *in situ* scenario and discussing future possibilities and limitations of the method.

3.2 Data and Methodology

All experiments were conducted at the Algal Laboratories of the Institute of Marine and Antarctic Studies in Hobart, at the University of Tasmania, Australia. The experiment was divided into five sequential phases; 1) ice tank preparation, 2) algae culturing, 3) hyperspectral imaging, 4) chl-a sampling and 5) data processing.

3.2.1 Inverted ice-tank design and preparation

The inverted ice tank was built as an "upside down" representation of the sea ice environment comprising, from the bottom to the top, a light source, air, glass, ice and water interfaces (Figure 3.1). The tank's area of frozen ice is 0.85 m x 0.85 m and ice growth is initiated using 30 litres of filtered deionized water frozen overnight (at -20 °C) followed by the addition of 70 litres of pre-chilled (-1.7 °C) 0.2 µm filtered seawater. The initial addition of fresh water is necessary to ensure that the freezing seawater adhered to the base of the tank and didn't float to the surface by expulsion of the hypersaline brine. The filtered seawater layer (36 ppt) was left to freeze for two days followed by the removal of excess hypersaline brine resulting in an ice thickness of approximately 70 mm. Additional pre-chilled seawater (-1.7 °C, 36 ppt) was then added to achieve a 20 – 30 mm water layer above the ice which remained unfrozen at a temperature of approximately -1.8 °C. Images of the ice surface before algae inoculation are shown in Figure 3.2a, b.

The upward directed light source is a Cree Xlamp XP-E High-Efficiency white LED and has a typical double bell spectral curve characteristic of white LED light sources (Figure 3.1). It covers the Photosyntetically Active Radiation (PAR) (from 400 to 700 nm) range and provides moderate intensities in the regions of interest where ice algae show their main absorption peaks (e.g. Fritsen et al., 2011). The lighting system was deliberately installed to be consistent with measured under-ice PAR irradiance intensities. For example, using a Li-COR PAR sensor to measure light flux at the ice-water interface of the inverted ice tank, we measured light levels ranging from 31.4 to 58.6 µmol photon m^{-2} s^{-1} from the dark areas to bright areas. This is comparable to *in situ* measurements beneath Arctic (e.g. Lund-Hansen et al., 2014) or Antarctic sea-ice (e.g. SooHoo et al., 1987). The glass sheet between the light source, the ice, and water layers is optically clear allowing

transmission of >90% of light and having minimal influence on the optical properties of the transmitted light.

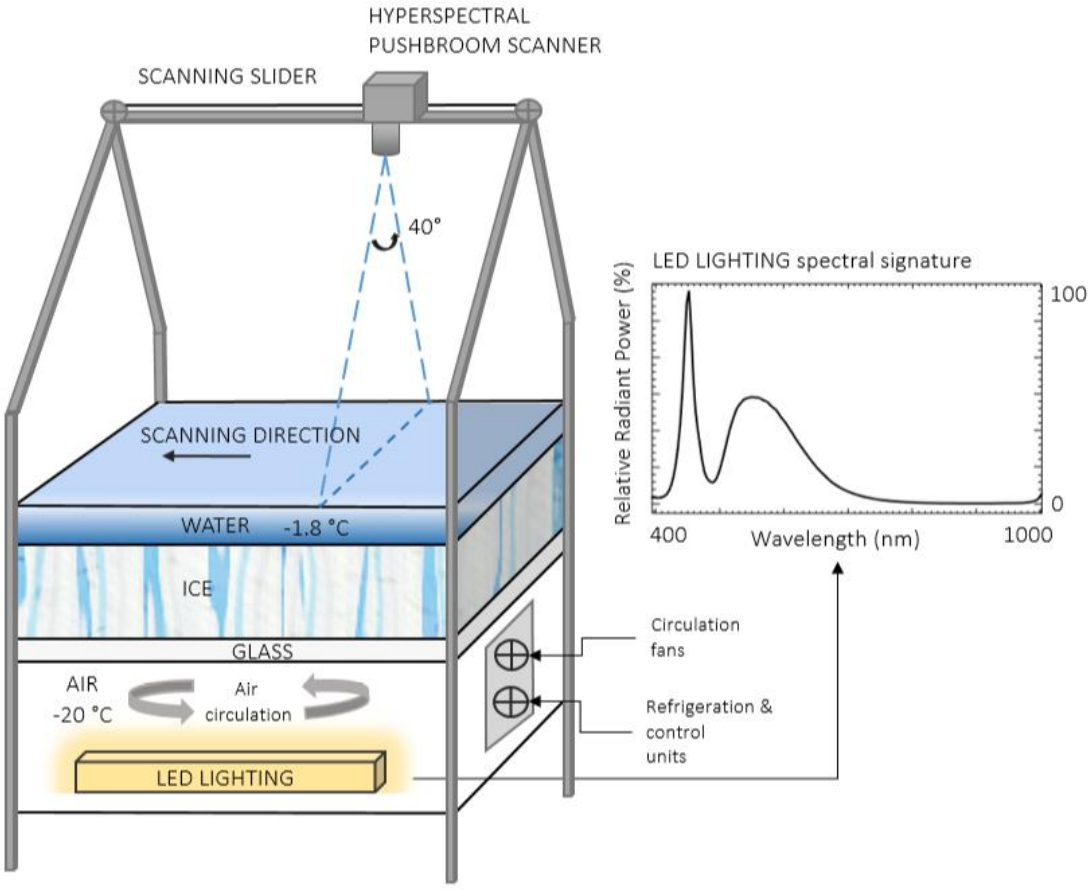

Figure 3.1 Illustration of the inverted sea-ice simulation tank and spectral signature of the LED artificial light source. The hyperspectral pushbroom scanner was mounted onto a motorized sliding rail at 1.2 m distance above the ice/water interface. The layered surfaces (glass, ice, water) cover an area of 0.85 m× 0.85 m. The distance from the camera fore-optics to the ice layer is 1 m. The illustration is not to scale.

3.2.2 Ice algae culturing and inoculation

Algal cultures consisting of *Fragilariopsis cylindrus*, *Nitzschia stellata* and *Navicula glaciei* were extracted from Antarctic sea ice in 2015, and maintained semi-continuously in L10 media (Guillard and Ryther, 1962) under cool white fluorescent light (60 µmol photon m^{-2} s^{-1}, 12:12 light/dark cycle) at 2°C ± 1°C. Each algal species was grown separately in a continuous batch system, bubbled with 0.2 um filtered air and amended with L1 nutrients (Guillard and Ryther, 1962). Before inoculation, cells were acclimated to -1°C over a 12-hour period to limit any cold induced shock from the ice-tank environment. Once ready for inoculation, varying volumes were extracted from the parent cultures and added to a set of eight cylinders to spatially distribute algal biomass at

increasing concentrations. This provided an increasing scale of biomass abundance intensities among the eight cylinders.

The cylinders were 80 mm in diameter and 50 - 60 mm high and were placed 20 - 30 mm deep in the ice layer and left emerging above the water surface layer (Figure 3.2d). Two types of material were chosen for the cylinders; opaque PVC tubes and optically clear acrylic tubes. Based on the expected concentrations, the biomass abundance intensities inoculated in the eight cylinders were denominated as follows: two empty controls (C1 and C2) in PVC and acrylic, respectively; a Very Low (VL) in PVC; a Low (L) in acrylic; a Medium (M) in acrylic; a Medium High (MH) in PVC; a High (H) in acrylic; and a Very High (VH) in PVC. Figure 3.2d shows the VH PVC cylinder after inoculation.

3.2.3 Hyperspectral imaging

A pushbroom SPECIM AISA KESTREL 10 (AK10) hyperspectral line scanner was employed for imaging the algal distributions at the ice-water interface (Figure 3.2b and Figure 3.2c). Imaging with the pushbroom sensor required a scan to be conducted in a forward motion across the target of interest in order to create the image (Figure 3.1). Thus, the AK10 was integrated into a motorized slider with precise adjustable speeds for this purpose (Figure 3.2b). The AK10 has a 40 degrees Field of View (FOV) and comprises a total of 2048 pixels that can be binned into 1020 to improve the Signal to Noise Ratio (SNR) per pixel. The sensor's spectral range goes from 400 to 1000 nm and allows for customized spectral resolution and integration times (frequency) to be set according to the survey scenario. The motorized slider was placed 1.2 meter above the ice-water interface (1 meter considering the camera fore-optics) allowing the camera to achieve a spatial across-track resolution of 0.9 mm which covered a scan line width of 728 mm. The imaging frequency was set to 5 Hz and the sliding rail speed around 8 to 10 mm s^{-1} providing along-track resolution of 0.8 to 0.9 mm (thus 0.9 mm square pixels in the composed image). Hereafter, a spatial resolution of 0.9 mm will refer to the 0.9 x 0.9 mm squared nature of the image pixel size. We selected the slider speed and frequency to maximize the intensity of the acquired signal, or SNR. For this experiment, we repeated the scanning process at three different spectral resolutions of 1.7 nm, 3.4 nm and 6.8 nm in order to assess the effect of spectral resolution. All three frames were binned to 1020 pixels. The hyperspectral imaging was performed in the dark with no influence from any other external light source except the tank's LED light source (Figure 3.2a). HI on the tank was performed three days after inoculation of algae.

3.2.4 Chl-a sampling

In order to provide a semi-quantitative validation of the six cylinders' chl-a concentrations, the cylinders were sampled using a 10 mL lab-pipette by scratching the ice whilst simultaneously sucking up any content at the ice-water interface in 5 different 1 cm^2 random spots within each

cylinder. 1 cm^2 sample sub-areas were roughly measured with a mm-scale ruler resting above the cylinders while operating the pipette. The 50 mL samples for each cylinder were immediately filtered onto Whatman GF/F filters, extracted for 24 h in ethanol, and analyzed for chl-a content according to Holm-Hansen and Riemann (1978) using a Turner 10AU fluorometer.

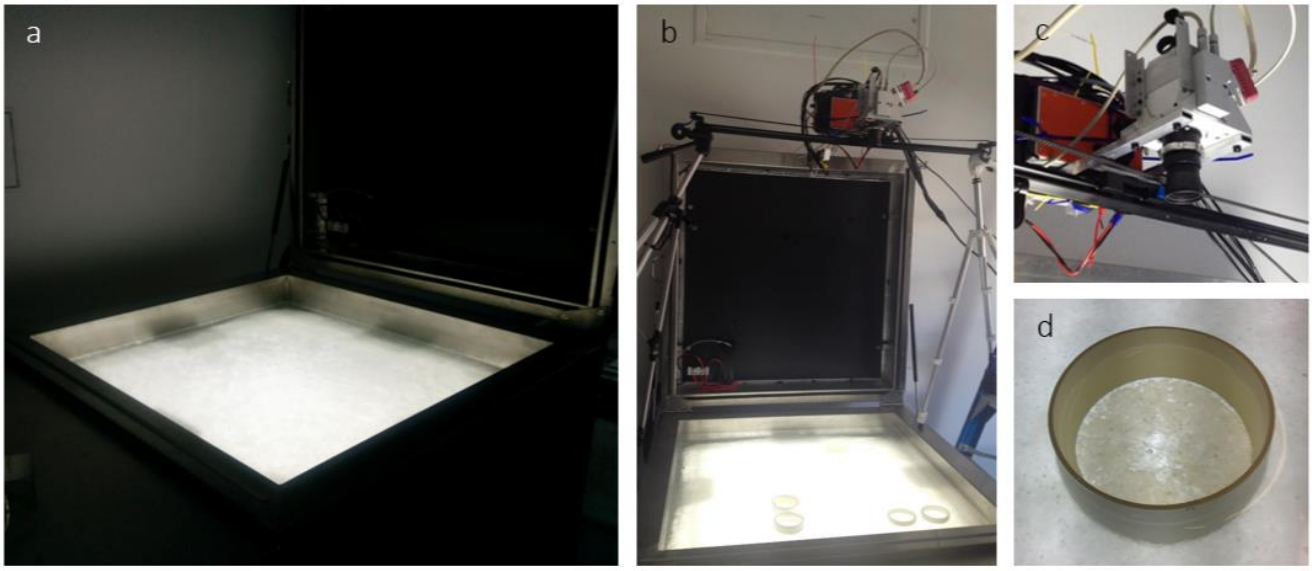

Figure 3.2 a) Image of the inverted sea-ice simulation tank in the dark room setting with all external light sources off. b) Image of the inverted ice tank together with the motorized slider and the cylinder's set-up. c) The SPECIM AISA Kestrel 10 hyperspectral imager. d) High (H) algae abundance cylinder after two days of algae inoculation.

3.2.5 Data processing

The images were composed from the acquired line-scans using SPECIM Lumo Recorder software. All hyperspectral images were converted to radiance values ($W\ m^{-2}\ sr^{-1}\ nm^{-1}$) per pixel from the raw digital numbers (DN) using ENVI software and the provided calibration files. The images are then pre-processed using MATLAB. Pre-processing involved selecting a region of interest (ROI) and spectral filtering. Selecting an ROI was done manually, and this process discarded the extra imaged areas that are not the ice water interface such as the steel borders of the ice tank (Figure 3.2b). Even though the images resulted in high SNR by measuring just below the saturation level, we performed a Savitzky-Golay filter with a third polynomial order and a filter width of five (Tsai and Philpot, 1998; Vidal and Amigo, 2012). The filter aimed to smooth out the high-frequency noise whilst preserving the relevant spectral features at low intensity wavelengths. In order to capture the differences between different algae abundances from light transmitted through the artificial sea ice, Principal Component Analysis (PCA) was performed on the three images taken at the three different spectral resolutions. The hyperspectral images consist of a three-dimensional (x, y, λ) data cubes where x and y represent the spatial dimension and λ the spectral dimension. PCA exploration

method was applied in this case to track the most variable features across the spectral dimension of the hyperspectral images and to outline relevant spectral bands carrying the relevant information on ice-algal biomass (Amigo et al., 2015; Rodarmel and Shan, 2002).

Transmitted radiance measured with the AK10 was compared to publicly available data from a series of Remotely Operated Vehicle (ROV) transects performed in the Arctic by Nicolaus and Katlein, (2013) to provide a comparison with spectral data collected under *in situ* conditions. Radiance along these transects, was measured using an ROV instrumented with a TriOS RAMSES radiance sensor (of 3 nm spectral resolution). Operating depths ranged from 1 to 8 m, for different sea-ice types which varied from snow-free to variable snow cover (from 2 to 10 cm thickness), from First Year Ice (FYI) to Multi Year Ice (MYI) (from 0.3 m to 3.8 m thickness). Detailed information about each transect can be found in Nicolaus and Katlein, (2013). The ROV data set is available online under doi:10.1594/PANGAEA.78671.

3.3 Results

The arrangement of the algal cylinders in the ice tank is shown in Figure 3.3a as an RGB composite image. The figure also displays the ice-algal biomass range from VL to VH as inoculated across the cylinders. The results of the PCA for the HI frame taken at 1.7 nm are shown in Figure 3.3b, c, d. The first principal component (PC1) accounts for 99.8 % of the spectral variability (Figure 3.3b) and represents variations in light intensity across the ice tank. This is confirmed by the loadings of PC1 that clearly match the spectral intensity of the LED light source (Figure 3.3c and Figure 3.1). The light intensity is higher at the centre and decreases towards the edges of the ice tank. This difference in light intensity across the tank is mostly attributed to the non-diffuse (directional) light field emitted by the light source and the shadow structures in the image caused by the circulation fans and the presence of their sustaining structure between the light source and the ice. Another factor influencing light intensity variability was the different ice thickness observed from 7-9 cm at the centre to 5 cm at the edges (due to physical complications of achieving freezing conditions in those locations). PC1 does not contain any information regarding biomass variability but indicatively maps the light intensity distribution over the ice surface.

The second Principal Component (PC2) accounts for 0.09 % of the spectral variation in the hyperspectral image but displays a coherent relationship to the algal cylinder densities. High and low PC2 intensity areas match with low and high biomass values, respectively. Control cylinders (C1 and C2) stand out as high intensity areas opposing to H and VH cylinders (Figure 3.3d). Results from the chl-a sampling are in agreement with the visual observations for VL (0.036 mg m^{-2}), L (0.164 mg m^{-2}), M (0.366 mg m^{-2}), MH (0.636 mg m^{-2}). Chl a sampling in cylinders H (2.712 mg m^{-2}) and VH (1.804 mg m^{-2}) did not match with the increasing inoculation scale with H cylinder having a higher chl-a concentration than VH. Loadings of PC2 in Figure 3c indicate that low PC2 intensity in Figure 3d is associated with increasing loading values at the peaks at approximately 450 and 680 nm

(Figure 3.3c). These peaks closely match with ice algae absorption bands (Fritsen et al., 2011; Legendre and Gosselin, 1991) suggesting a strong association between PC2 and ice-algal biomass. Within cylinder patchiness is also observed as darker spots of low PC2 intensity, particularly for cylinders MH, H and VH (Figure 3.3d).

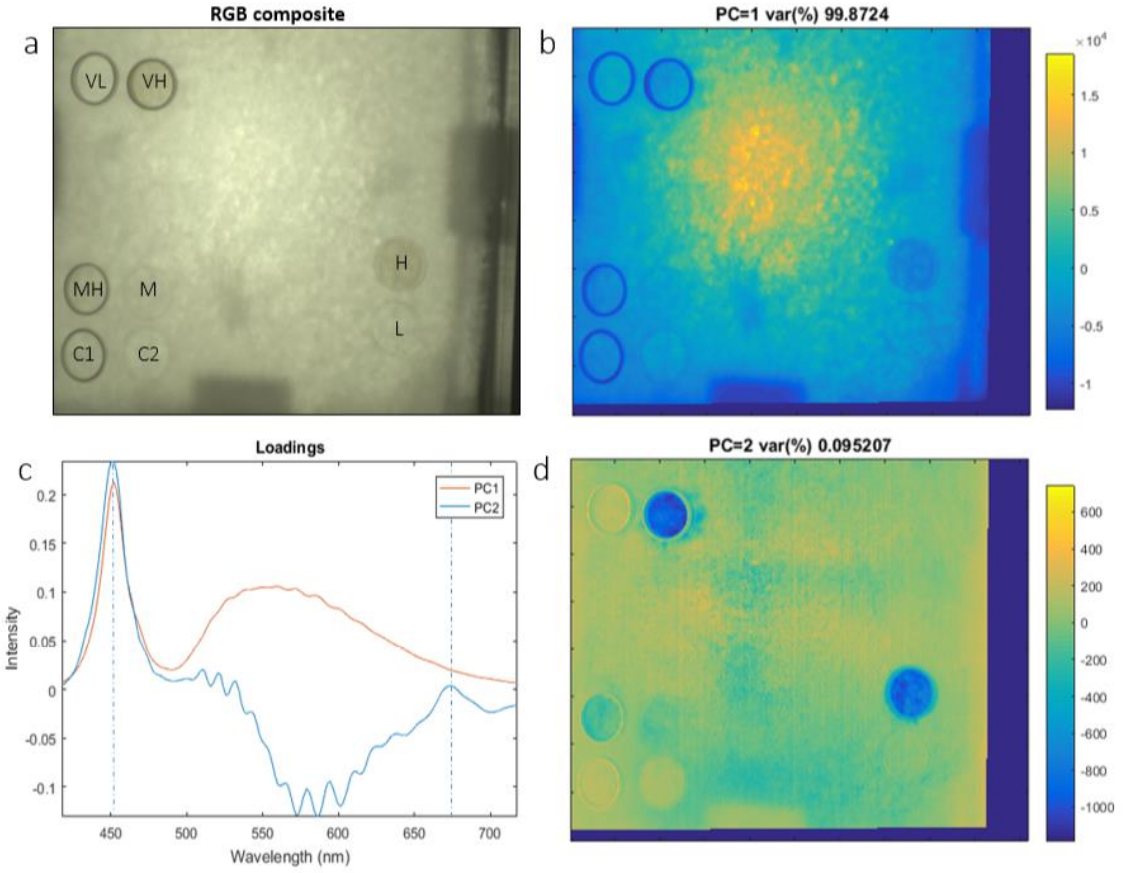

Figure 3.3 Results of PCA applied to the 1.7 nm spectral resolution frame of the ice surface. a) RGB composite of the hyperspectral image after algae inoculation displaying the performed biomass redistribution among cylinders. The RGB composite image is similar to what is observable by the human eye or normal imagery. b) First principal component (PC1) representing light intensity variability within the image. c) PCA loadings for each of the principal components. Algae absorption bands are clearly visible in PC2 at ~450 and 680 nm. d) Second principal component (PC2) representing algae biomass abundance variability. The colour bar is unit-less as representing PC intensities.

Loadings of PC2 are not purely representative of ice algae. Figure 3.3c shows that PC2 is also influenced by another element of variability affecting the spectral range between 500 and 650 nm. Opposite to ice algae, loadings on this component are low while algae related loading peaks (450 and 680 nm) are high. This high contrast can be observed at the edges of the PVC cylinders in Figure 3.3d thus suggesting that PC2 is influenced by variation caused by such cylinders and therefore slightly influencing the rest of the PC2 intensities across the image. This enhances PC2 intensity image features such as the shading of the circulation fans and the PVC cylinders themselves (Figure

3.3d). Variability on the third principal component was also explored but did not show any relevant information.

The large disagreement between chl-a sampling in cylinder H and VH is attributed to leakage of algal-cells from cylinder VH to the surroundings as can be observed in Figure 3.3d at the top left. This leakage might have occurred during the hyperspectral image acquisition or later during chl-a sampling due to ice melting. Another cause might be the relatively poor efficacy of the chl-a sampling method compared to the within-cylinder variability for H and VH observed as dark spots spread across the 80 cm^2 cylinder area (Figure 3.2c).

The analysis performed for the three different spectral resolutions (1.7, 3.4, 6.8 nm respectively) demonstrates that while a spectral resolution of 3.4 nm is capable of performing the same differentiation as 1.7 nm, resolutions of > 6 nm are not able to capture fine scale variability of biomass according to this first method exploration (Figure 3.4). This is most likely related to the fine range of ice algal spectral absorption features.

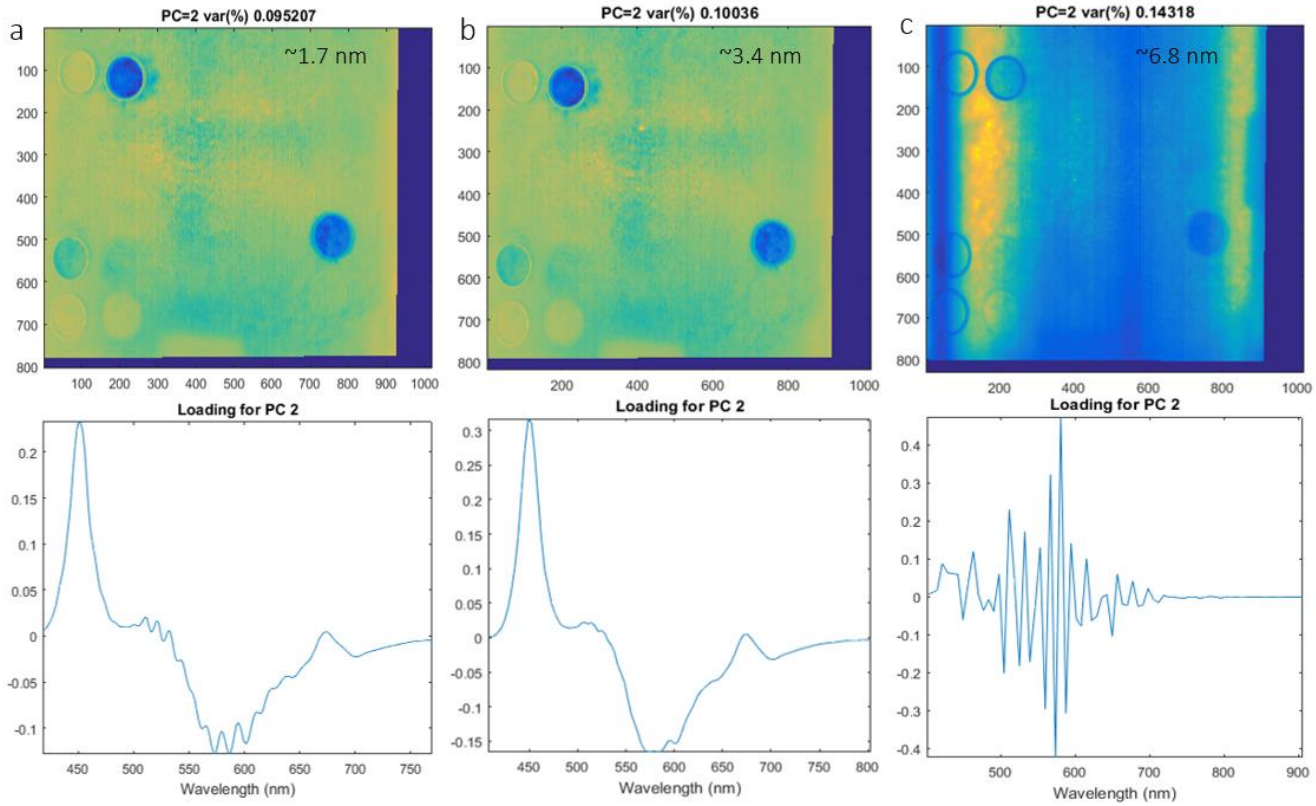

Figure 3.4 Principal component 2 (PC2) representing algae biomass variability for different spectral resolutions 1.7 nm a), 3.4 nm b), 6.8 nm c), respectively. The difference in biomass PC2 loadings between 1.7 and 3.4 nm is minimal. The figure outlines the working spectral resolution range for hyperspectral imaging aimed to capture algae biomass abundance. The test suggests that sensors with spectral resolution above 6.8 nm cannot be used for the purpose and for example discards the use of snapshot hyperspectral sensors compared to pushbroom scanners. The colour bar is omitted.

The AK10 measured radiance per pixel across the tank. It is observed that radiance intensities measured in the tank are in the same spectral radiance range compared to the measurements by Nicolaus and Katlein (2013) across different types of sea ice conditions and ROV depths (Figure 3.5). The ROV transects numbers are chosen as indexed in the original dataset (Nicolaus and Katlein,2013).

3.4 Discussion

In this study, we present the first results of a laboratory experiment employing an HI camera for differentiating ice algae biomass distribution at the ice-water interface. Employing a sliding pushbroom hyperspectral sensor over an inverted sea-ice tank allows to test the ability of hyperspectral imaging for capturing the detailed spatial distribution of sea-ice algae and test a range of hyperspectral sensor configurations, such as spectral resolution and integration time.

Sea ice is a three phase medium (principally consisting of ice, brine and air bubbles) with high scattering properties and contains optically active substances in the PAR range such as Colored Dissolved Organic Matter (CDOM) but in particular microalgae (Grenfell et al., 2006; Perovich, 1996; Xie et al., 2014). Light reaching the ice sub-surface can be reduced to less than 1% of the incoming solar radiation depending on surface and ice properties (e.g. due to snow, presence of melt-ponds, ice thickness, ice structure, etc.) resulting in very low under-ice light levels (Petrich et al., 2012). Sea ice also affects the geometric proprieties of the light field exiting the medium due to its lamellar structure funneling light in a downward direction and generating a forward peaked light field (Katlein et al., 2014).

We have presented a proof of concept study conducted under controlled laboratory conditions to test HI technology as a new remote sensing technique to map ice algal distribution at the bottom of the sea ice. The hyperspectral frames acquired with a 0.9 mm square pixel spatial resolution and spectral resolutions of 1.7 nm and 3.4 nm were able to provide spectral differentiation between different algal concentrations at the ice-water interface in our experimental set-up. The results were validated by the pre-determined cylinder inoculation scale and chl-a sampling within the cylinders. It is noted that our chl-a measurements do not provide an exact determination of chl-a within the cylinders but serves as a semi-quantitative measure of the algal biomass to allow for between cylinder comparison.

Spectral resolutions > 6 nm were not able to provide such discrimination due to the finer spectral scale of algae absorption features compared to the coarser transmitted light curve measured. This result has further importance in selecting appropriate sensors for this detection of ice algae. For example, snapshot hyperspectral sensors are easier to use (more portable and not constantly requiring six orientation parameters) than pushbroom sensors which require constant and accurate forward motion and are sensitive to drift. However, to attain adequate SNR, and due to the finite number of pixels on a focal plane array, snapshot HI sensors necessarily make a trade-off in

the resolution of the various dimensions of data of the hypercube sacrificing either spatial or spectral resolution. Considering the low-light of the under-ice environment, the high micro-scale spatial variability of ice algae and its fine-scale spectral features, snapshot HI would be very limited in this type of application.

3.4.1 Comparison of the experimental set-up with an *in situ* scenario

It might be argued that light intensity measured in the ice tank is different from the typically low intensity transmitted solar radiation found under sea ice. Thus, the capability of a HI sensor to perform in low light conditions in a dynamic setting would be put into question. The effect of increasing distances from the sensor to the sea-ice bottom (water-column thickness) would further accentuate this issue. Our study compared measured radiance intensity levels with the AK10 to multiple in situ situations showing consistent light levels even for the worst-case scenarios around algae absorption bands (690 nm) (Figure 3.5). Additionally, the measurements maximized the SNR by reaching near saturation light levels. We expect that with the same settings, lower light levels would affect SNR but would still yield accurate information on algae spatial distribution.

The different spectral signature of the LED light source compared to sunlight radiation is not expected to influence PCA results in an *in situ* scenario. The spectral bands representing algae variability are quite narrow (as seen in PC2 loadings in Figure 3.3c), and PCA was capable of decomposing between the spectral composition of the light source (with variability due to changes in overall intensity, as PC1) and algae related absorption bands (as PC2). Lange et al., (2016) observed a similar behavior *in situ* when employing Empirical Orthogonal Functions (EOFs) (analogous to PCA) outlining how secondary modes (or PCs) are free of the dominant signal spectral variability and better represent chl-a absorption.

A similar ice structure to that found in the field, with lamellar ice crystals, brine and air pockets, was also observed within the ice tank (using macro photography). This caused the light to be in a diffuse and scattered form similar to *in situ* observations (Petrich et al., 2012). The spatial variability of light intensity caused by the lamp and variations in the ice thickness is not considered disadvantageous. Snow is the most common and greatest attenuator of light in the snow – sea-ice layered matrix and produces a similar effect creating high variability in light intensities within very short distances (e.g. Nicolaus et al., 2013). Indeed, our experimental results suggest the method's indifference to light intensity variability (e.g. induced by spatially variable snow and ice thickness). This observation would need to be further investigated for a real sea-ice sampling scenario that comprises additional optically active elements. However, our results outline the potential of the technique to focus only on relevant spectral features associated to sea-ice algae presence and biomass variability. From an optical HI perspective, the experimental set-up therefore properly represented the four components of the layered structure of real sea ice (air, ice, water, algae).

Whether it will be possible to control and mimic natural ice features including the skeletal layer, and quantify columnar ice growth, are considerations for future experiments.

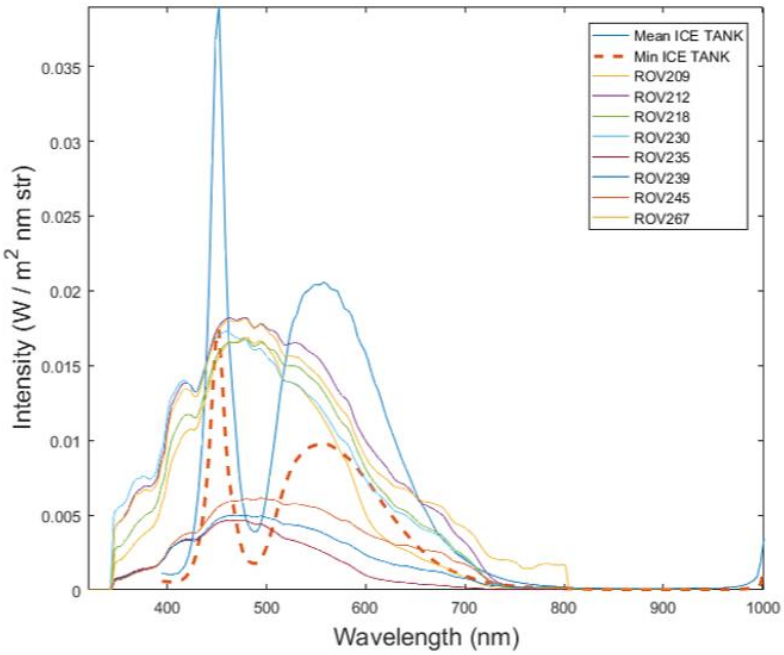

Figure 3.5 Comparison of radiance levels measured in the inverted ice tank with a series of Arctic under-ice radiance transects measured *in situ* with a Remotely Operated Vehicle (ROV) for different sea-ice conditions. The ice tank radiance is obtained from the hyperspectral frames. Mean ICE TANK is the mean between all pixels in the frame whereas Min ICE TANK is the pixel with minimum intensity (taken in a non-shadowed area). ROV transects data are publicly available from the study performed by Nicolaus and Katlein (2013) in Arctic sea ice. Sea-ice conditions varied from snow to no snow cover (from 2 to 10 cm thickness), from First Year Ice (FYI) to Multi Year Ice (MYI) (from 0.3 to 3.8 m thickness) and ROV water depth varied from 1 to 8 m.

Ice algae were inoculated 3 days prior to the imaging in the ice tank and resided at the ice-water interface only (approximately 5 mm deep in the ice structure). While measured chl-a concentrations are proportional to *in situ* observations both in the Arctic (Arrigo et al., 2010) and the Antarctic (Meiners et al., 2012), depending on the region, *in situ* ice algae concentrations might be vertically variable (Arrigo, 2014; Meiners et al., 2012). Notwithstanding, higher concentrations of sea -ice algae are most frequently found in the bottom <10 cm of the ice, and can also be found exclusively attached at the ice water-interface (Arrigo, 2014; Lund-Hansen et al., 2016). Another consideration in interpreting the spectral data is the physiological status of the algal cultures. All three cultures were in an exponential growth phase prior to inoculation and acclimated to 60 µmol photon m^{-2} s^{-1}, which was a comparable irradiance to that provided by the ice tank. In natural conditions, sea-ice algae can be exposed to different levels of irradiance and can respond physiologically to these changes. For example, shade-adaptation requires that intracellular chlorophyll a is upregulated to

maximise the capacity for growth and different compounds of accessory pigments can be produced under different irradiance conditions (Fritsen et al., 2011; SooHoo et al., 1987). In an *in situ* scenario, this and other biological components of the within-ice community (dead algae cells, and detritus) are likely to influence the spectral signatures observed with HI sensors by slightly shifting the spectral bands better representing algae variability in PCA analysis.

3.4.2 A new type of vision under the ice: possibilities, limitations and future work

The main advantage of the proposed application of HI is the ability to capture light at high spectral and spatial resolutions (in this case mm scales) in a non-invasive manner with great potential for studies aimed at investigating ice-algal spatial distribution, variability and environmental controls (Campbell et al., 2015; Lange et al., 2016b; Lund-Hansen et al., 2016). Studies employing hyperspectral imaging for different types of underwater biomes have been performed on mycrophytobenthos (Chennu et al., 2013) and coral reef biota (Caras and Karnieli, 2015).

By establishing local *in situ* correlations between chl-a and spectral indices such as NDIs (Melbourne-Thomas et al., 2015) or EOFs (Lange et al., 2016b) the hyperspectral image processing workflow can then be theoretically extended to regression analysis and quantification of chl-a per pixel unit. Planned future work will investigate the possibility of applying different statistical approaches to the acquired imagery.

In the present tests, HI frames captured radiance at mm resolution but biomass differences were only validated among the cylinders. Variability in PC2 intensity was observed across the rest of the entire ice tank (outside of the cylinders) probably due to the random inoculation. Nevertheless, we can't prove that these fine-scale intensity variations are associated to fine-scale (sub-millimetre) patterns in algal spatial distribution. Even though we visually observed a leakage pattern in PC2 at sub-millimetre resolution from a cylinder (Figure 3.3d), at this stage we are not able to quantitatively validate this due to the difficulty of sampling chl-a at such small scales.

Different scanning distances from the ice surface can yield different HI spatial resolutions ranging from sub-millimetre to the meter scale. Employing the sensor at increased distances from the ice sub-surface would allow to scan and map higher spatial extents at the cost of spatial resolution. However, influences caused by the anisotropic properties of the under-ice light field need to be carefully taken into consideration when measuring radiance from multiple angular directions such as the ones obtained from a large FOV HI sensor (Katlein et al., 2016, 2014). Water column correction would also need to be considered and corrected for, if greater surveying depths are to be considered (Johnsen et al., 2013).

The use of close-range hyperspectral imaging is an emerging area of study with technical challenges to overcome for marine applications. In the marine environment, technical challenges are often

accentuated for spectral analysis and sensor deployment. In the under-ice environment, we are faced with further limitations such as selecting an appropriate material for the camera housing that maintains its optical integrity and can operate under very low temperatures. To the authors knowledge, only a few published studies are currently available on deploying hyperspectral imaging cameras under water, but the technology certainly presents great potential from a marine remote sensing perspective (Chennu et al., 2013; Johnsen et al., 2013).

HI systems could theoretically be deployed on Autonomous Underwater Vehicles (AUVs) or Remotely Operated Vehicles (ROVs) (Johnsen et al., 2013). In the present test, we employed a stable and relatively accurate motorized slider moving at slow speeds (8 to 10 mm s^{-1}) and relatively low frequency (5 Hz). Much more investigation is required for assessing HI systems performance on an underwater vehicle of any kind.

Chapter 4

An under-ice hyperspectral and RGB imaging system to capture fine-scale biophysical properties of sea ice

4.1 Introduction

Sea-ice biophysical properties play a central role in controlling primary production and ecosystem function within the polar oceans (Arrigo, 2017; Kohlbach et al., 2018; Leeuwe et al., 2018). Primary physical properties of the sea-ice environment include snow depth, ice thickness, sea-ice texture/structure, and under-ice topography. Biological properties often refer to ice algal biomass and include ice algal community composition and physiological condition. Ice algal biomass is strongly dependent on sea-ice physical properties, and both show variability at multiple spatial and temporal scales (Cimoli et al., 2017c or Chapter 2; Lange et al., 2016a; Miller et al., 2015).

Ice algal biomass has been observed to display patchiness ranging from the mesoscale to the millimetre-scale and can undergo changes on a daily, weekly and monthly basis (Cimoli et al., 2017c or Chapter 2; Lange et al., 2017; Meiners et al., 2017). The spatio-temporal variability of ice biological properties is determined by some of the sea ice physical properties such as snow depth and ice thickness, governing light availability for the organisms. In addition, ice algal biomass has been linked to sea-ice structure, under-ice roughness and their complex interplay with the biogeochemical properties of the water column controlled by currents and boundary layer exchange processes (Fernández-Méndez et al., 2018; Krembs et al., 2002; Lund-Hansen et al., 2016; Monti et al., 1996; Ryan et al., 2006).

A standard proxy for algal biomass in land-fast sea-ice is bottom chlorophyll-a (chl-a) (mg m-2). This has traditionally been derived from melted ice core bottom sections. Typically bottom ice is sampled in 0.03 to 0.1 m long sections, i.e. where most of the biomass is typically found (Meiners et al., 2018). Capturing and quantifying variability in algal biomass together with some of its associated physical drivers over the full range of spatial scales, is extremely challenging. Data for both polar oceans remain sparse in space and time (Leu et al., 2015; Meiners et al., 2018, 2012). Challenges are in part attributed to the difficulties in conducting fieldwork in polar regions, but also to the spatially limited and invasive nature of traditional point sampling methods such as ice coring. Due to ice algae residing on the underside of sea ice, satellite or airborne remote sensing techniques cannot be used, thereby limiting data collection to field sampling. This has had implications on our

capability to properly estimate polar marine primary production, to identify complex under-ice food web dynamics, and assess sea-ice ecosystem responses to environmental change (Leu et al., 2015; Miller et al., 2015).

In response to this limitation in sampling methods, under-ice bio-optical methods have emerged as a non-invasive alternative to capture ice algal biomass variability at different spatial scales. These methods are based on the formulation of relationships between spectral radiance or irradiance measurements in the Photosynthetically Active Radiation (PAR, from 400 to 700 nm) range from underneath the ice, and the amount of integrated ice-core chl-a (e.g., see Mundy et al., (2007) or Cimoli et al., (2017c) or Chapter 2 for a thorough review). Upward looking hyperspectral radiometers mounted on L-shaped deployment arms (or L-arms) have provided means to produce spectra-chl-a relationships by sampling over different spots within an area or non-invasive monitoring of change through time (Campbell et al., 2014; Melbourne-Thomas et al., 2015; Mundy et al., 2007). Derived bio-optical relationships can then be applied to datasets obtained from mapping platforms such as Remotely Operated Vehicles (ROVs) (Lund-Hansen et al., 2018; Meiners et al., 2017) or instrumented under-ice trawls (Lange et al., 2017; van Franeker et al., 2009). ROVs permit to sample at the floe-scale area of hundreds of square meters while under-ice trawls are able to cover transects up to 2 kilometers in length (Lange et al., 2016a). While these approaches have pushed the spatial boundaries of the surveying, their ability to capture the fine-scale variability of sea bio-physical properties remains limited due to their point sampling nature (Forrest et al., 2019). Wide solid angles or cosine corrected sensors necessarily integrate over wide surface footprints, particularly when vehicle movements exceed sensor integration times. Large footprints also hinder the effective coupling with the high spatial resolutions achieved by acoustic methods to capture under-ice topography (Lucieer et al., 2016), or with photogrammetric methods to capture fine-scale snow depth variability, and sea-ice surface properties (Cimoli et al., 2017b or Chapter ; Irvine-Fynn et al., 2014; Li et al., 2019). Importantly, the obtained resolutions are not always compatible with some of the scales of spatial variability observed for under-ice habitats.

Hyperspectral imaging (HI) has been experimentally tested and proposed as an additional method to look at under-ice biomass variability from cm to sub-mm pixel scales over square-meter areas (Cimoli et al., 2017a). Preliminary results suggest that there is potential for HI to be extended to survey tenths of meters transects swaths although until now no *in situ* application has been trialed.

From a biogeoscience perspective, HI aims to identify, quantify (measure) and map - chemical, physical, and biological properties - in each of the highly spectrally resolved pixels of the target image. As the technology becomes more portable and accessible, it has found a wide range of applications. A relevant analogous example is HI cameras equipped onto Unmanned Aerial Systems (UAS) which are filling an essential gap between classical ground, full-size aircraft, and satellite sensing systems allowing more mapping at increased resolutions with ease of repeatability (Aasen et al., 2018; Adão et al., 2017; Jaud et al., 2018; Lucieer et al., 2014).

Underwater applications of HI are still in a development phase but are presenting opportunities to monitor and map shallow benthic habitats (Chennu et al., 2017; Mogstad et al., 2019) and intertidal microphytobenthic environments (Chennu et al., 2013). HI cameras have also been mounted onto deep-sea ROVs and shown to be a useful taxonomic tool for macrofauna (Dumke et al., 2018b) and mapping of manganese nodules (Dumke et al., 2018a).

Using HI to investigate processes at the sea ice-water interface presents a new level of technical and logistical challenges. The low temperatures and the difficulty of deploying instruments (and divers) under polar sea-ice are the most obvious. Measuring transmitted light rather than reflected light, however, poses the most constraints. Also, pushbroom HI sensors need to be carefully configured so that the integration time and imaging frequency match the required spatial resolution (Aasen et al., 2018). Acquired images then typically require a series of radiometric and geometric corrections which are far from trivial for dynamic under-water platforms. Challenges are accentuated in an environment where low, yet variable, downwelling transmitted light availability pushes sensors to their limits. The translucent nature of sea ice would also render the utilization of active light sources, commonly employed in underwater HI applications, a highly arguable approach. The under-ice realm can be a highly dynamic environment, and where the utilization of common geo-positioning and communication methods employed in typical aerial HI surveys is much more challenging due to the ice cover and viewing geometry (Aasen et al., 2018; Yeh and Tsai, 2015).

This study aims to develop and test the feasibility of the first version of an under-ice sliding hyperspectral imaging (HI) system developed to produce *in situ* transects several meters long at sub-millimeter spatial resolution. Along with the HI camera, a professional consumer-grade RGB camera was included in the payload for Structure from Motion (SfM) digital photogrammetry. SfM digital photogrammetry has revolutionized surface topographic mapping by providing a relatively low-cost solution that can provide accurate, high-resolution 3D structures of surfaces of interest through a set of highly overlapping pictures. Particularly relevant is the example of consumer-grade cameras being equipped on UAS to considerably increase the spatial extent of these surveys. For underwater applications, the methodology presents additional challenges which are still subject of research, but present an equal amount of opportunities (Friedman et al., 2012; Maas, 2015; McCarthy and Benjamin, 2014; Raoult et al., 2016). Under-ice, few studies have presented the potential of orthomosaic composition from RGB imagery retrieved from underwater vehicles (e.g., (Johnsen et al., 2018)), although SfM potential to generate quantitative topography has not been explored before.

Our HI system was tested between November-December 2018 under land fast-sea ice off Cape Evans, Antarctica. The relatively smooth and accessible under-ice surface of land-fast sea ice makes it an appealing first target for testing the technology. The site allows deployment the system which can slide at a fixed distance underneath the ice. Fast ice also hosts some of the most productive (per volume) microalgal habitats in marine systems (Arrigo, 2017; Arrigo et al., 2014), making it a highly relevant first test target. To the author's knowledge, no published study has applied HI or

photogrammetry to the under-ice environment before, nor have HI technologies been tested in polar ice-covered marine waters.

Overall our study has the following four objectives:

1) To develop and present a novel system capable of capturing fine-scale under-ice biophysical properties based on underwater HI and RGB imagery and photogrammetry.

2) To illustrate the logistical and technical approaches taken for this first *in situ* trial.

3) To provide a sample of the primary data outputs of the system and an exploration of the potential data processing workflows aimed to estimate biomass variability and under-ice 3D structure.

4) To present an outlook for the potential of the method, address future system development needs and highlight the method caveats that require further research.

4.2 Materials and procedures

4.2.1 System design considerations

A detailed discussion on the theoretical principles for underwater HI applications can be found in (Johnsen et al., 2013) and an extension of such theory from an under-ice perspective can be found in (Cimoli et al., 2017c or Chapter 2). Here we only discuss the aspects that have driven the design of the under-ice system.

Depending on the camera settings and the desired aims, HI sensors can capture features at different scales ranging from millimeter close-range imagery to continuous swaths of data at the mesoscale. The mapping scale is determined by the sensor distance from the target and the mounting platform. Hyperspectral images require to be orthorectified to enable extraction of meaningful and accurate metric information of the feature of interest (e.g., distances, shapes, and areas). This is ultimately necessary to compute the biochemical properties of the target (Aasen et al., 2018), and to allow for accurate repeat surveys and co-registration with other datasets.

The modality in which the frame is acquired can be in either push-broom or as 2D snap-shot imagers. Pushbroom HI line scanners are optimal when it comes to cover large surfaces under dynamic conditions as spectral and spatial information are acquired at the same instance. Pushbroom HI also comes at the best compromise with respect to fundamental sensor properties such as image quality, sensitivity, spectral coverage and spectral, spatial and radiometric resolutions (Aasen et al., 2018; Huang et al., 2014). However, in order to compose a rectified pushbroom orthoimage, sensors are required to be moving relative to the imaged surface at precisely matched speeds, imaging frequencies (or frame rates), all whilst acquiring a highly stable attitude (pitch, roll, and heading) and distance from the target (Aasen et al., 2018; Ramirez-Paredes

et al., 2016; Yeh and Tsai, 2015). Consequently, pushbroom HI is particularly sensitive when integrated onto dynamic platforms surveying under real environmental conditions and requires the full set of six-position (X, Y, Z) and orientation (pitch, roll and heading) parameters (pose) assigned for every scan-line. An additional suite of sensors is therefore required to be integrated, and/or additional data products need to be included post-processing for robust HI geometric correction. These include highly precise Global Navigation Satellite Systems (GNSS) / Inertial Measurements Units (IMUs), Digital Elevation Models (DEMs) and orthomosaics of the imaged surface and/or a series of Ground Control Points (GCPs) (Aasen et al., 2018).

Considering that light levels beneath sea-ice are typically very low, ranging from 0.1 to 10% of the incoming solar radiation, HI scans are forced to move at reasonably low speeds so that the Signal to Noise Ratio (SNR) is maximized, requiring integration times and imaging frequency to be optimized (resulting in relatively long integration times and slow imaging frequency required for low-light levels). This makes HI imaging of transmitted under-ice radiance challenging for dynamic underwater conditions and future deployment onto platforms (e.g., ROVs) that are susceptible to continuous buoyancy, speed, drag, and currents adjustments. Also, under-ice navigation and positioning is far from trivial and/or comes at high costs.

The developed approach here aims instead to scan relatively smooth under-ice surfaces by sliding or "skiing" at a predefined fixed distance from the ice at precisely controllable speeds (Figure 4.1). This enables the scanning movement to remain considerably stable, reducing some of the requirements aforementioned. The transect is prepared to be a pre-defined straight-line between 10 to 40 meters in length, limited in this prototype by the length of tether (Figure 4.2). Ideally, the set-up is expected to permit stable scanning speeds matched to the low-light levels experienced and the need of pushbroom HI orthorectification suppressed (or minimized). To achieve a steady, slow, and controllable movement, two WG1500 manual worm gear winches (Dutton Lainson, NE, USA) were established at each end-point of the surveyed transects (Figure 4.2). Stainless steel wires are attached from each winch to the respective end of the aluminum frame legs of the payload rig, which allowed the system to precisely slide back and forth through controlled winch rotations (Figure 4.2).

Such a sliding concept is only possible on under-ice surfaces which are relatively flat - a common feature of land-fast sea ice in both the Arctic (Lund-Hansen et al., 2018, 2014) and in Antarctica (Wongpan et al., 2018). Fast-ice not only is a relevant target for first tests of the technology but also provides a relatively simpler optical set-up where algae are mostly residing at the bottom of the ice – at least during spring (Meiners et al., 2018). Under rougher under-ice surfaces (e.g., pack ice, platelet ice, ice fissures and cracks caused by pressure ridges or medium to large brinicles) the scanning advancement of the system could result impeded with such a skies-based concept.

Figure 4.3 displays the core components of the internal payload that were fitted in the system enclosure. An overview of all sensors, equipment specifications, and their purpose for this first test can be found in Table 4.1.

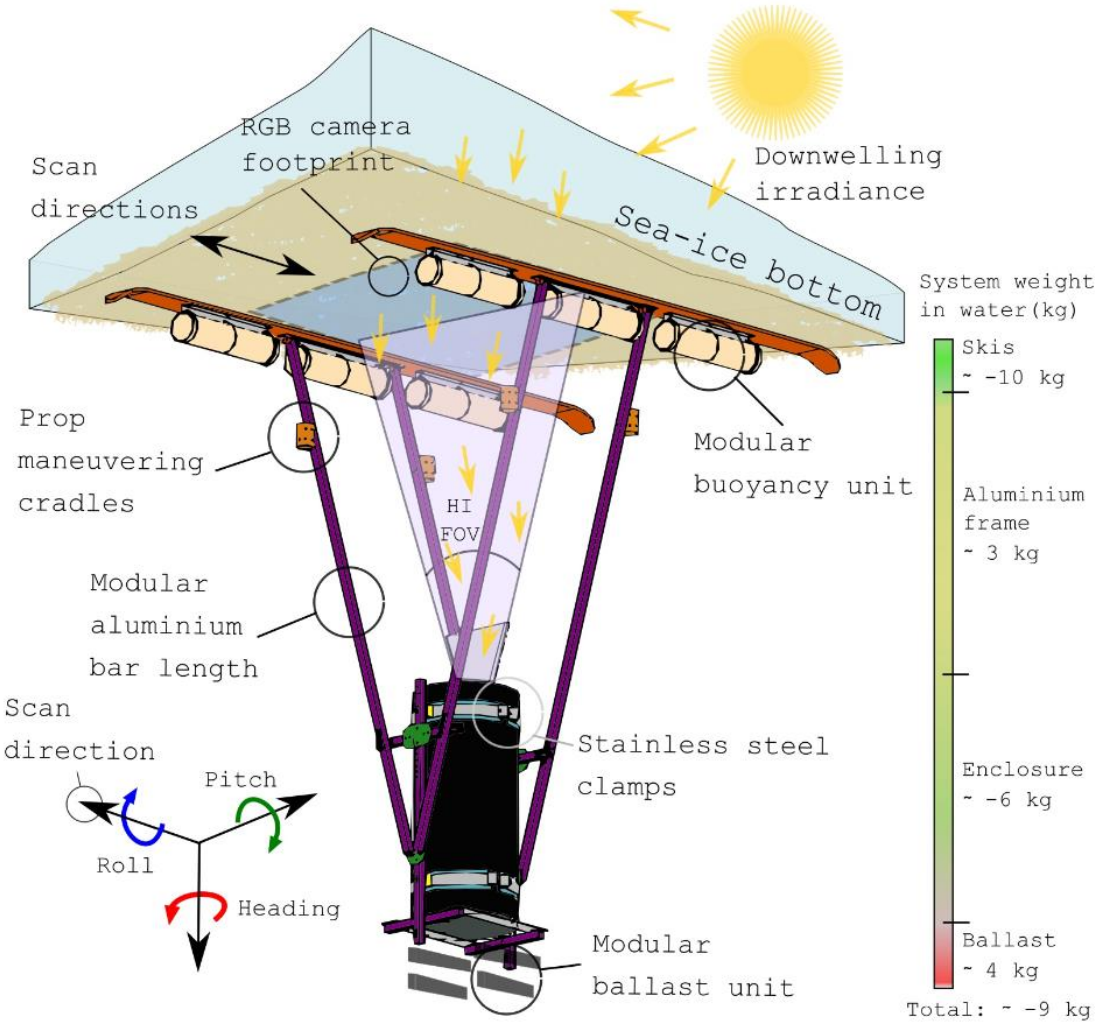

Figure 4.1 Concept design of the under-ice hyperspectral and RGB imaging system to capture fine-scale biophysical properties of sea ice. The system is designed to retrieve bio-optical relationship from downwelling sea-ice transmitted radiance. The sliding system aims to smoothly scan transects tenths of meters. It has a variable ski span of 0.82 to 1.2 m, a ski length of 1.48 m and a height of approximately 2 m. Its modular buoyancy system allows adjustment of the upward push against the ice and stabilizes the structure under different payload set-ups. The figure also shows the payload attitude reference system relative to the sensors orientation (heading, roll, and pitch). HI refers to Hyperspectral Imaging and FOV to Field of View.

To select an appropriate distance between the imaging sensors and the ice, we considered the trade-off between HI and RGB imaging specifications together with a series of environmental and logistical constraints (see Cimoli et al., (2017c) or Chapter 2 for a trade-offs overview). For example, spatial resolution and image footprint are inversely correlated since increased distances from the ice yields a larger footprint at the cost of pixel size. Increasing the distance from the ice also enlarges

the Depth of Field (DOF), which is an important factor to consider for close-range optical HI and RGB imaging applications. The DOF should be large enough to cover at least the sea-ice skeletal layer where most of the algal biomass is concentrated. Nonetheless, while gaining distance from the ice seems appealing to increase survey area, it increases logistical and technical problems which are relevant to the deployment of a large sliding platform beneath thick ice cover. Such problematics add up to the known effects of the water column on measured light intensity and spectral composition in the visible range (Morel and Maritorena, 2001). Overall, the increased costs of deploying optical sensors underwater need to be considered together with the additional challenges of geometric and chromatic correction of underwater images associated to the diverse refractive indices across the seawater-glass-air interface (Bryson et al., 2012; Menna et al., 2016; Telem and Filin, 2010). Such aberrations are not trivial to correct and depend on multiple factors such as the sensors optical parameters and settings, deployment mode (e.g., distance from the ice and FOV inclinations), water optical properties and the underwater housing lens design (e.g., flat vs dome) and material (e.g., thickness of the acrylic window).

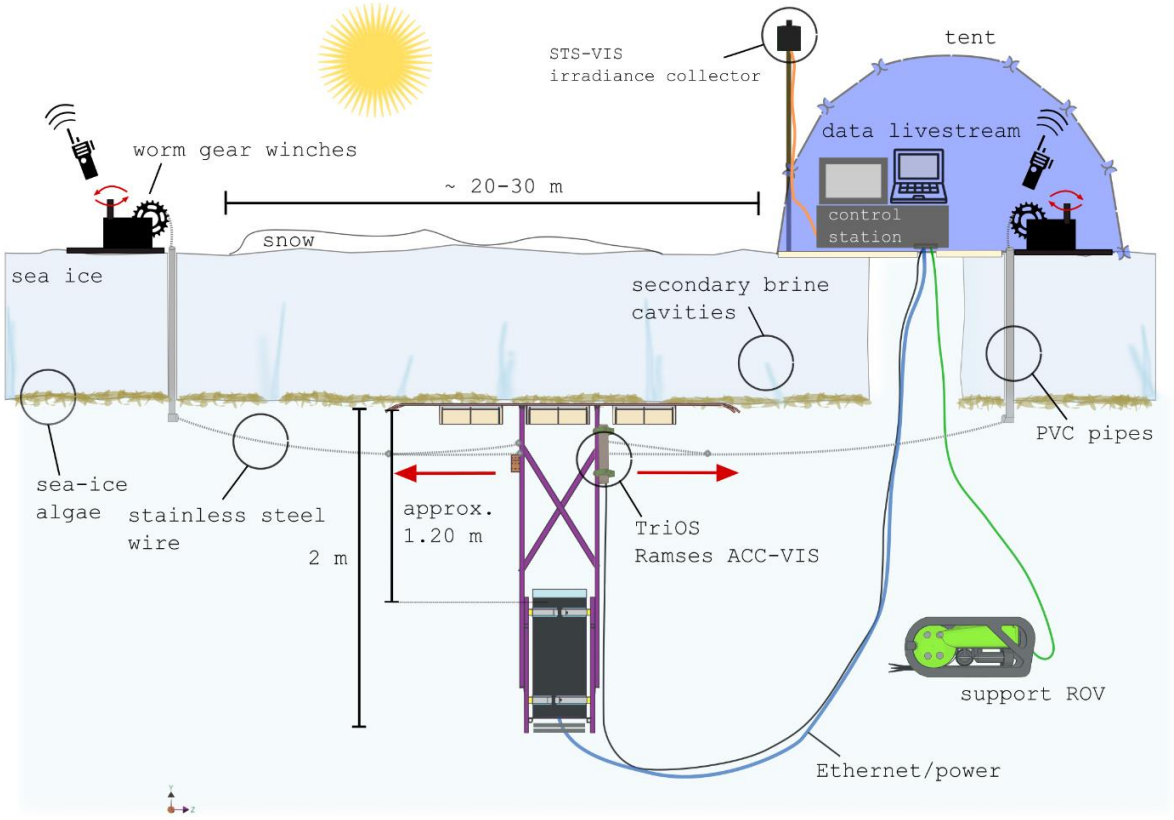

Figure 4.2 Field deployment and operation concept for the under-ice hyperspectral imaging and RGB scanning system. Two worm gear winches provide highly controllable slow movement back and forth along predefined transect. Movement commands are provided via radio communication and manual winching. The support remotely operated vehicle (ROV) is used to establish a tow-line between the deployment hole and the opposite transect endpoint. The deployment and operation require at least three people. Figure is not to scale.

For this prototype test, we found that an enclosure with a flat-port fitted with sensors separated approximately one meter from the ice would be a good compromise considering our equipment, deployment capabilities and the spatial variability of the target (sea-ice algae) that we were surveying (Figure 4.3). The custom-built and low-cost aluminum frame that set the distance from the sensor to the ice was approximately 1.20 ± 0.10 m in length (variable by changing the angle of the legs and steel clamps position). It also allowed the legs to be modified to any desired length if required (Figure 4.1 and Figure 4.2). The span between the 1.48-m-long skies ranged from 0.82 to 1.2 meters. It was confirmed that no components of the frame or skis interfered with the sensors FOVs and that FOVs of both sensors largely overlapped for coherent HI and 3D data interpretation.

Since the system travels at a fixed distance from the target, the horizontal and vertical footprint of the sensors can be estimated for the entire transect using standard imaging formulas (e.g., see Appendix B in Cimoli et al., 2017b). Nonetheless, a flat-port causes magnification of images due to the multiple refractions at the air-acrylic-water interfaces, thus reducing the apparent FOV (Menna et al., 2016). The amount of magnification is generally ≤ 1.33 and can be theoretically obtained using Snell's law. However, such calculations are not straightforward and require a series of sensor optical parameters and sensor specifications, not always easily retrievable. Some include entrance pupil distance relative to the port and imaging object, underwater focus distance and port thickness, among others. To precisely calculate the sensor footprint on the ice, a simpler way is to image objects of known length from which we can retrieve pixel size and derive horizontal and vertical footprint thereafter.

Finally, it is important to consider that miniaturization of remote sensing payloads is always preferable but is inevitably associated with increased cost and/or complexity (Aasen et al., 2018; Adão et al., 2017). We must then consider logistical and technical constraints as significant factors that could impede the deployment of a cost-effective solution. It was also preferable to use commercially available and off-the-shelf components when possible, to foster ease of replicability. For example, it was considered mandatory for the system to be surface powered and to be able to stream data to operator and change sensors acquisition parameters based on observed circumstances in real-time. The latter is not straightforward, considering a large amount of data is generated over the multiple high-frequency imaging processes. Costly underwater fiber optic connectors and tethers were avoided by allocating an internal Digital Processing Unit (DPU) within the enclosure, which directly interfaced with the multiple sensors and allowed for on-board data storage (Figure 4.3). Power and communication with the surface were enabled through an Ethernet/power cable permitting for Virtual Network Computing (VNC). Altogether, these design features come at the cost of payload volume, and the entire payload was fitted into a cylindrical enclosure with an internal diameter of 0.23 m and a length of 0.6 m (Figure 4.3).

The overall height of the system (including the frame legs and skis - Figure 4.1) was approximately 2 m which required a well-regulated buoyancy to keep the system vertical and pushing against the ice with moderate upward pressure to allow for smooth scanning. This was achieved through

modular buoyancy and ballast units that regulated the system's vertical buoyancy and stability based on local conditions as displayed in Figure 4.1.

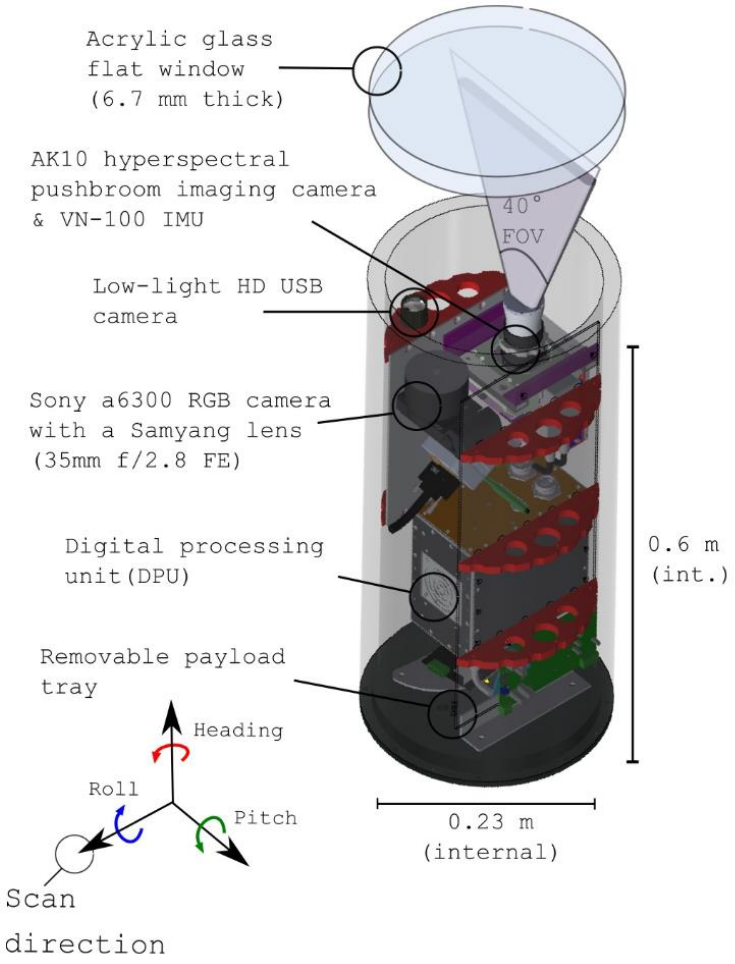

Figure 4.3 An overview of the payload main internal components, their allocation within the enclosure and volume required to host the payload. AK10 stands for AISA Kestrel 10. The figure also includes the payload attitude reference system relative to the sensors orientation (heading, roll and pitch).

One benefit of the system's frame size is that it allows the incorporation of external sensors in the future. For example, for our first tests, we included a upward-looking TriOS Ramses ACC-VIS spectrally resolved irradiance sensor near the ice-water interface to measure light directly exiting the sea-ice matrix (seen in Figure 4.2 and specified in Table 4.1).

4.2.2 Technical design and specifications

The core equipment of the developed system is summarized in Table 4.1 and consisted of an AISA Kestrel 10 pushbroom HI camera (AK10) (Specim Spectral Imaging Ltd., Oulu, Finland), a DPU (Specim Spectral Imaging Ltd., Oulu, Finland) and a Sony a6300 mirrorless digital camera together with a Samyang 35 mm prime lens. Accessories include a Low-Light HD USB camera (Blue Robotics

Inc., California, USA) a VN-100 Inertial Measurement Unit (IMU) (VectorNav Technologies, LLC, Dallas, USA) and a Garmin 18x LVC GPS (Garmin, USA). In our independent external payload, we included a TriOS Ramses ACC hyperspectral cosine corrected spectroradiometer (TriOS Mess- und Datentechnik GmbH, Rastede, Germany) and a set of four daisy-chained Subsea Lumen Lights (Blue Robotics Inc., California, USA).

Figure 4.4 illustrates the power supply and data transmission paths from the surface elements to the enclosure interior and the external payloads. The internal payload is fitted inside an off-the-shelf black anodized cylindrical aluminum enclosure manufactured by PREVCO (PREVCO Subsea, Fountain Hills, USA) that seals via two nitrile O-rings for each end plate and is rated to a depth of 100 m (Figure 4.3). The end-cap is fitted with a single underwater connector and a pressure release/vacuum hole. The connector used for external communication and power supply with the surface was a 13-contacts circular SubConn power/Ethernet.

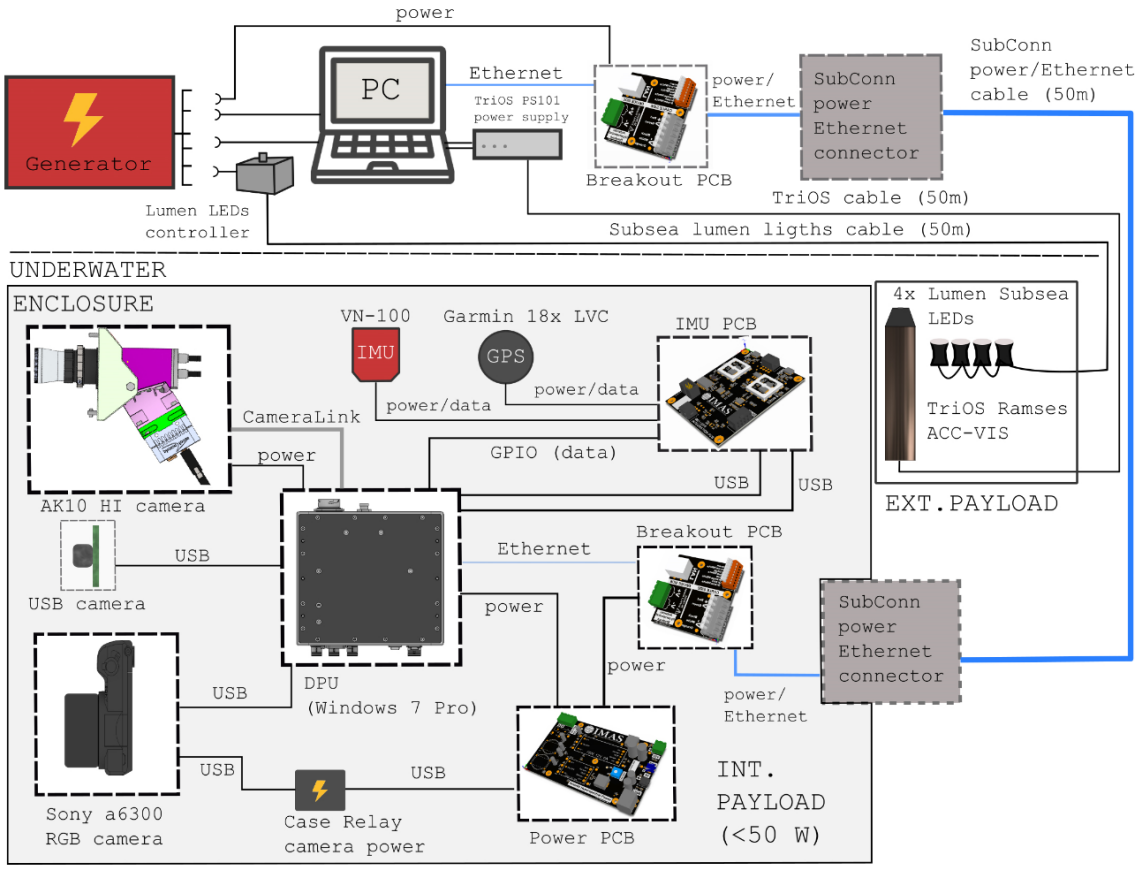

Figure 4.4 Schematics of the electronic power and communication streams for the internal and the additional external under-ice payloads.

All components of the payload were mounted around a custom-made vertical aluminum tray (20.32 by 60.96 cm) that hangs from the enclosure end cap for full swift removal and insertion of the

payload (Figure 4.3 and Figure 4.5a). The umbilical used is a 13 contacts SubConn power/ethernet (Type: D-P-P4TP24#/4C18#, 50 m long) and is received on the surface by another Circular 13 contacts connector. Data and power streams were then divided within the enclosure and above the surface from the connectors by unregulated breakout PCBs (Figure 4.4). The Ethernet stream within the enclosure connects directly to the DPU, allowing for VNC from the above surface PC. In our set-up, we used the freely available TightVNC software (https://www.tightvnc.com/) for this purpose. Most sensors were interfaced and powered through the DPU using their respective data/power cables, as shown in Figure 4.4 and operated through their own software. Only the Sony a6300 was powered using a different route. The power stream within the enclosure went through a power regulator PCB that fed the DPU directly and the Sony a6300 camera via Tether Tools Case Relay (Tether Tools, Phoenix, USA), and a Relay camera coupler for the Sony a6300.

An alternative low-cost solution was designed to synchronize and time stamp pushbroom frames with attitude (roll, pitch, and heading) data from the IMU. The IMU PCB in Figure 4.4 collected NMEA strings from the GPS and sent them through USB serial connection to the DPU for local time synchronization. The VN-100 IMU uses a 1 PPS sync input from the GPS as a trigger and reference to start its internal timer and to synchronize it to the GPS clock. This means that for each packet of data that the IMU outputs, it stamps the packet with an accurate GPS timestamp. Within the DPU the data is recorded using a Python script (run through Eclipse IDE and PyDev). The script takes the IMU packet producing a file with the IMU data (heading, pitch, and roll) and the NMEA string (position and GPS time) from the GPS and then correlates the IMU's internal "stopwatch time" to GPS time. The script also adds local PC time for reference with other sensors. GPS lock was performed before deployment (above the surface). Once underwater, the Garmin 18x LVC transmitted NMEA and 1PPS signals even when it could not see satellites. The NMEA times continued to update, but according to the internal real-time clock on the GPS. This, however, means that a short drift may happen in the GPS clock reference time over long iterations.

The AK10, DPU, IMU, and GPS together have a power consumption of <42 W. The Sony a6300 power consumption was estimated to be <7.5 W. The Low-Light USB camera was only used as additional visual support and was run through iSPY open-source software (https://www.ispyconnect.com/) for live-stream footage and video recording and had a power consumption of < 1 W. The total power requirement of the internal payload is estimated to be <50 W which can be easily powered by conventional generators. The total VNC data rate oscillates well below 1 Gbit/s (up to 75 m) supported by the SubConn cable, which leaves enough space for additional sensor streaming and data transfer.

The external payload components were operated separately using their respective cables by standard means. The TriOS Ramses ACC VIS was set-up with a connecting cable (50 m) and a TriOS PS101 power supply operated through the TriOS MSDA_XE software. The four Lumen Lights LEDs location were powered and dimmed through their separate 50 m lumen cables.

Table 4.1 Summary of all optical sensors utilized in the internal and external components of the developed system together with their specifications (top part). The table also includes specifications of other components required to run the system (bottom part). FOVh and FOVv stand for the vertical and horizontal field of view. Underwater FOV is only an ≤ estimate approximation based on simplified theoretical formulas. FWHM refers to Full Width to Half Maximun

Sensor	**Fore-optics/lens**	**Field of View (FOV_h/FOV_v)**	**Number of spatial pixels**	**Spectral range**	**Spectral resolution and FWHM**
Specim AISA Kestrel 10 pushbroom sensor	aperture: F/2.4 focal length: 35.375	40°/0.0388° in air ~29.88°/0.029° underwater	2048x1 or 1024x1 (binned)	400-1000 nm	1.75 / 3.5 / 7 nm/pixel (depending on binning)
Sony a6300 with Samyang AF 35 mm FE	max aperture F/2.8 focal length: 35 mm	37.2°/25.12° in air ~27.5°/18.7° underwater	6000x4000	Visible	RGB
Low Light USB HD cam	focal length: 2.97 mm	80°/64° in air ~57.3°/46.6° underwater	1920x1080	Visible	RGB
TriOS Ramses ACC	cosine corrected diffuser	Cosine response	Point sampling	320-950 nm	3.3 nm/pixel
STS-VIS	CC-3-DA cosine corrected diffuser	Cosine response	Point sampling	350-800 nm	3.0 nm/pixel (50 μm slit version)
Other components					
Digital Processing Unit (DPU)	Used to interface and operate all internal sensors/cameras with the surface PC using VNC and has custom electronics from Specim. Specifications are: Windows 7 Pro, Intel Core i5, 64 bit, 8GB RAM, PIXCI EB1 frame grabber, CameraLink converter, 500 GB HyperX SATA SSD.				
VN-100 IMU	Measures system attitude used for future geo-rectification of HI imagery (see Appendix A). Operated through the DPU via a Python script. Specifications: 0.5° Static Pitch/Roll, 1.0° Dynamic Pitch/Roll, 5°/hr Gyro In-Run Bias (typ.), 800 Hz IMU Data, ±16 g Accelerometer Range, ±2000˚/sec Gyroscope Range, no GPS unit is included in this model.				
Garmin GPS 18x LVC	Used for above surface GPS lock and time-stamp synchronization (see Appendix A). Specifications: 12-channel GPS receiver tracks, up to 12 satellites, one-pulse-per-second logic-level output with a rising edge aligned to within 1 microsecond of UTC. 1 Hz, output data in NMEA 0183 format.				
Lumen Subsea Lights (LEDs)	Four units attached as external payload. Intensity manipulated from above surface using a custom build-control. Specifications: max brightness of 1,500 lumens dimmable, beam angle of 135 deg. in water and colour temperature of 6,200 Kelvin.				

4.2.3 Field site and transect preparation

First trials of the system occurred during November-December 2018 under highly productive Antarctic land-fast sea ice off Cape Evans (77.6371733 ° S, 166.4018691° E) (Meiners et al., 2018; Ryan et al., 2006; Wongpan et al., 2018). As seen in Figure 4.4c, we did not experience any platelet ice during the period of our surveys, contrary to what was experienced over the same site during other studies (Lucieer et al., 2016; Wongpan et al., 2018). The area was characterized by a relatively homogenous sea-ice thickness of approximately 1.8 ± 0.01 m, except for ridged or cracked areas, and this was confirmed by our sampling. The area was also largely snow-free due to wind-induced snowdrift and displacement. An ice hole site was selected from which three transects with variable surface conditions could be surveyed. Transect directions pointed towards Northwest (NW), West (W) and Southwest (SW). In this study, we provide only a data sample from the western transect as this paper aims to describe the technical performance of the payload and its potential for research applications (see objectives). The analysis of the remaining transects and biophysical investigation of the under-ice habitat at Cape Evans will be presented in a later study.

The 2 m x 1.8 m ice-hole was made through a combination of 6” Jiffy auger holes and hot-water drilling. A polar haven tent was erected on top of the hole to maintain a safe and constant-temperature working environment for the equipment. To create a tow-line for the winch system, a 6” Jiffy auger hole was drilled at the end-side of each targeted transect. From this hole, a rope with a deadweight was immersed and rendered visible from the under-ice. A Seabotix LBV-300 ROV (Teledyne Marine, Seabotix, California, USA) equipped with a grabber arm was deployed from the central hole to grab and retrieve the tow-line from the smaller hole at the end of the transect (Figure 4.2). Following the installation of the winches, the rope was replaced with the winch wire and this was attached to the under-ice sled.

4.2.4 Deployment and data acquisition

The AK10 only allows for manual focus, and the system does not currently have the capability for remote focusing. The focus distance is required to be set to the predefined scanning distance of the system of approximately 1.2 m. Nonetheless, we need to consider that the focal distance and DOF have the potential to change underwater under a flat port set-up to ultimately affect image sharpness. We, therefore, used an underwater focusing target immerged in the ice hole together with a dummy acrylic glass port to focus the camera under dry conditions while mimicking the underwater optical set-up. The Sony a6300 interface allowed for remote autofocus.

We selected sunny and completely cloud-free days for our deployments to maximize under-ice transmitted light (and thus HI SNR). Before deployment, the enclosure was vacuumed using a standard vacuum pump and PREVCO vacuum kit manifold assembly to an internal pressure of -15 in.-Hg in gauge for leak testing and to reduce internal condensation risks. Although the air in

Antarctica is typically very dry, this process is important to avoid any condensation within the enclosure due to the considerable heat produced by sensors and equipment compared to the exterior temperature.

Due to its voluminous shape and weight, the system required 2-3 persons to be manually deployed into the ice hole. The system was then manually pushed below the 1.8 m thick sea ice by two people using rods inserted into the incorporated cradles (see Figure 4.1 and Figure 4.5 b). The system can then be rotated into the desired transect direction (e.g., western).

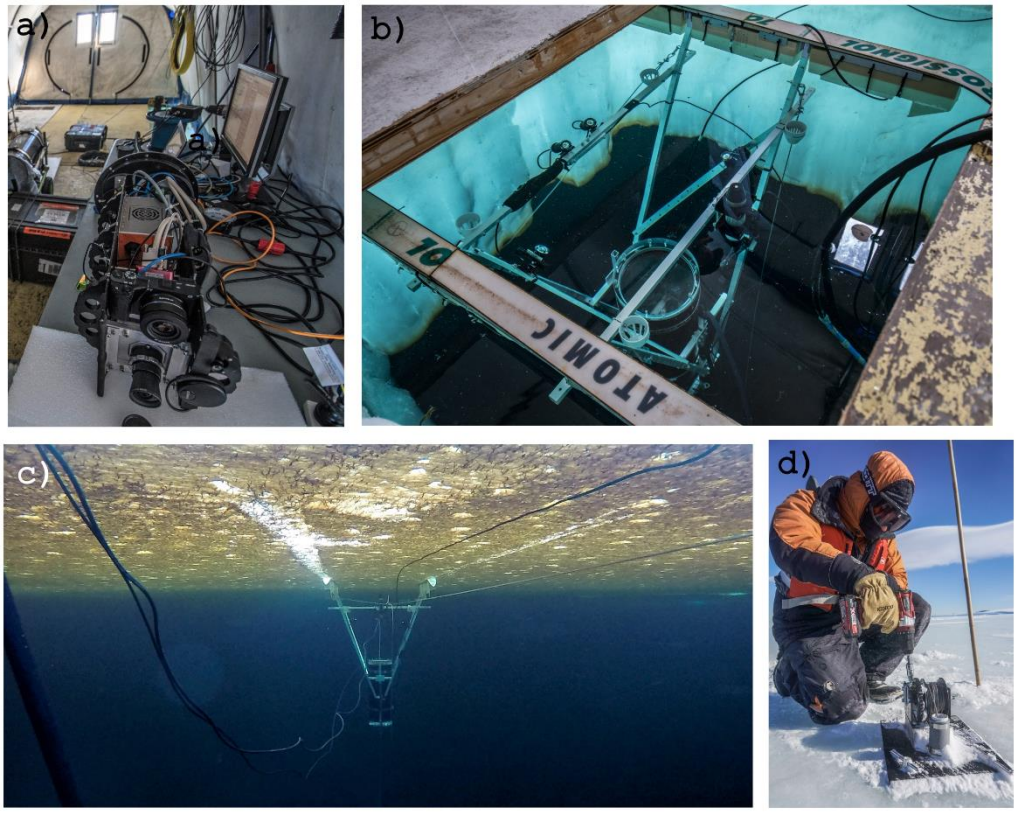

Figure 4.5 Field pictures of the first deployment at Cape Evans, Antarctica. a) The system control station together with the removable payload tray. b) The system deployed in the water prior to under-ice immersion. Visible is the external payload composed of the TriOS Ramses ACC and a set of four Lumen Subsea LEDs, and the prop maneuvering cradles. c) The system scanning over the selected transect underneath the highly productive fast-ice of Cape Evans. d) One of the worm gear winches at the opposite side of the transect in speed-up mode using a drill adapter.

Once under-ice, the system was winched 3-4 meters away from the hole and the tent to avoid interference in the light conditions beneath the ice. We were able to speed up the worm gear winches (designed to be slow for data acquisition) using a winch adapted electric drill as seen in Figure 4.5d to move the system into the right position for data collection. An initial assessment of

the HI signal intensity from directly under-ice was then performed. The optimal traveling speed and HI and RGB imaging settings were then maximized for both SNR and image quality.

The AK10 data storing and imaging settings, including integration time, imaging frequency, spatial and spectral binning were controlled in real-time using the Lumo Recorder software (Specim Spectral Imaging, Oulu Finland). For HI, the spatial and spectral dimensions were binned to 1024 spatial pixels across track, and a spectral resolution of 3.5 nm (178 bands), respectively. Whilst the spectral dimension could have been further binned to 7.5 nm for increasing the signal; this was avoided as too coarse spectral resolutions are known to hamper the application of some of the HI processing methods for ice algae (Cimoli et al., 2017a or Chapter 3). The HI frequency was set to 10 Hz and an exposure time of 99 ms (maximum setting available). The ideal sled system speed for these settings was found to be around 0.008 ms^{-1} corresponding roughly to 1 rotation of our worm gear winch per second. The read-out frequency of the IMU was also set to 10 Hz aiming for HI and IMU data time-stamp synchronization at the decisecond (ds) level. The survey distance of 1.18 m between the HI sensor and the ice resulted in a HI footprint width on the ice of approximately 0.61 m and a pixel size of 0.00625 m. The Lumo Recorder software was programmed to acquire 100 samples of a dark frame image with the shutter closed at the end of each acquired hyperspectral image. Dark frame images were taken for the subsequent radiometric correction of the imagery through the removal of dark current noise.

The Sony a6300 is operated through the Sony Imaging Edge software “Remote” feature. The software allows live streaming the camera view and permits exposure control, ISO, time-lapse shooting interval, and AF settings to be modified. We found that at the selected winch speed, an imaging interval of 0.1 Hz was sufficient to guarantee abundant forward overlap (>90 %). This relatively large sampling interval, together with the slow movement allowed the camera to be set to AF, which resulted in sharp and focused images. The ISO was set to 250; aperture maximized to f/2.8 and shutter speed set to 1/250 sec for most of the circumstances. The altitude of the camera was around 1.2 m, which yielded an estimated footprint width of 0.586 m in water and a resolution of 0.0001 m. All images were captured in the Sony RAW format (.ARW) to allow for any eventual image pre-processing approaches (e.g., see appendix in (Cimoli et al., 2017b)).

The radiometrically calibrated Ramses ACC-VIS was synchronized to acquire an under-ice irradiance sample at the same time as each Sony a6300 RGB image (0.1 Hz) was taken. In this way, it is possible to link every image to a Ramses ACC-VIS radiometric irradiance sample and locate images spatially across the transect through the retrieved camera positions following SfM digital photogrammetry.

The STS-VIS radiometer was set-up to acquire a measurement of incoming downwelling solar irradiance every minute considering the highly stable conditions during the surveys and the relatively low variability in sun angle.

Following system retrieval, HI, RGB imagery and IMU navigation data files were downloaded directly from the SATA SSD within the DPU. VNC allows for direct data transfer from the payload to the surface, but the operation is time-consuming for large files such as the HI imagery data files.

4.2.5 Data processing

Both hyperspectral image analysis and SfM photogrammetry are active research topics for many land-based applications. The adaptation of established terrestrial procedures to novel under-ice applications requires targeted studies aiming to identify, test, and evaluate their performance in an under-ice context. Here we present only preliminary data outputs of the developed system and assess their quality and potentials from a biophysical perspective. We do this by looking exclusively at the western transect and selecting a successful subsample for hyperspectral image analysis and processing (Figure 4.6), namely block B. For the RGB imagery and photogrammetry, we retrieve for the first time a high-resolution orthomosaic and DEM of the under-ice using commercially available software. For HI, we adapt some of the known methods in under-ice bio-optical literature to the hyperspectral images and illustrate potential new ones.

4.2.5.1 RGB imagery and SfM digital photogrammetry

It is well known that image quality and poor camera network geometries can considerably affect SfM model's reconstruction and the extraction of accurate metric information. Image quality in non-metric cameras is influenced by the camera sensor, lens quality, mechanical stability, and the overall image acquisition process under dynamic conditions. Poor camera network geometry refers to the lack of forward or side overlap in the imagery and/or lack of oblique imagery. Underwater, SfM photogrammetry is further challenged when using flat-ports due to the multiple refraction processes that magnify FOV, affect the focal length and produce a series of geometrical (e.g., radial distortion) and chromatic aberrations in the images directly affecting camera calibration algorithms in SfM, which ultimately affect the reconstructed model.

While image quality per se was not considered problematic in our transect dataset, the flat port did cause non-negligible effects on the imagery (e.g., noticeable pincushion distortion). To solve such aberrations and obtain an accurate camera calibration one can formulate the complex mathematical models of the imaging process in water (Łuczyński et al., 2017; Treibitz et al., 2012) or perform a rigorous camera calibration using underwater targets with precisely known geometry (Shortis, 2015). Another option is to rely on camera self-calibration, which refers to the calibration process using only image point correspondences for large and well-composed datasets (Oniga et al., 2018; Piazza et al., 2018). However, self-calibration is challenging in our dataset as camera network geometry is particularly weak when dealing with elongated strips with only nadir images and no side overlap and/or oblique imagery (Piazza et al., 2018). Systematic errors produced in such datasets can cause bending and non-linear deformations in the photogrammetric models as

confirmed by our tests (Menna et al., 2017; Piazza et al., 2018). Here we apply a simple preliminary solution to the camera calibration problem using a constrained self-calibration approach by taking advantage of the flat under-ice surface, the known transect lengths and a series of identifiable reference points that were also measured from above the surface.

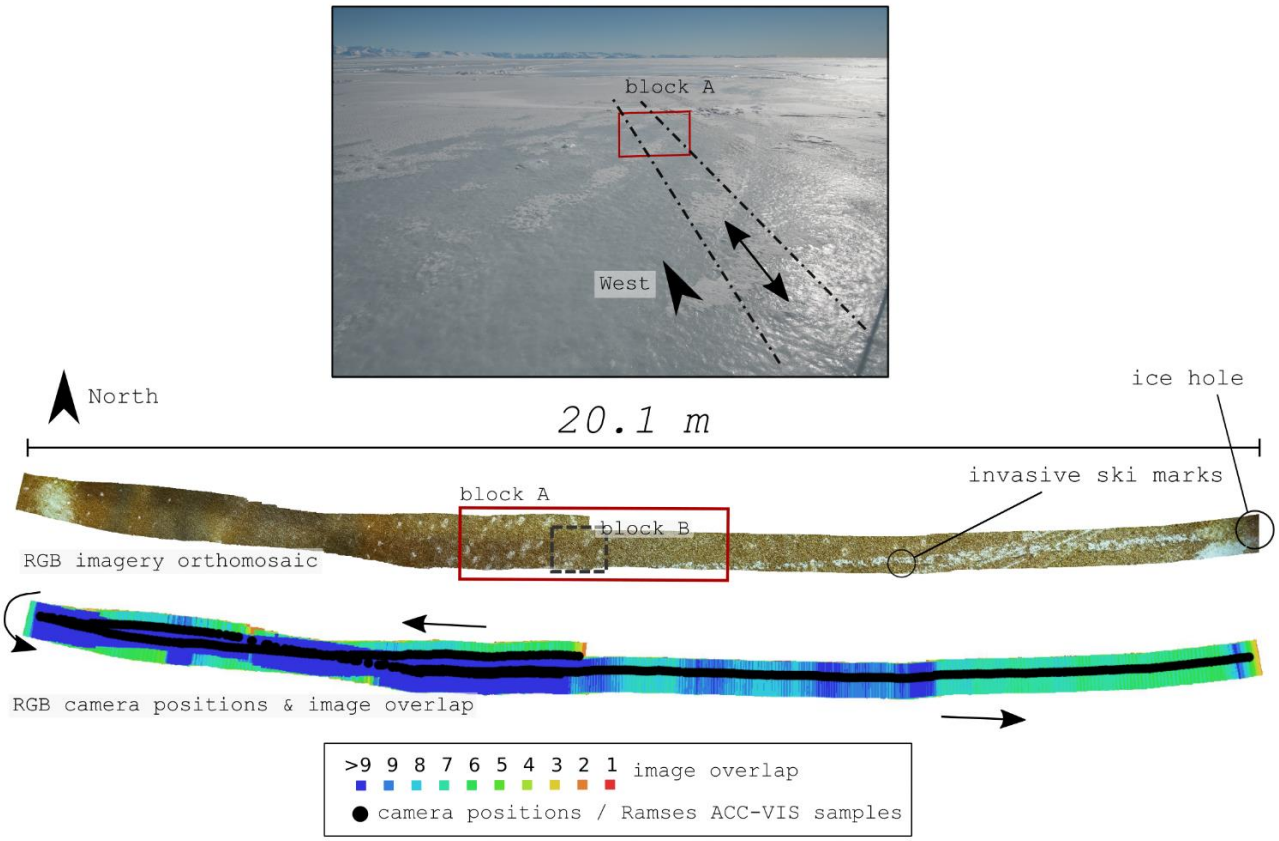

Figure 4.6 Overview of the surveyed western transect produced with structure from motion (SfM) digital photogrammetry using the RGB imagery. Camera positions and Ramses ACC irradiance samples were synchronized to the same sampling frequency, so they match in space. Blocks A and B within the transect were selected for further image analysis. On top is a photograph of the transect direction viewed from above the surface. Displaying the typical survey conditions (little to zero snow) of the study area.

Prior to photogrammetric processing, 733 Sony RAW images acquired for the western transect were first imported into Adobe Lightroom where an initial lens correction and manual batch compensation for pincushion distortion was performed. Lightroom considers camera lens profiles into its corrections, and this empirical "trial-and-error" approach is simply to partially reduce bending of the model to a near straight level. Duplicate images were discarded as labeled repetitions during sled idle times, and the remaining images were exported from Lightroom as .JPG files for further SfM processing.

The 3D reconstruction of the under-ice surface was created using Agisoft Metashape (Agisoft Metashape User Manual - Professional Edition, Version 1.5, n.d.). Metashape (previously Photoscan), is a software package which has been extensively used for 3D modeling and

photogrammetry over a wide range of geoscience applications (Fonstad et al., 2013). The workflows for under-ice DEM and orthomosaic generation are described here. Photo alignment accuracy is selected as medium (for computational reasons) and provided a first estimate of camera calibration parameters and the reconstructed scene. The produced sparse point cloud model at this stage was noticeably bent and deformed. We proceeded to filter outlier's and low accuracy points using the gradual selection tools. Due to the smooth nature of the surface (Figure 4.5c), we assumed that all the surface areas with little algal cover were level with a reference height of 0.0 m, and created a dense and well-distributed network of reference level markers with a Z position (altitude) 0.0 m. We also added the known transect length as a scale bar length reference together with a series of points that were identifiable and could be referenced to above surface positions whose relative position could be measured with a measuring tape. For our entire western transect, we allocated 32 of these reference points, termed Ground Control Points (GCPs) (Tonkin and Midgley, 2016; Westoby et al., 2012).

All these level reference GCPs are assigned with a high marker accuracy of 0.002 m in Metashape reference settings options. The model is then processed using the Optimization of camera alignment feature where non-linear deformations can be removed by optimizing the estimated point cloud and camera calibration parameters based on these known reference marker coordinates ("Agisoft Metashape User Manual - Professional Edition, Version 1.5," n.d.). During this optimization, Metashape adjusts estimated point coordinates and camera parameters minimizing the sum of reprojection error and reference coordinate misalignment error.

The Metashape workflow is then followed by Dense Cloud reconstruction (medium quality and aggressive depth filtering), 3D mesh from the dense cloud (Arbitrary surface type, medium quality, enabled interpolation and aggressive depth filtering), Texture mapping (orthophoto mapping mode and mosaic blending mode) and finally DEM and Orthophoto production. The scaled orthomosaic and DEM were exported in .TIF format to QGIS and the DEM was processed with a hillshade function for visualization purposes.

4.2.5.2 Hyperspectral imaging and radiometer data

The retrieved HI images of block A and B consisted of a three-dimensional (x, y, λ) data cube where x and y represent the spatial dimensions, and λ the spectral dimension. The first two steps of the HI processing workflow include radiance conversion of digital numbers (DN) and pushbroom image rectification. The system was designed so that little to no geometric rectification and IMU data integration is required. This was the case for block A and B of the analyzed transect (Figure 4.6).

Per-pixel radiance conversion was done using Specim Caligeo PRO software (Spectral Imaging, Specim Ltd., Finland) which addresses noise and geometric aberrations inherent to the sensor and performs the conversion of DN into downwelling spectral radiance L_d (λ, mW m_2 sr^{-1} nm^{-1}) using the *in situ* acquired dark current frames and the associated calibration files. For the present study,

spectral bands <400 nm and >700 nm were considerably noisy and outside the range of interest, therefore spectral subsetting was applied reducing the data to a total of 89 bands.

The block B HI subsamples are then smoothed using a Savitzky-Golay low-pass filter with a polynomial order of 3 and frame length of 9 aiming to reduce noise in the transmitted signals without hindering the retrieval of fine spectral features (Savitzky and Golay, 1964; Schafer, 2011).

Following this procedure, we adapted methodologies previously applied to track biomass variability from under-ice spectra such as Normalized Difference Indices (NDIs) and Principal Component Analysis (PCA) (also known as EOF) (Cimoli et al., 2017a or Chapter 3; Lange et al., 2016a; Melbourne-Thomas et al., 2015; Mundy et al., 2007). Every pixel within the HI subsample was integral-normalized to reduce the amplitude component of spectral variability and to focus on differences in spectral shape, a pre-processing standardization method previously applied in sea-ice bio-optical literature (Meiners et al., 2017; Melbourne-Thomas et al., 2015; Wongpan et al., 2018).

PCA for hyperspectral remote sensing is typically employed for dimensionality reduction, to reveal complex relationships among spectral features or for the identification of prevalent spectral characteristics. PCA has been widely used in optical oceanography for extracting information about seawater constituents from spectral data (e.g., [64], [65]). In our case, PCA was applied to the spectral dimension of block B data cube to explore and highlight the most variable features and relationships across all pixels in the block B image (Amigo et al., 2015; Cimoli et al., 2017a or Chapter 3).

Spectral indices, such as NDIs, have been linearly correlated to the logarithm of sampled chl-a in multiple sea-ice studies (Lange et al., 2016a; Melbourne-Thomas et al., 2015; Wongpan et al., 2018). Since we have not developed a specific spectra-biomass relationship for our site that applies to the developed HI payload yet, a couple of identified optimal NDIs from the land-fast sea-ice of Davis Station and McMurdo Sound, Antarctica by (Wongpan et al., 2018) were selected and utilized as a proxy of biomass. Before index implementation, block B was spatially binned to 2x2 pixels, reducing the spatial resolution from 0.624 mm to 1.2 mm, but boosting per pixel signal. The following NDI equation was then applied to every pixel in the image:

$$NDI(\lambda_1,\lambda_2)=\frac{L_d(\lambda_1)- L_d(\lambda_2)}{L_d(\lambda_1)+L_d(\lambda_2)} \qquad (1)$$

Where λ_1 and λ_2 are wavelength bands selected across the sensor spectral range and L_d (λ, mW m^2 sr^{-1} nm^{-1}) is the solar downwelling radiance transmitted through the ice. From (Wongpan et al., 2018), we selected 441:426 nm and 648:567 nm as two different NDIs in different areas of the spectrum and applied the NDI equation to every pixel in the block B image. In this study, we used radiance to compute the indexes rather than under-ice radiance normalized to surface irradiance

(or transflectance, (Nicolaus et al., 2013)). Changes in above surface illumination conditions (e.g., solar geometry and atmospheric effects) within the block A and B image subsample were considered negligible.

In addition to adapting PCA and NDIs to under-ice HI, we also tested for the use of an index called Area under curve Normalised to Maximal Band depth between 650-700 nm ($ANMB_{650\text{-}700}$) of the continuum removed spectrum (Malenovský et al., 2006). $ANMB_{650\text{-}700}$ has been successfully applied for chl-a and chl-b mapping using HI of Norwegian spruce trees (Malenovský et al., 2006), and Antarctic moss beds (Malenovský et al., 2017), and here we use it as a proxy of chl-a or ice algal biomass.

For this index, we applied the same Savitzky-Golay low-pass filter and the 2x2 spatial binning factor, but no integral normalization is performed. Instead, the entire image is normalized by the highest spectrum intensity within the block, which corresponds to an algal free cavity in the ice visible in the image (shown later in the results section). This provides a proxy of light transmittance over roughly the last 5 to 15 cm of ice bottom and enhances visibility of the absorption peak of chl-a at 670 nm of each pixel spectrum. The continuum removal transformation on the spectrum is a fundamental pre-processing step to enhance and standardize the specific absorption features of biochemical constituents (Kokaly and Clark, 1999). It allows for the normalization of the transmittance spectra so that individual absorption features can be compared from a common baseline. Following a localized continuum removal, we can calculate the Area Under Curve in the range between 650 and 695 nm where chl-a attains one of its absorption peaks:

$$AUC_{650\text{-}700} = \frac{1}{2}\sum_{j=1}^{n-1}\left(\lambda_{j+1}-\lambda_j\right)\left(\rho_{j+1}+\rho_j\right) \qquad (2)$$

Where ρ_j and ρ_{j+1} are values of the continuum-removed transmitted spectra at the j and j+1 bands, λ_j and λ_{j+1} are wavelengths of the j and j+1 bands, and n is the number of the used spectral bands. We can then calculate the $ANMB_{650\text{-}700}$ index as:

$$ANMB_{650-700} = \frac{AUC_{650-700}}{MBD_{650-700}} \qquad (3)$$

Where $MBD_{650\text{-}700}$ is a maximal band depth of the continuum-removed reflectance, generally at one of the spectrally stable wavelengths of strongest chl-a absorption around 670-680 nm. Normalization of $AUC_{650\text{-}700}$ by $MBD_{650\text{-}700}$ is a crucial step for strengthening the relationship between $ANMB_{650\text{-}700}$ and the chl-a content for higher chl-a concentrations. The logic behind this

spectral index is exploiting well-known changes of the transmittance signature shapes produced within these wavelengths mainly by the changes in algal chl-a content.

In order to validate the robustness of the HI data compared to traditional means of acquiring under-ice spectra, hyperspectral irradiance variability measured with the Ramses ACC-VIS across the entire transect (samples shown as black dots in Figure 4.6) was computed and compared with spectra of every pixel in block B. The Ramses ACC-VIS data further allow us to gain an estimate of downwelling irradiance intensity exiting the ice-water interface and was used to gain an insight of the light levels experienced under-ice. These can then be used to baseline the signal quality of the data achieved using our HI system under those specific conditions. The TriOS Ramses ACC-VIS was radiometrically calibrated using the factory provided calibration files (traceable within international standards) during the data acquisition process.

4.3 Results

4.3.1 Deployment and operation performance

The system was successfully deployed and retrieved for the three targeted transects (NW, W, and SW). For the western transect analyzed here, a total of 736 RGB images and Ramses ACC-VIS irradiance samples were acquired, in both forward and backward directions (Figure 4.6). The overall scanning operation lasted approximately 2.5 hours, not including system set-up. Considering the air (-5 to 5 ° C) and water (-1.8° C) temperatures experienced, the electronics in the housing functioned well under the challenging environmental conditions and were kept above freezing point by heat produced from the multiple electronics. HI-sensor temperature sensors indicated that temperature was maintained at around 17°C over the entire western transect.

As shown in Figure 4.7, the system was able to produce natively well-composed pushbroom hyperspectral images without the need for any rectification methods and/or supplementary attitude and navigation data (e.g., see block A in Figure 4.7c).

However, occasional lagging instances in the sled-motion during scanning of some sections of the transect hampered smooth pushbroom HI data acquisition. Sometimes these lags were long enough (0.5-3 seconds instances) that data collection had to be interrupted and the sled system to be forwarded until the movement was smooth again. In other cases, they were acceptable and could eventually be corrected through the integration of the IMU data algorithms and image correction filters (e.g., Figure 4.7 lagging instance). Transect blocks requiring rigorous geometric rectification and post-processing are out of the scope of this study and will be investigated in the future through the development of targeted geometric HI correction algorithms.

Transects also did not always followed a straight line, but instead, the trajectory displayed a slight bend as can be seen from Figure 4.6. This means that the system showed changes in heading according to its attitude reference system (heading, roll, pitch) shown in Figure 4.1 and Figure 4.3. Transect bending is only noticeable when considering long distances rather than over the shorter accomplished HI scans. However, this track deviation did have an impact on the imaged transect as forward, and backward travels did not perfectly overlap in some instances producing unnatural invasive marks such as the visible ski tracks in Figure 4.5.

4.3.2 RGB imagery and photogrammetry

For the western transect, 615 camera positions were aligned successfully, and optimization produced an overall flat 3D model of the under-ice surface (Figure 4.5 and Figure 4.7a). Dense reconstruction of the model resulted in a rich and well-composed dense point cloud (100,199,561 points). The first estimation of the total area covered was 13 m^2 for the western transect. The final resolution of the displayed orthomosaic was 0.0994 mm/pixel and for the DEM 0.821 mm/pixel with a point density of 1.48 points mm^{-2}. The total RMSE of the Euclidean distance between the generated reference level markers and the corresponding estimated points in the reconstructed 3D model was 0.0762 m (0.0623 m X error, 0.0322 m Y error, and 0.0297 m Z error). While this error does not reflect a rigorous accuracy assessment of the absolute geometric accuracy of the model, our interest in these first trials was in the ability to retrieve complex topographic features. The relative (within model) accuracy and point density are sufficiently high for this purpose.

The RGB orthomosaic illustrates the high level of algal biomass under the land-fast sea ice of Cape Evans. This encompasses both gentle changes in illumination and also different shades of brown and green coloration over the full 20.1 m transect (Figure 4.6). Zooming into block A, Figure 4.7a displays complex networks of ice algal aggregations and patches together with the presence of large bright cavities embodying large secondary brine channels (Petrich and Eicken, 2016). The DEM hillshade in Figure 4.7 b shows that while at first sight, the under-ice at Cape Evans seems like a featureless surface, it has high levels of relief complexity attributed mainly to an extensive network of secondary pore spaces (Petrich and Eicken, 2016). Looking at Figure 4.6, they appear to occur in specific areas of the western transect. These pore cavities range widely in size and depth and are believed to be a result of a series of sea ice thermodynamic processes of brine flushing and merging of channels during the advancement of the summer season (e.g., Polashenski et al., (2012)).

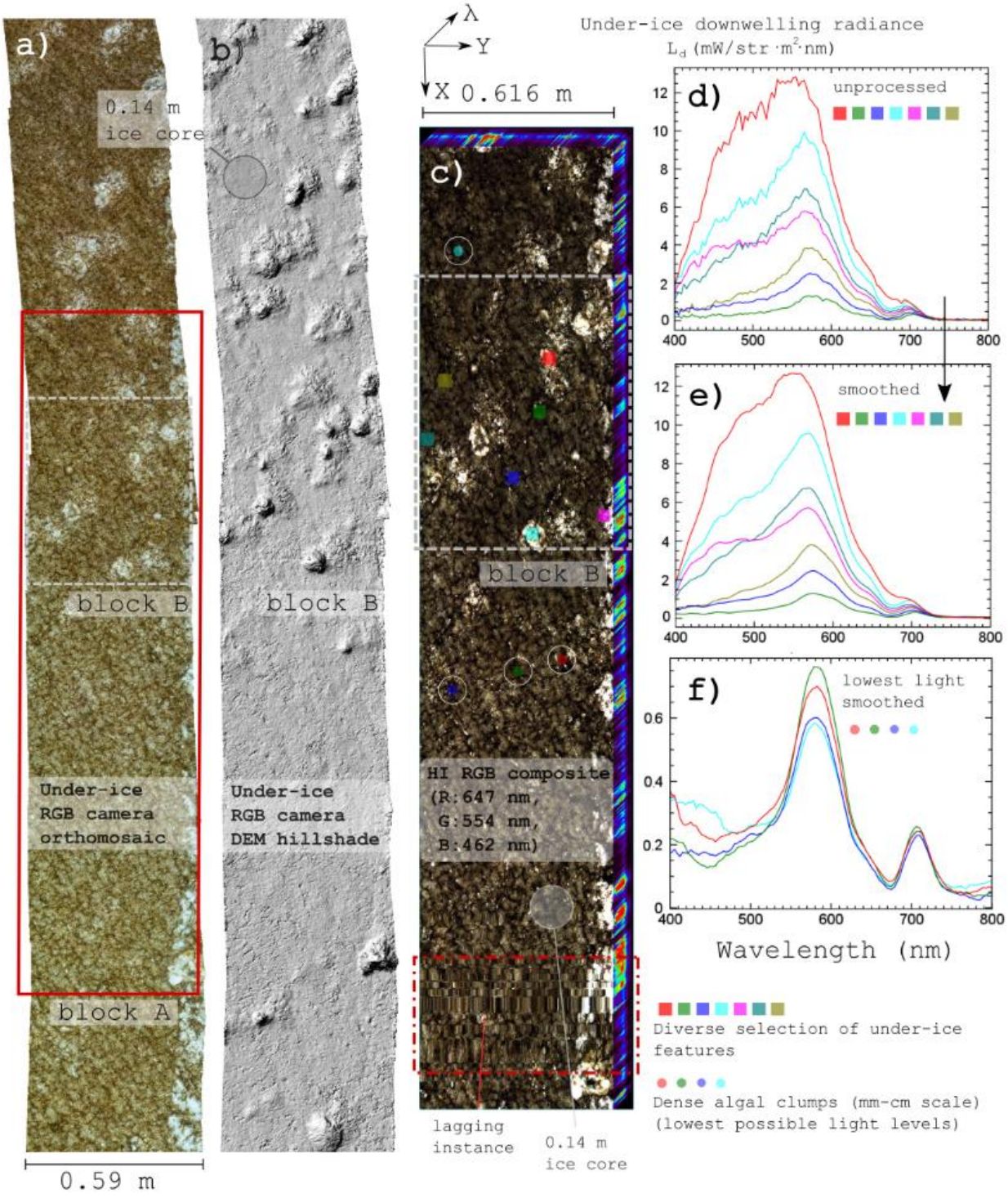

Figure 4.7 Display of the main data products of the developed under-ice payload. Block A and block B refer to two different subsections within the western transect that were selected for further analyses. a) Under-ice orthomosaic produced from the RGB imagery. b) Hillshade of the SfM derived digital elevation model (DEM) illustrating relief structure produced by the large cavities. c) Visual representation of the hyperspectral data cube for block A including block B as an RGB composite. Panel d) and e) display the high variability of radiance spectra for a selected variety of spots (*continued to the next page…*)

within block B (both unprocessed and smoothed with a Savitzky-Golay filter respectively). Panel f) display four of the darkest pixels within the image associated to extremely dense algal clumps. For all plots, spectrum shows a × 4 pixels spectral average which corresponds to approx. 1.2 mm pixel size. Native pixel size is 0.624 mm. A 0.14 m Kovacs ice core areal coverage is provided for scale reference only.

An ice core footprint of 0.14 m in diameter is provided as a reference scale for these large brine pores in Figure 4.7a and c. However, the total depth of the cavities is difficult to capture with digital photogrammetry, and we could only image and reconstruct up to a certain depth depending on their width. Smaller subtle relief and undulations of the under-ice surface are also observable from the DEM hillshade (Figure 4.7b). Since these are not recognizable as white spots from the imagery itself, they are perhaps not strictly related to brine release processes but rather ice undulations of yet unknown origin. The DEM hillshade also captures micro-rugosity in the 3D model attributed to protrusion of dense algal clumps mostly formed by the diatom species *Berkeleya adeliensis* (F. Kennedy pers. communication). The hillshade map also displays a specific orientation pattern assumed to be driven by the underlying water currents. *Berkeleya adeliensis* was found to be the predominant species together with the interstitial diatom *Nitzschia stellata* from microscopic observations.

Current-driven orientation of algae strands and the biophysical complexity of the under-ice habitat were also observed in the high-resolution Sony a6300 RGB images shown in Figure 4.8. These images not only display the native quality of the RGB imagery but also show additional important biophysical properties of the under-ice habitat such as the sea-ice skeletal layer and its crystal orientation (Figure 4.8a) (Petrich and Eicken, 2016; Weeks and Gow, 1978). Figure 4.8a was taken nearby the ice hole, and the difference between what appears to be the hanging *Berkeleya adeliensis* and interstitial diatom species is clearly visible. Later into the transect in Figure 4.8b, a certain degree of algal orientation can also be observed together with some of the large secondary brine channels. Zooming in on Figure 4.8b, we also observed high concentrations of oxygen bubbles produced by the photosynthesizing algae. Also, several types of under-ice fauna were visible along the high-resolution imagery dataset such as ctenophores (Figure 4.8a) and amphipods (Figure 4.8b).

4.3.3 Hyperspectral imaging and radiometric data

A visual representation of the block A hyperspectral data cube within the western transect is shown in Figure 4.7c. The quality of the image composition shows minimal geometric noise and a robust geometrical resemblance with the RGB orthomosaic for the entire block A subsample. The cube also shows an example of one of the lagging instances in the sliding sled system as previously noted.

The right-hand plots in Figure 4.7 display the quality of the measured spectral signatures in terms of overall intensity for the under-ice downwelling radiance L_d (λ, mW m^2 sr^{-1} nm^{-1}) unprocessed

(Figure 4.7d) and smoothed (Figure 4.7e). It is clear that high variability of light intensity and spectral shape can be found across a series of features within the < 1 m^2 area of block B. Such variability can change up to one order of magnitude and is mostly ruled by the presence of the secondary brine channels together with the drastic differences in algal concentrations and aggregations, but also due to the different algal species/morphotypes (e.g., hanging vs. interstitial) among other factors. Despite the highly contrasting under-ice light regime induced by the large brine features, the camera dynamic range allowed to optimize settings to the lower light areas (e.g., algal patches) without saturating the pixels over the secondary brine pores.

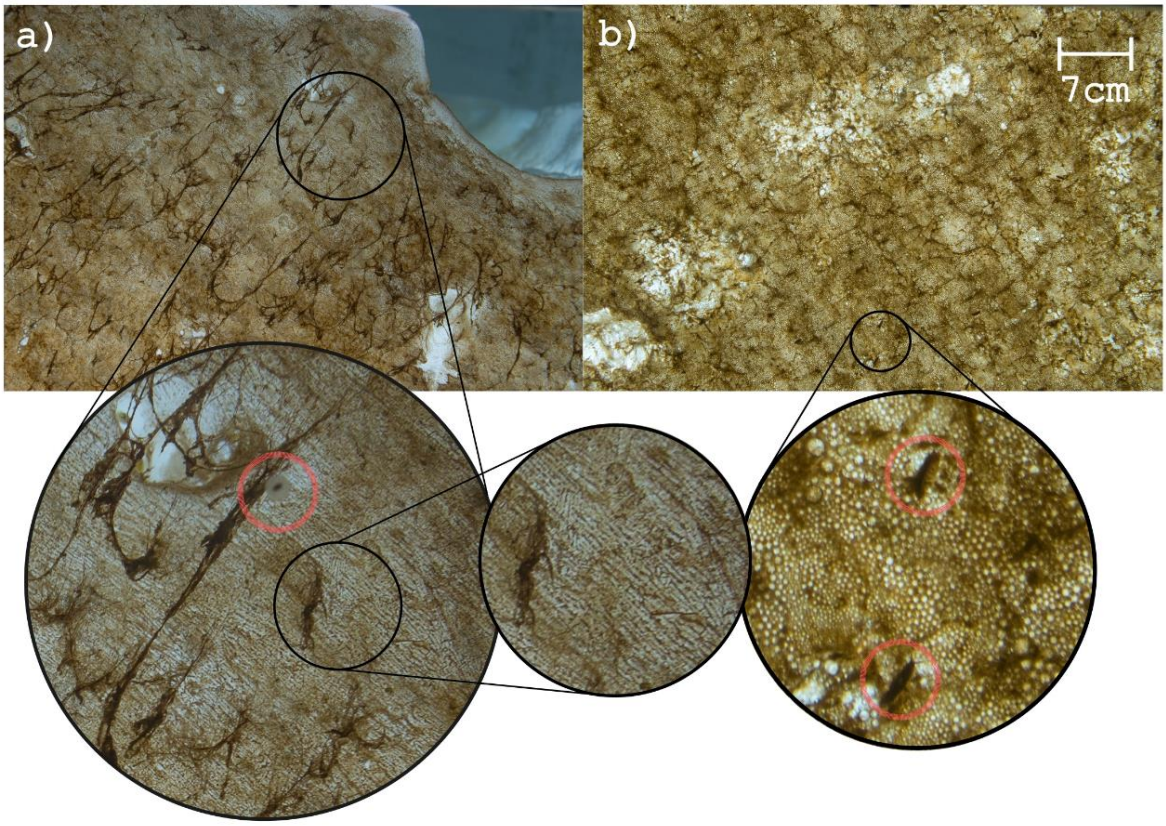

Figure 4.8 Two upward looking RGB image samples taken from the Sony a6300 camera dataset shown at full resolution. Both images display some examples of spotted under-ice feeders (circled). Left image shows a ctenophore (comb jelly) and right image shows a couple of circled amphipods. a) Image taken nearby the visible deployment ice hole. The image zooms into a large brine channel and further on the highly detailed under-ice skeletal layer. b) Image taken midway on the transect displaying the high concentration of oxygen bubbles produced by the photosynthesizing ice algae.

Absorption by algal associated chl-a is easily observable over almost all pixels in the image as a reduction in intensity over the 440 ± 20 nm and 680 ± 10 nm bands. Higher ice algal biomass reduces transmitted radiance in the blue part of the spectrum and produces a compressed curve in the green part of the spectrum (Legendre and Gosselin, 1991). Absorption features by ice algae tend

to drastically decrease nearby and within the secondary brine channels (e.g., red spectrum in Figure 4.7d-e) except in circumstances where we find dense algal webs hanging in the middle of these cavities (e.g., celeste spectrum in Figure 4.7d) or highly concentrated algal clumps scattered around these cavities. From the entire block A image, we also selected some of the lowest light pixels we could find, and their spectrum can be seen in Figure 4.7f. The SNR noticeably decreases for such targets, and the blue region (400 to 500 nm) seems to be noise dominated. Nonetheless, the spectrum still displays strong chl-a signatures in the 680 ± 10 nm band curve and an overall meaningful signal.

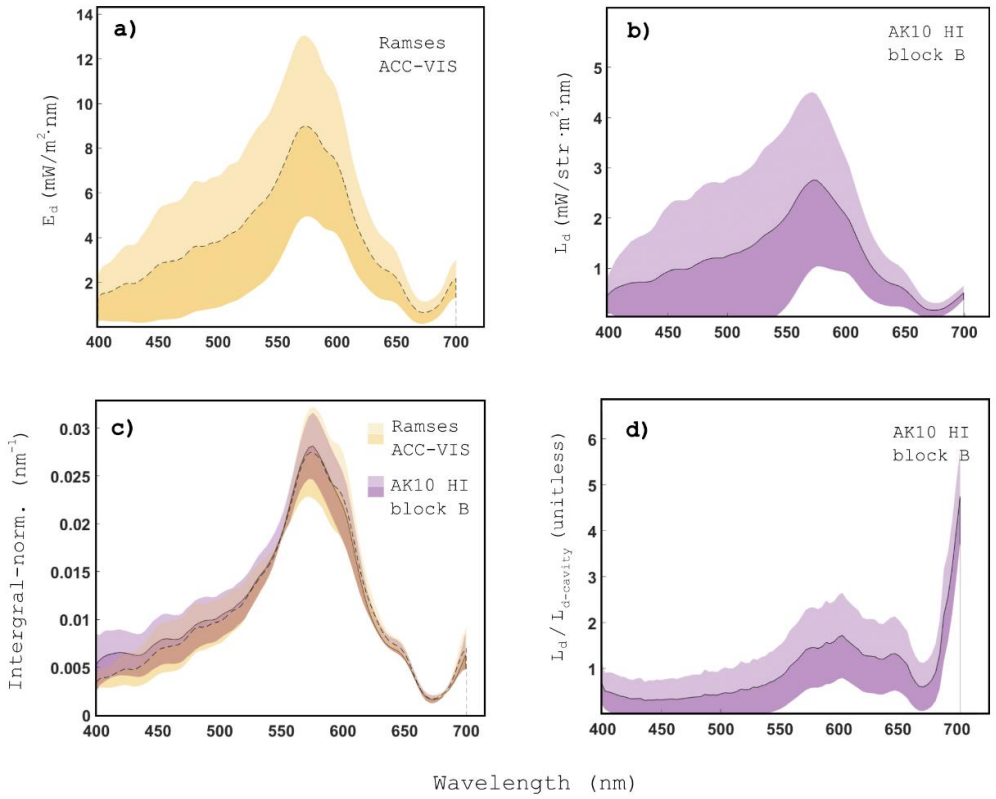

Figure 4.9 a) Mean ± one standard deviation of downwelling under-ice irradiance (E_d) spectra from the TriOS RAMESES ACC-VIS located near the ice water interface for the full 20.1 m transect. b) Mean ± one standard deviation of under-ice downwelling radiance spectra (L_d) from all the pixels of block B hyperspectral image subsample from the AK10. c) Mean ± one standard deviation of under-ice irradiance and radiance spectra normalized by area under curve for the Ramses ACC-VIS over all the transect and for all pixels of block B AK10 hyperspectral image. d) Mean ± one standard deviation of under-ice downwelling radiance (L_d) normalized by the maximum radiance pixel of all block B and corresponding to one of the cavities or secondary brine channels seen in the image ($L_{d\text{-cavity}}$) .

The mean irradiance spectrum ± standard deviation (sd) measured with the Ramses ACC-VIS for the length of the whole 20.1 meters transect is shown in Figure 4.9a. The total irradiance energy integrated over the PAR range (400-700 nm), $E_{d,PAR}$ (λ, W m^2) averaged 0.35 (λ, W m^2), with a 0.20 sd, and a total range of 0.07 - 1.5 (λ, W m^2). Figure 4.9a also helps to characterize the spectrum variability across the entire transect. Interestingly, a similar degree of variability (although in terms

of radiance) is experienced within the < 1 m2 block B subsample as seen in Figure 4.9b showing the mean spectrum ± sd of all pixels of block B. Figure 4.9c displays the integral-normalized mean spectrum of all the pixels of the block B hyperspectral data cube overlaid by the integral-normalized mean spectrum of the entire western transect using the Ramses-ACC-VIS. Figure 4.9d displays all pixels of the block B image normalized by the highest light intensity pixel in the images which is attributed to the light exiting one of the secondary large brine channels or cavities (seen Figure 4.7). This plot indicates properties of the transmitted light over the bottom layer of the ice where >98% of the biomass thrives. The normalized spectra were used to compute the $ANMB_{650\text{-}700}$ index. The normalization greatly accentuates the absorption features of chl-a in the blue area centered at 450 nm and the red peak centered around 670 nm.

PCA results are shown in Figure 4.10. The loadings of the first nine principal components explaining > 99.54 % of spectral variability within the image are shown for completeness. Figure 4.9 also displays the loading scores applied to each pixel of block B for the first three principal components (PC1, PC2 and PC3) together with an RGB composite of block B. PCA results show well resolved and coherent principal components similar to what was reported previously in the literature employing PCA (or EOF) using under-ice radiance and irradiance sensors *in situ* (Lange et al., 2016a; Melbourne-Thomas et al., 2015), or for HI in artificial sea-ice simulation tanks (Cimoli et al., 2017a or Chapter 3). The PC1 loadings account mainly for variability in light intensity attributed to a mixture of factors and embody the general trend of the under-ice light spectrum. PC2 seems to be more influenced by the two contrasting dip areas around 440 ± 20 nm and 680 ± 10 nm suggesting a possible correlation with algal chl-a pigments. Nonetheless, PCA at this stage serves as an exploratory tool and it remains difficult to assess the nature of PC3 and the remaining PCs without further analyses of pigment composition e.g., through High-Performance Liquid Chromatography (HPLC) (e.g., (Arrigo et al., 2014; Wongpan et al., 2018)). The PCA score images also evidence some subtle line artifact features across the scanning direction of the hyperspectral image (Figure 4.10). These are attributed to small vibrations or micro-lagging instances whose visibility is enhanced following integral-normalization and PCA processing.

The results of the NDI (648:567 nm) and $ANMB_{650\text{-}700}$ indices applied as relative proxies of biomass variability to block B are presented in Figure 4.11a and b, respectively. Interestingly, Figure 4.11 suggests that both indices provide a similar result in terms of biomass distribution patterns and capture spatial scales previously unprecedented. However, NDIs seems to produce nosier images compared to $ANMB_{650\text{-}700}$. It might be argued that the $ANMB_{650\text{-}700}$ is based on the curve shape information of the light transmitted through the algal layer and such normalization was not applied to compute NDIs. However, both methods were tested and showed that using quantitative changes of transmitted radiance intensity produced less noisy images in case of NDIs.

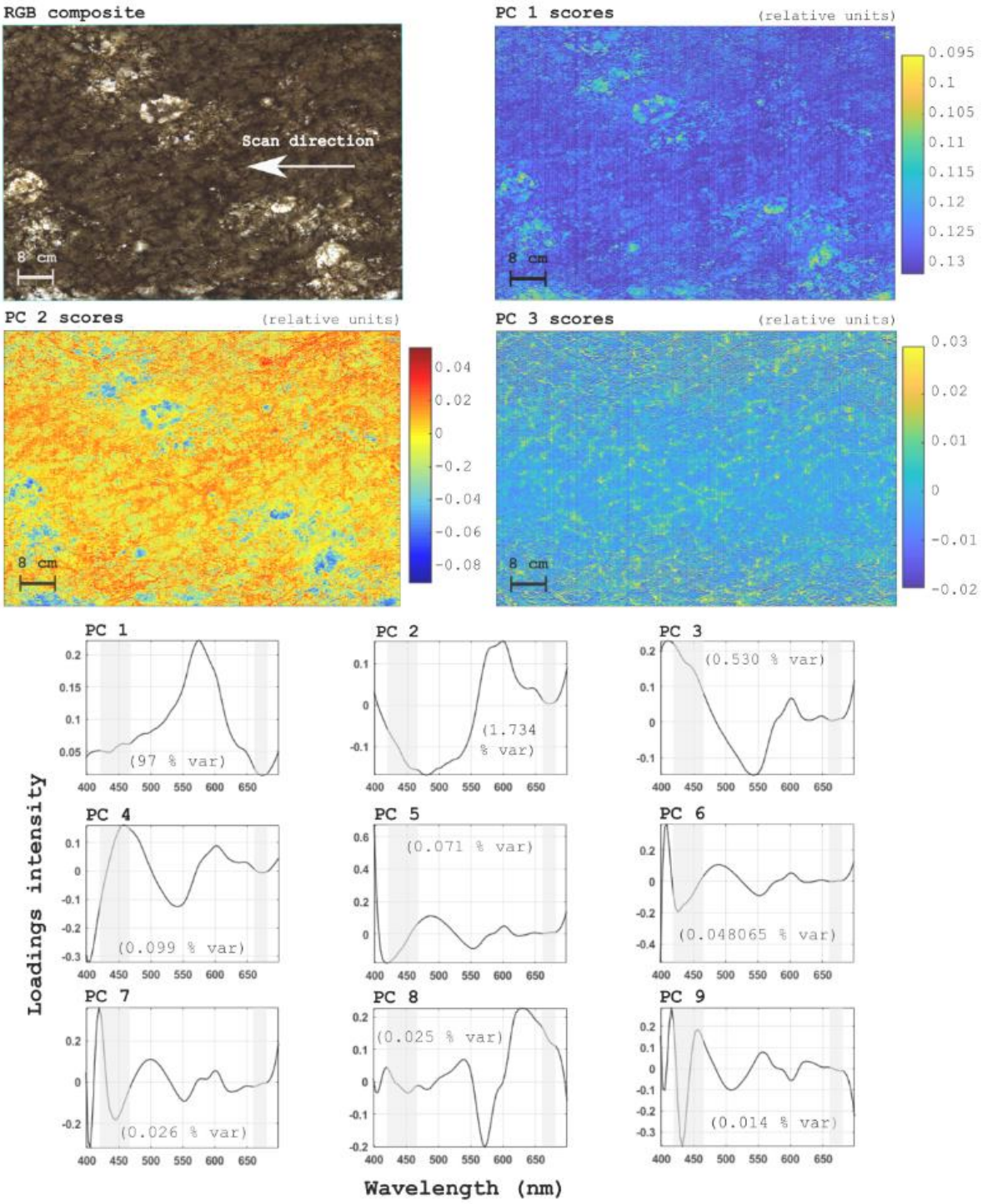

Figure 4.10 Results of principal component analysis (PCA, also known as EOF), applied to the spectral dimension of block B (hyperspectral image subsample of the western transect). Top images display the first three PC scores applied to every pixel of the image using corresponding loadings for each component. Bottom plots display the loadings for each wavelength for each principal component. Plot display as well the proportion of variance explained by each corresponding component. (*continued to the next page…*)

Light grey areas highlight the maximum chl-a absorption regions at 440 and 670 nm. Spatial resolution for PCA was maintained to a native 0.625 mm.

NDIs applied to block B over the blue/violet area (441:426 nm) were also tested and provided similar results although with slightly noisier imagery (not shown). A final interesting observation is the anisotropic noise pattern observed in both NDIs (648:567 nm) (Figure 4.11 a) and PCA across the scanning direction of the image (Figure 4.10). This is observable as noisier zones at the top and bottom of the image.

4.4 Discussion

4.4.1 Under-ice hyperspectral imaging data quality and processing

The present study outlines a novel platform incorporating two emerging underwater optical methods for capturing fine-scale biophysical properties of the under-ice habitat non-invasively. Passive HI and digital photogrammetry were tested for the first time to observe the ice-water interface and were deployed using a relatively simple under-ice sled. The sliding concept took advantage of the fixed and smooth surface of land-fast sea ice to minimize costly set-ups and yielded geometrically coherent hyperspectral imagery without the need of georectification. To the authors knowledge, only three underwater HI payload designs have been documented before. The Ecotone UHI (Ecotone, Trondheim, Norway) is a commercial solution designed for deep or shallow ROV-based seafloor observations and utilizes active light sources (Dumke et al., 2018a; Foglini et al., 2019). The Ecotone UHI has also been equipped onto Unmanned Seafloor Vehicles (USV) for shallow seafloor mapping (Mogstad et al., 2019). The other two are documented in (Chennu et al., 2017, 2013) and comprise a stationary time-lapse observations and a diver- operated set-up.

In terms of data processing, the aim was to provide a preliminary outlook of the system's data outputs and its potentials. The preliminary results presented here indicate that it is possible to apply simple, yet effective, algorithms to retrieve chl-a per surface area on a sub-mm per pixel basis over tenths-of-meters-long transects. Figure 4.9 shows that the under-ice spectral signatures of traditional and novel sensors are comparable. They are also comparable with studies over similar Antarctic land-fast sea-ice areas (e.g., (Wongpan et al., 2018)). Established under-ice bio-optical methods for retrieving sea-ice biomass proxies *in situ* (e.g., NDIs or PCA models) were also successfully adapted to the acquired hyperspectral imagery (Figure 4.10 and Figure 4.11). NDIs values outputted are observed to match the range of values over the same or similar sea-ice areas (Wongpan et al., 2018) and PCA loadings shown strong similarities in shape if compared with results from other studies both in real sea ice and in artificial ice tanks (Cimoli et al., 2017a or Chapter 3; Lange et al., 2017); the difference being that in this study they were retrieved on a sub-mm per-pixel basis.

PCA results retrieved chl-a signatures over its PC2 component and reaffirm the utility of PCA for explorative analyses. For example, the pronounced "shoulder" deviation towards 470 nm in PC2 loadings is likely associated with a higher concentration of accessory algal pigments such as fucoxanthin (Kirk, 2011; Lund-Hansen et al., 2015). PCA analyses also suggest the possibility to retrieve PC/EOF based regression models to develop chl-a-spectra relationships, algorithms that have been proven successful for a wide range of sea-ice conditions (Cimoli et al., 2017a or Chapter 3; Lange et al., 2016a; Melbourne-Thomas et al., 2015).

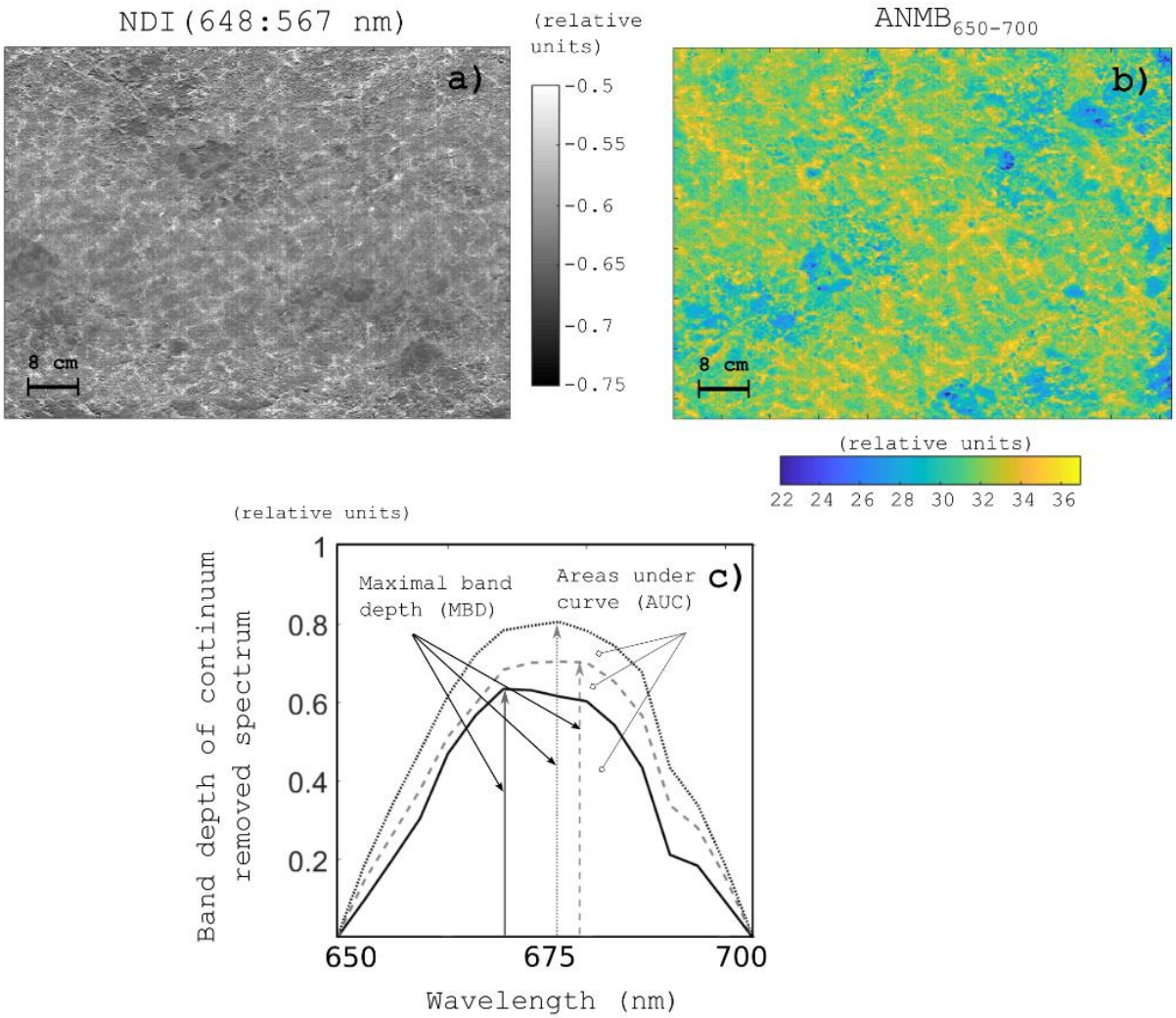

Figure 4.11 Application of spectral indexes as proxies of chl-a distribution over block b HI subsample. a) Results from the application of a commonly used index in sea-ice bio-optical literature, the normalized difference index (NDI), applied for wavelengths 648:567 nm on block B hyperspectral image subsample. b) Application of a novel index to sea-ice bio-optical literature, the area under curve normalized to maximal band depth (ANMB) between wavelengths 650 to 700, applied to the same block B. c) Plot of continuum removed spectrum of three random pixels within block B to help visualizing the $ANMB_{650–700}$ concept and its association with chl-a absorption. For the color bars, higher values (towards red) correspond to higher expected biomass. Spatial resolution for the indices was binned to 1.2 mm.

The use of the NDIs positioned at wavelengths 648:567 and 441:426 nm was also tested with meaningful per-pixel biomass proxy representations although images were characterized by consistent pixel noise, particularly for the blue region of the spectrum (Figure 4.11). This is probably attributed to the lower SNR inherent to mm-scale hyperspectral resolution image pixels compared to wide-footprint radiometric sensors. SNR changes due to variations in intensity and shape of the retrieved spectra, which varies as the target constituent concentrations change and as the noise changes depending on sensor settings and specifications. The high ice algal biomass typically found at Cape Evans (see Arrigo, (2017) for biomass ranges), favours algal associated spectral shapes, but heavily reduced light availability and consequently per pixel SNR on the overall spectrum, particularly in the blue region where chl-a attains one of its major absorption ranges (e.g. for the NDI 441:426, see Figure 4.9b and d). In fact, from Figure 4.11a, we can observe how noise is drastically reduced over the high light intensity brine channel areas. (Wongpan et al., 2018) and (Forrest et al., 2019) also highlighted how in general NDIs were producing poor relationships at the Cape Evans site. However, this might be because of different reasons such as the presence of platelet ice (which we did not experience during our study), the consequent poor spatial variability in biomass at the measured scale, or perhaps the difficulty in ice-coring and sampling chl-a from sloughing platelet ice (Forrest et al., 2019).

The $ANMB_{650\text{-}700}$ index explored here is directly linked to the absorption properties of chl-a in the red region of the spectrum. It takes the advantage of hyperspectral data to finely integrate over the narrow absorption peak of chl-a in the 650 to 700 nm range. While it is not guaranteed that a meaningful quantitative relationship with sampled chl-a will be retrieved, the index performed better than NDIs for our case by providing less noisy and coherent images (Figure 4.11b and c). Increases in chl-a concentration (with absorption maximum around 665 to 680 nm) causes chl-a absorption feature to deepen at the 680 ± 10 nm dip. While the spectrum of the transmitted radiance in this range can show signs of saturation, the adjacent wavebands at longer wavelengths remain sensible to changes as the peak broadens and thus extending the area under curve (Figure 4.11c) (Malenovský et al., 2006). The index was also designed to reduce the impact of other confounding factors of the imaged target within its complex 3D environment (Malenovský et al., 2006), and this might also supported the index performance in our case. A continuum-removed integrative index could also have worked better than a band ratio (e.g. NDIs) under this high biomass case (and therefore less light and SNR) as it integrates a larger area (AUC) hence providing a stronger signal per-pixel (Figure 4.11c). In fact, the performance of ANMB and similar indices is expected to deteriorate under low chlorophylls (chl-a and chl-b) amounts (Malenovský et al., 2013, 2006).

Future work in this area will explore the performance and comparison of these indices for the Cape Evans site, and to work on the retrieval of quantitative correlations tailored to our encountered sea-ice conditions that are suitable to be applied to HI data. It was also noticed how different pre-processing, normalization and standardization techniques (not all shown here) affected the visualization of indexes applied to the images and the performance of exploration methods such as

PCA. Such observations prompt for the investigation of optimal workflows to process and analyze under-ice HI data.

4.4.2 System performance and future developments

While most of the transect could be scanned as planned, some issues were experienced during the scanning process such as invasive ski marks and occasional lagging which hampered pushbroom image composition (Figure 4.6 and 8). Nonetheless, the low gear winch system was capable of delivering extremely slow speeds in a stable manner as observed in the imagery. The observed angular deviations are comparable to data for professional gimbal stabilization systems for UAV applications (Arroyo-Mora et al., 2019). They had negligible effects on the HI image composition and RGB imagery in our case due to the close-range set-up and the extremely slow speeds. The only trade-off of the system is that the winches had to be manually rotated which is a time-consuming and personnel demanding process. For future deployments, we plan to automate and motorize the winch system. The changes in transect heading are likely attributed to a combination of small-scale ice irregularities, inhomogeneous surface drag and/or the effect of intermittent currents observed from our underwater footage. There is also the possibility of a loosened ski frame support which went unnoticed. The cause of the lagging could be attributed to these roll changes but could not be precisely identified either. Investigation of the RGB imagery did not point to a particular ice condition that could have induced the lagging. A too strong buoyancy force against the ice (-9 kg in water, Figure 4.1) might have increased surface drag to a counterproductive level.

These aspects can firstly be improved by developing an improved sliding system and refining its technical design. However, greater advantage is envisaged in exploring manual or automatic pushbroom HI rectification techniques through the incorporation of overlapping RGB orthomosaics, also known as co-registration (Fang et al., 2018; Habib et al., 2016; Turner et al., 2014). This approach co-registers the hyperspectral imagery based on a reference RGB orthomosaic through image matching procedures (e.g., feature matching, and transformation based on matching points (Aasen et al., 2018)). The only requirements for co-registration are spatially similar and overlapping HI and RGB imagery and good accuracy for the RGB orthomosaic reference. Advances in camera calibration and triangulation procedures permit the generation of RGB orthomosaics with high geometric fidelity using a limited amount of GCPs and/or consumer-grade navigation data (Fonstad et al., 2013; Marcer et al., 2017; Tonkin and Midgley, 2016). Although a more accurate assessment is still required, the western transect RGB orthomosaic resulted in a highly resolved and metrically scaled photogrammetric model which could be used for co-registration for example (Figure 4.6 and Figure 4.7a and b). This was possible as our camera calibration and model reconstruction heavily benefitted from a constant sea-ice thickness and imaging altitude which allowed to impose an artificial network of GCPs of precisely known positions in the 3D space. The same approach would not be possible under highly heterogeneous topographies or would not be as effective for highly dynamic imaging conditions. Under these sub-optimal circumstances, the options could be to

retrieve an accurate camera model using underwater calibration targets (Maas, 2015; Shortis, 2015), to estimate it through its mathematical formulation and/or to implement the use of dome ports (Menna et al., 2016). Another option remains the addition of physical GCPs. Compared to the seafloor, the sea-ice can be used as an opportunistic reference surface where Ground Control Points (GCPs) visible below and above the ice can be allocated (e.g., Nicolaus and Katlein, 2013). GCP positioning can then be accomplished using conventional GNSS devices and manual measuring or by referencing them in a local reference system. This is advantageous as positioning underwater typically requires the acquisition of acoustic data, which may depend on information from the under-ice vehicle/platform to a research vessel through a network of deployed transponders (Cazenave et al., 2011; Meiners et al., 2017; Williams et al., 2014). This process requires considerably more effort and resources and would arguably suit the precision required by line scanning orthorectification methods.

By taking advantage of the referenceable sea-ice surface and co-registration methods we could then theoretically develop algorithms analogous to aerial HI algorithms based on the scaled RGB orthomosaics, the partially rectified HI scans and the acquired consumer-grade IMU data (Fang et al., 2018; Habib et al., 2016; Yeh and Tsai, 2015). These future developments will aim to support the geometric correction of distortions caused by the dynamics of the HI frame, such as the lagging instances (Figure 4.7c). In addition, robust geometric correction will pave the way for a more independent system that can operate under rougher under-ice topographies and at increased distances from the ice. The system needs to strive towards increased distance from the ice, and ease of operability under diverse under-ice conditions. As the technology develops, there is also potential to drastically reduce the weight and volume of the payload. Eventually, this may allow the development of HI payloads for Remotely Operated Vehicles (ROVs) or AUVs to drastically increase the spatial extent of the surveys, although there are physical and technical challenges associated which are briefly discussed in the last sub-section.

4.4.3 Potential applications of under-ice hyperspectral and RGB imaging payloads

Compared to standard imagery or multispectral imagery, HI provides narrow spectral resolutions, high bit depths, and actual radiometric and referenceable units. Higher spectral fidelity sensors with reasonable spectral resolution would not only be beneficial to produce quantitative estimates of fine scale sea-ice biophysical properties, but also to develop tailored relationships for each study area and move towards more universal approaches and algorithms (Cimoli et al., 2017a or Chapter 3). The complex under-ice perspective will undoubtedly pose new challenges and constraints. However, several additional indices or machine learning approaches coupled with radiative transfer modelling efforts could be tested and adapted to produce more robust and universal relationships to retrieve diverse biophysical properties. Some examples can be found in forestry and agriculture (Adão et al., 2017; Malenovský et al., 2013; Wang et al., 2016), ocean colour

(Blondeau-Patissier et al., 2014; Matus-Hernández et al., 2018), chemometrics (Amigo et al., 2015) and other environments (Chennu et al., 2013; Malenovský et al., 2015).

Low-cost imagery sensors—such as RGB, near-infrared (NIR) or multispectral— have also served well in multiple close-range remote sensing applications to retrieve qualitative and quantitative information from biological targets (Näsi et al., 2018; Shen et al., 2019; Taghizadeh et al., 2011). For the under-ice environment, RGB imagery has been used to qualitatively assess the spatial distribution of algae (Ambrose et al., 2005; Fernández-Méndez et al., 2018; Katlein et al., 2015b). Therefore, RGB or multispectral imagery should be considered from a cost-benefit analysis perspective based on desired research aims and available resources.

In theory, hyperspectral resolution data has the potential to resolve beyond pure biomass estimates towards more sophisticated biological traits such as ice algal photophysiology (Jesus et al., 2008; Malenovský et al., 2015; Perkins et al., 2016), species composition (Jesus et al., 2008; Mehrubeoglu et al., 2013; Xi et al., 2015), pigment detection (Blackburn, 2007; Pettersen et al., 2014; Taylor et al., 2013) and feature classification and mapping (Caras and Karnieli, 2015; Dumke et al., 2018b; Foglini et al., 2019). An interesting field is also being explored in the retrieval of primary production estimates from spectral data in combination with in-vitro photosynthetic parameters for ice algae (Lange et al., 2017; Müller et al., 2016) or with PAM fluorometry for microphytobenthic communities (Méléder et al., 2018).

Compared to point sampling radiometers, the main advantage of imaging payloads is the possibility to capture the information at ultra-high spatial resolutions (in this case sub-mm scales) in a non-invasive manner (e.g., Chennu et al., (2013)). Under sea ice, this will allow future studies to investigate multi-scale ice-algal dynamics and how they covary with environmental drivers over space and time (Campbell et al., 2015; Cimoli et al., 2017c or Chapter 2; Lund-Hansen et al., 2016, 2014). With little additional effort, the RGB imagery and close-range digital photogrammetry provided an accessible tool to producing ultra-high resolution orthomosaic and 3D models of the under-ice surface.

Surface topography is a well-known factor driving spatial distributions in many marine ecosystems (e.g., Dustan et al., (2013)). Under-ice, the potential of high-resolution HI and 3D data fusion could contribute to new opportunities to monitor some of the sea-ice biophysical interactions which were previously difficult to capture. The effects of under-ice topography on sea-ice algal biomass distributions has long been queried and investigated (Gutt, 1995; Krembs et al., 2002, 2001). Recent studies have further observed and inquired about the role of under-ice topography and underlying currents on algal biomass distribution at multiple spatial scales (Katlein et al., 2015b; Lange et al., 2015; Lund-Hansen et al., 2016). Hydrodynamic shadows can foster the accumulation of diatoms, algal aggregates, and may also provide shelter for under-ice fauna (Fernández-Méndez et al., 2018; Hop and Pavlova, 2008; Werner, 1997). The RGB imagery not only can provide under-ice roughness but it could also serve to gain further insight into grazing dynamics by sympagic fauna (Figure 4.8).

The effects of sea-ice structure and physical properties also go beyond effects on biomass distribution and are known to influence algal photophysiology, species composition and production (Arrigo et al., 1995; Arrigo, 2017; Fernández-Méndez et al., 2018; Leeuwe et al., 2018). Although intrinsically different from some of the Arctic examples cited above, the dataset presented here clearly illustrates a complex biophysical scene for Antarctic land-fast sea ice even within a square meter area (Figure 4.9 and 10). For example, we found large secondary brine channels to characterize specific areas of the scanned transect (Figure 4.6). These augmented transmitted light conditions that showed localized maxima of up to one order of magnitude (Figure 4.7). The question arises whether these under-ice features have an impact on algal distribution, species composition, and/or photophysiology, or if they play any role in hydrodynamic regimes and under-ice grazing dynamics. The presented methodology may contribute to a better understanding of some of these complex biophysical interactions.

4.4.4 Caveats and future challenges

Our sliding system has been designed for deployments over relatively smooth under-ice bottoms. Nonetheless, the principles of operation of HI and digital photogrammetry remain applicable to any ice type, provided that under-ice light levels are sufficient. In cases where the sliding concept is not applicable (e.g., rough pack ice), platforms will need to be equipped with sensors to accurately trace HI sensor attitude and dynamics.

In this study, the HI payload was operated under thick (1.8 m) and almost snow free fast ice (Figure 4.6). To account for low under-ice irradiance levels (0.35± 0.20 W m^{-2}) the system was operated at extremely slow scanning speeds (0.008 ms^{-1}). These irradiance values are comparable to under-ice light levels and variability for Arctic fast-ice during spring (Nicolaus et al., 2013), and help to provide a baseline for the range of under-ice irradiances intensities for which our payload could acquire meaningful HI signals. However, many other sea-ice conditions remain to be explored (e.g., with deep snow packs) and which may pose significant technical challenges. Low light levels will push sensors to their sensitivity limits, necessarily affect SNR and hinder the integration of pushbroom HI payloads onto more efficient and dynamic underwater platforms, such as ROV and AUVs. A series of studies have already employed pushbroom HI sensors for seafloor mapping using ROVs (Dumke et al., 2018b, 2018a; Foglini et al., 2019), diver operated systems (Chennu et al., 2017) or unmanned surface systems (Mogstad et al., 2019). A first study has also discussed HI feasibility onto Unmanned Underwater Vehicles (AUVs) (Sture et al., 2017). However, these applications positively benefitted from artificial light sources that illuminate the imaged scan line, or were performed in shallow, clear tropical waters. For mapping under-ice environments, there is a trade-off between sensor integrations times, imaging frequencies, and platform dynamicity under low light conditions that will need further investigation (Cimoli et al., 2017c or Chapter 2).

The inclusion of underwater IMUs, relative positioning systems, and implementation of targeted under-ice pushbroom HI orthorectification methods will open up new avenues for this type of research. While active lights sources could be eventually considered for under-ice mapping, the resulting mixture between reflected and transmitted light through a complex and translucent medium would render data processing and interpretation extremely challenging. In fact, our system features a set of artificial light sources as shown in Figure 4.5b and schematized in Figure 4.4. Using a custom-built control (Figure 4.4), the LEDs were tested and observed to provide a slight increase in the measured signal. However, it was preferred for the scans here presented to avoid their use to avoid complicated data interpretations. The effect of strong LEDs on relatively low-light adapted algal communities could also question the invasiveness of the methodology.

Additional challenges arise due to the complex nature of sea-ice optical properties and the resulting anisotropic under-ice light field (Katlein et al., 2016, 2014). The anisotropic light field is shaped by the lamellar sea-ice features funneling light in the downwards direction creating a forward peaked light field. Lamellar structures associated with columnar ice were clearly observed in our site (e.g., Figure 4.8). Analogous above surface HI applications (e.g., equipped onto UASs) have acknowledged the impact of an anisotropic leaving reflectance on the retrieval of biochemical parameters using spectral data (Aasen and Bolten, 2018; Buchhorn et al., 2016; Zhao et al., 2015). In this study, we experienced noise artefacts over block B sample processed images as an increase in noise patterns at the upper and bottom edges of the image. This is most likely inherent to camera optical design and sensitivity heterogeneity across the spatial dimension, but it could also be in part attributed to light-field anisotropy. A forward peaked light field could mean a stronger signal at the center of the line scan and a decreasing signal towards the edges of our ~30 FOV. However, other possible causes should be taken into consideration (e.g., data processing artifacts) or the dense oxygen bubble layer causing multiple refraction effects (Figure 4.8). Eventually, the impact of an anisotropic under-ice light field, or other particular environmental conditions (e.g., oxygen bubbles), on HI data will need to be further assessed, and corrections developed towards improved estimates and interpretations.

We did not apply any corrections for the water column effects to either the RGB imagery or to the HI data processing workflow. This is acceptable as the water column in between the ice and the enclosure was < 1.1 m and our site was characterized by exceptionally clear waters (see Figure 4.5c). Antarctic surface waters are generally considered to have low particle loads with low backscattering (e.g., [121]). Nonetheless, as we increase sensor distance from the target, or in case of consistent under-ice phytoplankton abundance (e.g., [122]), the impact of the water column should be addressed with standard color correction approaches for RGB imagery (Åhlén et al., 2007; Bryson et al., 2015; Johnsen et al., 2013) and for the water column correction of hyperspectral radiometric data if possible (Johnsen et al., 2013; Yang et al., 2010).

Our sea-ice site also benefitted from optically “favorable” conditions where biomass was high and resided mostly in the bottom 3 cm of the ice. Due to the scattering properties of sea ice, the bottom 3 cm algal layer can be considered as an evenly illuminated “thin” sheet that was scanned with our

payload. While ice algal biomass is known to be generally concentrated at the ice bottom, where organisms enjoy more favorable living conditions (Arrigo, 2017; Meiners et al., 2012), there are many circumstances of vertically variable distributions (Meiners et al., 2012). Future applications of HI for sea ice with a certain degree of vertical biomass variability (e.g., in Antarctic pack ice) will need to consider these effects. Due to the scattering nature of sea ice, biomass in the sea-ice interior will probably have a negative impact on discernible spatial resolutions and image interpretation. Larger protruding algal filaments that are only loosely attached to the subsurface of the ice could also be a problem under dynamic currents for both HI and RGB imagery. In our case, filaments did not represent a significant problem as they were relatively short and under-ice currents during scanning seemed monodirectional, thus providing a relatively still scene (Figure 4.8). Finally, the feasibility and performance of HI to capture biomass variability under the extremely different biomass ranges found in the sea ice need to be assessed. A compilation of biomass ranges found in sea ice can be found in Arrigo (2017). A previous experimental study has shown HI to be able to discern biomass ranges as low as 0.036-2.72 mg m^{-2} (Cimoli et al., 2017a or Chapter 3), but much more work is required to investigate the impact of different concentrations on per-pixel SNR and regression algorithms performance.

Chapter 5

Hyperspectral imaging of sea ice cores to map microspatial variability of ice algal biomass

5.1 Introduction

Sea ice is a porous multiphase medium whose interstitial environment is inhabited by diverse phototrophic algal and heterotrophic communities (Arrigo, 2014). Sea-ice algae generally dominate ice-associated biomass and form the foundation of the polar marine foodwebs (Arrigo, 2017; Meiners et al., 2018; Tedesco et al., 2019). The dynamic and multiphase nature of sea ice imposes strong horizontal and vertical gradients of its physical properties, such as temperature, salinity, porosity and light availability (Petrich and Eicken, 2016; Sturm and Massom, 2016). These gradients continuously vary over time, fundamentally driving variations of ice algal biological properties (e.g., abundance, physiology, and community composition) (Arrigo, 2017; Meiners et al., 2012).

Ice algal biological properties are known to be extremely variable over space and time at spatial scales from kilometers down to millimeters (e.g., Cimoli et al., 2017c or Chapter 2; Meiners et al., 2012). Whilst most of the ice algae biomass generally resides at the ice-ocean interface, ice algae can also be found in interior and surface sea-ice layers (Arrigo, 2017; Meiners et al., 2012).

A mechanistic understanding of the sub-mm spatio-temporal organization of algal biomass in sea ice is lacking, thereby limiting our ability to quantitively predict and thus extrapolate its evolution. One reason perhaps is the lack of methods capable of non-invasively tracking algal biomass across different scales, both vertically and horizontally, concurrently with its physical drivers.

Biophysical properties refer to the dynamically coupled sea-ice physical and biological attributes. There is evidence that dominant scales of variation for under-ice biophysical properties can range from the micro-scale- (0.001 m^2) to the mesoscale (10 m^2) (Ambrose et al., 2005; Lund-Hansen et al., 2016; Rysgaard et al., 2001), which cannot be practically be resolved using point-based sampling methods (e.g., Forrest et al., 2019; Lange et al., 2017). Traditional sea-ice field sampling methods include ice coring (Miller et al., 2015), under-ice bio-optical sensing techniques via L-arms (e.g., Campbell et al., 2014; Melbourne-Thomas et al., 2015; Mundy et al., 2007; Wongpan et al., 2018) or unmanned underwater vehicles (UUVs) (Cimoli et al., 2017c or Chapter 2; Lange et al., 2016a; Meiners et al., 2017). The use of under-ice optical sensing from UUVs has extended the spatial

coverage of algal surveys (e.g., covering meso- to floe-scale areas), although resolutions still remain coarse as a result of single-point sampling of underwater radiance (or irradiance) sensors (Forrest et al., 2019; Lange et al., 2016a; Meiners et al., 2017).

There is a clear gap in field-sampling methods that permit the quantification of fine-scale horizontal and vertical distributions or dynamics of ice algae biomass. Accurate, quantitative hyperspectral imaging is one method that can help to identify both a) the drivers of the sea-ice biomass structure, and b) assessing the spatial the variability that is relevant to larger scale analyses.

Hyperspectral Imaging (HI) can be used to quantify biogeochemical properties of a target in each spectrally-resolved pixel within an image (e.g., Aasen et al., 2018; Aasen and Bolten, 2018; Johnsen et al., 2013). *In situ* HI is revolutionizing the scales of observation of both terrestrial (e.g., Anderson and Gaston, 2013; Mitchell et al., 2012; Turner et al., 2018) and marine (e.g., Chennu et al., 2017, 2013; Mogstad et al., 2019) ecosystems. HI can also be used under controlled laboratory conditions to scan specific samples from the target so we can better understand its spectral behavior and baseline it measurements taken *in situ*. This permits us to gain detailed understating of any particular subject interaction with light but also allows to capture dimensions and dynamics that are not visible from the *in situ* surface perspective (e.g., vertical variability).

Some examples include scanning of glacial ice cores to detect chemical impurities (Garzonio et al., 2018), scanning of soil cores to map fine-scale organic carbon hotspots (Hobley et al., 2018), and scanning of sediments to determine pigment concentrations in microbial phototrophs (Butz et al., 2015; Chennu et al., 2015).

We have recently demonstrated how HI can qualitatively capture biomass variability at sub-mm spatial resolution in artificial laboratory ice (Cimoli et al., 2017a or Chapter 3) and *in situ* under Antarctic fast ice (Cimoli et al., 2019 or Chapter 4). Cimoli et al., (2019) describes an under-ice mobile payload capable of delivering rectified sub-mm resolution hyperspectral swaths of the ice-water interface.

However, these previous studies of HI in sea ice lack a quantitative estimation of chl-a abundance resolving only relative abundance estimates using explorative methods such as Principal Component Analysis (PCA) loadings as proxies. In this research we extend the HI method to map the fine-scale vertical distribution of sea-ice algae through optical quantification of chl-a. Spectral indices, based on transmittance measurements of ice-core sections are tested through regression models against extracted chlorophyll-a values. The retrieved regression models can then be applied to the hyperspectral imagery acquired both *in situ*, and to the ice cores itself to retrieve quantitative chl-a concentrations for each pixel in the images, thus extending our capabilities for scalable observation of under-ice habitats.

5.2 Materials and methods

5.2.1 Hyperspectral imaging

The method proposed here employs light (e.g. from an artificial LED light source) transmitted through the vertical axis (longitudinal) and horizontal (lateral) sections of an ice core (Figure 5.1a). Sea-ice in an optically complex and translucent, medium that allows us to conceptualize retrieval of bio-optical properties from measurements in transmittance mode (Perovich, 2017, 2003) from across section of the ice core. Sensing of transmitted radiance, rather than reflected, aims to emulate under-ice close-range bio-optical remote sensing approaches to estimate chl-a quantities in sea ice (Cimoli et al., 2017c or Chapter 2; Mundy et al., 2007).

The proposes ex situ HI set-up consists of a push-broom hyperspectral imaging scanner (AISA Kestrel, Specim Ltd) mounted onto a motorized rail (Revolve Camera, USA) with the optics (F/2.8, 40° wide) focused on a sample holder beneath the scanner (Figure 5.1a). The scanner moves at a constant speed whilst capturing spectral data within frames of approximately 0.45 mm resolution with a spectral range of 400-1000 nm at 1.7 nm resolution. Depending on the sea-ice characteristics and study objectives, one can select the thickness and shape of the ice core samples to scan and sections are placed within a black box to reduce influence of external light (Figure 5.1a). Considering the ice sample thickness and shape, the AK10 camera settings and motorized slider speed can be precisely tuned to maximize transmitted signal to produce natively rectified imagery with pixels of standard geometry (i.e., square and not distorted).

The right distance from the camera entrance lens to the imaged target is required to keep most of the core volume in focus. A test pattern/grid was used to keep most of the sample's target thickness within the focal depth of the optics (Figure 5.1e).

Two different LEDs were employed as artificial light sources to illuminate the cores. These included a white LED, constituting the typical dual peaked spectrum shape (Figure 5.1b) and a solar LED, designed to resemble the solar spectrum (Figure 5.1c). Using two different LEDs gave us the ability to test the robustness of the method independent of the light source in order to be able to assess how scans using different lights might be combined or compared. The LEDs were set to emit at relatively low intensity, yielding E_d, PAR of < 30 mol s^{-1} to avoid potentially harmful effects of excessive light exposure to algal communities which are typically dark adapted. Reducing the light intensity comes at the expense of signal to noise ratio (SNR), however it does provide us with comparable SNR to *in situ* under-ice hyperspectral scanning environments which are acquired using only passive light transmitted through the sea ice to support transferability of retrieved relationship to *in situ* imagery (Cimoli et al., 2019 or Chapter 4).

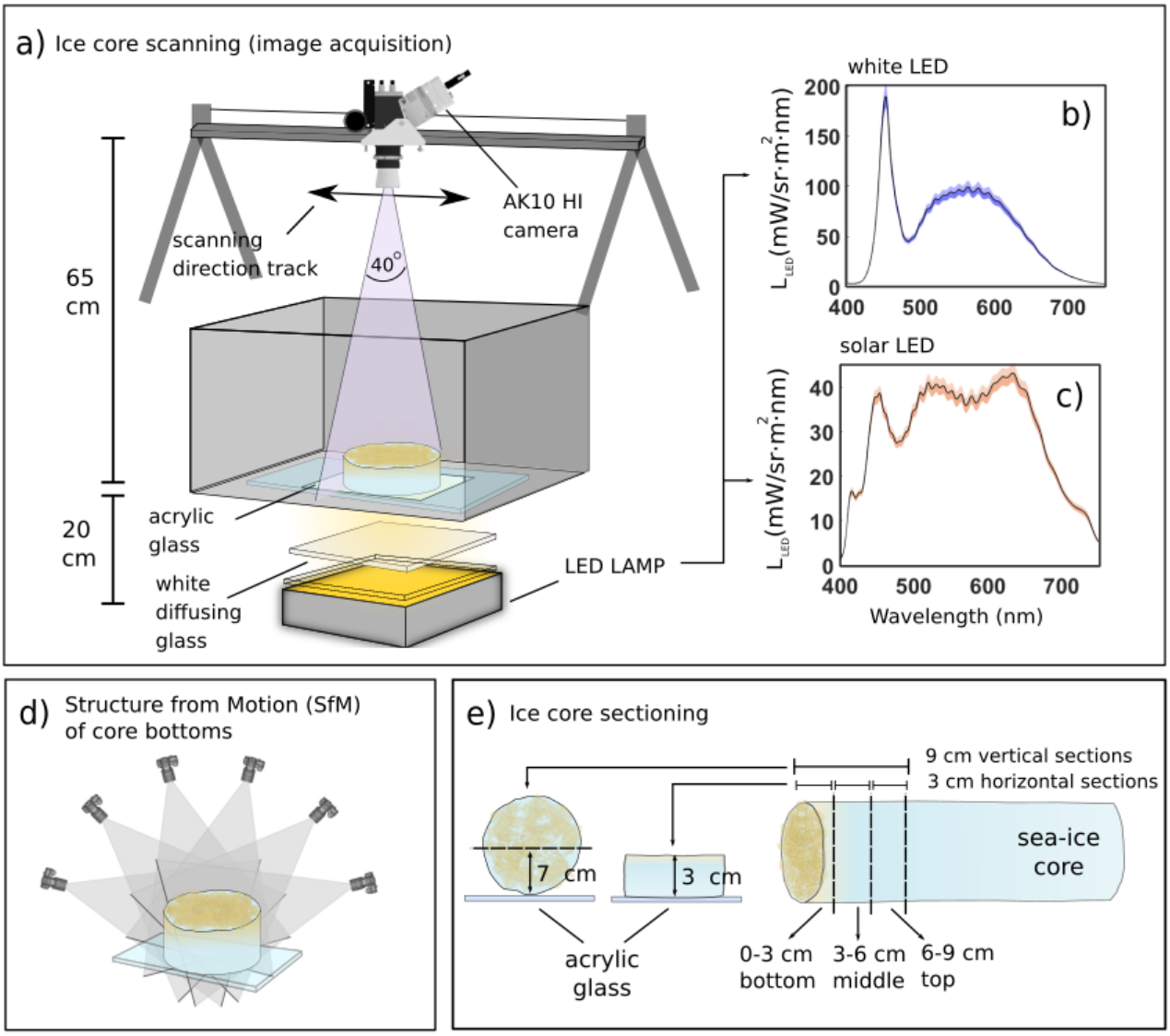

Figure 5.1 An overview of the data acquisition workflow and hyperspectral imaging optical set-up. (a) The ice core scanning set-up based on transmitted artificial illumination. (b) and (c) illustrate the mean ± standard deviation of radiance (L) emitted by the white and solar LED lamps entering the acrylic glass tray surface, respectively. d) 3D model reconstruction using Structure from Motion (SfM) digital photogrammetry on horizontal bottom-core sections. e) Ice core sample preparation for hyperspectral image acquisition along vertical and horizontal ice-core surfaces. A total of 6 vertical scans and 54 horizontal scans were acquired in this study.

The optical set-up illuminates the entire sections of the core with a diffuse and homogenous light. Figure 5.1b and c present the radiance mean ± standard deviation (sd) of all pixels across the imaged acrylic surface area. This homogenous light field was established by selecting the appropriate distance between the ice core and the LED (approx. 20 cm in this example) and including a semi-opaque white glass substrate diffuser (Figure 5.1a). The core sections were placed on top of a 15 x 15 cm acrylic glass tray inside a black box to reduce external light contamination(Figure 5.1a).

Field measurements in were conducted inside a dark and generator powered shipping container used as laboratory. Nevertheless, measurements could also be performed on a dark tent, with the system being powered using an appropriate battery supply system. The measurement set-up is flexible and easy executed by a single operator.

5.2.2 Study area and ice coring

A field camp was established at Cape Evans, Antarctica (77.637 ° S, 166.401° E), from the 14th of November to the 5th of December 2018. The sea-ice across the study area was characterized by a homogenous thickness of 180 ± 1 cm, except for occasional ridged or crack areas. The distinct under-ice biophysical environment was visually explored using a Seabotix LBV-300 Remotely operated Vehicle (ROV) (Teledyne Marine, Seabotix, California, USA) which is further described in the results section 4.1.

Sea-ice surface conditions in the area were typically snow-free due to wind-induced drift and displacement. Few snow patches were present and were categorized as with a 0.5-1 cm hard old snow layer or 1 to 5 cm compacted snow relief. These conditions remained consistent during the 21-day study period.

Forty-two ice cores were extracted using a Kovacs Mark V ice corer (14 cm internal diameter). Cores were extracted between the 19th of November to the 2nd of December and are sequentially numbered as per extraction. Of the 42 cores extracted, 22 were taken from bare ice (snow free) areas, 12 from the area with 0.5-1 cm thin snow covering , and 7 cores on the 1-5 cm snow drifts, and 1 on a 10 cm snow patch. After retrieval, the bottom ~60 cm of each core was immediately cut off using an ice saw and sealed into a black food-grade plastic bag to protect them from sunlight and promptly taken into the dark field laboratory for HI analysis and further processing.

Structure from Motion (SfM) digital photogrammetry was tested on the bottom surface of selected sea ice cores to capture the microtopography of the 0.015 m^2 horizontal sections of the ice core (starting at the ice-water interface) (Figure 5.1d). SfM is simple way to obtain highly resolved and scaled 3D models of objects or surfaces of interest using a set-of overlapping pictures and a photogrammetric software. Bottom cores images were collected with a Nikon D500 digital camera and Tamron SP 90mm F/2.8 Di MACRO 1:1 VC USD macro lens. We used Agisoft Metashape software for processing, and followed standard workflows as outlined in the software (Agisoft Metashape User Manual - Professional Edition, Version 1.5, n.d.). Models were scaled using known lengths and distances within the ice cores.

5.2.3 Hyperspectral image acquisition

5.2.1.1 Vertical ice core sections

For this study, vertical scans of 6 of the 42 ice cores were acquired with a length of 9 cm (Figure 5.1e). The solar LED lights were only used for the vertical scans. HI imaging frequency was set to 10 Hz with an integration time ranging from 90-99 ms in combination with a sliding rail speed of ~0.4-0.5 cm s^{-1}. We did not apply any in-camera spectral binning and this resulted in a native spectral resolution of 1.7 nm (356 bands). Spatial binning was applied to reduce the image to 1024 pixels across the scanning direction (seen in Figure 5. 1) in order to boost SNR and gain additional depth of field (DoF).

The entrance pupil of the camera was located approximately 55 cm from the center line of the core (Figure 5.1e). Across-track scan lines were around 40 cm with a spatial resolution of 0.039 cm and vertical cores width covered 360 pixels over the across-track scan line.

5.2.1.2 Horizontal ice core sections

Horizontal ice-core sections were prepared by cutting off the lower-most 3 cm (Figure 5.1e) section from the core. This sampling was done for all 42 cores. Six selected cores from the 42 were additionally processed by sectioning the core at 3 cm intervals starting at the ice water interface at 0 to 3 cm, 3 to 6 cm, and 6 to 9 cm (Figure 5.1e). Such procedure provided additional twelve horizontal core sections for scanning, yielding a total of 54 horizontal core samples and allowed to explore horizontal variation of biomass deeper into the ice column, and to increase our sample size and range. The sections are placed with the bottommost part looking upwards (Figure 5.1e). All bottom 0-3 cm sections were imaged.

No in-camera spectral binning was applied, yielding a native spectral resolution of 1.7 nm (356 bands). Spatial binning was applied to reduce to 1024 pixels across the scanning direction in order to boost SNR and gain additional DoF. Both LEDs were used intermittently for imaging, and different settings were used as per different light intensities. Eighteen sections scans were taken using the white LED. Imaging frequency was set to 15-20 Hz with 60-75 ms integration time and the sliding rail speed ~0.8-1.1 cm s^{-1}. Thirty-six section scans were taken using the solar LED. Imaging frequency was set to 10 Hz with integration time ranging from 90-99 ms and sliding rail speed to ~0.4-0.5 cm s^{-1}. The entrance pupil to core surface distance was around 62 cm achieving an across-track scan line of around 45.6 cm and a spatial of resolution of 0.044 cm which resulted in around 80500 pixels per horizontal core surface area of 0.015 m^2.

5.2.1.3 Under-ice in situ

In situ hyperspectral images were taken beneath the sea ice from the same locations from which the ice cores were extracted using an underwater HI and photogrammetric payload fully described in

(Cimoli et al., 2019 or Chapter 4). This tethered under-ice sled utilized the same AK10 camera as the ice-core scanning set-up. The system was designed to capture both hyperspectral imagery and fine scale topography along 20-40 m transects at sub-mm spatial resolution. To fulfil the purpose of this study, we selected a small 60 x 70 cm hyperspectral image subsample, namely block B, from a transect which was presented previously in Cimoli et al., (2019) and Chapter 4. This image region exhibited highly variable biomass distribution as well as interesting cavities and reliefs in the under-ice topography. For block B image acquisition, both spatial and spectral dimensions were binned at-sensor. This yielded a native spatial resolution of 0.0624 cm, and a spectral resolution of 3.5 nm (178 bands), respectively.

5.2.4 Hyperspectral image preprocessing and exploration

The image preprocessing and exploration workflow is illustrated in Figure 5.2. All of the acquired raw imagery was converted from Digital Numbers (DN) to radiometric values of upwelling transmitted radiance L_t (λ, mW m^2 sr^{-1} nm^{-1}) (Figure 5.2) as per standard procedures (e.g., Aasen et al., 2018) and as previously described for this environment in Cimoli et al., (2019) and Chapter 4. All horizontal and vertical imagery of cores were manually masked to ensure that only pixels within the ice-core surface were analysed. Spectral sub-setting was applied to keep only Photosynthetically Active Radiation (PAR) between 400 and 700 nm. This allowed us to focus on chl-a absorption features, which boosted processing time and reduced noise interference outside of this range. This resulted in 89 spectral bands for the *in situ* imagery and 179 for the core imagery.

For HI studies of sea ice, Principle Component Analysis (PCA) has been used to capture per-pixel fine-scale spatial variability of the first two principal components (PCs) scores embodying light intensity variability and biomass proxies in both laboratory artificial sea-ice (Cimoli et al., 2017a or Chapter 3) and *in situ* (Cimoli et al., 2019 or Chapter 4). Mean-centered PCA was employed here on the pre-processed imagery of both vertical and horizontal ice core sections (Figure 5.2). Each pixel of the image adds up as a sample into the PCA algorithm. In order for PC scores to be comparable among different images of different cores, all vertical cores are pooled into a common PCA pixel sample pool and all horizontal cores sections were pooled together into a separate pixel sample pool. Pixels from vertical and horizontal core sections are not pooled into the same PCA due to their different optical setting. No PCA was applied to the *in situ* imagery of block B as this was explored previously in Cimoli et al., (2019) or Chapter 4.

Transmitted radiance, $L_t(\lambda)$, of each pixel of the horizontal core sections, is normalized by the corresponding averaged LEDs radiance $L_{LED}(\lambda)$ as shown in Figure 5.1a and b using the following formula:

$$T(\lambda) = \frac{L_t(\lambda)}{L_{LED}(\lambda)} \qquad (4)$$

This provides spectrally resolved per-pixel directional transmittance over the entire core surface area (Figure 5.2a). The *in situ* block B image is also normalized to directional transmittance using the same formula but instead per-pixel $L_{d,t}(\lambda)$ is divided by the average of the highest intensity pixels within the image block, corresponding to an algal free cavity in the ice present $L_{d,cavity}(\lambda)$ (seen in Figure 5.2 as bright white spot):

$$T_d(\lambda) = \frac{L_{d,t}(\lambda)}{L_{d,cavity}(\lambda)} \qquad (5)$$

This provides a proxy of light transmittance over roughly the last 5 to 10 cm of ice bottom (Figure 5.2b). To reduce processing times and increase SNR, the Block B image was binned spatially in a 2x2 array resulting in a resolution of 0.12 mm pixels. Per-pixel smoothing of all the core spectra (thicker, thus noisier) is done using a Savitzky-Golay low-pass filter (Savitzky and Golay, 1964; Schafer, 2011) with a polynomial order of 3 and frame length of 9 (Figure 5.2). The aim was to reduce noise in the transmitted signals without impacting on the shapes of spectral features associated with chl-a. The same filter is applied per-pixel to the block B image.

5.2.5 Pigment quantification

After scanning the ice-core sections with the hyperspectral imager, the samples were left to thaw in dark containers at 4°C . After thawing, the final melt volume was vigorously mixed to break up cell aggregates and 50 mL sub-samples samples were taken from agitated sample and were filtered onto Whatman GF/F filters using a diaphragm vacuum pump. The filters were then placed in ethanol for 24 h extraction of chl-a. The extracted Chl a was measured according to methods described by Holm-Hansen and Riemann, (1978) and as suggested in standard protocols (Miller et al., 2015) using a fluorometer (10AU, Turner design). Fluorometric chl-a estimates were in volumetric concentrations (ug L^{-1}). In order to convert to areal concentrations (mg m^{-2}), we multiplied the volumetric concentration by the total melt volume of the ice-core sections and divided this by the surface area of the 14 cm diameter core (0.015 m^2).

While a more complete suite of pigments could be retrieved through the processing and analysis of HPLC samples, in this thesis, the focus its given only to the application for the method for detection of biomass distribution in the form of chl-a only. Processing of HPLC data and the exploration of bio-optical approaches for the discrimination of algal pigment compositions and photo acclimation strategies will be the subject of future studies (e.g., Johnsen et al., 1994).

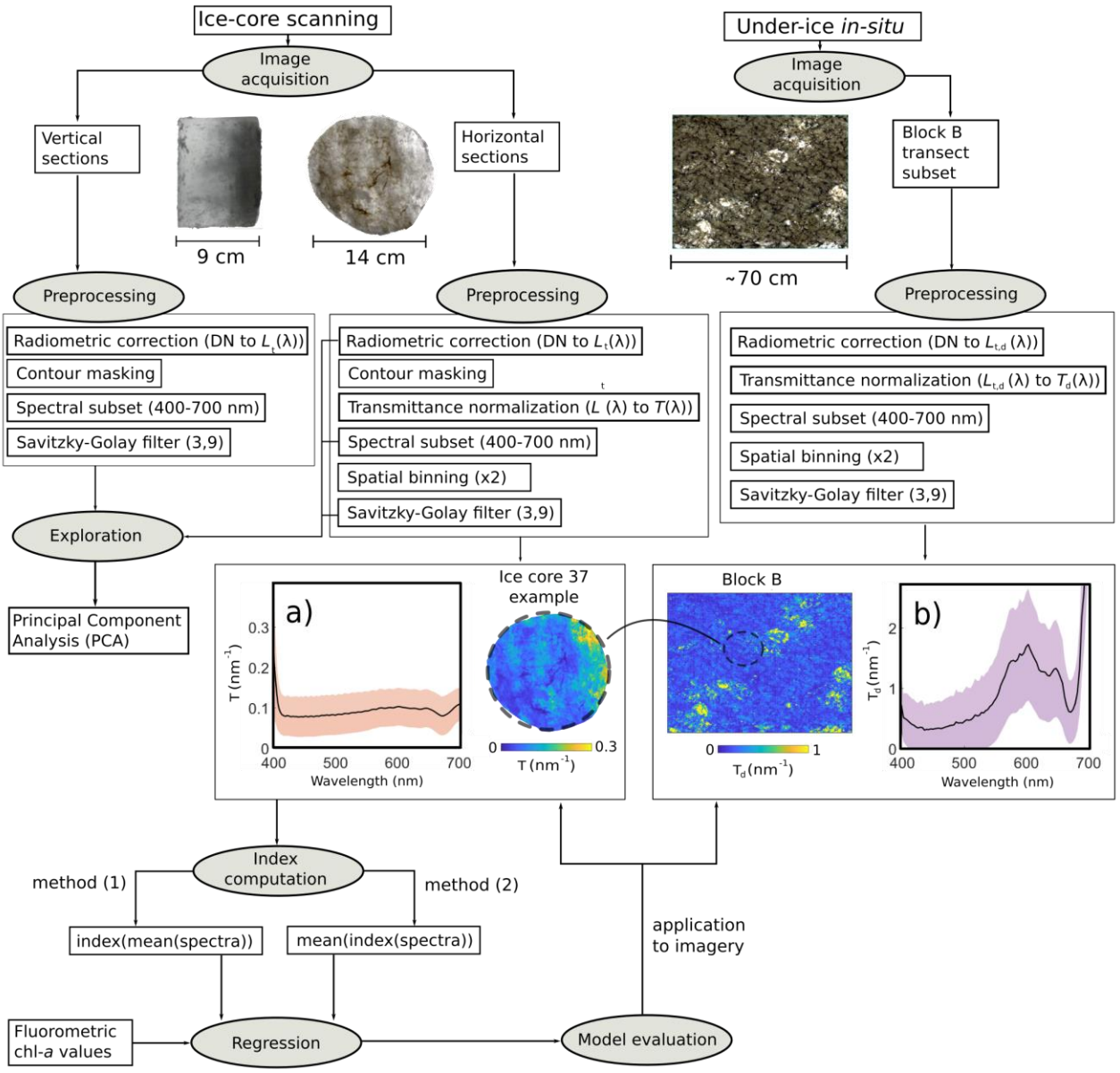

Figure 5.2 A flowchart of the data-processing procedure to yield per-pixel biomass (as chl-a) estimates from hyperspectral imagery of core sections and *in situ.* a) and b) display the mean ± standard deviation of directional transmittance at 668 nm through an example ice core (ice core 37) and the under-ice imagery, respectively. The under-ice HI procedure is detailed in Cimoli et al., (2019) (Chapter 4). L(λ) stands for spectral radiance and T(λ) and T_d(λ) for spectral transmittance and downwelling spectral transmittance, respectively. DN stands for Digital Number of raw imagery data.

5.2.6 Spectral indices

Traditional and alternative spectral indices representing proxies of biomass abundance were regressed against fluorometric chl-a estimates. The aim was to retrieve a model that could be applied on a per pixel basis on the preprocessed imagery. In order to retrieve an index value for each core section, two approaches are available: (1) apply the index algorithm to the mean spectrum of all pixels of the core image, index(mean(spectra)) or (2) apply the index to each pixel spectrum of the image and then perform a mean of the index, mean(index(spectra)) (Figure 5.2). These will not be identical as the index formulae that use multiple wavelengths in algebraic structures will generally not be commutative. In addition, one aim of the regression is to apply it to a per pixel basis hyperspectral imagery retrieved *in situ* under low-light conditions (e.g., Cimoli et al., 2019 or Chapter 4). Thus, computing indexes based on an averaged and smoothed spectrum may not be adequate for application over individual pixel spectra in the images. Here we limit our analyses to apply and assess the model's performance based on method (1) only, and we leave the comparison and assessment to a later stage.

The mean of the spectra of all pixels within each preprocessed core surface is then performed according to method (1) (Figure 5.2). The mean directional transmittance spectrum ± standard deviation (sd) of an example horizontal core section (core 37) is shown in Figure 5.2a. For comparison, the mean spectrum ± sd of all preprocessed pixels within block B (which includes the ice core 37 sample location) is shown in Figure 5.2b.

Sea-ice bio-optical studies have mostly relied on Normalized Difference Indices (NDIs) to relate under-ice transmitted spectra to chl-a (e.g., Lange et al., 2016; Melbourne-Thomas et al., 2015; Mundy et al., 2007). Here we calculate an NDI for each horizontal ice core section using the following equation:

$$NDI(\lambda_1, \lambda_2) = \frac{T_u(\lambda_1) - T_u(\lambda_2)}{T_u(\lambda_1) + T_u(\lambda_2)} \qquad (6)$$

Where T_u ($\lambda_{1\text{-}2}$) is transmittance at two selected wavelengths λ_1 and λ_2. Optimal NDI wavelength selection was done by calculating NDIs for all possible wavelength combinations, correlated with chl-a values and plotted them onto a Pearson correlation surface (Mundy et al., 2007). Two of the best NDI wavelength combinations were selected based on the following criteria: a good Pearson correlation coefficient (p), a wide separation across bands to avoid autocorrelation, and different areas including chl-a absorption features (e.g., 430-460 nm vs 650-700 nm area).

This was followed by testing two additional integrative spectral indexes targeted to our study area and sensor set-up. The first one is the Area Under Curve ($AUC_{650\text{-}700}$) calculated between 650-700

nm of the localized continuum removed spectrum (Malenovský et al., 2006; Melbourne-Thomas et al., 2015). And the second is the Area under curve Normalised to Constant Band depth ($ANCB_{650-700}$), also followed by localized continuum removal between 650 and 700 nm (Malenovský et al., 2013). The localized continuum removal transformation on the spectrum is fundamental to enhance and standardize the specific absorption features of biochemical constituents (Kokaly and Clark, 1999). It allows for the normalization of the transmittance spectra so that individual absorption features can be compared from a common baseline. Following continuum removal, we can calculate the AUC in the range between 650 and 700 nm with the following equation:

$$AUC_{650-700} = \frac{1}{2}\sum_{j=1}^{n-1}\left(\lambda_{j+1} - \lambda_j\right)\left(\rho_{j+1} + \rho_j\right) \qquad (7)$$

where ρ_j and ρ_{j+1} are values of the continuum-removed transmittance at the j and j+1 bands, λ_j and λ_{j+1} are wavelengths of the j and j+1 bands, and n is the number of the used spectral bands. We can then calculate the $ANCB_{650-700}$ index as:

$$ANCB_{650-700} = \frac{AUC_{650-700}}{CBD_{677}} \qquad (8)$$

Where CBD_{677} is a constant band depth of the continuum-removed reflectance, generally at one of the spectrally stable wavelengths of strong chlorophyll absorption, 677 nm selected in this case. The range 650-700 nm was chosen to include the most sensitive area of chl-a absorption for our study area as seen from the transmittance plots (Figure 5.2a and b).

5.2.7 Regression model development, evaluation and application

Simple linear regression was employed to derive bio-optical relationships between integrated chl-a from the horizontal core section scans and the spectral indices described above. Natural logarithm transformation was applied to chl-a (ln(chl-a [mg m^{-2}])) to deal with the high range of values measured and with the high variance at high chl-a values (heteroscedasticity). This is a common approach in sea-ice bio-optical model development and allows for direct comparison across different studies developing indexes for under-ice biomass mapping (Lange et al., 2016a; Melbourne-Thomas et al., 2015; Wongpan et al., 2018). The constructed log-linear model takes then the following form:

$$\ln(chla) = \alpha + \beta\ (INDEX) \qquad (9)$$

In addition, as suggested in Chennu et al., (2013), we consider the incorporation of logarithmic transformation of an index into the model construction. In this way we can account for exponentially decreasing light intensity being transmitted through a scattering and absorbing medium, such as the bottom of the ice. Thus, we construct a log-log regression model taking the following form:

$$\ln(chla) = \alpha + \beta\ (\ln(INDEX)) \qquad (10)$$

In order to evaluate the performance of each model, we consider the model calibration Root Mean Square Error (RMSE) and coefficient of determination (R^2) for each model. To account for underestimation of the prediction power of the model by the calibration (or training) error, we include adjusted criteria such as the adjusted R^2 and the Akaike Information Criterion (AIC) (James et al., 2013; Zhao et al., 2016).

In addition, we perform a 10-fold cross-validation (CV) to determine how the learning procedure performs on independent data (James et al., 2013; Lange et al., 2016a). The data are subset into 10 different random folds. The fitting of the model and the error calculations are then repeated 10 times, one for each subset. Each time, nine folds (or subsets) of the data are combined to train/fit the model, and then tested to the 10th remaining fold (i.e., holdout data).

Based on the results of the statistical analyses, we select the best performing model and apply it on a per pixel basis to a set of selected preprocessed horizontal ice-core surfaces (process seen in Figure 5.2). The same model was also applied to the preprocessed *in situ* imagery of block B (Figure 5.2). Since the footprint of ice core 37 could be located within the block B under ice image using post-coring ROV imagery, it is utilized as validation point for a rough assessment of prediction accuracy in a completely unseen environment. No model was applied to the vertical core sections as we considered the relationship to be non-applicable due to the diverse optical setting.

5.3 Results

5.3.1 Under-ice habitat and ice core samples

The under-ice habitat was characterized by a spotted pattern of large cavities and brine channel openings ranging in diameter roughly from 7 to 15 cm as seen in Figure 5.3a. This pattern of cavities

was visible up to 200 m from the ice hole in all directions, although there were visible occasional patches that portrayed little to none of these features. No platelet ice was observed during the survey period as previously experienced at this site during other study periods (Lucieer et al., 2016; Wongpan et al., 2018) (Figure 5.3a). Figure 5.3b illustrates the location of the block B image within the transect of the sliding under-ice HI system (Cimoli et al., 2019 or Chapter 4). SfM digital photogrammetry applied to the bottom of the ice cores surfaces successfully produced highly resolved and scaled 3D models of the under-ice bottom topography with unprecedented detail (Figure 5.3c-e). The broad-scale landscape seemingly portrayed the under ice sub-surface as relatively flat (also visible in Cimoli et al., 2019 or Chapter 4), whereas the SfM of the ice cores revealed the fine scale of some of the sea-ice biophysical properties (Figure 5.3c-e). These features included the sea-ice skeletal layer (characteristic of fast-ice), together with sub-cm sized brine channels (Figure 5.3c and 3d). Figure 5.3d illustrates a large-scale brine channel of 2.5 cm in diameter together with complex microscale reliefs associated with algal clumps, and other reliefs perhaps associated with localized refreezing events. Figure 5.3e captures one of the large brine cavity features, which is 12 cm in diameter and with a depth of 9 cm.

Overall, for the 42 horizontal bottom core sections (0 to 3 cm), we observed a mean chl-a of 18.74 mg m^{-2} (± 18.04), with a minimum of 1.1 mg m^{-2} and a maximum of 117.5 mg m^{-2}. The six horizontal middle core sections (3 to 6 cm) yielded a mean chl-a of 0.61 mg m-2 (± 0.4), a minimum of 0.13 mg m^{-2} and a maximum of 1.2 mg m^{-2}. Finally, for the six horizontal top core sections (6 to 9 cm), the mean chl-a was 0.64 mg m^{-2} (± 0.48) with a minimum of 0.14 mg m^{-2} and a maximum of 1.35 mg m^{-2}.

Figure 5.3c-e shows the oblique view of the cores and highlights small-scale differences in biomass density within and across cores. For this study area, these differences seemed to be driven by species composition (e.g., algal strands vs interstitial, see Cimoli et al., (2019) or Chapter 4) and some of the ice physical features such as the presence of the cavity features. Immediately visible is the difference in overall biomass from the large cavity core 30 (3.37 mg m^{-2}) and cores 17 (29.5 mg m^{-2}) and 14 (27.7 mg m^{-2}) in Figure 5.3. The ice algae community at the site was dominated by two diatom species, *Nitzschia stellata*, an interstitial species, and *Berkeleya adeliensis*, which forms short strands into the water column. *Berkelya adeliensis* is associated with dark spots or clumps visible across the oblique images of the ice-core 3D models (Figure 5.3c-d), while *Nitzschia stellata* dominates the interstitial lamellar structure of the ice (also visible in Figure 5.2a-b).

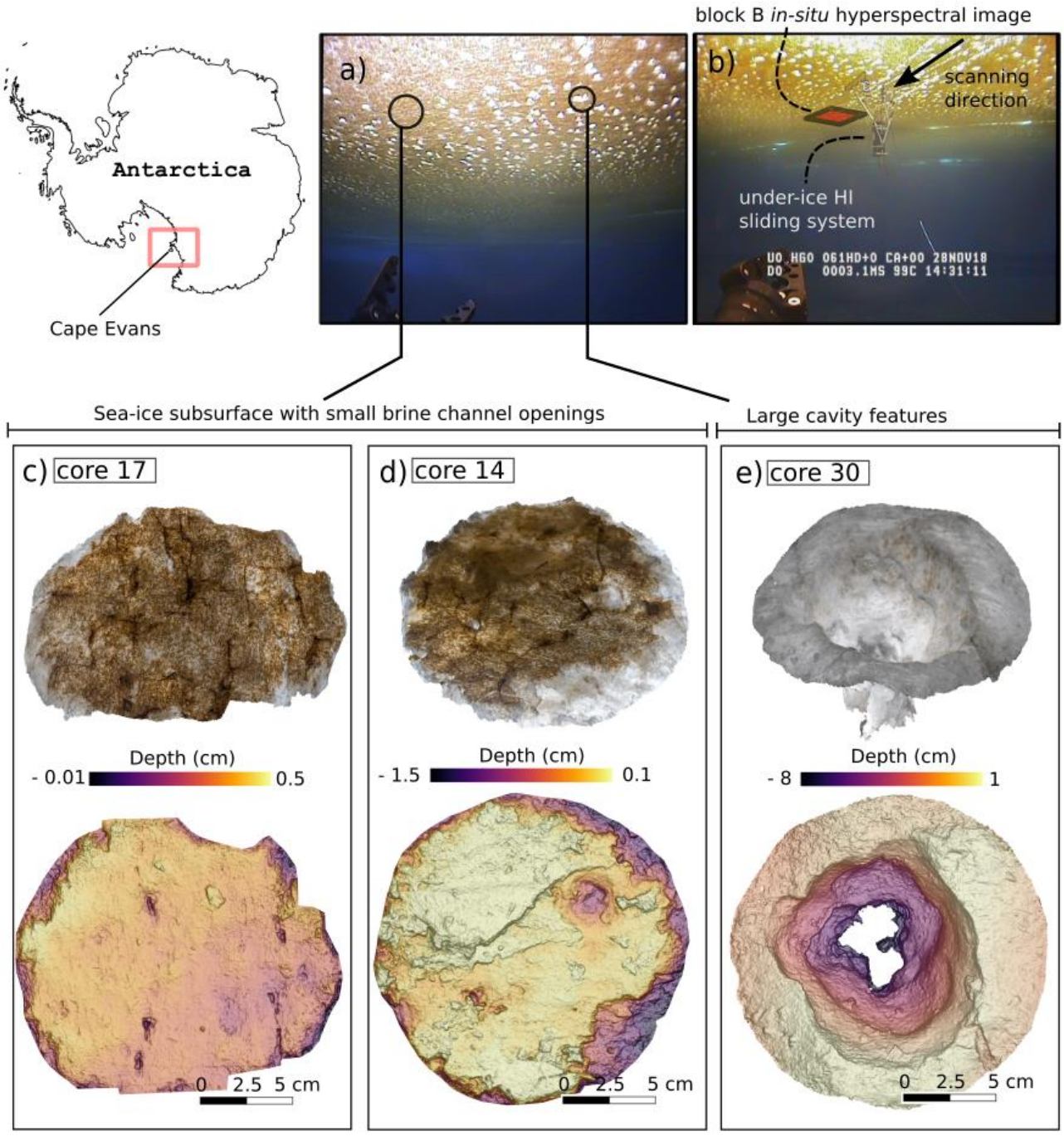

Figure 5.3 a) The distinct under-ice habitat encountered at Cape Evans, Antarctica during Spring 2018, characterized by scattered large cavity features varying widely in diameter and depth. b) Block B under-ice image location and acquisition using the under-ice HI sliding system described in Cimoli et al. (2019) (Chapter 4). c), d) and e) display an oblique view of the bottom-core surface 3D models (top) and the complex micro-spatial variability of the under-ice structural features (below). Skeletal layer characteristics of land-fast sea are visible along with scale of observable brine channels and cavities.

5.3.2 Ice cores image exploration using PCA

The results of the PCA applied to both vertical and horizontal sections of the ice cores are shown in Figure 5.4. PC loadings derived separately from the vertical and horizontal ice cores scans matched almost exactly with differences of <0.001% and were thus combined (Figure 5.4a). PC1 accounted for >99.8 % of variability and loadings clearly represented the shape of the LED spectrum used for image acquisition of the displayed sections (seen in Figure 5.1c). Per-pixel PC1 scores evidently mapped variability in light intensity transmitted through the core, consistent with what has been found in other studies (Cimoli et al., 2017a), and provide a proxy of ice transparency. PC2 loadings explained <0.05% of variability and remarkably resembled the chl-a absorption spectrum with absorption peaks in the 440 and 670 nm areas (Arrigo et al., 2014; Morel and Bricaud, 1981; Wongpan et al., 2018). PCs orthogonality dampened the influence of variability in light intensity, bypassing the need of normalization, and allowed PC2 to portray a good proxy of chl-a over the vertical and horizontal sections of the ice cores (Figure 5.4b). The impact of the core's circular geometry, which induces inhomogeneity in light intensity being transmitted across the core width, is also reduced with this procedure. Additional PCs did not display any differentiable spectral characteristics at this stage and were therefore not investigated further. Figure 5.4 displays PCA results over three example vertical ice-core sections (cores 22, 42 and 30). Core 30 fully comprises one of the peculiar large cavity features and was further explored through its horizontal core scans (bottom, middle and top as per Figure 5.1a).

5.3.3 Regression of spectral indices with chl-a and model selection

The NDI Pearson's correlation surface with chl-a is shown in Figure 5.5a and resembles patterns mapped using traditional L-arm surveys (e.g., Mundy et al., 2007). The selected optimal NDI wavelength combinations based on the described criteria's resulted in NDI (587:621) and NDI (517:449) (Figure 5.5a). The relationships between tested spectral indices and ln(chl-a [mg m^{-2}] are shown in Figure 5.5b-f together with corresponding regression lines and 95 % confidence intervals. Point sample origin (e.g., bottom, middle, top) and the utilized light source (white or solar LED) is also highlighted in the regression plots to assess any eventual influences on the derived bio-optical relationships.

While all indices resulted in significant correlations (R^2 > 0.5), $ANCB_{650\text{-}700}$ and $\log(AUC_{650\text{-}700})$ indices performed considerably better than both NDIs and $AUC_{650\text{-}700}$ for our study case (Figure 5.5). Table 5.1 further summarizes calibration and cross-validation performance of tested spectral indices linearly regressed against measured chl-a values and includes the retrieved model coefficients (α intercept and β slope). Based on both calibration and CV statistics, $\log(AUC_{650\text{-}700})$ functioned best, explaining up to 85% of variation. Log-transformation for the rest of the indices

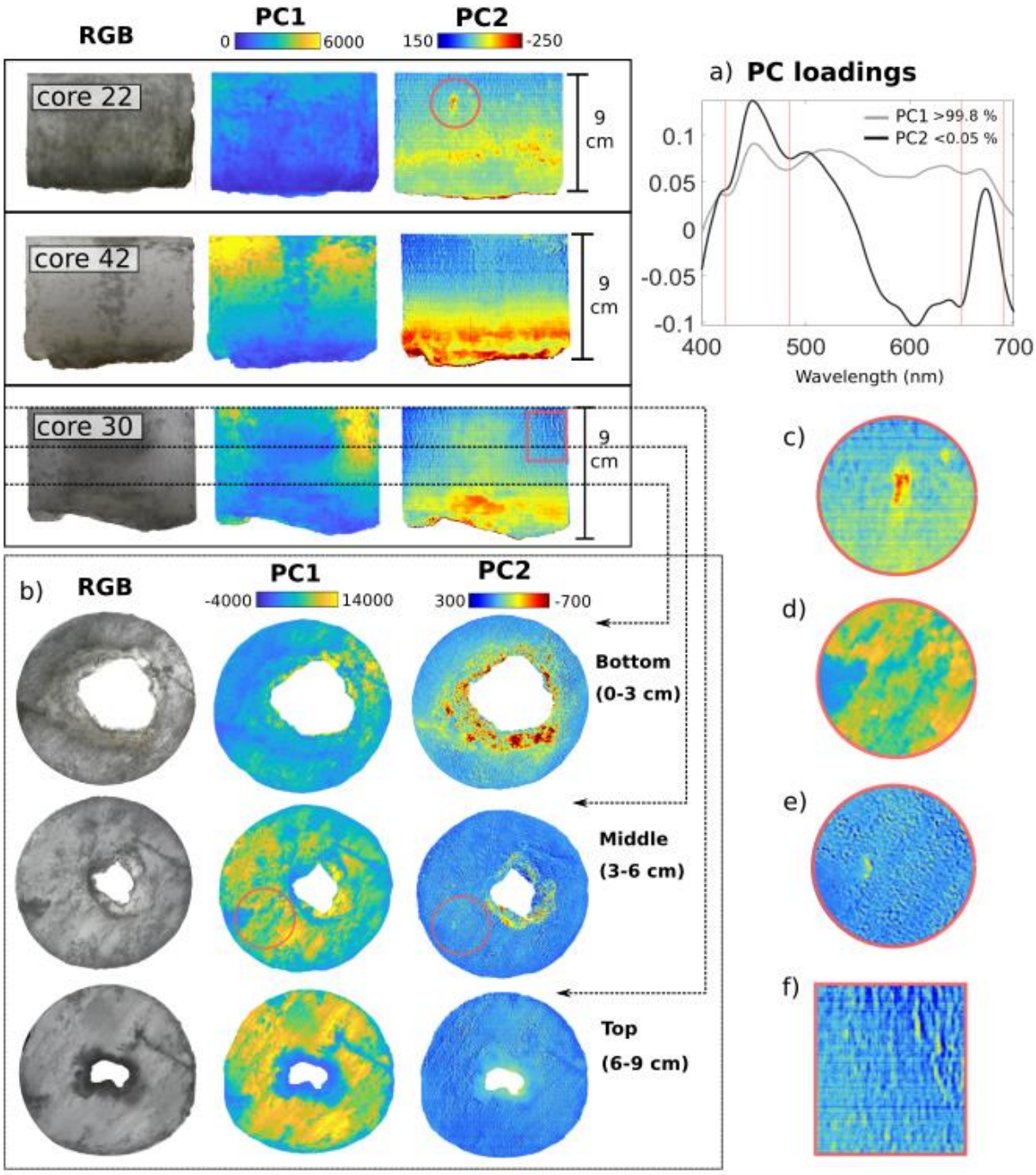

Figure 5.4 Results of Principal Component Analysis (PCA) applied to three selected vertical ice-core scans (cores 22, 42 and 30). a) PCs loadings, PC1 accounts for >99.8 % of variation and loadings embody the spectral signature of the light source. PC1 scores map a proxy of light intensity. PC2 accounts for <0.05 % of variation and loadings are strongly associated with the chl-*a* absorption spectrum. PC2 scores map a proxy of biomass within the ice core vertical and horizontal dimensions. b) Horizontal scans and analysis of core 30 characterized by a large cavity feature (see Figure 5.3).Panels c)-f) illustrate zoomed views of selected features of interest such as brine pockets and channels inhabited by ice algae. PCA was performed separately on vertical and horizontal section data.

(e.g., log(NDI) and log(ANCB)) only contributed to downgrade the relationship performance and the display and analyses of such relationships was therefore omitted. We note that a similar index to the ANCB was previously suggested as a relative proxy of biomass in Cimoli et al., (2019) or Chapter 4, namely the Area under curve Normalised to Maximal Band depth between 650-700 nm ($ANMB_{650-700}$) of the continuum removed spectrum (Malenovský et al., 2006). The only difference was that AUC was normalized by a constant wavelength across all spectrums rather the variable maximal (Yanez-Rausell et al., 2015). The difference between both was insignificant, with ANMB performing slightly worse and was therefore also omitted.

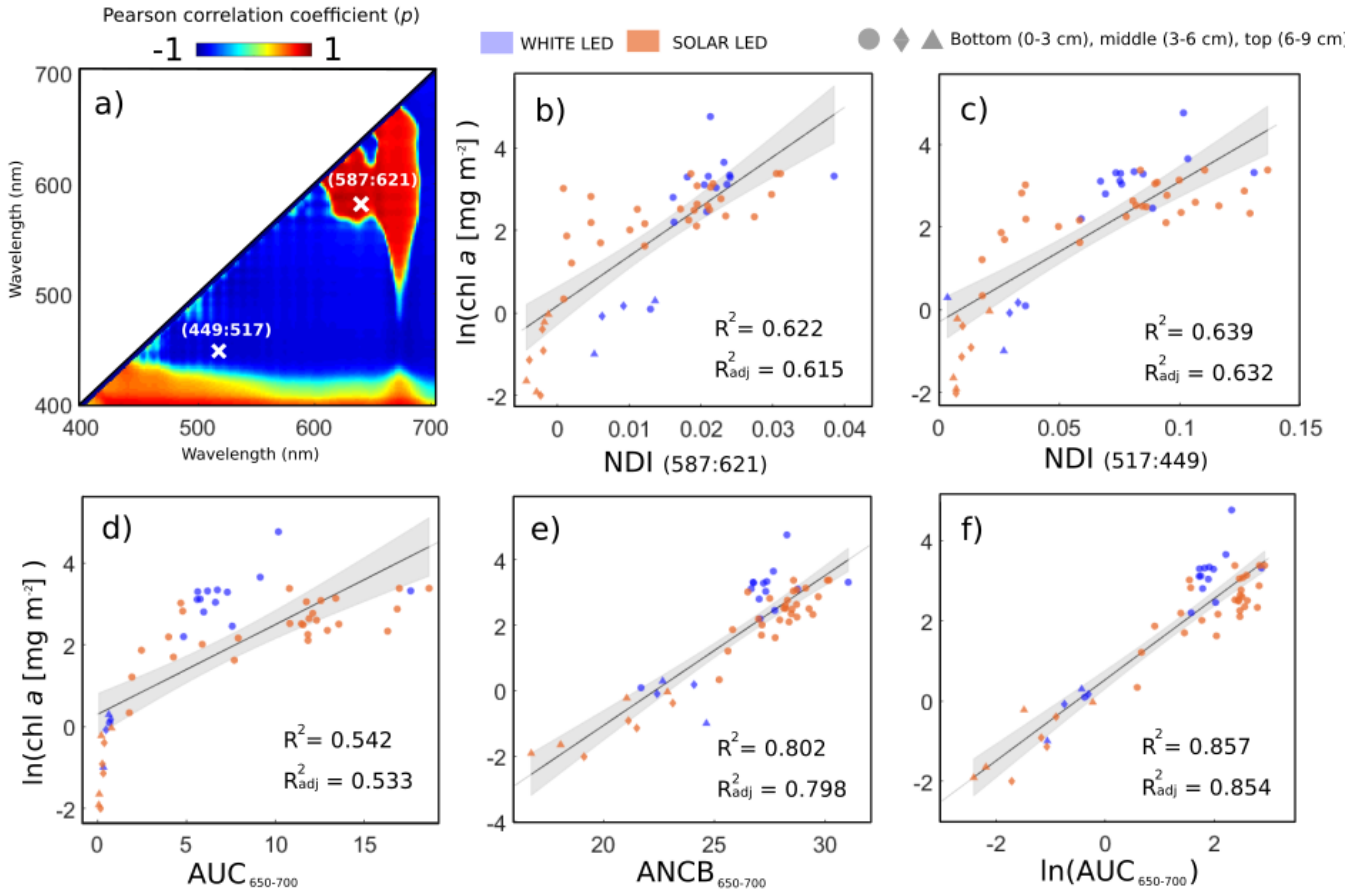

Figure 5.5 Linear regressions between log-transformed fluorometrically-derived chl-*a* values and derived spectral indices using index computation method (1). Panel a) shows the Pearson correlation surface between all NDI waveband combinations and chl-a values displaying the selected optimal wavelengths. a) and b) illustrate NDI(587:621) and NDI(517:449) tested against sampled chl-*a*. d), e) and f) display regression performance of newly developed integrative spectral indices when tested against sampled chl-*a*. All regression plots differentiate samples coming from different light sources (e.g., white versus solar LEDs) and vertical positioning (e.g., bottom, middle, or top). Regressions lines include 95% confidence interval of the coefficients (shadowed grey areas).

5.3.4 Mapping the microspatial variability of chl-a

The predictive linear model built on log($AUC_{650-700}$) was applied to the preprocessed imagery of four selected ice core bottom sections on a per-pixel basis (see workflow in Figure 5.2). Coefficients of the selected model regressed using the log($AUC_{650-700}$) algorithm can be found in Table 5.1.

Results from the algorithm application to the bottom sections of cores 18, 27, 30 and 42 are shown in Figure 5.6 along with their respective RGB composites. Sampled chl-a values of each ice core in both linear and log space are included in the figure for comparison. The average of all pixels within each of the four core samples are consistent with their respective sampled values and differences are <25%.

This approach resulted in a quantitative map showing the variability within single ice core surfaces and the ability to compare results between different samples. Figure 5.6 emphasizes the extent of total biomass variability between cores that were extracted along a 30 m transect and shows how biomass variability patterns can drastically differ across cores.

Results from applying the same model to the preprocessed *in situ* imagery of block B are shown in Figure 5.7. Figure 5.7a provides an idea of the scale of block B and depicts its location within the scanned Western transect that was described previously (Cimoli et al., 2019 or Chapter 4). An ice core footprint overlapping block B was also mapped with RGB imagery taken with a GoPro HERO5 mounted onto the ROV following the under-ice HI surveys (Figure 5.7b). This single validation point is used to compare sampled vs. estimated chl-a in block B (Figure 5.7c). The mean of all pixels within the footprint visible in Figure 5.7c provide a value of 5.3 mg m^{-2} chl-a whereas ice core 37 yielded a value of 7.5 mg m^{-2} (2.2 mg m^{-2} difference) of chl-a. Figure 5.7c exemplifies a quantitative map of chl-a with a spatial resolution of 1.2 mm.

5.4 Discussion

During the period of our study at Cape Evans in 2018 the sea ice was characterized by a distinct under-ice setting featuring particular fine-scale biological and topographical pattern of brine channel openings. It was outside the scope of this study to explain the complex biophysical interactions driving these patterns, as the main aim was to highlight the capabilities of new methodologies to capture both physical and biological properties of this ice habitat. The wide range of topographical features (e.g., brine channel openings and large cavities) found in this area, together with two different types of algae patchily distributed over the under-ice surface made for an interesting first case study to showcase the potential of this methodology.

PCA is commonly employed in hyperspectral image processing to detect features of interest or for reducing the dimensionality of an image data set. Here, PCA provided a straight-forward approach

to retrieve proxies of chl-a distribution in vertical and horizontal ice core sections (as PC2 maps) without the need of any complementary pigment data.

Table 5.1 Results of analyses by the linear regressions models for estimating chl-a in sea ice based on traditional and newly adapted spectral indices for ice algal biomass mapping. α and β refer to the regression model intercept and slope respectively. R^2 refers to the coefficient of determination. RMSE refers to Root Mean Square Error.

Spectral index	α	β	Calibration				Cross-validation (CV)	
			R^2	RMSE	R^2_{adj}	AIC	MSE_{cv}	$RMSE_{cv}$
NDI (587:621)	0.181	120.294	0.622	1.013	0.615	156.646	1.071	1.035
NDI (517:449)	-0.294	34.053	0.639	0.990	0.632	154.162	1.064	1.031
$AUC_{650-700}$	0.301	0.219	0.542	1.115	0.533	167.054	1.291	1.136
$ANCB_{650-700}$	-10.21	0.457	0.802	0.733	0.798	121.709	0.552	0.742
log ($AUC_{650-700}$)	0.537	1.01	0.857	0.623	0.854	104.224	0.394	0.628

PCA results from the vertical core scans (Figure 5.4) showed that PC1 provided a finely resolved proxy of the ice core transparency, which is likely associated to its textural classification and brine volume (e.g. fluid content) but also in part to the amount of biomass (with also influences overall transmitted light intensity). For example, as we approach the very bottom of the core (at the ice water interface) the skeletal layer separates into individual ice lamellae and as a result the ice is more porous and coarser. The permeability of the skeletal layer results in considerable brine loss following retrieval of the ice core from the water. As the brine leaves the permeable layer, the difference between the ice-air refractive indices increases compared to ice-brine/seawater one, thus an increase in scattering occurs, resulting in less light being transmitted. The horizontal PC1 perspective in Figure 5.4b and d shows how light transmission seems to decrease (from yellow to blue) as we move down to the bottom of the core (from 9 to 0 cm) consistent with a decrease in lamellar texture and as the skeletal layer establishes.

PC2 score plots of the vertical core scans allowed us for the first time to visualize snapshots of fine-scale vertical distribution of ice algal biomass (Figure 5.4). As expected, highest densities were observed in a very thin biofilm at the bottom edge of the skeletal layer. However, different microscale patterns can be observed further up into the 9 cm vertical sections; particularly within the first 0-3 cm of more permeable ice of the skeletal layer. PC2 maps for the large cavity core (ice core 30 in Figure 5.4) displayed a higher biomass through the center width and within the cavity, relative to the rest of the core. Looking at core 30 horizontal sections in Figure 5.4b, a decreasing biomass trend is then observable as the cavity narrows. This can possibly be attributed to the extra habitable ice surface that is exposed to the nutrient rich seawater. Nonetheless, the sampled biomass of core 30 was on the lower-end of the biomass scale, compared to the rest of bottom cores samples, which maybe a result of localized brine flushing and raises interesting questions about possible cavity-biomass interactions.

PC2 loadings of both vertical and horizontal ice core scans further illustrated the widespread occurrence of brine pockets, channel openings and other brine-channel related structures (zoomed

for detail Figure 5.4c, e and f). Ice algae are known to thrive within these complex permeable networks (Arrigo, 2017, 2014) and their presence is highly correlated with sea-ice porosity and habitable pore space (e.g., Krembs et al., 2000; Li et al., 2016). Although no complimentary physical data are available for this study for validation, PC2 was able to illustrate these physical features and the associated ice algal biomass associated with them.

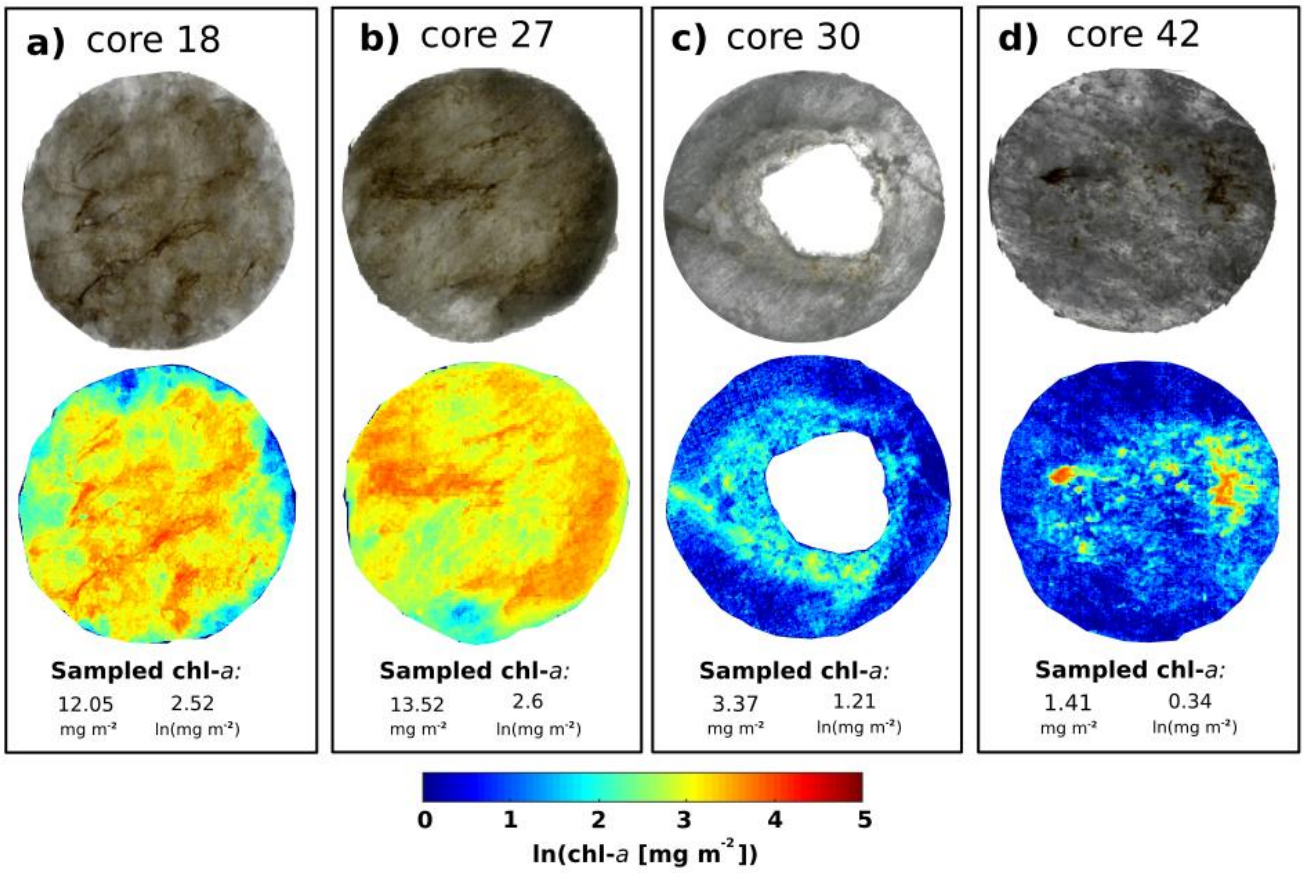

Figure 5.6 Panels a-d) display the RGB composite of selected bottom-core sections (top) and the application of the best performing regression model to the respective preprocessed hyperspectral images (below). The best performing linear model was derived using the log($AUC_{650-700}$) index (see Table 1). Sampled fluorometrically-derived chl-a values of each core section are provided to indicate scale of magnitude of biomass to be compared with the mapped ln(chl-a[mg m^{-2}]). High variability in biomass abundance can be observed within the 0.015 m^2 core surfaces as well as across cores.

We did not apply the regression model to the vertical ice-core scan as these were acquired in a set-up that was deemed optically diverse and inhomogeneous in light intensity. There are practical and theoretical trade-offs associated with scanning the entire thickness of the core. However, the potential exists to address these limitations, through adequate image acquisition or targeted preprocessing workflows (e.g., spatially dependent transmittance normalization). Furthermore, while only the 9 cm of the entire core circular thickness were here scanned, the hyperspectral scanning concept is applicable for any desired core length or section morphology (e.g., slabs) with

adequate set-up modifications. Nonetheless, we note that our study area was characterized by a relatively simple composition of organic material, mostly algal derived, and simpler translucent lamellar texture common in fast-ice areas. PCA was therefore able to separate the variability in the light source spectrum from the variability of chl-a. This separation might not be as straightforward in areas of diverse sea-ice biogeochemical compositions (e.g., high detritus and CDOM concentrations) or for highly scattering and more granular sea-ice core sections, but for the fast ice bottom core sections sampled here the method was satisfactory.

Thorough either explorative (PCA), or quantitative approaches (regression models), this method opens up the potential for investigating and parameterizing complex vertical bio-physical dynamics. For example, understanding how algae migrate through the ice whilst it is being formed and growing (Kauko et al., 2018; Meiners et al., 2012) and how established bottom ice algae respond to bottom ice ablation. This data, when combined with high resolution spatial and temporal data of temperature and salinity will allow for habitable space to be examined alongside nutrient fluxes, in order to understand how they impact on the vertical variability of algae distribution throughout the sea-ice season (Fritsen et al., 2011; Krembs et al., 2001; Li et al., 2016). In addition, this methodology could be applied to explore how ice algae directly respond to changes in their environment through vertical migration following either self-shading or unfavorable light conditions (Aumack et al., 2014) or how they respond to unfavorable ice temperatures decreasing brine volumes (Lund-Hansen et al., 2014). Capturing such fine scale dynamics using this HI approach is a more efficient and quantitatively accurate method than cutting ice cores using conventional methods, e.g. sawing. It also allows to extend imaging to larger areas compared to PAM fluorescence imaging techniques (e.g., Hawes et al., 2012; Lund-Hansen et al., 2016).

Beyond the capability to qualitatively capture variability in chl-a proxies, the proposed methodology provided an alternative baseline for the retrieval of bio-optical relationships in sea ice. Previous HI studies in sea ice have focused on assessing HI suitability for ice algal habitat mapping, and lacked the availability of relationships applicable to the particular study environment (Cimoli et al., 2019, 2017a or Chapter 4 and 3 respectively). Indeed, bio-optical algorithms capable of mapping biomass in sea ice are usually derived from L-arms techniques (e.g., Melbourne-Thomas et al., 2015). L-arms equipped with radiometers measure relatively wide under-ice footprints of transmitted irradiance (or radiance) followed by the extraction of overlapping core samples to produce series of regression points (e.g., Cimoli et al., 2017c or Chapter 2 ; Lange et al., 2016). In general, derived relationships are limited in their transferability between study sites and between seasons, as differences in sea-ice and snow physical properties can considerably change the optical pathway of measured light along with ice algae photophysiological conditions (e.g., pigments composition and packing). This fundamentally determines the retrieved model coefficients, with considerable effects on the robustness of model to be applied to new datasets (Cimoli et al., 2017c or Chapter 2; Lange et al., 2016a; Melbourne-Thomas et al., 2015). Existing relationships retrieved from different sensors, which integrate radiance over large solid angles and greatly differing in

Signal to Noise Ratios (SNR), are arguably not compatible to the per-pixel radiance signals from fine scale HI pixels (e.g., Forrest et al., 2019).

Here we employed our new ice-core scanning concept to compensate for some of the aforementioned caveats, but also for elaborating relationships that are suitable for HI sensors in an efficient manner.

Using radiometer-equipped L-arms, several studies have produced significant linear relationships between ln(chl-a[mg m^{-2}]) and spectral NDIs as a simple, yet effective, algorithm that yields relatively good correlation performance under various circumstances (e.g., Campbell et al., 2014; Lange et al., 2016; Melbourne-Thomas et al., 2015; Mundy et al., 2007). However, NDIs have not always have struggled to produce meaningful relationships, in particular, previous research within our study area and ice type (high algal biomass fast ice off Cape Evans) have struggled to formulate reliable bio-optical regression models (Forrest et al., 2019; Wongpan et al., 2018). This was attributed mostly to the presence of platelet ice, which during sampling, results in considerable biomass losses but also to the narrow biomass variability range experienced or perhaps sampled as a consequence of sloughing. Another reason could be attributed to the particularly high biomass concentrations found in the area (e.g., Wongpan et al., 2018) whereas high biomass concentrations are known to negatively affect linear relationships through the saturation of various vegetation indices (e.g., Malenovský et al., 2013; Tan et al., 2018; VESCOVO et al., 2012). In response, we further explored the performance of alternative spectral indices that could better suit the encountered sea-ice biophysical conditions at Cape Evans, and that take full advantage of the HI potential (high spectral resolution).

Using our ice core scanning set-up, we found that the two optimal NDIs selected for our study at wavelengths combinations, 587:621 and 517:449, performed relatively well in explaining up to 62% and 63% in biomass variability respectively. Results are not be compared with previous studies in the same area using L-arms, as sea-ice conditions were drastically different (Forrest et al., 2019; Wongpan et al., 2018). This HI scanning method poses an advantage in that what is spectrally measured is then sampled in full, with no biomass loss through the coring and measurement procedure that is caused by brine drainage or platelet slough off. Another advantage is that we are able to precisely contour relevant per-pixel radiance and operate within the exact surface area that is being sampled for chl-a.

Despite being able to produce significant correlations with biomass, both NDIs and $AUC^{650\text{-}700}$ seemed to suffer considerably from index saturation at the medium to high biomass values dataset (> 1 ln[chl-a mg m^{-2}]), as seen Figure 5.5b-c. These values relate mainly y to the bottom cores which dominated most of the dataset samples.

An alternative integrative index, $ANCB_{650\text{-}700}$ was tested in this research and performed very well (Figure 5.5e). The spectral index exploits changes in the transmittance signature shapes produced

within 650-700 nm range. These wavelengths are expected to be related to changes in algal chlorophyll content.

The high chl-a absorption associated with biomass abundance was more pronounced around the 650-700 nm area, compared to the 440-450 nm one, where noise was dominant (Figure 5.2b). This was attributed to the highly concentrated bottom algal layer that following a 1.8 m thick ice cover, reduced light levels considerably to $E_{d,400-700\ nm}$ = 0.35 ± 0.20 (λ, W m^{-2}), particularly in the 400 to 500 nm visible range of the spectrum (Figure 5.2b). It is believed that the performance of the ANCB$_{650\text{-}700}$ benefitted from the lack of snow cover (or its minimal presence). Snow is a strong absorber following the 600 nm mark (e.g., Perovich, 2007) and its presence is expected to have a negative influence on the retrieval of relationships for the 650-700 range of the spectrum. In fact, a limitation of the ANCB index seems to be the ability to retrieve chlorophylls below a certain threshold as the spectral influence of background features predominates (Malenovský et al., 2013).

Log-transformation of the integrative index log(AUC$_{650\text{-}700}$) outperformed ANCB and responded even better for biomass saturation by accounting for the exponential decrease in light being transmitted through the core sections as suggested by (Chennu et al., 2013) (Figure 5.5f). It also produced a more evenly distributed spread of the data points.

Bottom chl-a concentrations in sea ice can range widely in both Arctic and Antarctic sea-ice (Arrigo, 2017). Integrated values reported for Antarctic fast-ice range between <0.1 up to 219 mg m^{-2} (Meiners et al., 2018). Considering the strong variability in biomass observed within single core surfaces (Figure 5.6) and *in situ* (Figure 5.7), sampling and averaging over smaller areas would help to increase the range of chl-a values available to produce regression models. This variability is suppressed if averaged through the entire ice 14 cm-diameter core surface. By including the horizontal core sections, sampled from 3 to 9 cm up in the ice core we were able to quantify ice algal biomass over a wider range of concentrations that fall within the range of patchiness visible from the under-ice perspective (e.g., areas surrounding large cavities) (Figure 5.3). Nonetheless, sampling chl-a over smaller surface areas that are referenceable in the HI products should be further pursued to support this aspect (e.g., reducing ice core diameters, or sub sectioning of horizontal cores slices).

It was also found that the use of different artificial light sources with different spectra and intensities (Figure 5.1b and 1c), did not affect the retrieval of coherent correlations following normalization to transmittance. This indicates that it is possible to derive relationships by pooling data together from analogous scanning set-ups. Simple linear regressions based on spectral indices as the ones developed here are highly interpretable and perform well. However, as sea ice science continues to create ever-growing datasets, integrating samples from multiple seasons and areas will help to increase the value of this method. Only in time will we truly profit from the high dimensionality of hyperspectral data through the implementation of new statistical learning models that will increase the robustness of this method to understand the range of sea-ice biophysical conditions.

The log(AUC) model was applied to the preprocessed imagery and we were able to produce time highly resolved quantitative maps of chl-a (mg m^{-2}) at mm scale resolution; both of extracted core sections and *in situ* under-ice (Figure 5.6 and 7). So far, surveys of ice algal biomass variability have been rather discrete in sampling resolution (e.g., 0.5-2 meters apart). Apart from ice coring surveys, broader footprints derived from different sensor types necessarily integrate in signal variance and therefore in biomass variability; variability which might be important to capture to understand processes that happen at the microspatial scale.

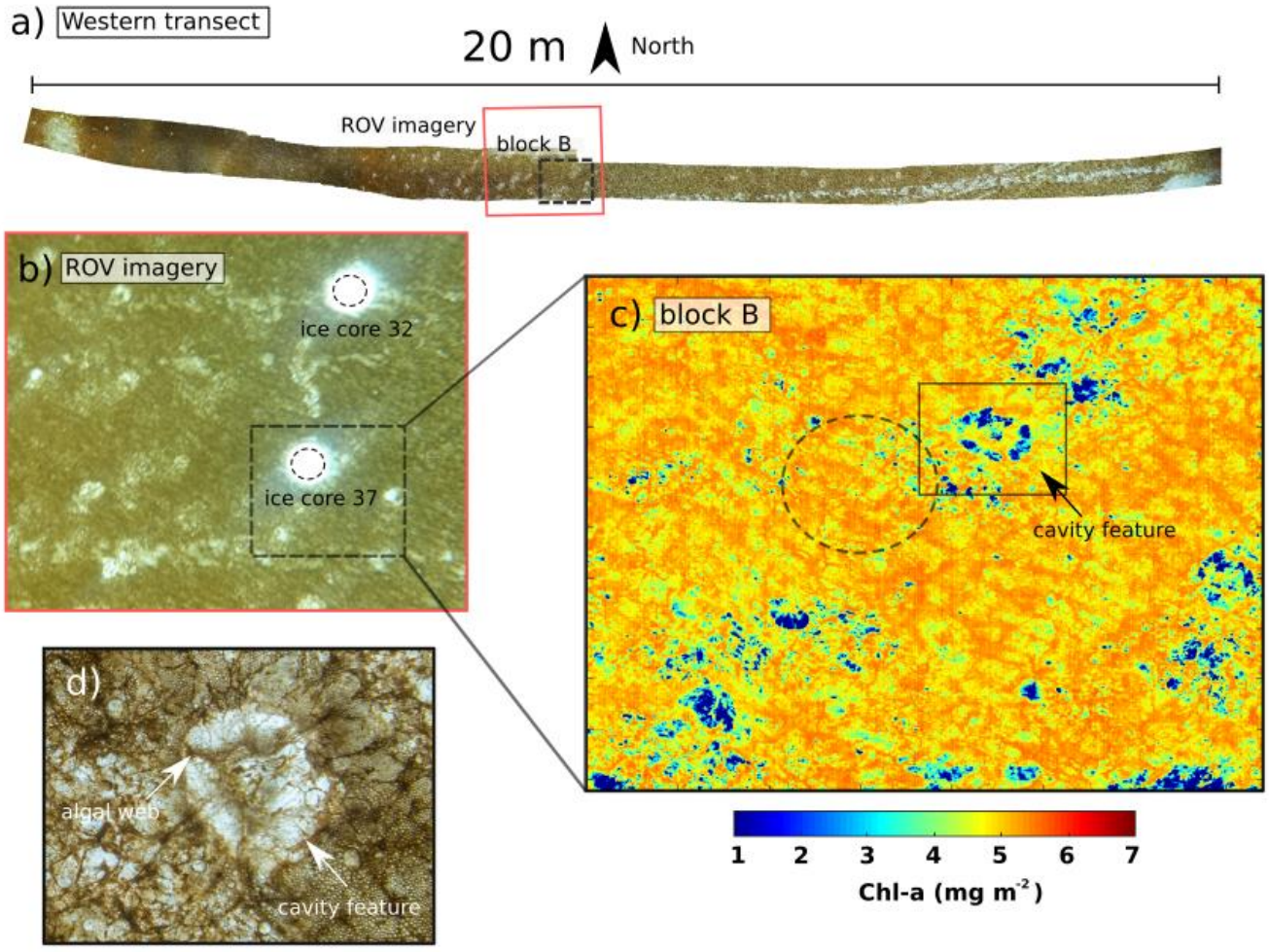

Figure 5.7 Application of best performing regression model to the under-ice imagery. a) Framing of block B hyperspectral image subsample within the entire transect provides an idea of scale. b) Displays a GoPro HERO5 image taken post under-ice hyperspectral image acquisition and ice coring over block B. Panel c) shows the first attempt for quantitative mapping of chl-a by applying the log(AUC) index regression model on a per pixel basis to the preprocessed block B imagery. d) A high-resolution image of one of the large cavity features from block B and comprising an overlapping algal-web like structure. These algal-webs were common features on top of the cavities.

The chosen study site provided remarkable evidence of sea ice algae patchiness at multiple spatial scales, particularly at the microscale. For example, spatial variability within single ice-core surfaces (Figure 5.6) portrayed more heterogenous patterns compared to the <1 m^2 image of block B (Figure 5.7c). At the same time, chl-a variability measured across cores taken less than 30 m apart (for example, cores 18, 27 30 and 42 shown in Figure 5.6), was observed to be capable of varying of one order of magnitude and two orders of magnitude if we consider all cores taken across the entire area (e.g., max observed 117 mg m^{-2}).

Sampled vs predicted single estimates of chl-a on block B image pose an issue for the presented maps. It remains challenging to validate HI products at such fine-scales (mm size pixels) as comparative methodologies are lacking. Common ice coring devices can only sample up to a certain diameter size. PAM fluorescence imaging could offer some ground truthing although it can only provide biomass proxies for considerably smaller frames sizes (30 x 23 mm) and only on extracted cores (Hawes et al., 2012). Therefore, traditional sampling of chl-a over smaller surface areas that are referenceable within the HI products should be pursued to support this challenge. It will also help to increase the range of chl-a values available to produce regression models.

Another aspect that has to be considered in future research, is that the applied relationships are derived by scanning the 3 cm thick layers only, and the remaining ~177 cm of the ice core was omitted from the analyses. This is was suitable approach for our study area as >98% of the biomass was concentrated within the bottom 3 cm of the ice ; a common feature for the fast ice off Cape Evans (McMinn et al., 2012; Ryan et al., 2006). *In situ* imagery were preprocessed accordingly by converting to transmittance through the last bottom centimeters of the ice thickness. This was achieved by normalizing by the transmitted radiance coming from the large cavity openings (Figure 5.2). There are however different sea-ice types with more pronounced variations in vertical biomass variability (Arrigo, 2017; Meiners et al., 2012) and also sea ice that does not exhibit cavity features which were used for normalization in this study. The workflow presented here will therefore require modification for different ice environments. These modifications might include the integration of scans from core sections higher into the ice core, artificially coring cavity-like features, or normalizing irradiances using simple radiative transfer models to account for the unsampled ice (e.g., Arrigo et al., 1991; Forrest et al., 2019; Hamre et al., 2004).

Overall, while there is still considerable methodological research to be done before HI becomes a standard operating procedure for sea-ice algal biomass mapping, we have here shown successfully how the combination of data from of sea-ice cores and *in situ* HI can be used to map and explore this crucial polar habitat. When combined with SfM digital photogrammetry, fine scale biomass mapping can support an improved understanding of the effect of under-ice topography, crystal orientation and roughness on sea ice algae biomass patchiness (Cimoli et al., 2019 or Chapter 4; Krembs et al., 2002, 2000; Lund-Hansen et al., 2016). At medium to large scales, studies have already correlated the effect of water currents coupled with topographical features to induce particular biomass distributions (Dalman et al., 2019; Katlein et al., 2015b; Monti et al., 1996). At the boundary layer,

effects of shear stress from underlying currents and nutrient exchange processes on biomass variability at the microscale remain understudied.

It was observed at our study site how biological properties of a community, such as species composition, can further contribute to the complexity of spatial variability patterns. Different species can conglomerate into biomass clumps held together by extracellular polymeric substances (EPS). These strand communities are then interspersed among the more diffusely distributed interstitial communities, leading to strong small-scale biomass gradients (Figure 5.7c). The role of the large cavities and their interactions with algal communities is yet to be assessed. While they can provide additional surface area for the algae to colonize, these cavities encompass radiance levels that are orders of magnitude higher than the average conditions, with unknown effects on surrounding microorganisms (Cimoli et al., 2019 or Chapter 4). The processes responsible for the formation of these large cavities remain unknown at this stage, as per lack of complementary sea-ice physical data. From the retrieved imagery, algal strands are often visible covering these cavities in web-like formations (Figure 5.7d), thus raising questions on the biophysical interactions taking place on such features. Fine scale sea-ice biophysical dynamics can further complicate the causation effects if we consider that ice algal growth can potentially create a feedback to changes in sea-ice physical properties through heat absorption and melting (Zeebe et al., 1996) or through EPS production affecting ice microstructure (Krembs et al., 2011).

Finally, the influence of grazing from pelagic feeders can also play a role on patchiness and distribution although little is known about their quantitative influence at any scale. Time-lapse approaches coupling under-ice HI and RGB systems (Cimoli et al., 2019 or Chapter 4), integrated with ice core scanning, could further help assessing grazer-biomass interactions at relevant spatial scales.

This method of transmittance HI under sea ice is still in its infancy and there are still considerable technical challenges to be overcome (Cimoli et al., 2019 or Chapter 4). This preliminary study highlights the potential for HI to be mounted onto either Remotely Operated Vehicles (ROVs) or Unmanned Underwater Vehicles (UUVs) to drastically increase the spatial and temporal mapping capability of under-ice environments (e.g., Johnsen et al., 2013; Mogstad et al., 2019; Sture et al., 2017).

Chapter 6

Conclusion and outlook

Capturing the spatio-temporal variability of ice algal biomass concomitantly with its drivers remains crucial to advancing our mechanistic understanding of sea-ice ecosystems. Classical approaches have struggled to quantify patterns of biomass variability non-invasively at most scales of observation; particularly at the microscale (< 0.1 m). The lack of understanding of small-scale processes is detrimental for our extrapolation and predictive capabilities at larger scales. As a consequence, predictions of the future state of the sea-ice ecosystems remains associated with high uncertainties, with flow on implications to assess the future of polar marine food webs and high latitude biogeochemical cycling.

Sea ice is known for its optically complex, yet translucent nature and this prompted the investigation to test the use of Hyperspectral Imaging (HI) technologies in transmittance mode to capture the fine scale variability of some of its biophysical properties. Through the development of an under-ice HI platform, and an ice-core scanner, this thesis paved the way for new ways to capture the microspatial variability of biomass proxies on both *in situ* and on extracted ice cores A workflow was developed to integrate the two approaches which allowed for the retrieval of bio-optical relationships linking spectra to sea ice core chlorophyll-a data. In addition, Structure from Motion (SfM) digital photogrammetry was analogously explored as part of the under-ice HI payload and on ice cores (using macro photography) to retrieve microscale under-ice bottom topographies with minimum additional effort.

HI in transmittance mode applied to an optically complex medium such as sea ice was previously unexplored and involved a thorough assessment through gradual testing stages. This thesis covered the assessment of the methodology starting from pioneering laboratory simulations which informed the first *in situ* data acquisitions.

In Chapter 2 the thesis provides a comprehensive literature review that covered both the motivations for decisions made in developing the methodology and the theoretical background under pinning its development.

The environmental drivers of ice algal biomass spatial variability were reviewed and illustrated in a multi-scale spatial context. These were grouped into six categories; (i) sea ice formation, decay and age, (ii) sea ice structure, temperature, nutrients and salinity, (iii) under-ice topography, (iv) snow, light and surface properties, (v) grazing and (vi) regional characteristics.

Through systematically progressing through each of these studies, treating ice algal biomass spatial variability and its drivers, gaps in the understanding of how such drivers influence patchiness were identified. The review then emphasized the necessity to improve our sampling techniques to bridge some of these gaps. Compared to traditional ice-coring surveys, under-ice close-range remote sensing methods have emerged as a potential game-changing approach for mapping biomass in sea ice concomitantly with some of its drivers. Radiative transfer in sea ice, and the development of bio-optical relationships that link measured spectra with chl-a, stand at the theoretical foundation of these techniques. Therefore, fundamental concepts of these two fields needed to be briefly examined, and previous studies developing chl-a-spectra relationships tabulated and reviewed. The great advantage of this close-range remote sensing technique is that it is non-invasive. This allows for change detection studies of biomass abundance together with other sea-ice properties in the same location, avoiding destructive analyses such as ice coring.

A second advantage of the methodology is that sensors can be installed on Unmanned Underwater Vehicles (UUVs), thus paving the way to sea-ice biomass mapping at unprecedented spatial resolutions over the mesoscale (e.g., Meiners et al., 2017). Prior to this research project, only single point cosine corrected (irradiance), or finite angle (radiance) sensors have been employed to map light transmission through sea ice and to derive biomass (chl-a as best proxy) estimates. In comparison to standard point sampling radiometers, HI was presented in this review as a novel under-ice methodology that could augment capabilities of emerging under-ice bio-optical surveys to capture data in a spatially continuous dimension. This is extremely relevant if we consider the high variability of both ice algal biomass and sea-ice physical properties at multiple spatial scales. HI potential was thoroughly discussed from an under-ice remote sensing perspective. Distinct limitations and challenges arise for passive HI under-ice if compared to more established HI applications in terrestrial remote sensing. Some of these include the low-light availability beneath sea ice, imaging in transmission mode, anisotropic light fields and the general challenges of deploying optical instruments underwater. The trade-offs between typical remote sensing ambitions (e.g., high SNR, spatial and spectral resolutions and spatial coverage) and the particular technical (e.g., sensor specifications and deployment) and environmental constraints of the under-ice environment (e.g., ice and snow conditions and water currents) were assessed and schematized. Indeed, as the developed survey-methodologies are to be conducted in technically limiting and logistically challenging conditions, it was important to assess whether adapting such technologies to polar under-ice environments was feasible in the first place.

In Chapter 3, an experimental set-up consisting of an ‘inverted’ sea-ice simulation tank was presented and utilized to provide a first proof-of-concept of HI for ice algal habitat mapping. These first trials of HI technology captured transmitted light through an algal-colonized artificial sea-ice layer at unprecedented spectral (1.7, 3.4 and 6.8 nm) and spatial resolutions (0.9 mm square pixel size). Decomposition of the hyperspectral data through Principal Component Analysis (PCA) outlined two main components of variability in the images; the first (PC1) representing the intensity of the transmitted light and the second (PC2) representing a proxy of algal biomass across the ice

tank. The optical set-up provided by the sea-ice tank was compared to real *in situ* conditions. Light reaching the artificial ice-water interface was spatially variable (due to an inhomogeneous light field emitted by the light source) and diffuse. Integrated PAR values were compared to *in situ* observations to establish if the inverted sea-ice simulation tank presented an adequate optical set-up for investigating the application of HI cameras for ice-algal studies.

It was concluded that the conditions established generally resembled scenarios found *in situ* where the light field transmitted through the ice is highly diffuse (due to multiple scattering) and where intensity variations reaching the ice-water interface mimic variability in snow or ice thickness. *In situ* ice algal biomass is mostly concentrated at the ice-water interface with algae presenting multiple degrees of 'patchiness'. This was also the case for the simulated ice tank due to the way in which the tank's ice surface was inoculated.

In this preliminary experiment, HI was able to differentiate between low and high biomass abundances and was validated over a discrete scale of six-cylinder units with increasing concentrations. Further observations, such as within-cylinder patchiness and algae leakage from a cylinder observed in the PCA analysis plots, suggested that HI can be used to discriminate algae variability at cm- to mm-scales. Our assessment of three different spectral resolutions indicated that while bandwidths of 1.7 nm and 3.6 nm successfully captured algae biomass spatial variability, bandwidths over 6 nm struggled to yield such differentiation. This suggested that a sensible sensor configuration is important for ice algal habitat mapping.

Following laboratory trials, Chapter 4 introduced a novel modular, low-speed sliding system based on HI and digital photogrammetry for *in situ* under-ice habitat mapping. The particular "inverted" under-ice perspective posed new challenges and limitations to HI technology and these were thoroughly discussed in this technical study. It was demonstrated that the new system was able to map a ~20 m-long transects with geometrically consistent pushbroom hyperspectral imagery, together with overlapping Digital Elevation Models of the under-ice surface, at sub-mm spatial resolution. Despite the low irradiance levels experienced ($E_{d,PAR}$ = 0.35 ± 0.20 (λ, W m^{-2})), the developed HI payload attained suitable per-pixel under-ice signals for employing established bio-optical approaches without the need of active light sources. Minor issues with the sliding system where experienced (e.g., occasional lagging and ski marks) that affected data acquisition along sections of the transect, but these seemed to be mitigated with system modifications and/or data processing techniques. Indeed, future work on this aspect will address the rectification and compilation of the remaining transect data. In particular, considerable potential is foreseen for the investigation of pushbroom image rectification approaches taken advantage of the generated RGB orthomosaics (e.g., co-registration).

Chapter 5 describes a field-deployable sea-ice core hyperspectral scanning set-up. It is based on measuring artificial illumination transmitted through vertical (longitudinal) and horizontal (lateral) sections of the translucent ice cores. Through its integration with data retrieved under-ice, this chapter aimed to conceptualize new workflows to quantitively map biomass microspatial

variability both on cores and *in situ*. Using multidimensional exploration methods (e.g., PCA) on the acquired core imagery, it was shown that this approach can capture vertical and horizontal 'snap-shots' of the microspatial distribution of chl-a proxies (PC2 , explaining <0.05 % variability). Advantageously, this method does not require any complementary pigment data input and shows considerable potential for investigating ice algal vertical dynamics. Coupled with mapping of light transmission proxies (as PC1 scores, explaining > 99.8 % variability), exploration methods further hinted at the possibility to relate principal components with some sea-ice physical properties (e.g., ice texture, porosity and brine channel structure). Nonetheless, without any detailed auxiliary physical data available, physical observations remained speculative.

Following the assessment of targeted image preprocessing workflows, the set-up was further utilized as a benchmark station to test the regression of traditional spectral indices (NDIs) and alternative ones (continuum removed $AUC_{650\text{-}700}$, $ANCB_{650\text{-}700}$ and $\log(AUC_{650\text{-}700})$) against chl-a values measured in melted ice core sections. The performance of the derived bio-optical regression models was statistically assessed and compared. It was found that log(AUC), an integrative spectral index that accounts for the exponentially decreasing light intensity being transmitted through the ice, performed best, explaining up to 85 % of variation in chl-a. The hyperspectral resolution potential to finely integrate over a predefined spectral range seemed to underscore the limitations of simpler normalized difference indices in our results.

The best performing index was then applied to horizontal core scans and *in situ* imagery retrieved using the under-ice system. This constituted the first attempt to yield quantitative estimates of chl-a (mg m^{-2}) on a per-pixel basis. While preliminary observations show agreement between predicted estimates and sampled values, further validation efforts are required to assess the reliability of the approach both on cores and *in situ*. Sampling chl-a over smaller surface areas that are referenceable in the HI products should be pursued to support this aspect, and to increase the range of chl-a values available to produce regression models.

Following normalization of spectra to relative transmittance, the adaptability of the ice core scanning system to merge data from different set-ups was also investigated (e.g., using different light sources). The positive results encourage the adaptation of similar systems to expand datasets derived from different sea-ice areas and seasons. In this way we can work towards the development of statistical learning models that go beyond linearity and increase robustness under diverse sea-ice bio-optical settings.

An aspect worth mentioning is that the fast ice explored in this study is comprised of a relatively simple optical set-up, whereby a highly diffusive light field homogenously illuminated a densely concentrated biofilm located at the ice-water interface (with at least >98% of the biomass occurring within the lowermost 3 cm from the ice bottom). Different vertical gradients in biomass are however possible, with sea-ice algae being able to migrate or grow further up into the first 0.1 m of ice, but can also thrive as interior or surface communities (Meiners et al., 2012). The effects of different vertical biomass gradients embedded into a highly scattering medium will need to be

assessed and is expected to have an impact on discernible spatial resolutions of the biomass proxies captured with HI (as can be expected when imaging an object within a translucent medium). Chl-a estimates retrieved using the under-ice normalization approach explored here might be affected by the vertical distribution of ice algal biomass within the sea ice. In particular, the cavity normalization approach presented in Chapters 4 and 5 consider only the lowermost 3 cm, and it will need to be put into question in future studies where biomass varies considerably over the vertical scale.

6.1 Unravelling under-ice biophysical processes at Cape Evans

Following on from Chapters 4 and 5, the techniques developed in this thesis have the potential to fill a niche gap in the investigation of some of the complex under-ice biophysical interactions and allow the development of intriguing new research questions. Considerable future work remains to be done with the under-ice data acquired during the 2018 campaign. The next steps will be crucial to exemplify the full potential of the developed systems to characterize patterns of biomass variability at unprecedented scales and to gain a better understanding of coupled physical-biological under-ice habitat processes.

The full set of transect data acquired at Cape Evans in 2018 will first be geometrically corrected, rectified and merged into a common coordinate system while exploring new means of co-registering the RGB orthomosaics and HI data along with sensors attitude data (from the custom made IMU and GPS custom integration) in an underwater context. Once transects results are rectified and processed, the best-performing bio-optical regression models will be applied and validated to the full set of corrected transect imagery to yield quantitative maps of ice algal biomass across different scales. Upcoming work in this aspect will aim to increase the sample size of sea-ice core data acquired using the hyperspectral core-scanning approach in order to enhance the performance of biomass-spectra regression models (e.g., using machine learning with algorithms such as regression trees or Support Vector Machines). Focus will be initially given to models that are more suitable to HI sensor data while attaining increased prediction capability for the highly productive fast ice of Cape Evans. Ideally, model predictor variables of the learning models will aim for the inclusion of the highly resolved spectral and spatial information provided by HI or of other sea-ice biophysical variables that define the sea-ice optical properties (e.g., inclusion of sea-ice physical properties such ice thickness and snow depth, or other algal photophysiological proxies).

Means to normalize downwelling radiance data to account for changes induced by different illuminations (e.g., differences in sun angle, light intensity and atmospheric effects) and sea-ice conditions (e.g., thin snow cover against bare ice) along the transect will need to be devised and assessed at this stage.

Transect chl-a maps will allow the quantification of ice algal biomass horizontal spatial variation over previously unexplored spatial scales and will permit application of improved geostatistical

analyses such as variograms (Oliver and Webster, 2014). Secondarily, it would further help to identify and parametrize key environmental drivers of ice algal biomass for the explored study site (e.g., Meiners et al., 2017; Katlein et al., 2015a). 3D relief and HI data fusion techniques could further support a better assessment of environmental controls by employing statistical tools like analysis of variance (Steffens et al., 2006) or spatial autocorrelation (Rysgaard et al., 2001) as historically applied for ice-coring surveys.

The acquired RGB imagery and digital photogrammetry provided ultra-high-resolution DEMs and orthomosaics of the under-ice habitat. RGB imagery presents diverse opportunities to qualitatively and quantitatively map and investigate under-ice features of interest (e.g., under-ice fauna or crystal orientation and texture) along with highly detailed under-ice roughness and relief. For example, coupling under-ice HI with rugosity parameters derived from the under-ice DEMs, as a measure of surface roughness, might improve our understanding of algal aggregation in complex under-ice topographies such as the cavity features observed, analogous to existing coral or benthic mapping studies (e.g., Dustan et al., 2013; Friedman et al., 2012). Standard upward looking RGB cameras as additional payloads not only help to confirm the status of the under-ice physical environment and in assisting data interpretation (Fritsen et al., 2011), but can provide further support to assess grazer presence and dynamics in relation to ice types and conditions (Brown et al., 2017; Melbourne-Thomas et al., 2016).

6.2 Towards payload integration onto UUVs for under-ice mapping

The developed under-ice payload was tested only in fast-ice conditions providing relatively flat and smooth bottom ice surfaces. This allowed the deployment of a simple, yet effective, sliding platform that produced coherent HI mosaics without the need of complicated image correction algorithms or sophisticated underwater positioning equipment. While the relatively flat Antarctic fast ice is highly productive and a crucial feature of Antarctic coastal marine ecosystems, means to deploy our method under different conditions should be further investigated. There is a need to investigate alternative acquisition methods to map the under-ice habitat of rugose ice surfaces and, at greater distances from the ice and at higher speeds in order to increase the spatial extent of the surveys.

The general challenges remain rather technical and are basically associated with the low under-ice light levels that restrict passive optical remote sensing. Low light has cascading impacts on the Signal to Noise Ratio (SNR), pushbroom scanning velocities and sensor stability required to acquire meaningful HI data. It ultimately negatively affects surveying time and areal coverage of any passive optical sensor

In Chapter 4, challenges associated with mounting pushbroom HI payloads onto more dynamic and less precisely controllable platforms were outlined. Despite these challenges, the pathway forward

includes the integration of HI payloads onto UUVs that can stably navigate at pre-defined distances from the ice and the development of autonomous stationary solutions. Autonomous and remote platforms (e.g., ROVs, AUVs, landers, tripods and USVs) designed for optical monitoring of polar marine ecosystems are undergoing continuous technological advances allowing to carry an even wider array of sensors and push exploration boundaries to new surveying targets (e.g., Dumke et al., 2019; Johnsen et al., 2018; Ludvigsen et al., 2013; Mogstad et al., 2020; Mogstad and Johnsen, 2017; Sture et al., 2017).

In particular, the tethered and highly controllable nature of several new Remotely Operated Vehicle (ROV) models makes them among the most preferable options to begin tackling some of the challenges found for under-ice algal habitat mapping with HI. Continuous technological advances in camera sensitivity and optical efficiency, together with an increasing accessibility to efficient underwater marine geo-positioning and attitude tracking technology is expected to help overcome some of these limitations. Unmanned Aerial Systems (UASs) provide an analogy whereby the scientific literature offers a plethora of data processing approaches that can be applied in an under-ice context (Aasen and Bolten, 2018; Turner et al., 2017). Another option to consider is the exploration of upward looking active light sources that homogenously illuminate the HI sensor footprint during image acquisition. Active HI studies of the deep seafloor have benefitted from the utilization of active light sources mounted onto ROVs to acquire meaningful HI data under complete absence of light at depths of approximately 4200 m (Dumke et al., 2018a, 2018b). However, when imaging the seafloor, we are dealing with the processes of absorption and reflection of exclusively downwelling light (either artificial, solar or both), for a semi-opaque medium. The integration of active light sources for under-ice habitat mapping will arguably involve a more complex data processing and interpretation procedure. Upwelling artificial light sources that are spectrally different from the downwelling sunlight, would interact with a transmissive, absorbing and highly scattering and variable medium. Characterizing radiative transfer under such a setting is non-trivial and the retrieval of bio-optical regression models using the proposed core scanning method would be put into question.

In addition, mapping photoactive pigments with strong artificial light sources needs to account for the tradeoff between the amount of light being utilized to boost SNR, against its impacts on algal communities that are typically adapted to low light. Such considerations would need to be evaluated based on the desired study aims and the algal light-adaption history for the specific area and time of the year.

Tests could be performed both *in situ* or on sea-ice simulation tanks and would allow the investigation of these approaches along with key technical parameters of the methodology. For example, HI data quality could be evaluated with and without additional upwelling light sources and under different circumstances from the ones here presented, e.g. by changing imaging heights (thus varying spatial resolutions), light intensity levels and imaging parameter settings (such as movement speed and imaging frequency).

6.3 A science outlook

To take advantage of studies that can be conducted within fully controlled environments, such as within a laboratory ice tank, it would be pertinent to explore capabilities of HI beyond pure biomass variability detection. Indeed, this thesis focused only on using HI data to estimate biomass distribution (with chl-a as proxy), it appears feasible that HI data can resolve more sophisticated biological properties such as pigment assemblages and species composition. Changes in the composition of light absorbing pigments can reflect different sea-ice algal photophysiological conditions (Galindo et al., 2017; Johnsen and Hegseth, 1991).

Mapping the temporal and spatial evolution of ice algae photophysiological conditions along with community composition would be extremely useful for improving the understanding of ice algal primary productivity, phenology and will support biogeochemical modelling to predict future conditions (Arrigo et al., 2014; Leu et al., 2015; Lizotte, 2001).

Techniques for growth rate, photo acclimation and health status with respect to biomass estimations can be explored an adapted from phytoplankton oriented studies and will be crucial for elucidating this aspect in and under-ice remote sensing context (e.g., Babin et al., 2008; Brunet et al., 2011; Johnsen et al., 2011, 2009). Close-range hyperspectral remote sensing in terrestrial plants is a rapidly advancing means to discretely measure and map environmental stress from targeted spectral indices and machine learning approaches (e.g., Behmann et al., 2014; Malenovský et al., 2015). Hyperspectral and multispectral data have also been used to estimate pigment content of these higher order plants from airborne surveys (Blackburn, 2007, 2006), and pigment content of other biochemical targets under laboratory conditions (Ling et al., 2019; Zhao et al., 2016). Similar approaches could be applied to ice algal communities and tested both *in situ*, or by ice-core scanning (both vertically or horizontally). Differentiation of pigment content could be achieved through hyperspectral signal decomposition and analyses aimed to resolve relative amounts of different types of pigments, or through the development of novel spectral indices adapted to the under-ice algal habitat. For marine algae, several studies have already discussed the possibility of discretely distinguishing algae photophysiological conditions from close-range imaging spectroscopy (e.g., Jesus et al., 2008; Perkins et al., 2016).

Research prospects are also envisaged in the optical taxonomy and detection of community compositions from the under-ice signals as analogously done in phytoplankton and vegetation studies (Moisan et al., 2011; Volent et al., 2009; Zhang et al., 2015). For this purpose, different spectral decomposition techniques could be tested a priori through isolated laboratory approaches with known algae species and concentrations (e.g., Mehrubeoglu et al., 2013; Moberg et al., 2002).

An interesting field is also being explored in the retrieval of primary production estimates from spectral data in combination with either in-vitro photosynthetic parameters for ice algae (Lange et al., 2017; Müller et al., 2016) or with PAM fluorometry for microphytobenthic communities

(Méléder et al., 2018). Analogously, indices derived from spectral data could be combined with Eddy Covariance (EC) methods to retrieve carbon fluxes outside the footprint of the EC system, as studied, e.g., in terrestrial environments (Huemmrich et al., 2019; Noumonvi et al., 2019; Zarco-Tejada et al., 2013). EC methods have been developed for marine (Butterworth and Miller, 2016) and under-ice (Else et al., 2015) environments alluding to exciting possibilities to combine both under-ice HI and EC methodologies to estimate ice algal production on larger scales.

Altogether various aspects remain to be investigated prior to method standardization. But as technological barriers are overcome and data processing workflows are being further explored and established, the outcomes of this thesis suggest that HI combined with photogrammetric techniques will offer a methodological turning-point for mapping fine-scale sea-ice biophysical dynamics in retrieved ice cores and *in situ*.

It will be of interest to map and quantify patterns of biomass variability with the developed under-ice payload across different regions, seasons and ice types in order to recognize and parametrize its respective scales of variation and the underlying physical drivers. It will then be of paramount importance to link such patterns with sea-ice physical properties that are retrievable from other aerial remote sensing products, at larger scales, allowing the extrapolation of estimates to regional scales.

References

Aasen, H., Bolten, A., 2018. Multi-temporal high-resolution imaging spectroscopy with hyperspectral 2D imagers – From theory to application. Remote Sensing of Environment 205, 374–389. https://doi.org/10.1016/j.rse.2017.10.043

Aasen, H., Honkavaara, E., Lucieer, A., Zarco-Tejada, P.J., 2018. Quantitative Remote Sensing at Ultra-High Resolution with UAV Spectroscopy: A Review of Sensor Technology, Measurement Procedures, and Data Correction Workflows. Remote Sensing 10, 1091. https://doi.org/10.3390/rs10071091

Adão, T., Hruška, J., Pádua, L., Bessa, J., Peres, E., Morais, R., Sousa, J.J., 2017. Hyperspectral Imaging: A Review on UAV-Based Sensors, Data Processing and Applications for Agriculture and Forestry. Remote Sensing 9, 1110. https://doi.org/10.3390/rs9111110

Agisoft Metashape User Manual - Professional Edition, Version 1.5, n.d. 130.

Åhlén, J., Sundgren, D., Bengtsson, E., 2007. Application of underwater hyperspectral data for color correction purposes. Pattern Recognition and Image Analysis 17, 170–173. https://doi.org/10.1134/S105466180701021X

Ambrose, W.G., Quillfeldt, C. von, Clough, L.M., Tilney, P.V.R., Tucker, T., 2005. The sub-ice algal community in the Chukchi sea: large- and small-scale patterns of abundance based on images from a remotely operated vehicle. Polar Biology 28, 784–795. https://doi.org/10.1007/s00300-005-0002-8

Amigo, J.M., Babamoradi, H., Elcoroaristizabal, S., 2015. Hyperspectral image analysis. A tutorial. Analytica Chimica Acta 896, 34–51. https://doi.org/10.1016/j.aca.2015.09.030

Anderson, K., Gaston, K.J., 2013. Lightweight unmanned aerial vehicles will revolutionize spatial ecology. Frontiers in Ecology and the Environment 11, 138–146. https://doi.org/10.1890/120150

Arndt, S., Meiners, K.M., Ricker, R., Krumpen, T., Katlein, C., Nicolaus, M., 2017. Influence of snow depth and surface flooding on light transmission through Antarctic pack ice. J. Geophys. Res. Oceans n/a-n/a. https://doi.org/10.1002/2016JC012325

Arrigo, K., Dieckmann, G., Gosselin, M., Robinson, D., Fritsen, C., Sullivan, C., 1995. High resolution study of the platelet ice ecosystem in McMurdo Sound, Antarctica:biomass, nutrient, and production profiles within a dense microalgal bloom. Marine Ecology Progress Series 127, 255–268. https://doi.org/10.3354/meps127255

Arrigo, K.R., 2017. Sea ice as a habitat for primary producers, in: Thomas, D.N. (Ed.), Sea Ice. John Wiley & Sons, Ltd, pp. 352–369. https://doi.org/10.1002/9781118778371.ch14

Arrigo, K.R., 2014. Sea Ice Ecosystems. Annual Review of Marine Science 6, 439–467. https://doi.org/10.1146/annurev-marine-010213-135103

Arrigo, K.R., Brown, Z.W., Mills, M.M., 2014. Sea ice algal biomass and physiology in the Amundsen Sea, Antarctica. Elementa: Science of the Anthropocene 2, 000028. https://doi.org/10.12952/journal.elementa.000028

Arrigo, K.R., Mock, T., Lizotte, M.P., 2010. Primary Producers and Sea Ice, in: Thomas, D.N., Dieckmann, G.S. (Eds.), Sea Ice. Wiley-Blackwell, pp. 283–325.

Arrigo, K.R., Perovich, D.K., Pickart, R.S., Brown, Z.W., van Dijken, G.L., Lowry, K.E., Mills, M.M., Palmer, M.A., Balch, W.M., Bahr, F., Bates, N.R., Benitez-Nelson, C., Bowler, B., Brownlee, E.,

Ehn, J.K., Frey, K.E., Garley, R., Laney, S.R., Lubelczyk, L., Mathis, J., Matsuoka, A., Mitchell, B.G., Moore, G.W.K., Ortega-Retuerta, E., Pal, S., Polashenski, C.M., Reynolds, R.A., Schieber, B., Sosik, H.M., Stephens, M., Swift, J.H., 2012. Massive Phytoplankton Blooms Under Arctic Sea Ice. Science 336, 1408–1408. https://doi.org/10.1126/science.1215065

Arrigo, K.R., Sullivan, C.W., Kremer, J.S., 1991. A Bio-optical Model of Antarctic Sea Ice. Journal of Geophysical Research 96.

Arroyo-Mora, J., Kalacska, M., Inamdar, D., Soffer, R., Lucanus, O., Gorman, J., Naprstek, T., Schaaf, E., Ifimov, G., Elmer, K., Leblanc, G., 2019. Implementation of a UAV–Hyperspectral Pushbroom Imager for Ecological Monitoring. Drones 3, 12. https://doi.org/10.3390/drones3010012

Aumack, C.F., Juhl, A.R., Krembs, C., 2014. Diatom vertical migration within land-fast Arctic sea ice. Journal of Marine Systems 9.

Babin, M., Roesler, C.S., Cullen, J.J., 2008. Real-time coastal observing systems for ecosystem dynamics and harmful algal blooms: theory, instrumentation and modelling. UNESCO Publishing, Paris.

Barillé, L., Le Bris, A., Méléder, V., Launeau, P., Robin, M., Louvrou, I., Ribeiro, L., 2017. Photosynthetic epibionts and endobionts of Pacific oyster shells from oyster reefs in rocky versus mudflat shores. PLoS One 12. https://doi.org/10.1371/journal.pone.0185187

Behmann, J., Steinrücken, J., Plümer, L., 2014. Detection of early plant stress responses in hyperspectral images. ISPRS Journal of Photogrammetry and Remote Sensing 93, 98–111. https://doi.org/10.1016/j.isprsjprs.2014.03.016

Bioucas-Dias, J.M., Plaza, A., Camps-Valls, G., Scheunders, P., Nasrabadi, N., Chanussot, J., 2013. Hyperspectral Remote Sensing Data Analysis and Future Challenges. IEEE Geoscience and Remote Sensing Magazine 1, 6–36. https://doi.org/10.1109/MGRS.2013.2244672

Blackburn, G.A., 2007. Wavelet decomposition of hyperspectral data: a novel approach to quantifying pigment concentrations in vegetation. International Journal of Remote Sensing 28, 2831–2855. https://doi.org/10.1080/01431160600928625

Blackburn, G.A., 2006. Hyperspectral remote sensing of plant pigments. Journal of Experimental Botany 58, 855–867. https://doi.org/10.1093/jxb/erl123

Blondeau-Patissier, D., Gower, J.F.R., Dekker, A.G., Phinn, S.R., Brando, V.E., 2014. A review of ocean color remote sensing methods and statistical techniques for the detection, mapping and analysis of phytoplankton blooms in coastal and open oceans. Progress in Oceanography 123, 123–144. https://doi.org/10.1016/j.pocean.2013.12.008

Bluhm, B.A., Swadling, K.M., Gradinger, R., 2017. Sea ice as a habitat for macrograzers, in: Thomas, D.N. (Ed.), Sea Ice. John Wiley & Sons, Ltd, pp. 394–414. https://doi.org/10.1002/9781118778371.ch16

Boetius, A., Albrecht, S., Bakker, K., Bienhold, C., Felden, J., Fernández-Méndez, M., Hendricks, S., Katlein, C., Lalande, C., Krumpen, T., Nicolaus, M., Peeken, I., Rabe, B., Rogacheva, A., Rybakova, E., Somavilla, R., Wenzhöfer, F., RV Polarstern ARK27-3-Shipboard Science Party, 2013. Export of algal biomass from the melting Arctic sea ice. Science 339, 1430–1432. https://doi.org/10.1126/science.1231346

Brown, T.A., Assmy, P., Hop, H., Wold, A., Belt, S.T., 2017. Transfer of ice algae carbon to ice-associated amphipods in the high-Arctic pack ice environment. J Plankton Res 39, 664–674. https://doi.org/10.1093/plankt/fbx030

Brugel, S., Nozais, C., Poulin, M., Tremblay, J., Miller, L.A., Simpson, K.G., Gratton, Y., Demers, S., 2009. Phytoplankton biomass and production in the southeastern Beaufort Sea in autumn 2002 and 2003. Mar Ecol Prog Ser 377, 63–77. https://doi.org/10.3354/meps07808

Brunet, C., Johnsen, G., Lavaud, J., Roy, S., 2011. Pigments and photoacclimation processes, in: Roy, S., Llewellyn, C., Egeland, E.S., Johnsen, G. (Eds.), Phytoplankton Pigments. Cambridge University Press, Cambridge, pp. 445–471. https://doi.org/10.1017/CBO9780511732263.017

Bryson, M., Johnson-Roberson, M., Pizarro, O., Williams, S.B., 2015. True Color Correction of Autonomous Underwater Vehicle Imagery. Journal of Field Robotics n/a-n/a. https://doi.org/10.1002/rob.21638

Bryson, M., Johnson-Roberson, M., Pizarro, O., Williams, S.B., 2012. Colour-Consistent Structure-from-Motion Models using Underwater Imagery., in: Robotics: Science and Systems. Citeseer, pp. 1–8.

Buchhorn, M., Raynolds, M.K., Walker, D.A., 2016. Influence of BRDF on NDVI and biomass estimations of Alaska Arctic tundra. Environ. Res. Lett. 11, 125002. https://doi.org/10.1088/1748-9326/11/12/125002

Butterworth, B.J., Miller, S.D., 2016. Automated Underway Eddy Covariance System for Air–Sea Momentum, Heat, and CO2 Fluxes in the Southern Ocean. J. Atmos. Oceanic Technol. 33, 635–652. https://doi.org/10.1175/JTECH-D-15-0156.1

Butz, C., Grosjean, M., Fischer, D., Wunderle, S., Tylmann, W., Rein, B., 2015. Hyperspectral imaging spectroscopy: a promising method for the biogeochemical analysis of lake sediments. J. Appl. Remote Sens 9, 096031. https://doi.org/10.1117/1.JRS.9.096031

Campbell, K., Mundy, C.J., Barber, D.G., Gosselin, M., 2015. Characterizing the sea ice algae chlorophyll a–snow depth relationship over Arctic spring melt using transmitted irradiance. Journal of Marine Systems 147, 76–84. https://doi.org/10.1016/j.jmarsys.2014.01.008

Campbell, K., Mundy, C.J., Barber, D.G., Gosselin, M., 2014. Remote Estimates of Ice Algae Biomass and Their Response to Environmental Conditions during Spring Melt. ARCTIC 67, 375. https://doi.org/10.14430/arctic4409

Caras, T., Karnieli, A., 2015. Ground-Level Classification of a Coral Reef Using a Hyperspectral Camera. Remote Sensing 7, 7521–7544. https://doi.org/10.3390/rs70607521

Castellani, G., Losch, M., Lange, B.A., Flores, H., 2017. Modeling Arctic sea-ice algae: Physical drivers of spatial distribution and algae phenology. Journal of Geophysical Research: Oceans 122, 7466–7487. https://doi.org/10.1002/2017JC012828

Cazenave, F., Zook, R., Carroll, D., Flagg, M., Kim, S., 2011. DEVELOPMENT OF THE ROV SCINI AND DEPLOYMENT IN MCMURDO SOUND, ANTARCTICA 20.

Chang, C.-I., Chang, C.-I., 2013. Hyperspectral data processing: algorithm design and analysis. Wiley-Interscience, Hoboken, NJ.

Chave, J., 2013. The problem of pattern and scale in ecology: what have we learned in 20 years? Ecology Letters 16, 4–16. https://doi.org/10.1111/ele.12048

Chennu, A., Färber, P., De'ath, G., de Beer, D., Fabricius, K.E., 2017. A diver-operated hyperspectral imaging and topographic surveying system for automated mapping of benthic habitats. Scientific Reports 7. https://doi.org/10.1038/s41598-017-07337-y

Chennu, A., Färber, P., Volkenborn, N., Al-Najjar, M.A.A., Janssen, F., de Beer, D., Polerecky, L., 2013. Hyperspectral imaging of the microscale distribution and dynamics of microphytobenthos in intertidal sediments: Hyperspectral imaging of MPB biofilms. Limnology and Oceanography: Methods 11, 511–528. https://doi.org/10.4319/lom.2013.11.511

Chennu, A., Grinham, A., Polerecky, L., de Beer, D., Al-Najjar, M.A.A., 2015. Rapid Reactivation of Cyanobacterial Photosynthesis and Migration upon Rehydration of Desiccated Marine Microbial Mats. Front. Microbiol. 6. https://doi.org/10.3389/fmicb.2015.01472

Cimoli, E., Lucieer, A., Meiners, K.M., Lund-Hansen, L.C., Kennedy, F., Martin, A., McMinn, A., Lucieer, V., 2017a. Towards improved estimates of sea-ice algal biomass: experimental assessment of hyperspectral imaging cameras for under-ice studies. Annals of Glaciology 1–10. https://doi.org/10.1017/aog.2017.6

Cimoli, E., Marcer, M., Vandecrux, B., Bøggild, C.E., Williams, G., Simonsen, S.B., 2017b. Application of Low-Cost UASs and Digital Photogrammetry for High-Resolution Snow Depth Mapping in the Arctic. Remote Sensing 9, 1144. https://doi.org/10.3390/rs9111144

Cimoli, E., Meiners, K., Lucieer, A., Lucieer, V., in review. An under-ice hyperspectral and RGB imaging system to capture fine-scale biophysical properties of sea ice. Cold Regions Science and Technology.

Cimoli, E., Meiners, K.M., Lucieer, A., Lucieer, V., 2019. An Under-Ice Hyperspectral and RGB Imaging System to Capture Fine-Scale Biophysical Properties of Sea Ice. Remote Sensing 11, 2860. https://doi.org/10.3390/rs11232860

Cimoli, E., Meiners, K.M., Lund-Hansen, L.C., Lucieer, V., 2017c. Spatial variability in sea-ice algal biomass: an under-ice remote sensing perspective. Adv. Polar Sci. 268–296. https://doi.org/10.13679/j.advps.2017.4.00268

Cox, G.F.N., Weeks, W.F., 1983. Equations for determining the gas and brine volumes in sea ice samples. Journal of Glaciology 29, 306–316.

Craig, S.E., Jones, C.T., Li, W.K.W., Lazin, G., Horne, E., Caverhill, C., Cullen, J.J., 2012. Deriving optical metrics of coastal phytoplankton biomass from ocean colour. Remote Sensing of Environment 119, 72–83. https://doi.org/10.1016/j.rse.2011.12.007

Dalman, L.A., Else, B.G.T., Barber, D., Carmack, E., Williams, W.J., Campbell, K., Duke, P.J., Kirillov, S., Mundy, C.J., 2019. Enhanced bottom-ice algal biomass across a tidal strait in the Kitikmeot Sea of the Canadian Arctic. Elem Sci Anth 7, 22. https://doi.org/10.1525/elementa.361

Dumke, I., Ludvigsen, M., Ellefmo, S.L., Soreide, F., Johnsen, G., Murton, B.J., 2019. Underwater Hyperspectral Imaging Using a Stationary Platform in the Trans-Atlantic Geotraverse Hydrothermal Field. IEEE Trans. Geosci. Remote Sensing 57, 2947–2962. https://doi.org/10.1109/TGRS.2018.2878923

Dumke, I., Nornes, S.M., Purser, A., Marcon, Y., Ludvigsen, M., Ellefmo, S.L., Johnsen, G., Søreide, F., 2018a. First hyperspectral imaging survey of the deep seafloor: High-resolution mapping of manganese nodules. Remote Sensing of Environment 209, 19–30. https://doi.org/10.1016/j.rse.2018.02.024

Dumke, I., Purser, A., Marcon, Y., Nornes, S.M., Johnsen, G., Ludvigsen, M., Søreide, F., 2018b. Underwater hyperspectral imaging as an in situ taxonomic tool for deep-sea megafauna. Scientific Reports 8, 12860. https://doi.org/10.1038/s41598-018-31261-4

Dustan, P., Doherty, O., Pardede, S., 2013. Digital Reef Rugosity Estimates Coral Reef Habitat Complexity. PLOS ONE 8, e57386. https://doi.org/10.1371/journal.pone.0057386

Edelman, G.J., Gaston, E., van Leeuwen, T.G., Cullen, P.J., Aalders, M.C.G., 2012. Hyperspectral imaging for non-contact analysis of forensic traces. Forensic Science International 223, 28–39. https://doi.org/10.1016/j.forsciint.2012.09.012

Ehn, J.K., Mundy, C.J., 2013. Assessment of light absorption within highly scattering bottom sea ice from under-ice light measurements: Implications for Arctic ice algae primary production. Limnology and Oceanography 58, 893–902.

Eicken, H., Lange, M.A., Dieckmann, G.S., 1991. Spatial variability of sea-ice properties in the northwestern Weddell Sea. J. Geophys. Res. 96, 10603–10615. https://doi.org/10.1029/91JC00456

Else, B.G.T., Rysgaard, S., Attard, K., Campbell, K., Crabeck, O., Galley, R.J., Geilfus, N.-X., Lemes, M., Lueck, R., Papakyriakou, T., Wang, F., 2015. Under-ice eddy covariance flux measurements of heat, salt, momentum, and dissolved oxygen in an artificial sea ice pool. Cold Regions Science and Technology 119, 158–169. https://doi.org/10.1016/j.coldregions.2015.06.018

F. Cota, G., Ralph E. H., S., 1991. Ecology of bottom ice algae: II. Dynamics, distributions and productivity Journal of Marine Systems.

Fang, H., Hu, B., Yu, Z., Xu, H., He, C., Li, A., Liu, Y., 2018. Semi-automatic geometric correction of airborne hyperspectral push-broom images using ground control points and linear features. International Journal of Remote Sensing 39, 4115–4129. https://doi.org/10.1080/01431161.2018.1455237

Feng, H., Chen, G., Xiong, L., Liu, Q., Yang, W., 2017. Accurate Digitization of the Chlorophyll Distribution of Individual Rice Leaves Using Hyperspectral Imaging and an Integrated Image Analysis Pipeline. Front Plant Sci 8. https://doi.org/10.3389/fpls.2017.01238

Fernández-Méndez, M., Olsen, L.M., Kauko, H.M., Meyer, A., Rösel, A., Merkouriadi, I., Mundy, C.J., Ehn, J.K., Johansson, A.M., Wagner, P.M., Ervik, Å., Sorrell, B.K., Duarte, P., Wold, A., Hop, H., Assmy, P., 2018. Algal Hot Spots in a Changing Arctic Ocean: Sea-Ice Ridges and the Snow-Ice Interface. Frontiers in Marine Science 5. https://doi.org/10.3389/fmars.2018.00075

Fiala, M., Kuosa, H., Kopczyńska, E.E., Oriol, L., Delille, D., 2006. Spatial and seasonal heterogeneity of sea ice microbial communities in the first-year ice of Terre Adélie area (Antarctica). Aquatic Microbial Ecology 43, 95–106.

Flores, H., Atkinson, A., Kawaguchi, S., Krafft, B., Milinevsky, G., Nicol, S., Reiss, C., Tarling, G., Werner, R., Bravo Rebolledo, E., Cirelli, V., Cuzin-Roudy, J., Fielding, S., van Franeker, J., Groeneveld, J., Haraldsson, M., Lombana, A., Marschoff, E., Meyer, B., Pakhomov, E., Van de Putte, A., Rombolá, E., Schmidt, K., Siegel, V., Teschke, M., Tonkes, H., Toullec, J., Trathan, P., Tremblay, N., Werner, T., 2012. Impact of climate change on Antarctic krill. Marine Ecology Progress Series 458, 1–19. https://doi.org/10.3354/meps09831

Foglini, F., Grande, V., Marchese, F., Bracchi, V.A., Prampolini, M., Angeletti, L., Castellan, G., Chimienti, G., Hansen, I.M., Gudmundsen, M., Meroni, A.N., Mercorella, A., Vertino, A., Badalamenti, F., Corselli, C., Erdal, I., Martorelli, E., Savini, A., Taviani, M., 2019. Application of Hyperspectral Imaging to Underwater Habitat Mapping, Southern Adriatic Sea. Sensors 19, 2261. https://doi.org/10.3390/s19102261

Fonstad, M.A., Dietrich, J.T., Courville, B.C., Jensen, J.L., Carbonneau, P.E., 2013. Topographic structure from motion: a new development in photogrammetric measurement. Earth Surf. Process. Landforms 38, 421–430. https://doi.org/10.1002/esp.3366

Forrest, A.L., Lund-Hansen, L.C., Sorrell, B.K., Bowden-Floyd, I., Lucieer, V., Cossu, R., Lange, B.A., Hawes, I., 2019. Exploring Spatial Heterogeneity of Antarctic Sea Ice Algae Using an Autonomous Underwater Vehicle Mounted Irradiance Sensor. Front. Earth Sci. 7. https://doi.org/10.3389/feart.2019.00169

Fraser, R., Olthof, I., Lantz, T.C., Schmitt, C., 2016. UAV Photogrammetry for Mapping Vegetation in the Low-Arctic. Arctic Science.

Frey, K.E., Perovich, D.K., Light, B., 2011. The spatial distribution of solar radiation under a melting Arctic sea ice cover. Geophysical Research Letters 38, n/a-n/a. https://doi.org/10.1029/2011GL049421

Friedman, A., Pizarro, O., Williams, S.B., Johnson-Roberson, M., 2012. Multi-Scale Measures of Rugosity, Slope and Aspect from Benthic Stereo Image Reconstructions. PLOS ONE 7, e50440. https://doi.org/10.1371/journal.pone.0050440

Fritsen, C.H., Iturriaga, R.H., Sullivan, C.W., 1992. Influence of particulate matter on spectral irradiance fields and energy transfer in the Eastern Arctic Ocean, in: Gilbert, G.D. (Ed.), . pp. 527–541. https://doi.org/10.1117/12.140679

Fritsen, C.H., Wirthlin, E.D., Momberg, D.K., Lewis, M.J., Ackley, S.F., 2011. Bio-optical properties of Antarctic pack ice in the early austral spring. Deep Sea Research Part II: Topical Studies in Oceanography 58, 1052–1061. https://doi.org/10.1016/j.dsr2.2010.10.028

Galindo, V., Gosselin, M., Lavaud, J., Mundy, C., Else, B., Ehn, J., Babin, M., Rysgaard, S., 2017. Pigment composition and photoprotection of Arctic sea ice algae during spring. Marine Ecology Progress Series 585, 49–69. https://doi.org/10.3354/meps12398

Garrison, D.L., Kurt, B., 1991. Surface-layer sea ice assemblages in Antarctic pack ice during the austral spring: environmental conditions, primary production and community structure. Marine Ecology Progress Series 161–172.

Garzonio, R., Di Mauro, B., Cogliati, S., Rossini, M., Panigada, C., Delmonte, B., Maggi, V., Colombo, R., 2018. A novel hyperspectral system for high resolution imaging of ice cores: Application to light-absorbing impurities and ice structure. Cold Regions Science and Technology 155, 47–57. https://doi.org/10.1016/j.coldregions.2018.07.005

Gosselin, M., Legendre, L., Therriault, J.-C., Demers, S., Rochet, M., 1986. Physical control of the horizontal patchiness of sea-ice microalgae. Mar Ecol Prog Ser 29, 289–298.

Gradinger, R., 2009. Sea-ice algae: Major contributors to primary production and algal biomass in the Chukchi and Beaufort Seas during May/June 2002. Deep Sea Research Part II: Topical Studies in Oceanography, The Western Artic Shelf-Basin Interactions (SBI)Project, Vol.2 56, 1201–1212. https://doi.org/10.1016/j.dsr2.2008.10.016

Gradinger, R., Ikävalko, J., 1998. Organism incorporation into newly forming Arctic sea ice in the Greenland Sea. Journal of Plankton Research 20, 871–886.

Granskog, M.A., Kaartokallio, H., Kuosa, H., Thomas, D.N., Ehn, J., Sonninen, E., 2005. Scales of horizontal patchiness in chlorophyll a, chemical and physical properties of landfast sea ice in the Gulf of Finland (Baltic Sea). Polar Biol 28, 276–283. https://doi.org/10.1007/s00300-004-0690-5

Grenfell, T.C., Light, B., Perovich, D.K., 2006. Spectral transmission and implications for the partitioning of shortwave radiation in arctic sea ice. Annals of Glaciology 44, 1–6.

Gutt, J., 1995. The occurrence of sub-ice algal aggregations off northeast Greenland. Polar Biol 15, 247–252. https://doi.org/10.1007/BF00239844

Habib, A., Han, Y., Xiong, W., He, F., Zhang, Z., Crawford, M., 2016. Automated Ortho-Rectification of UAV-Based Hyperspectral Data over an Agricultural Field Using Frame RGB Imagery. Remote Sensing 8, 796. https://doi.org/10.3390/rs8100796

Hamre, B., Winther, J.-G., Gerland, S., Stamnes, J.J., Stamnes, K., 2004. Modeled and measured optical transmittance of snow-covered first-year sea ice in Kongsfjorden, Svalbard. J. Geophys. Res. 109, C10006. https://doi.org/10.1029/2003JC001926

Hancke, K., Lund-Hansen, L.C., Lamare, M.L., Højlund Pedersen, S., King, M.D., Andersen, P., Sorrell, B.K., 2018. Extreme Low Light Requirement for Algae Growth Underneath Sea Ice: A Case Study From Station Nord, NE Greenland. J. Geophys. Res. Oceans n/a-n/a. https://doi.org/10.1002/2017JC013263

Hawes, I., Lund-Hansen, L.C., Sorrell, B.K., Nielsen, M.H., Borzák, R., Buss, I., 2012. Photobiology of sea ice algae during initial spring growth in Kangerlussuaq, West Greenland: insights from imaging variable chlorophyll fluorescence of ice cores. Photosynthesis Research 112, 103–115. https://doi.org/10.1007/s11120-012-9736-7

Hobley, E., Steffens, M., Bauke, S.L., Kögel-Knabner, I., 2018. Hotspots of soil organic carbon storage revealed by laboratory hyperspectral imaging. Scientific Reports 8, 13900. https://doi.org/10.1038/s41598-018-31776-w

Holm-Hansen, O., Riemann, B., 1978. Chlorophyll a Determination: Improvements in Methodology. Oikos 30, 438. https://doi.org/10.2307/3543338

Holzinger, A., Allen, M.C., Deheyn, D.D., 2016. Hyperspectral imaging of snow algae and green algae from aeroterrestrial habitats. Journal of Photochemistry and Photobiology B: Biology 162, 412–420. https://doi.org/10.1016/j.jphotobiol.2016.07.001

Hop, H., Pavlova, O., 2008. Distribution and biomass transport of ice amphipods in drifting sea ice around Svalbard. Deep Sea Research Part II: Topical Studies in Oceanography, Carbon flux and ecosystem feedback in the northern Barents Sea in an era of climate change 55, 2292–2307. https://doi.org/10.1016/j.dsr2.2008.05.023

Horner, R., Ackley, S.F., Dieckmann, G.S., Gulliksen, B., Hoshiai, T., Legendre, L., Melnikov, I.A., Reeburgh, W.S., Spindler, M., Sullivan, C.W., 1992. Ecology of sea ice biota. Polar Biology 12, 417–427.

Huang, H., Liu, L., Ngadi, M., 2014. Recent Developments in Hyperspectral Imaging for Assessment of Food Quality and Safety. Sensors 14, 7248–7276. https://doi.org/10.3390/s140407248

Huemmrich, K.F., Campbell, P., Landis, D., Middleton, E., 2019. Developing a common globally applicable method for optical remote sensing of ecosystem light use efficiency. Remote Sensing of Environment 230, 111190. https://doi.org/10.1016/j.rse.2019.05.009

Irvine-Fynn, T.D.L., Sanz-Ablanedo, E., Rutter, N., Smith, M.W., Chandler, J.H., 2014. Measuring glacier surface roughness using plot-scale, close-range digital photogrammetry. Journal of Glaciology 60, 957–969. https://doi.org/10.3189/2014JoG14J032

James, G., Witten, D., Hastie, T., Tibshirani, R., 2013. An Introduction to Statistical Learning, Springer Texts in Statistics. Springer New York, New York, NY.

Janssens, J., Meiners, K.M., Tison, J.-L., Dieckmann, G., Delille, B., Lannuzel, D., 2016. Incorporation of iron and organic matter into young Antarctic sea ice during its initial growth stages. Elem Sci Anth 4. https://doi.org/10.12952/journal.elementa.000123

Jaud, M., Le Dantec, N., Ammann, J., Grandjean, P., Constantin, D., Akhtman, Y., Barbieux, K., Allemand, P., Delacourt, C., Merminod, B., 2018. Direct Georeferencing of a Pushbroom, Lightweight Hyperspectral System for Mini-UAV Applications. Remote Sensing 10, 204. https://doi.org/10.3390/rs10020204

Jesus, B., Mouget, J.-L., Perkins, R.G., 2008. Detection of Diatom Xanthophyll Cycle Using Spectral Reflectance. Journal of Phycology 44, 1349–1359. https://doi.org/10.1111/j.1529-8817.2008.00583.x

Johnsen, G., Bricaud, A., Nelson, N., Prézelin, B.B., Bidigare, R.R., 2011. In vivo bio-optical properties of phytoplankton pigments, in: Roy, S., Llewellyn, C., Egeland, E.S., Johnsen, G. (Eds.), Phytoplankton Pigments. Cambridge University Press, Cambridge, pp. 496–537. https://doi.org/10.1017/CBO9780511732263.019

Johnsen, G., Hegseth, E.N., 1991. Photoadaptation of sea-ice microalgae in the Barents Sea. Polar Biology 11, 179–184.

Johnsen, G., Norli, M., Moline, M., Robbins, I., von Quillfeldt, C., Sørensen, K., Cottier, F., Berge, J., 2018. The advective origin of an under-ice spring bloom in the Arctic Ocean using multiple observational platforms. Polar Biology. https://doi.org/10.1007/s00300-018-2278-5

Johnsen, G., Sakshaug, E., 2007. Biooptical characteristics of PSII and PSI in 33 species (13 pigment groups) of marine phytoplankton, and the relevance for pulse-amplitude-modulated and

fast-repetition-rate fluorometry [1]. Journal of Phycology 43, 1236–1251. https://doi.org/10.1111/j.1529-8817.2007.00422.x

Johnsen, G., Samset, O., Granskog, L., Sakshaug, E., 1994. In vivo absorption characteristics in 10 classes of bloom-forming phytoplankton: taxonomic characteristics and responses to photoadaptation by means of discriminant and HPLC analysis. Mar. Ecol. Prog. Ser. 105, 149–157. https://doi.org/10.3354/meps105149

Johnsen, G., Volent, Z., Dierssen, H., Pettersen, R., Ardelan, M.V., Søreide, F., Fearns, P., Ludvigsen, M., Moline, M., 2013. Underwater hyperspectral imagery to create biogeochemical maps of seafloor properties, in: Subsea Optics and Imaging. Elsevier, pp. 508–540e.

Johnsen, G., Volent, Z., Sakshaug, E., Sigernes, F., Pettersson, L., 2009. 6. Remote sensing in the Barents Sea. Tapir Academic Press, Trondheim.

Juhl, A.R., Krembs, C., 2010. Effects of snow removal and algal photoacclimation on growth and export of ice algae. Polar Biol 33, 1057–1065. https://doi.org/10.1007/s00300-010-0784-1

Kaartokallio, H., Granskog, M.A., Kuosa, H., Vainio, J., 2017. Ice in subarctic seas, in: Thomas, D.N. (Ed.), Sea Ice. John Wiley & Sons, Ltd, pp. 630–644. https://doi.org/10.1002/9781118778371.ch27

Katlein, C., Arndt, S., Nicolaus, M., Perovich, D.K., Jakuba, M.V., Suman, S., Elliott, S., Whitcomb, L.L., McFarland, C.J., Gerdes, R., Boetius, A., German, C.R., 2015a. Influence of ice thickness and surface properties on light transmission through Arctic sea ice. J. Geophys. Res. Oceans 120, 5932–5944. https://doi.org/10.1002/2015JC010914

Katlein, C., Fernández-Méndez, M., Wenzhöfer, F., Nicolaus, M., 2015b. Distribution of algal aggregates under summer sea ice in the Central Arctic. Polar Biology 38, 719–731. https://doi.org/10.1007/s00300-014-1634-3

Katlein, C., Nicolaus, M., Petrich, C., 2014. The anisotropic scattering coefficient of sea ice. Journal of Geophysical Research: Oceans 119, 842–855. https://doi.org/10.1002/2013JC009502

Katlein, C., Perovich, D.K., Nicolaus, M., 2016. Geometric Effects of an Inhomogeneous Sea Ice Cover on the under Ice Light Field. Frontiers in Earth Science 4, 1–10.

Kattner, G., Thomas, D., Haas, C., Kennedy, H., Dieckmann, G., 2004. Surface ice and gap layers in Antarctic sea ice: highly productive habitats. Marine Ecology Progress Series 277, 1–12. https://doi.org/10.3354/meps277001

Kauko, H.M., Olsen, L.M., Duarte, P., Peeken, I., Granskog, M.A., Johnsen, G., Fernández-Méndez, M., Pavlov, A.K., Mundy, C.J., Assmy, P., 2018. Algal Colonization of Young Arctic Sea Ice in Spring. Front. Mar. Sci. 5. https://doi.org/10.3389/fmars.2018.00199

Kauko, H.M., Taskjelle, T., Assmy, P., Pavlov, A.K., Mundy, C.J., Duarte, P., Fernández-Méndez, M., Olsen, L.M., Hudson, S.R., Johnsen, G., Elliott, A., Wang, F., Granskog, M.A., 2017. Windows in Arctic sea ice: Light transmission and ice algae in a refrozen lead. J. Geophys. Res. Biogeosci. 2016JG003626. https://doi.org/10.1002/2016JG003626

Kirk, J.T.O., 2011. Light and photosynthesis in aquatic ecosystems, 3rd ed. ed. Cambridge University Press, Cambridge, UK ; New York.

Kohlbach, D., Graeve, M., A. Lange, B., David, C., Peeken, I., Flores, H., 2016. The importance of ice algae-produced carbon in the central Arctic Ocean ecosystem: Food web relationships revealed by lipid and stable isotope analyses. Limnol. Oceanogr. 61, 2027–2044. https://doi.org/10.1002/lno.10351

Kohlbach, D., Graeve, M., Lange, B.A., David, C., Schaafsma, F.L., van Franeker, J.A., Vortkamp, M., Brandt, A., Flores, H., 2018. Dependency of Antarctic zooplankton species on ice algae-

produced carbon suggests a sea ice-driven pelagic ecosystem during winter. Glob Chang Biol. https://doi.org/10.1111/gcb.14392

Kohlbach, D., Lange, B.A., Schaafsma, F.L., David, C., Vortkamp, M., Graeve, M., Franeker, V., A, J., Krumpen, T., Flores, H., 2017. Ice Algae-Produced Carbon Is Critical for Overwintering of Antarctic Krill Euphausia superba. Front. Mar. Sci. 4. https://doi.org/10.3389/fmars.2017.00310

Kokaly, R.F., Clark, R.N., 1999. Spectroscopic determination of leaf biochemistry using band-depth analysis of absorption features and stepwise multiple linear regression. Remote Sensing of Environment 67, 21. https://doi.org/10.1016/S0034-4257(98)00084-4

Krembs, C., Eicken, H., Deming, J.W., 2011. Exopolymer alteration of physical properties of sea ice and implications for ice habitability and biogeochemistry in a warmer Arctic. PNAS 108, 3653–3658. https://doi.org/10.1073/pnas.1100701108

Krembs, C., Gradinger, R., Spindler, M., 2000. Implications of brine channel geometry and surface area for the interaction of sympagic organisms in Arctic sea ice. Journal of Experimental Marine Biology and Ecology 243, 55–80. https://doi.org/10.1016/S0022-0981(99)00111-2

Krembs, C., Mock, T., Gradinger, R., 2001. A mesocosm study of physical-biological interactions in artificial sea ice: effects of brine channel surface evolution and brine movement on algal biomass. Polar Biology 24, 356–364. https://doi.org/10.1007/s003000000219

Krembs, C., Tuschling, K., v. Juterzenka, K., 2002. The topography of the ice-water interface – its influence on the colonization of sea ice by algae. Polar Biology 25, 106–117. https://doi.org/10.1007/s003000100318

Lange, B.A., Katlein, C., Castellani, G., Fernández-Méndez, M., Nicolaus, M., Peeken, I., Flores, H., 2017. Characterizing Spatial Variability of Ice Algal Chlorophyll a and Net Primary Production between Sea Ice Habitats Using Horizontal Profiling Platforms. Front. Mar. Sci. 4. https://doi.org/10.3389/fmars.2017.00349

Lange, B.A., Katlein, C., Nicolaus, M., Peeken, I., Flores, H., 2016a. Sea ice algae chlorophyll a concentrations derived from under-ice spectral radiation profiling platforms. J. Geophys. Res. Oceans 121, 8511–8534. https://doi.org/10.1002/2016JC011991

Lange, B.A., Katlein, C., Nicolaus, M., Peeken, I., Flores, H., 2016b. Sea ice algae chlorophyll a concentrations derived from under-ice spectral radiation profiling platforms. J. Geophys. Res. Oceans. https://doi.org/10.1002/2016JC011991

Lange, B.A., Michel, C., Beckers, J.F., Casey, J.A., Flores, H., Hatam, I., Meisterhans, G., Niemi, A., Haas, C., 2015. Comparing Springtime Ice-Algal Chlorophyll a and Physical Properties of Multi-Year and First-Year Sea Ice from the Lincoln Sea. PLOS ONE 10, e0122418. https://doi.org/10.1371/journal.pone.0122418

Langhorne, P.J., Hughes, K.G., Gough, A.J., Smith, I.J., Williams, M.J.M., Robinson, N.J., Stevens, C.L., Rack, W., Price, D., Leonard, G.H., Mahoney, A.R., Haas, C., Haskell, T.G., 2015. Observed platelet ice distributions in Antarctic sea ice: An index for ocean-ice shelf heat flux. Geophys. Res. Lett. 42, 2015GL064508. https://doi.org/10.1002/2015GL064508

Leeuwe, M. van, Tedesco, L., Arrigo, K.R., Assmy, P., Campbell, K., Meiners, K.M., Rintala, J.-M., Selz, V., Thomas, D.N., Stefels, J., 2018. Microalgal community structure and primary production in Arctic and Antarctic sea ice: A synthesis. Elem Sci Anth 6. https://doi.org/10.1525/elementa.267

Legendre, L., Gosselin, M., 1991. In situ spectroradiometric estimation of microalgal biomass in first-year sea ice. Polar Biol 11, 113–115. https://doi.org/10.1007/BF00234273

Letnes, P.A., Hansen, I.M., Aas, L.M.S., Eide, I., Pettersen, R., Tassara, L., Receveur, J., Floch, S. le, Guyomarch, J., Camus, L., Bytingsvik, J., 2019. Underwater hyperspectral classification of deep sea corals exposed to 2-methylnaphthalene. PLOS ONE 14, e0209960. https://doi.org/10.1371/journal.pone.0209960

Leu, E., Mundy, C.J., Assmy, P., Campbell, K., Gabrielsen, T.M., Gosselin, M., Juul-Pedersen, T., Gradinger, R., 2015. Arctic spring awakening – Steering principles behind the phenology of vernal ice algal blooms. Progress in Oceanography, Overarching perspectives of contemporary and future ecosystems in the Arctic Ocean 139, 151–170. https://doi.org/10.1016/j.pocean.2015.07.012

Levin, S.A., 1992. The Problem of Pattern and Scale in Ecology: The Robert H. MacArthur Award Lecture. Ecology 73, 1943–1967. https://doi.org/10.2307/1941447

Li, T., Zhang, B., Cheng, X., Westoby, M.J., Li, Z., Ma, C., Hui, F., Shokr, M., Liu, Y., Chen, Z., Zhai, M., Li, X., 2019. Resolving Fine-Scale Surface Features on Polar Sea Ice: A First Assessment of UAS Photogrammetry Without Ground Control. Remote Sensing 11, 784. https://doi.org/10.3390/rs11070784

Li, Z., Li, R., Wang, Z., Haas, C., Dieckmann, G., 2016. Upper limits for chlorophyll a changes with brine volume in sea ice during the austral spring in the Weddell Sea, Antarctica. Acta Oceanologica Sinica 35, 68–75. https://doi.org/10.1007/s13131-015-0740-6

Light, B., Maykut, G.A., Grenfell, T.C., 2004. A temperature-dependent, structural-optical model of first-year sea ice. J. Geophys. Res. 109, C06013. https://doi.org/10.1029/2003JC002164

Ling, B., Goodin, D.G., Raynor, E.J., Joern, A., 2019. Hyperspectral Analysis of Leaf Pigments and Nutritional Elements in Tallgrass Prairie Vegetation. Front. Plant Sci. 10. https://doi.org/10.3389/fpls.2019.00142

Liu, Z., Li, C., Wang, Y., Huang, W., Ding, X., Zhou, B., Wu, H., Wang, D., Shi, J., 2011. Comparison of Spectral Indices and Principal Component Analysis for Differentiating Lodged Rice Crop from Normal Ones, in: Computer and Computing Technologies in Agriculture V. Springer, pp. 84–92.

Lizotte, M.P., 2001. The contributions of sea ice algae to Antarctic marine primary production. American zoologist 41, 57–73.

Lu, G., Fei, B., 2014. Medical hyperspectral imaging: a review. J Biomed Opt 19. https://doi.org/10.1117/1.JBO.19.1.010901

Lubac, B., Loisel, H., 2007. Variability and classification of remote sensing reflectance spectra in the eastern English Channel and southern North Sea. Remote Sensing of Environment 110, 45–58. https://doi.org/10.1016/j.rse.2007.02.012

Lucieer, A., Malenovský, Z., Veness, T., Wallace, L., 2014. HyperUAS-Imaging Spectroscopy from a Multirotor Unmanned Aircraft System. Journal of Field Robotics 31, 571–590. https://doi.org/10.1002/rob.21508

Lucieer, V., Nau, A., Forrest, A., Hawes, I., 2016. Fine-Scale Sea Ice Structure Characterized Using Underwater Acoustic Methods. Remote Sensing 8, 821. https://doi.org/10.3390/rs8100821

Łuczyński, T., Pfingsthorn, M., Birk, A., 2017. The Pinax-model for accurate and efficient refraction correction of underwater cameras in flat-pane housings. Ocean Engineering 133, 9–22. https://doi.org/10.1016/j.oceaneng.2017.01.029

Ludvigsen, M., Johnsen, G., Lagstad, P.A., Sorensen, A.J., Odegard, O., 2013. Scientific operations combining ROV and AUV in the Trondheim Fjord, in: OCEANS-Bergen, 2013 MTS/IEEE. IEEE, pp. 1–7.

Lund-Hansen, L.C., Hawes, I., Nielsen, M.H., Sorrell, B.K., 2016. Is colonization of sea ice by diatoms facilitated by increased surface roughness in growing ice crystals? Polar Biology. https://doi.org/10.1007/s00300-016-1981-3

Lund-Hansen, L.C., Hawes, I., Sorrell, B.K., Nielsen, M.H., 2014. Removal of snow cover inhibits spring growth of Arctic ice algae through physiological and behavioral effects. Polar Biology 37, 471–481. https://doi.org/10.1007/s00300-013-1444-z

Lund-Hansen, L.C., Juul, T., Eskildsen, T.D., Hawes, I., Sorrell, B., Melvad, C., Hancke, K., 2018. A low-cost remotely operated vehicle (ROV) with an optical positioning system for under-ice measurements and sampling. Cold Regions Science and Technology 151, 148–155. https://doi.org/10.1016/j.coldregions.2018.03.017

Lund-Hansen, L.C., Markager, S., Hancke, K., Stratmann, T., Rysgaard, S., Ramløv, H., Sorrell, B.K., 2015. Effects of sea-ice light attenuation and CDOM absorption in the water below the Eurasian sector of central Arctic Ocean (>88°N). Polar Research 34. https://doi.org/10.3402/polar.v34.23978

Maas, H.-G., 2015. On the Accuracy Potential in Underwater/Multimedia Photogrammetry. Sensors 15, 18140–18152. https://doi.org/10.3390/s150818140

Maestrini, S.Y., Rochet, M., Legendre, L., Demers, S., 1986. Nutrient limitation of the bottom-ice microalgal biomass (southeastern Hudson Bay, Canadian Arctic)1. Limnol. Oceanogr. 31, 969–982. https://doi.org/10.4319/lo.1986.31.5.0969

Mäkynen, J., Saari, H., Holmlund, C., Mannila, R., Antila, T., 2012. Multi- and hyperspectral UAV imaging system for forest and agriculture applications, in: Druy, M.A., Crocombe, R.A. (Eds.), . p. 837409. https://doi.org/10.1117/12.918571

Malenovský, Z., Homolová, L., Zurita-Milla, R., Lukeš, P., Kaplan, V., Hanuš, J., Gastellu-Etchegorry, J.-P., Schaepman, M.E., 2013. Retrieval of spruce leaf chlorophyll content from airborne image data using continuum removal and radiative transfer. Remote Sensing of Environment 131, 85–102. https://doi.org/10.1016/j.rse.2012.12.015

Malenovský, Z., Lucieer, A., King, D.H., Turnbull, J.D., Robinson, S.A., 2017. Unmanned aircraft system advances health mapping of fragile polar vegetation. Methods in Ecology and Evolution 8, 1842–1857. https://doi.org/10.1111/2041-210X.12833

Malenovský, Z., Turnbull, J.D., Lucieer, A., Robinson, S.A., 2015. Antarctic moss stress assessment based on chlorophyll content and leaf density retrieved from imaging spectroscopy data. New Phytologist 208, 608–624. https://doi.org/10.1111/nph.13524

Malenovský, Z., Ufer, C., Lhotáková, Z., Clevers, J.G.P.W., Schaepman, M.E., Albrechtová, J., Cudlín, P., 2006. A NEW HYPERSPECTRAL INDEX FOR CHLOROPHYLL ESTIMATION: AREA UNDER CURVE NORMALISED TO MAXIMAL BAND DEPTH BETWEEN 650-725 NM. EARSeL eProceedings 5, 12.

Marcer, M., Stentoft, P.A., Bjerre, E., Cimoli, E., Bjørk, A., Stenseng, L., Machguth, H., 2017. Three Decades of Volume Change of a Small Greenlandic Glacier Using Ground Penetrating Radar, Structure from Motion, and Aerial Photogrammetry. Arctic, Antarctic, and Alpine Research 49, 411–425. https://doi.org/10.1657/AAAR0016-049

Massom, R.A., Eicken, H., Hass, C., Jeffries, M.O., Drinkwater, M.R., Sturm, M., Worby, A.P., Wu, X., Lytle, V.I., Ushio, S., Morris, K., Reid, P.A., Warren, S.G., Allison, I., 2001. Snow on Antarctic sea ice. Rev. Geophys. 39, 413–445. https://doi.org/10.1029/2000RG000085

Massom, R.A., Stammerjohn, S.E., 2010. Antarctic sea ice change and variability – Physical and ecological implications. Polar Science 4, 149–186. https://doi.org/10.1016/j.polar.2010.05.001

Matthes, L.C., Ehn, J.K., L.-Girard, S., Pogorzelec, N.M., Babin, M., Mundy, C.J., 2019. Average cosine coefficient and spectral distribution of the light field under sea ice: Implications for primary production. Elem Sci Anth 7, 25. https://doi.org/10.1525/elementa.363

Matus-Hernández, M.Á., Hernández-Saavedra, N.Y., Martínez-Rincón, R.O., 2018. Predictive performance of regression models to estimate Chlorophyll-a concentration based on Landsat imagery. PLOS ONE 13, e0205682. https://doi.org/10.1371/journal.pone.0205682

Maykut, G.A., Grenfell, T.C., 1975. The spectral distribution of light beneath first-year sea ice in the Arctic Ocean. Limnol. Oceanogr. 20, 554–563. https://doi.org/10.4319/lo.1975.20.4.0554

McCarthy, J., Benjamin, J., 2014. Multi-image Photogrammetry for Underwater Archaeological Site Recording: An Accessible, Diver-Based Approach. J Mari Arch 9, 95–114. https://doi.org/10.1007/s11457-014-9127-7

McDonald, S., Koulis, T., Ehn, J., Campbell, K., Gosselin, M., Mundy, C.J., 2015. A functional regression model for predicting optical depth and estimating attenuation coefficients in sea-ice covers near Resolute Passage, Canada. Annals of Glaciology 56, 147–154. https://doi.org/10.3189/2015AoG69A004

McMinn, A., Ashworth, C., Bhagooli, R., Martin, A., Salleh, S., Ralph, P., Ryan, K., 2012. Antarctic coastal microalgal primary production and photosynthesis. Mar Biol 159, 2827–2837. https://doi.org/10.1007/s00227-012-2044-0

McMinn, A., Hegseth, E.N., 2007. Sea ice primary productivity in the northern Barents Sea, spring 2004. Polar Biology 30, 289–294. https://doi.org/10.1007/s00300-006-0182-x

McMinn, A., Ryan, K.G., Ralph, P.J., Pankowski, A., 2007. Spring sea ice photosynthesis, primary productivity and biomass distribution in eastern Antarctica, 2002–2004. Marine Biology 151, 985–995. https://doi.org/10.1007/s00227-006-0533-8

Mehrubeoglu, M., Teng, M., Zimba, P., 2013. Resolving Mixed Algal Species in Hyperspectral Images. Sensors 14, 1–21. https://doi.org/10.3390/s140100001

Meier, W.N., 2016. Losing Arctic sea ice: observations of the recent decline and the long-term context, in: Thomas, D.N. (Ed.), Sea Ice. John Wiley & Sons, Ltd, Chichester, UK, pp. 290–303. https://doi.org/10.1002/9781118778371.ch11

Meiners, K.M., Arndt, S., Bestley, S., Krumpen, T., Ricker, R., Milnes, M., Newbery, K., Freier, U., Jarman, S., King, R., Proud, R., Kawaguchi, S., Meyer, B., 2017. Antarctic pack ice algal distribution: Floe-scale spatial variability and predictability from physical parameters. Geophysical Research Letters 44, 7382–7390. https://doi.org/10.1002/2017GL074346

Meiners, K.M., Michel, C., 2017. Dynamics of nutrients, dissolved organic matter and exopolymers in sea ice, in: Thomas, D.N. (Ed.), Sea Ice. John Wiley & Sons, Ltd, pp. 415–432. https://doi.org/10.1002/9781118778371.ch17

Meiners, K.M., Norman, L., Granskog, M.A., Krell, A., Heil, P., Thomas, D.N., 2011. Physico-ecobiogeochemistry of East Antarctic pack ice during the winter-spring transition. Deep Sea Research Part II: Topical Studies in Oceanography, Antarctic Sea Ice Research during the International Polar Year 2007-2009 58, 1172–1181. https://doi.org/10.1016/j.dsr2.2010.10.033

Meiners, K.M., Vancoppenolle, M., Carnat, G., Castellani, G., Delille, B., Delille, D., Dieckmann, G.S., Flores, H., Fripiat, F., Grotti, M., Lange, B.A., Lannuzel, D., Martin, A., McMinn, A., Nomura, D., Peeken, I., Rivaro, P., Ryan, K.G., Stefels, J., Swadling, K.M., Thomas, D.N., Tison, J.-L., van der Merwe, P., van Leeuwe, M.A., Weldrick, C., Yang, E.J., 2018. Chlorophyll- *a* in Antarctic Landfast Sea Ice: A First Synthesis of Historical Ice Core Data. Journal of Geophysical Research: Oceans. https://doi.org/10.1029/2018JC014245

Meiners, K.M., Vancoppenolle, M., Thanassekos, S., Dieckmann, G.S., Thomas, D.N., Tison, J.-L., Arrigo, K.R., Garrison, D.L., McMinn, A., Lannuzel, D., van der Merwe, P., Swadling, K.M., Smith, W.O., Melnikov, I., Raymond, B., 2012. Chlorophyll a in Antarctic sea ice from historical ice core data. Geophysical Research Letters 39, n/a-n/a. https://doi.org/10.1029/2012GL053478

Melbourne-Thomas, J., Corney, S.P., Trebilco, R., Meiners, K.M., Stevens, R.P., Kawaguchi, S., Sumner, M.D., Constable, A.J., 2016. Under ice habitats for Antarctic krill larvae: Could less mean more under climate warming? Geophysical Research Letters 43, 10,322-10,327. https://doi.org/10.1002/2016GL070846

Melbourne-Thomas, J., Meiners, K.M., Mundy, C.J., Schallenberg, C., Tattersall, K.L., Dieckmann, G.S., 2015. Algorithms to estimate Antarctic sea ice algal biomass from under-ice irradiance spectra at regional scales. Marine Ecology Progress Series 536, 107–121.

Méléder, V., Jesus, B., Barnett, A., Barillé, L., Lavaud, J., 2018. Microphytobenthos primary production estimated by hyperspectral reflectance. PLOS ONE 13, e0197093. https://doi.org/10.1371/journal.pone.0197093

Menna, F., Nocerino, E., Fassi, F., Remondino, F., 2016. Geometric and Optic Characterization of a Hemispherical Dome Port for Underwater Photogrammetry. Sensors 16, 48. https://doi.org/10.3390/s16010048

Menna, F., Nocerino, E., Remondino, F., 2017. FLAT VERSUS HEMISPHERICAL DOME PORTS IN UNDERWATERPHOTOGRAMMETRY. Int. Arch. Photogramm. Remote Sens. Spatial Inf. Sci. XLII-2/W3, 481–487. https://doi.org/10.5194/isprs-archives-XLII-2-W3-481-2017

Miller, L.A., Fripiat, F., Else, B.G.T., Bowman, J.S., Brown, K.A., Collins, R.E., Ewert, M., Fransson, A., Gosselin, M., Lannuzel, D., Meiners, K.M., Michel, C., Nishioka, J., Nomura, D., Papadimitriou, S., Russell, L.M., Sørensen, L.L., Thomas, D.N., Tison, J.-L., van Leeuwe, M.A., Vancoppenolle, M., Wolff, E.W., Zhou, J., 2015. Methods for biogeochemical studies of sea ice: The state of the art, caveats, and recommendations. Elementa: Science of the Anthropocene 3, 000038. https://doi.org/10.12952/journal.elementa.000038

Mitchell, J.J., Glenn, N.F., Anderson, M.O., Hruska, R.C., Halford, A., Baun, C., Nydegger, N., 2012. Unmanned aerial vehicle (UAV) hyperspectral remote sensing for dryland vegetation monitoring, in: Hyperspectral Image and Signal Processing: Evolution in Remote Sensing (WHISPERS), 2012 4th Workshop On. IEEE, pp. 1–10.

Moberg, L., Karlberg, B., Sørensen, K., Källqvist, T., 2002. Assessment of phytoplankton class abundance using absorption spectra and chemometrics. Talanta 56, 153–160.

Mogstad, A.A., Johnsen, G., 2017. Spectral characteristics of coralline algae: a multi-instrumental approach, with emphasis on underwater hyperspectral imaging. Applied Optics 56, 9957. https://doi.org/10.1364/AO.56.009957

Mogstad, A.A., Johnsen, G., Ludvigsen, M., 2019. Shallow-Water Habitat Mapping using Underwater Hyperspectral Imaging from an Unmanned Surface Vehicle: A Pilot Study. Remote Sensing 11, 685. https://doi.org/10.3390/rs11060685

Mogstad, A.A., Ødegård, Ø., Nornes, S.M., Ludvigsen, M., Johnsen, G., Sørensen, A.J., Berge, J., 2020. Mapping the Historical Shipwreck Figaro in the High Arctic Using Underwater Sensor-Carrying Robots. Remote Sensing 12, 997. https://doi.org/10.3390/rs12060997

Moisan, J.R., Moisan, T.A.H., Linkswiler, M.A., 2011. An inverse modeling approach to estimating phytoplankton pigment concentrations from phytoplankton absorption spectra. Journal of Geophysical Research 116. https://doi.org/10.1029/2010JC006786

Monti, D., Legendre, L., Therriault, J.C., Demers, S., 1996. Horizontal distribution of sea-ice microalgae: environmental control and spatial processes (southeastern Hudson Bay, Canada). Marine ecology progress series 133, 229–240.

Morel, A., Bricaud, A., 1981. Theoretical results concerning light absorption in a discrete medium, and application to specific absorption of phytoplankton. Deep Sea Research 28A, 1375–1393.

Morel, A., Maritorena, S., 2001. Bio-optical properties of oceanic waters- A reappraisal. Journal of Geophysical research 106, 7163–7180.

Müller, S., Vähätalo, A.V., Uusikivi, J., Majaneva, M., Majaneva, S., Autio, R., Rintala, J.-M., 2016. Primary production calculations for sea ice from bio-optical observations in the Baltic Sea. Elem Sci Anth 4. https://doi.org/10.12952/journal.elementa.000121

Mundy, C., Gosselin, M., Gratton, Y., Brown, K., Galindo, V., Campbell, K., Levasseur, M., Barber, D., Papakyriakou, T., Bélanger, S., 2014. Role of environmental factors on phytoplankton bloom initiation under landfast sea ice in Resolute Passage, Canada. Marine Ecology Progress Series 497, 39–49. https://doi.org/10.3354/meps10587

Mundy, C.J., Barber, D.G., Michel, C., 2005. Variability of snow and ice thermal, physical and optical properties pertinent to sea ice algae biomass during spring. Journal of Marine Systems 58, 107–120. https://doi.org/10.1016/j.jmarsys.2005.07.003

Mundy, C.J., Ehn, J.K., Barber, D.G., Michel, C., 2007. Influence of snow cover and algae on the spectral dependence of transmitted irradiance through Arctic landfast first-year sea ice. Journal of Geophysical Research 112. https://doi.org/10.1029/2006JC003683

Näsi, R., Honkavaara, E., Lyytikäinen-Saarenmaa, P., Blomqvist, M., Litkey, P., Hakala, T., Viljanen, N., Kantola, T., Tanhuanpää, T., Holopainen, M., 2015. Using UAV-Based Photogrammetry and Hyperspectral Imaging for Mapping Bark Beetle Damage at Tree-Level. Remote Sensing 7, 15467–15493. https://doi.org/10.3390/rs71115467

Näsi, R., Viljanen, N., Kaivosoja, J., Alhonoja, K., Hakala, T., Markelin, L., Honkavaara, E., 2018. Estimating Biomass and Nitrogen Amount of Barley and Grass Using UAV and Aircraft Based Spectral and Photogrammetric 3D Features. Remote Sensing 10, 1082. https://doi.org/10.3390/rs10071082

Nicolaus, M., Katlein, C., 2013. Mapping radiation transfer through sea ice using a remotely operated vehicle (ROV). The Cryosphere 7, 763–777. https://doi.org/10.5194/tc-7-763-2013

Nicolaus, M., Petrich, C., Hudson, S.R., Granskog, M.A., 2013. Variability of light transmission through Arctic land-fast sea ice during spring. The Cryosphere 7, 977–986. https://doi.org/10.5194/tc-7-977-2013

Nogami, S., Ohnuki, S., Ohya, Y., 2014. Hyperspectral imaging techniques for the characterization of Haematococcus pluvialis (Chlorophyceae). J. Phycol. 50, 939–947. https://doi.org/10.1111/jpy.12226

Norgren, P., Skjetne, R., 2014. Using Autonomous Underwater Vehicles as Sensor Platforms for Ice-Monitoring. Modeling, Identification and Control: A Norwegian Research Bulletin 35, 263–277. https://doi.org/10.4173/mic.2014.4.4

Norman, L., Thomas, D.N., Stedmon, C.A., Granskog, M.A., Papadimitriou, S., Krapp, R.H., Meiners, K.M., Lannuzel, D., van der Merwe, P., Dieckmann, G.S., 2011. The characteristics of dissolved organic matter (DOM) and chromophoric dissolved organic matter (CDOM) in Antarctic sea ice. Deep Sea Research Part II: Topical Studies in Oceanography 58, 1075–1091.

Noumonvi, K.D., Ferlan, M., Eler, K., Alberti, G., Peressotti, A., Cerasoli, S., 2019. Estimation of Carbon Fluxes from Eddy Covariance Data and Satellite-Derived Vegetation Indices in a Karst

Grassland (Podgorski Kras, Slovenia). Remote Sensing 11, 649. https://doi.org/10.3390/rs11060649

Olsen, L.M., Laney, S.R., Duarte, P., Kauko, H.M., Fernández-Méndez, M., Mundy, C.J., Rösel, A., Meyer, A., Itkin, P., Cohen, L., Peeken, I., Tatarek, A., Różańska-Pluta, M., Wiktor, J., Taskjelle, T., Pavlov, A.K., Hudson, S.R., Granskog, M.A., Hop, H., Assmy, P., 2017. The seeding of ice algal blooms in Arctic pack ice: The multiyear ice seed repository hypothesis. J. Geophys. Res. Biogeosci. 122, 2016JG003668. https://doi.org/10.1002/2016JG003668

Oniga, V.-E., Pfeifer, N., Loghin, A.-M., 2018. 3D Calibration Test-Field for Digital Cameras Mounted on Unmanned Aerial Systems (UAS). Remote Sensing 10, 2017. https://doi.org/10.3390/rs10122017

Palmer, J.M., Grant, B.G., 2010. The art of radiometry. SPIE Press, Bellingham, Wash.

Palmisano, A.C., 1987. Sea ice microbial communities. VII. Changes in under-ice spectral irradiance during the development of Antarctic sea ice microalgal communities. Marine Ecology-Progress Series 35, 165–173.

Parkinson, C.L., 2019. A 40-y record reveals gradual Antarctic sea ice increases followed by decreases at rates far exceeding the rates seen in the Arctic. Proc Natl Acad Sci USA 116, 14414–14423. https://doi.org/10.1073/pnas.1906556116

Perkins, R.G., Williamson, C.J., Brodie, J., Barillé, L., Launeau, P., Lavaud, J., Yallop, M.L., Jesus, B., 2016. Microspatial variability in community structure and photophysiology of calcified macroalgal microbiomes revealed by coupling of hyperspectral and high-resolution fluorescence imaging. Scientific Reports 6, 22343. https://doi.org/10.1038/srep22343

Perovich, D.K., 2017. Sea ice and sunlight, in: Thomas, D.N. (Ed.), Sea Ice. John Wiley & Sons, Ltd, pp. 110–137. https://doi.org/10.1002/9781118778371.ch4

Perovich, D.K., 2007. Light reflection and transmission by a temperate snow cover. Journal of Glaciology 53, 201–210.

Perovich, D.K., 2003. Complex yet translucent: the optical properties of sea ice. Physica B: Condensed Matter 338, 107–114. https://doi.org/10.1016/S0921-4526(03)00470-8

Perovich, D.K., 1996. The Optical Properties of Sea Ice. DTIC Document.

Perovich, D.K., 1989. A two-stream multilayer, spectral radiative transfer model for sea ice. DTIC Document.

Petrich, C., Eicken, H., 2016. Overview of sea ice growth and properties, in: Thomas, D.N. (Ed.), Sea Ice. John Wiley & Sons, Ltd, Chichester, UK, pp. 1–41. https://doi.org/10.1002/9781118778371.ch1

Petrich, C., Eicken, H., 2009. Growth, Structure and Properties of Sea Ice, in: Thomas, D.N., Dieckmann, G.S. (Eds.), Sea Ice. Wiley-Blackwell, pp. 23–77.

Petrich, C., Nicolaus, M., Gradinger, R., 2012. Sensitivity of the light field under sea ice to spatially inhomogeneous optical properties and incident light assessed with three-dimensional Monte Carlo radiative transfer simulations. Cold Regions Science and Technology 73, 1–11. https://doi.org/10.1016/j.coldregions.2011.12.004

Pettersen, R., Johnsen, G., Bruheim, P., Andreassen, T., 2014. Development of hyperspectral imaging as a bio-optical taxonomic tool for pigmented marine organisms. Organisms Diversity & Evolution 14, 237–246. https://doi.org/10.1007/s13127-013-0163-1

Piazza, P., Cummings, V., Guzzi, A., Hawes, I., Lohrer, A., Marini, S., Marriott, P., Menna, F., Nocerino, E., Peirano, A., Kim, S., Schiaparelli, S., 2019. Underwater photogrammetry in Antarctica: long-term observations in benthic ecosystems and legacy data rescue. Polar Biol. https://doi.org/10.1007/s00300-019-02480-w

Piazza, P., Cummings, V., Lohrer, D., Marini, S., Marriott, P., Menna, F., Nocerino, E., Peirano, A., Schiaparelli, S., 2018. DIVERS-OPERATED UNDERWATER PHOTOGRAMMETRY: APPLICATIONS IN THE STUDY OF ANTARCTIC BENTHOS. Int. Arch. Photogramm. Remote Sens. Spatial Inf. Sci. XLII–2, 885–892. https://doi.org/10.5194/isprs-archives-XLII-2-885-2018

Polashenski, C., Perovich, D., Courville, Z., 2012. The mechanisms of sea ice melt pond formation and evolution: MECHANISMS OF MELT POND EVOLUTION. J. Geophys. Res. 117. https://doi.org/10.1029/2011JC007231

Post, E., Bhatt, U.S., Bitz, C.M., Brodie, J.F., Fulton, T.L., Hebblewhite, M., Kerby, J., Kutz, S.J., Stirling, I., Walker, D.A., 2013. Ecological Consequences of Sea-Ice Decline. Science 341, 519–524. https://doi.org/10.1126/science.1235225

Ramirez-Paredes, J.-P., Lary, D.J., Gans, N.R., 2016. Low-altitude Terrestrial Spectroscopy from a Pushbroom Sensor. Journal of Field Robotics 33, 837–852. https://doi.org/10.1002/rob.21624

Raoult, V., David, P.A., Dupont, S.F., Mathewson, C.P., O'Neill, S.J., Powell, N.N., Williamson, J.E., 2016. GoPros™ as an underwater photogrammetry tool for citizen science. PeerJ 4. https://doi.org/10.7717/peerj.1960

Raymond, B., Meiners, K., Fowler, C.W., Pasquer, B., Williams, G.D., Nicol, S., 2009. Cumulative solar irradiance and potential large-scale sea ice algae distribution off East Antarctica (30°E–150°E). Polar Biology 32, 443–452. https://doi.org/10.1007/s00300-008-0538-5

Robineau, B., Legendre, L., Kishino, M., Kudoh, S., 1997. Horizontal heterogeneity of microalgal biomass in the first-year sea ice of Saroma-ko Lagoon (Hokkaido, Japan). Journal of Marine Systems, Canada-Japan SARES Project on First-Year Sea Ice 11, 81–91. https://doi.org/10.1016/S0924-7963(96)00030-9

Rodarmel, C., Shan, J., 2002. Principal component analysis for hyperspectral image classification. Surveying and Land Information Science 62, 115.

Ryan, K.G., Hegseth, E.N., Martin, A., Davy, S.K., O'Toole, R., Ralph, P.J., McMinn, A., Thorn, C.J., 2006. Comparison of the microalgal community within fast ice at two sites along the Ross Sea coast, Antarctica. Antarctic Science 18, 583. https://doi.org/10.1017/S0954102006000629

Rysgaard, S., Kühl, M., Glud, R.N., Hansen, J.W., 2001. Biomass, production and horizontal patchiness of sea ice algae in a high-Arctic fjord (Young Sound, NE Greenland). Marine Ecology Progress Series 223, 15–26.

Savitzky, Abraham., Golay, M.J.E., 1964. Smoothing and Differentiation of Data by Simplified Least Squares Procedures. Anal. Chem. 36, 1627–1639. https://doi.org/10.1021/ac60214a047

Schafer, R.W., 2011. What Is a Savitzky-Golay Filter? [Lecture Notes]. IEEE Signal Processing Magazine 28, 111–117. https://doi.org/10.1109/MSP.2011.941097

Shen, X., Cao, L., Yang, B., Xu, Z., Wang, G., 2019. Estimation of Forest Structural Attributes Using Spectral Indices and Point Clouds from UAS-Based Multispectral and RGB Imageries. Remote Sensing 11, 800. https://doi.org/10.3390/rs11070800

Shortis, M., 2015. Calibration Techniques for Accurate Measurements by Underwater Camera Systems. Sensors 15, 30810–30826. https://doi.org/10.3390/s151229831

Sibert, V., Zakardjian, B., Saucier, F., Gosselin, M., Starr, M., Senneville, S., 2010. Spatial and temporal variability of ice algal production in a 3D ice-ocean model of the Hudson Bay, Hudson Strait and Foxe Basin system: Modelling ice algal production in the Hudson Bay system. Polar Research 29, 353–378. https://doi.org/10.1111/j.1751-8369.2010.00184.x

Singh, H., Maksym, T., Wilkinson, J., Williams, G., 2017. Inexpensive, small AUVs for studying ice-covered polar environments. Science Robotics 2.

Smith, G.M., Milton, E.J., 1999. The use of the empirical line method to calibrate remotely sensed data to reflectance. International Journal of Remote Sensing 20, 2653–2662. https://doi.org/10.1080/014311699211994

Smith, W.O., Nelson, D.M., 1985. Phytoplankton bloom produced by a receding ice edge in the ross sea: spatial coherence with the density field. Science 227, 163–166. https://doi.org/10.1126/science.227.4683.163

SooHoo, J.B., Palmisano, A.C., Kottmeier, S.T., Lizotte, M.P., SooHoo, S.L., Sullivan, C.W., 1987. Spectral light absorption and quantum yield of photosynthesis in sea ice microalgae and a bloom of Phaeocystis pouchetii from McMurdo Sound, Antarctica. Marine Ecology-Progress Series 39, 175–189.

Søreide, J.E., Leu, E., Berge, J., Graeve, M., Falk-Petersen, S., 2010. Timing of blooms, algal food quality and Calanus glacialis reproduction and growth in a changing Arctic. Global Change Biology 16, 3154–3163. https://doi.org/10.1111/j.1365-2486.2010.02175.x

Spindler, M., 1994. Notes on the biology of sea ice in the Arctic and Antarctic. Polar Biology 14, 319–324.

Spindler, M., Dieckmann, G.S., 1986. Distribution and abundance of the planktic foraminifer Neogloboquadrina pachyderma. Polar Biol 5, 185–191. https://doi.org/10.1007/BF00441699

Stammerjohn, S., Maksym, T., 2016. Gaining (and losing) Antarctic sea ice: variability, trends and mechanisms, in: Thomas, D.N. (Ed.), Sea Ice. John Wiley & Sons, Ltd, Chichester, UK, pp. 261–289. https://doi.org/10.1002/9781118778371.ch10

Steffens, M., Granskog, M.A., Kaartokallio, H., Kuosa, H., Luodekari, K., Papadimitriou, S., Thomas, D.N., 2006. Spatial variation of biogeochemical properties of landfast sea ice in the Gulf of Bothnia, Baltic Sea. Annals of Glaciology 44, 80–87.

Steiner, N., Deal, C., Lannuzel, D., Lavoie, D., Massonnet, F., Miller, L.A., Moreau, S., Popova, E., Stefels, J., Tedesco, L., 2016. What sea-ice biogeochemical modellers need from observers. Elementa: Science of the Anthropocene 4, 000084. https://doi.org/10.12952/journal.elementa.000084

Sture, Ø., Ludvigsen, M., S⊘reide, F., Aas, L.M.S., 2017. Autonomous underwater vehicles as a platform for underwater hyperspectral imaging, in: OCEANS 2017 - Aberdeen. Presented at the OCEANS 2017 - Aberdeen, pp. 1–8. https://doi.org/10.1109/OCEANSE.2017.8084995

Sturm, M., Massom, R.A., 2016. Snow in the sea ice system: friend or foe?, in: Thomas, D.N. (Ed.), Sea Ice. John Wiley & Sons, Ltd, Chichester, UK, pp. 65–109. https://doi.org/10.1002/9781118778371.ch3

Swadling, K.M., Gibson, J.A.E., Ritz, D.A., Nichols, P.D., 1997. Horizontal patchiness in sympagic organisms of the Antarctic fast ice. Antarctic Science 9, 399–406. https://doi.org/10.1017/S0954102097000515

Taghizadeh, M., Gowen, A.A., O'Donnell, C.P., 2011. Comparison of hyperspectral imaging with conventional RGB imaging for quality evaluation of Agaricus bisporus mushrooms. Biosystems Engineering 108, 191–194. https://doi.org/10.1016/j.biosystemseng.2010.10.005

Tan, C., Wang, D., Zhou, J., Du, Y., Luo, M., Zhang, Y., Guo, W., 2018. Remotely Assessing Fraction of Photosynthetically Active Radiation (FPAR) for Wheat Canopies Based on Hyperspectral Vegetation Indexes. Front Plant Sci 9, 776–776. https://doi.org/10.3389/fpls.2018.00776

Taylor, B.B., Taylor, M.H., Dinter, T., Bracher, A., 2013. Estimation of relative phycoerythrin concentrations from hyperspectral underwater radiance measurements––A statistical approach. J. Geophys. Res. Oceans 118, 2948–2960. https://doi.org/10.1002/jgrc.20201

Tedesco, L., Vichi, M., 2014. Sea ice biogeochemistry: A guide for modellers. PloS one 9, e89217.

Tedesco, L., Vichi, M., Scoccimarro, E., 2019. Sea-ice algal phenology in a warmer Arctic. Sci. Adv. 5, eaav4830. https://doi.org/10.1126/sciadv.aav4830

Telem, G., Filin, S., 2010. Photogrammetric modeling of underwater environments. ISPRS Journal of Photogrammetry and Remote Sensing 65, 433–444. https://doi.org/10.1016/j.isprsjprs.2010.05.004

Thomas, D.N., Dieckmann, G.S., 2002. Antarctic sea ice–a habitat for extremophiles. Science 295, 641–644.

Tonkin, T.N., Midgley, N.G., 2016. Ground-Control Networks for Image Based Surface Reconstruction: An Investigation of Optimum Survey Designs Using UAV Derived Imagery and Structure-from-Motion Photogrammetry. Remote Sensing 8, 786. https://doi.org/10.3390/rs8090786

Treibitz, T., Schechner, Y., Kunz, C., Singh, H., 2012. Flat Refractive Geometry. IEEE Transactions on Pattern Analysis and Machine Intelligence 34, 51–65. https://doi.org/10.1109/TPAMI.2011.105

Tsai, F., Philpot, W., 1998. Derivative analysis of hyperspectral data. Remote Sensing of Environment 66, 41–51.

Tucker, W.B., Gow, A.J., Richter, J.A., 1984. On Small-Scale Horizontal Variations of Salinity in First-Year Sea Ice. Journal of Geophysical Research 89, 6505–6514.

Turner, D., Lucieer, A., Malenovský, Z., King, D., Robinson, S., 2014. Spatial Co-Registration of Ultra-High Resolution Visible, Multispectral and Thermal Images Acquired with a Micro-UAV over Antarctic Moss Beds. Remote Sensing 6, 4003–4024. https://doi.org/10.3390/rs6054003

Turner, D., Lucieer, A., Malenovský, Z., King, D., Robinson, S.A., 2018. Assessment of Antarctic moss health from multi-sensor UAS imagery with Random Forest Modelling. International Journal of Applied Earth Observation and Geoinformation 68, 168–179. https://doi.org/10.1016/j.jag.2018.01.004

Turner, D., Lucieer, A., McCabe, M.F., Parkes, S., Clarke, I., 2017. Pushbroom hyperspectral imaging from an unmanned aircraft system (UAS) - geometric processing workflow and accuracy assessment. https://doi.org/10.5194/isprs-archives-XLII-2-W6-379-2017

van Franeker, J.A., Flores, H., Van Dorssen, M., 2009. The surface and under ice trawl (SUIT). Frozen Desert Alive-The role of sea ice for pelagic macrofauna and its predators PhD thesis. University of Groningen 181–188.

Vancoppenolle, M., Meiners, K.M., Michel, C., Bopp, L., Brabant, F., Carnat, G., Delille, B., Lannuzel, D., Madec, G., Moreau, S., others, 2013. Role of sea ice in global biogeochemical cycles: emerging views and challenges. Quaternary science reviews 79, 207–230.

Verrelst, J., Malenovský, Z., Van der Tol, C., Camps-Valls, G., Gastellu-Etchegorry, J.-P., Lewis, P., North, P., Moreno, J., 2019. Quantifying Vegetation Biophysical Variables from Imaging Spectroscopy Data: A Review on Retrieval Methods. Surv Geophys 40, 589–629. https://doi.org/10.1007/s10712-018-9478-y

VESCOVO, L., WOHLFAHRT, G., BALZAROLO, M., PILLONI, S., SOTTOCORNOLA, M., RODEGHIERO, M., GIANELLE, D., 2012. New spectral vegetation indices based on the near-infrared shoulder wavelengths for remote detection of grassland phytomass. Int J Remote Sens 33. https://doi.org/10.1080/01431161.2011.607195

Vidal, M., Amigo, J.M., 2012. Pre-processing of hyperspectral images. Essential steps before image analysis. Chemometrics and Intelligent Laboratory Systems, Special Issue Section: Selected Papers from the 1st African-European Conference on Chemometrics, Rabat, Morocco, September 2010 Special Issue Section: Preprocessing methods Special Issue Section: Spectroscopic imaging 117, 138–148. https://doi.org/10.1016/j.chemolab.2012.05.009

Volent, Z., Johnsen, G., Sigernes, F., 2009. Microscopic hyperspectral imaging used as a bio-optical taxonomic tool for micro-and macroalgae. Applied optics 48, 4170–4176.

Wadhams, P., Lange, M.A., Ackley, S.F., 1987. The ice thickness distribution across the Atlantic sector of the Antarctic Ocean in midwinter. J. Geophys. Res. 92, 14535–14552. https://doi.org/10.1029/JC092iC13p14535

Wang, L., Zhou, X., Zhu, X., Dong, Z., Guo, W., 2016. Estimation of biomass in wheat using random forest regression algorithm and remote sensing data. The Crop Journal 4, 212–219. https://doi.org/10.1016/j.cj.2016.01.008

Warren, S.G., 1982. Optical proprieties of snow. Reviews of Geophysics and Space Physics 20, 67–89.

Weeks, W.F., Gow, A.J., 1978. Preferred Crystal Orientations in the Fast Ice Along the Margins of the Arctic Ocean. JOURNAL OF GEOPHYSICAL RESEARCH 83.

Welch, H.E., Bergmann, M.A., 1989. Seasonal development of ice algae and its prediction from environmental factors near Resolute, NWT, Canada. Canadian Journal of Fisheries and Aquatic Sciences 46, 1793–1804.

Werner, I., 1997. Grazing of Arctic under-ice amphipods on sea-ice algae. Mar Ecol Prog Ser 160, 93–99. https://doi.org/10.3354/meps160093

Westoby, M.J., Brasington, J., Glasser, N.F., Hambrey, M.J., Reynolds, J.M., 2012. 'Structure-from-Motion' photogrammetry: A low-cost, effective tool for geoscience applications. Geomorphology 179, 300–314. https://doi.org/10.1016/j.geomorph.2012.08.021

Williams, G., Maksym, T., Wilkinson, J., Kunz, C., Murphy, C., Kimball, P., Singh, H., 2014. Thick and deformed Antarctic sea ice mapped with autonomous underwater vehicles. Nature Geoscience 8, 61–67. https://doi.org/10.1038/ngeo2299

Wing, S.R., Leichter, J.J., Wing, L.C., Stokes, D., Genovese, S.J., McMullin, R.M., Shatova, O.A., 2018. Contribution of sea ice microbial production to Antarctic benthic communities is driven by sea ice dynamics and composition of functional guilds. Global Change Biology 24, 3642–3653. https://doi.org/10.1111/gcb.14291

Wongpan, P., Meiners, K.M., Langhorne, P.J., Heil, P., Smith, I.J., Leonard, G.H., Massom, R.A., Clementson, L.A., Haskell, T.G., 2018. Estimation of Antarctic Land-Fast Sea Ice Algal Biomass and Snow Thickness From Under-Ice Radiance Spectra in Two Contrasting Areas. Journal of Geophysical Research: Oceans. https://doi.org/10.1002/2017JC013711

Wynn, R.B., Huvenne, V.A., Le Bas, T.P., Murton, B.J., Connelly, D.P., Bett, B.J., Ruhl, H.A., Morris, K.J., Peakall, J., Parsons, D.R., others, 2014. Autonomous Underwater Vehicles (AUVs): Their past, present and future contributions to the advancement of marine geoscience. Marine Geology 352, 451–468.

Xi, H., Hieronymi, M., Röttgers, R., Krasemann, H., Qiu, Z., 2015. Hyperspectral Differentiation of Phytoplankton Taxonomic Groups: A Comparison between Using Remote Sensing Reflectance and Absorption Spectra. Remote Sensing 7, 14781–14805. https://doi.org/10.3390/rs71114781

Xie, H., Aubry, C., Zhang, Y., Song, G., 2014. Chromophoric dissolved organic matter (CDOM) in first-year sea ice in the western Canadian Arctic. Marine Chemistry 165, 25–35. https://doi.org/10.1016/j.marchem.2014.07.007

Yanez-Rausell, L., Malenovsky, Z., Rautiainen, M., Clevers, J.G.P.W., Lukes, P., Hanus, J., Schaepman, M.E., 2015. Estimation of Spruce Needle-Leaf Chlorophyll Content Based on DART and PARAS Canopy Reflectance Models. IEEE J. Sel. Top. Appl. Earth Observations Remote Sensing 8, 1534–1544. https://doi.org/10.1109/JSTARS.2015.2400418

Yang, C., Yang, D., Cao, W., Zhao, J., Wang, G., Sun, Z., Xu, Z., Kumar, M.S.R., 2010. Analysis of seagrass reflectivity by using a water column correction algorithm. International Journal of Remote Sensing 31, 4595–4608. https://doi.org/10.1080/01431161.2010.485138

Yeh, C.-K., Tsai, V.J.D., 2015. Direct georeferencing of airborne pushbroom images. Journal of the Chinese Institute of Engineers 38, 653–664. https://doi.org/10.1080/02533839.2015.1009410

Zarco-Tejada, P.J., Morales, A., Testi, L., Villalobos, F.J., 2013. Spatio-temporal patterns of chlorophyll fluorescence and physiological and structural indices acquired from hyperspectral imagery as compared with carbon fluxes measured with eddy covariance. Remote Sensing of Environment 133, 102–115. https://doi.org/10.1016/j.rse.2013.02.003

Zeebe, R.E., Eicken, H., Robinson, D.H., Wolf-Gladrow, D., Dieckmann, G., 1996. Modeling the heating and melting of sea ice through light absorption by microalgae. JOURNAL OF GEOPHYSICAL RESEARCH, 101, 1163–1181.

Zhang, X., Huot, Y., Bricaud, A., Sosik, H.M., 2015. Inversion of spectral absorption coefficients to infer phytoplankton size classes, chlorophyll concentration, and detrital matter. Applied Optics 54, 5805. https://doi.org/10.1364/AO.54.005805

Zhao, F., Li, Y., Dai, X., Verhoef, W., Guo, Y., Shang, H., Gu, X., Huang, Y., Yu, T., Huang, J., 2015. Simulated impact of sensor field of view and distance on field measurements of bidirectional reflectance factors for row crops. Remote Sensing of Environment 156, 129–142. https://doi.org/10.1016/j.rse.2014.09.011

Zhao, Y.-R., Li, X., Yu, K.-Q., Cheng, F., He, Y., 2016. Hyperspectral Imaging for Determining Pigment Contents in Cucumber Leaves in Response to Angular Leaf Spot Disease. Scientific Reports 6, 27790. https://doi.org/10.1038/srep27790

Zibordi, G., 2006. Immersion factor of in-water radiance sensors: assessment for a class of radiometers. Journal of Atmospheric and Oceanic Technology 23, 302–313.

Zibordi, G., Voss, K.J., 2014. In situ Optical Radiometry in the Visible and Near Infrared, in: Experimental Methods in the Physical Sciences. Elsevier, pp. 247–304. https://doi.org/10.1016/B978-0-12-417011-7.00010-6